Structure investigations of energetic and pharmaceutical nanoscale composites via AFM-TERS and SERS

Jakob Hübner

To cite this version:

Jakob Hübner. Structure investigations of energetic and pharmaceutical nanoscale composites via AFM-TERS and SERS. Chemical Physics [physics.chem-ph]. Université de Strasbourg, 2020. English. NNT : 2020STRAE009 . tel-03187894

HAL Id: tel-03187894
https://theses.hal.science/tel-03187894
Submitted on 1 Apr 2021

UNIVERSITÉ DE STRASBOURG

ÉCOLE DOCTORALE Physique et Chimie-Physique

Nanomatériaux pour des Systèmes Sous Sollicitations Extrêmes (NS3E)

UMR 3208 ISL-CNRS-UNISTRA

THÈSE présentée par :

Jakob HÜBNER

soutenue le : **26 juin 2020**

pour obtenir le grade de : **Docteur de l'Université de Strasbourg**

Discipline/ Spécialité : Chimie-Physique

Structure Investigations of Energetic and Pharmaceutical Nanoscale Composites via AFM-TERS and SERS

THÈSE dirigée par :

M. Spitzer, Denis	Dr. HDR, Directeur de Recherches à l'ISL, Université de Strasbourg

RAPPORTEURS :

M. SCHACHER, Felix	Prof. Dr. ; Université Friedrich-Schiller Jena
M. DOSSOT, Manuel	Dr. HDR ; Université de Lorraine ; LCPME, UMR 7564

AUTRES MEMBRES DU JURY :

Mme. MOUGIN, Karine	Dr. HDR ; Université de Haute-Alsace ; IS2M, UMR 7361
M. DECHER, Gero	Prof. Dr. ; Université de Strasbourg ; ICS, UPR 22
M. CHAIGNEAU, Marc	Dr. ; Director Nanoscopy Group ; HORIBA France SAS

God made the bulk; surfaces were invented by the devil.

Wolfgang Pauli

Acknowledgment

At this point I would like to express my gratitude to all who have assisted and motivated me during the period of this doctoral thesis.

At first, I would like to thank the French-German-Research Institute of Saint-Louis and the Région Grand Est for the financial support.

My special thanks go to Dr. HDR Denis Spitzer who made this thesis possible in the first place. Moreover, he introduced me in the topic and supported me in a manner which no one could possibly imagine to be any better. Moreover, I would like to thank Dr. Tanja Deckert-Gaudig and Prof. Dr. Volker Deckert for their theoretical and practical advices based on their outstanding knowledge of Tip Enhanced Raman Spectroscopy. Furthermore, my special thanks go to Prof. Dr. Carola Kryschi and Dr. Martin Klaumünzer for the excellent education during my bachelor and master studies, without this work would not have been possible. Also, I would like to thank all my colleagues who cordially included me in their team.

Moreover, I would like to thank Christine Begander, my parents and my family who made my studies possible by their unlimited support.

Finally, I want to express my special thanks to all my friends, especially Dr. Robert Rosenzweig, Peter Schlee, Patrick Hilbrenner and Valentin Kuffer who always stand on my site, motivate and support me in all situations.

Thank you very much!
Jakob Hübner

Notice:

The research chapters of this thesis (chapter 3, 4 and 5) are written in form of self-contained research articles. Consequently, the terms “abstract”, and “supporting information” are used. To avoid repetitions, the presented thesis does not contain a section on methodology and instrumentation, since the experimental details are given in the research chapters. Although the research chapters consist of individual articles, this thesis should give a coherent picture of structure investigations of organic nano-composites via near- and far-field Raman spectroscopy methods. At the time of submission to the examiners, the status of the publications is as follows:

Chapter 3 is published at:
Hübner, J.; Deckert-Gaudig, T.; Glorian, J.; Deckert, V. K.; Spitzer, D., Surface Characterization of Nanoscale Co-Crystals Enabled through Tip Enhanced Raman Spectroscopy. *Nanoscale* **2020**, *18*, 10306-10319, DOI: 10.1039/D0NR00397B

Chapter 4 is published online at *chemrxiv.org* and is currently under review in a scientific journal:
Hübner, J.; Pichot, V.; Lobry, E.; Deckert-Gaudig, T.; Deckert, V.; Spitzer, D., Formation Mechanism of Anisotropic RDX-TNT Core-Shell Nanoparticles and their Influence onto Nanodiamond Detonation Syntheses, *chemrxiv.org,* **2020**, DOI: 10.26434/chemrxiv.12005625.v1

Chapter 5 is published online at *chemrxiv.org* and is currently under review in a scientific journal:
Hübner, J.; Coty J.-B.; Busby, Y.; Spitzer, D., Formation Mechanisms of Sub-Micron Pharmaceutical Composite Particles Derived from Far- and Near Field Raman Microscopy, *chemrxiv.org*, **2020**, DOI: 10.26434/chemrxiv.12098478.v1

Once Chapter 3 and Chapter 4 have been accepted, the link to the reviewed and published versions will be found in the preprints under the indicated DOIs.

Table of Contents

1 Introduction

The kinetics of chemical and physical reactions depend not only on the used chemicals but also on their sizes, morphologies, surface compositions and molecular arrangements. This relationship can be observed, for example, in the adsorption of gases on particle surfaces or when chemicals are dissolved in a solvent. The influence of size, morphology, surface composition and arrangement becomes particularly clear in solid state reactions, *e.g.* combustions, of particulate precursors.[1-2] Therefore, a detailed knowledge of these parameters is essential in order to be able to describe their reactions in detail and thus produce tailor-made reactants for several applications. This task is relatively easy for reactants consisting of one compound only. For this purpose, it is normally sufficient to examine the particles using standard analytical methods. The chemical composition can be determined by nuclear magnetic resonance spectroscopy, infrared or Raman spectroscopy, for example. Particle morphologies and sizes, in turn, can be determined by microscopic methods such as transmission electron microscopy (TEM), scanning electron microscopy (SEM), scanning tunnel microscopy (STM) or atomic force microscopy (AFM). However, it becomes considerably more difficult if the reactant particles are formed from different chemical compounds. Especially, if the particles sizes are on the sub-micro or nanoscale. The influence of particle size and arrangement on the reaction behavior as well as their structural investigation will be briefly explained using the example of two different aluminum-based iron oxide/-hydroxide nanothermites (i) and (ii) which were both synthesized via a wet-chemical process.[1] The difference in the synthesis routine of both thermites lies only in the temperature, i.e. (i) is synthesized at 20°C and (ii) at 50°C. Nevertheless, (i) shows a significantly higher flame propagation velocity (472 ms^{-1}) than (ii) (323 ms^{-1}). This difference cannot only be explained by the chemical composition because differential scanning calorimetry analyses show that both thermites consist of almost the same composition. Hence, TEM was performed to obtain information about the structural arrangements of the two nanothermites. However, the TEM images shown in Figure 1 do not present any major structural differences between the two samples. Therefore, a further measuring method had to be found which allows simultaneous imaging of microscopic and spectroscopic results. For this purpose, energy dispersive X-ray (EDX) spectroscopy coupled with TEM was applied. This technique measures emitted element-specific X-rays and images

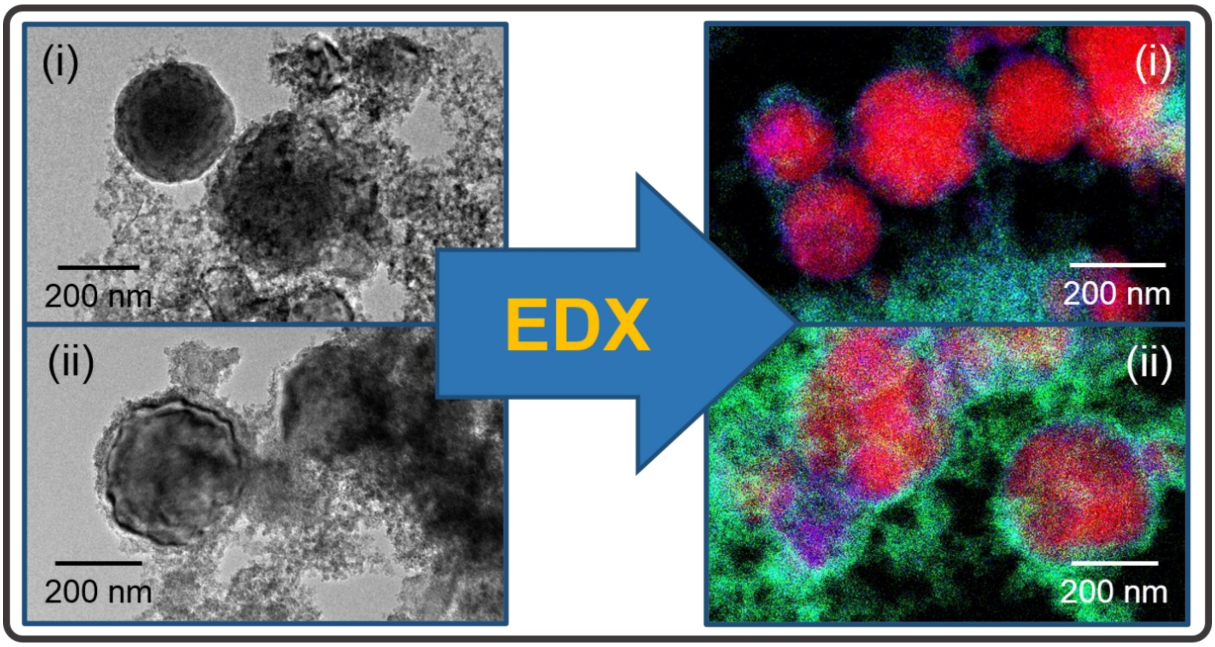

Figure 1.1. Left: TEM images of two aluminum-based iron oxide/-hydroxide nanothermites (i) and (ii). The TEM images present no significant structural difference. **Right:** EDX-TEM images of the same nanothermites . The EDX-TEM images reveal, that (i) is formed from aluminum particles (red) embedded in an iron oxide/-hydroxide matrix (iron: green, oxide: blue), whereas (ii) is formed by hierarchically structured aluminum/Iron oxide/-hydroxide core/shell particles embedded in an iron oxide/-hydroxide matrix.

them microscopically in nanometric resolution. Only through the application of EDX-TEM, the difference between the two nanothermites becomes apparent. Accordingly, (i) is formed from aluminum nanoparticles embedded in an iron oxide/-hydroxide matrix, whereas (ii) are built up by aluminum/iron oxide core/shell particles also embedded in an iron oxide/-hydroxide matrix (Figure 1.1, right). This structural difference finally allows to draw conclusions about the different reaction behaviors of the nanothermites (i) and (ii).

Is the combination of TEM and EDX therefore also the method of choice for structure investigations of organic nanocomposites? Unfortunately, it is not, and there are several reasons for this. On the one hand, electron microscopy methods like SEM and TEM provide a high energy input to the investigated sample. This high energy input can lead to dissociation of the molecules of organic nanocomposites. Especially organic energetic and pharmaceutical substances tend to do so. In addition, both SEM and TEM are carried out under high vacuum (10^{-5} – 10^{-7} mbar).[3] The applied high vacuum can cause sublimation of organic substances and thus falsify the measurement results. Moreover, EDX provides only information about the elemental composition of the sample. Organic substances (especially energetic substances), however, are formed mainly from carbon, hydrogen, nitrogen and oxygen. Hence, it is not possible with EDX-TEM to map the arrangement of the different molecules within a composite nanoparticle. Consequently, another analysis method must be found fulfilling the following requirements. Firstly, the method must be relatively gentle in terms of energy input to the sample and measurement environment. Secondly, the method must be able to distinguish between different molecules. And thirdly, the method must offer a high spatial resolution that allows individual particles to be examined.

All these requirements for the investigation of nanoscale composites are fulfilled by tip enhanced Raman spectroscopy (TERS). If the nanoscale composites aggregate to sub-micro composites, surface enhanced Raman spectroscopy (SERS) can be performed on a confocal Raman microscope to investigate these superstructures. As the name suggests, both methods are based on Raman spectroscopy. However, Raman spectroscopy requires a relatively large amount of sample molecules because the probability of a photon becoming Raman scattered is very low, which makes it impossible to study individual particles. The difference between SERS and conventional Raman spectroscopy is that in SERS the sample to be analyzed is first deposited on or near a nanostructured metal substrates (mainly gold or silver). If the sample is now irradiated with a laser, the valence electrons of the metal particles are excited to a collective oscillation. The collective oscillation of the valence electrons causes an enhancement of the electric field near the metal particle surfaces (<10 nm), especially, if they oscillate in resonance with the incident laser light (localized surface plasmon resonance).[4-5] If a sample is placed within this enhanced field, the probability that a photon becomes Raman scattered is drastically increased. This makes it possible to study individual nanoparticles. In special experimental setups, it is even possible to investigate the vibrations of single molecules with SERS.[6-7] Due to its ability to study small amounts of sample molecules, SERS is used in a variety of applications. Thus, SERS is used in bio-medical approaches like the detection of biomarkers, the detection of circulating tumor cells or detection of pathogens.[8-18] Moreover, SERS is used for the detection and the quantification of environmental toxins and chemicals.[7, 19-23] In addition, SERS can be used for analyzing drinking water and food.[24-25]

Tip enhanced Raman spectroscopy is an advanced technology based on SERS. TERS combines the outstanding properties of SERS with a scanning probe microscopy (SPM) method, such as STM or AFM. In contrast to SERS, where the sample is applied to metallic nanoparticle surfaces, the tip of a SPM is equipped with a metallic nanoparticle in TERS. This allows a sample to be microscopically scanned and the metal nanoparticle at the tip to be moved to any position on the sample. Accordingly, it is possible to bring the field-enhancing nanoparticle onto positions of interests of the sample surface and not the sample onto the metal nanoparticle. This and the fact that the electric field amplification is generated by a single nanoparticle makes TERS much more selective than SERS. In addition, TERS offers a lateral resolution of less than 1 nm making TERS a promising tool for structure investigations of organic nanoscale composites.[5, 26-28] TERS is used *inter alia* for analyzing organic molecules, self-assembled monolayers, chemical reactions, biological samples and for material characterization.[29-39]

Within this thesis, various organic and energetic organic nano and submicron composites are characterized via conventional Raman spectroscopy (far-field Raman), TERS and SERS (near-field Raman). The experimental details, the results and the conclusions which could be drawn from these investigations as well as a detailed description of the theoretical background of Raman scattering, SERS and TERS are presented in the following.

1.1 References

1. Hübner, J.; Klaumünzer, M.; Comet, M.; Martin, C.; Vidal, L.; Schäfer, M.; Kryschi, C.; Spitzer, D., Insights into Combustion Mechanisms of Variable Aluminum-Based Iron Oxide/-Hydroxide Nanothermites. *Combust. Flame* **2017,** *184*, 186-194.

2. Pichot, V.; Risse, B.; Schnell, F.; Mory, J.; Spitzer, D., Understanding ultrafine nanodiamond formation using nanostructured explosives. *Sci. Rep.* **2013,** *3* (1), 2159.

3. Williams, D. B.; Carter, C. B., Transmission Electron Microscopy. Springer US: 2009.

4. Stiles, P. L.; Dieringer, J. A.; Shah, N. C.; Van Duyne, R. P., Surface-enhanced Raman spectroscopy. *Annu. Rev. Anal. Chem.* **2008,** *1*, 601-626.

5. Deckert-Gaudig, T.; Taguchi, A.; Kawata, S.; Deckert, V., Tip-Enhanced Raman Spectroscopy – From Early Developments to Recent Advances. *Chem. Soc. Rev.* **2017,** *46*, 4077.

6. Benz, F.; Schmidt, M. K.; Dreismann, A.; Chikkaraddy, R.; Zhang, Y.; Demetriadou, A.; Carnegie, C.; Ohadi, H.; de Nijs, B.; Esteban, R.; Aizpurua, J.; Baumberg, J. J., Single-Molecule Optomechanics in Picocavities. *Science* **2016,** *354*, 726.

7. Langer, J.; Jimenez de Aberasturi, D.; Aizpurua, J.; Alvarez-Puebla, R. A.; Auguié, B.; Baumberg, J. J.; Bazan, G. C.; Bell, S. E. J.; Boisen, A.; Brolo, A. G.; Choo, J.; Cialla-May, D.; Deckert, V.; Fabris, L.; Faulds, K.; García de Abajo, F. J.; Goodacre, R.; Graham, D.; Haes, A. J.; Haynes, C. L.; Huck, C.; Itoh, T.; Käll, M.; Kneipp, J.; Kotov, N. A.; Kuang, H.; Le Ru, E. C.; Lee, H. K.; Li, J.-F.; Ling, X. Y.; Maier, S. A.; Mayerhöfer, T.; Moskovits, M.; Murakoshi, K.; Nam, J.-M.; Nie, S.; Ozaki, Y.; Pastoriza-Santos, I.; Perez-Juste, J.; Popp, J.; Pucci, A.; Reich, S.; Ren, B.; Schatz, G. C.; Shegai, T.; Schlücker, S.; Tay, L.-L.; Thomas, K. G.; Tian, Z.-Q.; Van Duyne, R. P.; Vo-Dinh, T.; Wang, Y.; Willets, K. A.; Xu, C.; Xu, H.; Xu, Y.; Yamamoto, Y. S.; Zhao, B.; Liz-Marzán, L. M., Present and Future of Surface-Enhanced Raman Scattering. *ACS Nano* **2020,** *14* (1), 28-117.

8. Chisanga, M.; Muhamadali, H.; Ellis, D. I.; Goodacre, R., Surface-Enhanced Raman Scattering (SERS) in Microbiology: Illumination and Enhancement of the Microbial World. *Appl. Spectrosc.* **2018,** *72* (7), 987-1000.

9. Dina, N. E.; Zhou, H.; Colniţă, A.; Leopold, N.; Szoke-Nagy, T.; Coman, C.; Haisch, C., Rapid Single-Cell Detection and Identification of Pathogens by Using Surface-Enhanced Raman Spectroscopy. *Analyst* **2017,** *142*, 1782.

10. Carmicheal, J.; Hayashi, C.; Huang, X.; Liu, L.; Lu, Y.; Krasnoslobodtsev, A.; Lushnikov, A.; Kshirsagar, P. G.; Patel, A.; Jain, M.; Lyubchenko, Y. L.; Lu, Y.; Batra, S. K.; Kaur, S., Label-Free Characterization of Exosome via Surface Enhanced Raman Spectroscopy for the Early Detection of Pancreatic Cancer. *Nanomedicine* **2019,** *16*, 88.

11. Zhao, Y.; Liu, L.; Kuang, H.; Wang, L.; Xu, C., SERS-Active Ag@Au Core–Shell NP Assemblies for DNA Detection. *RSC Adv.* **2014,** *4*, 56052.

12. Carroll, S.; Al-Rubeai, M., ACSD Labelling and Magnetic Cell Separation: A Rapid Method of Separating Antibody Secreting Cells from Non-Secreting Cells. *J. Immunol. Methods* **2005,** *296*, 171.

13. Pallaoro, A.; Hoonejani, M. R.; Braun, G. B.; Meinhart, C. D.; Moskovits, M., Rapid Identification by Surface-Enhanced Raman Spectroscopy of Cancer Cells at Low Concentrations Flowing in a Microfluidic Channel. *ACS Nano* **2015,** *9*, 4328.

14. Wu, X.; Luo, L.; Yang, S.; Ma, X.; Li, Y.; Dong, C.; Tian, Y.; Zhang, L.; Shen, Z.; Wu, A., Improved SERS Nanoparticles for Direct Detection of Circulating Tumor Cells in the Blood. *ACS Appl. Mater. Interfaces* **2015,** *7*, 9965.

15. Jarvis, R. M.; Brooker, A.; Goodacre, R., Surface-Enhanced Raman Spectroscopy for Bacterial Discrimination Utilizing a Scanning Electron Microscope with a Raman Spectroscopy Interface. *Anal. Chem.* **2004,** *76*, 5198.

16. Patel, I. S.; Premasiri, W. R.; Moir, D. T.; Ziegler, L. D., Barcoding Bacterial Cells: A SERS-Based Methodology for Pathogen Identification. *J. Raman Spectrosc.* **2008,** *39*, 1660.

17. Kelly, J.; Patrick, R.; Patrick, S.; Bell, S. E. J., Surface-Enhanced Raman Spectroscopy for the Detection of a Metabolic Product in the Headspace Above Live Bacterial Cultures. *Angew. Chem. Int. Ed.* **2018,** *57*, 15686.

18. Bodelon, G.; Montes-Garcia, V.; Lopez-Puente, V.; Hill, E. H.; Hamon, C.; Sanz-Ortiz, M. N.; Rodal-Cedeira, S.; Costas, C.; Celiksoy, S.; Perez-Juste, I.; Scarabelli, L.; La Porta, A.; Perez-Juste, J.; Pastoriza-Santos, I.; Liz-Marzan, L. M., Detection and Imaging of Quorum Sensing in Pseudomonas aeruginosa Biofilm Communities by Surface-Enhanced Resonance Raman Scattering. *Nat. Mater.* **2016,** *15*, 1203.

19. Zhu, Y.; Kuang, H.; Xu, L.; Ma, W.; Peng, C.; Hua, Y.; Wang, L.; Xu, C., Gold Nanorod Assembly Based Approach to Toxin Detection by SERS. *J. Mater. Chem.* **2012,** *22*, 2387.

20. Feng, J.; Xu, L.; Cui, G.; Wu, X.; Ma, W.; Kuang, H.; Xu, C., Building SERS-Active Heteroassemblies for Ultrasensitive Bisphenol A Detection. *Biosens. Bioelectron.* **2016,** *81*, 138.

21. Li, A.; Tang, L.; Song, D.; Song, S.; Ma, W.; Xu, L.; Kuang, H.; Wu, X.; Liu, L.; Chen, X.; Xu, C., A SERS-Active Sensor Based on Heterogeneous Gold Nanostar Core-Silver Nanoparticle Satellite Assemblies for Ultrasensitive Detection of Aflatoxinb1. *Nanoscale* **2016,** *8*, 1873.

22. Schmit, V. L.; Martoglio, R.; Scott, B.; Strickland, A. D.; Carron, K. T., Lab-on-a-Bubble: Synthesis, Characterization, and Evaluation of Buoyant Gold Nanoparticle-Coated Silica Spheres. *J. Am. Chem. Soc.* **2012,** *134*, 59.

23. Xu, L.; Yin, H.; Ma, W.; Kuang, H.; Wang, L.; Xu, C., Ultrasensitive SERS Detection of Mercury Based on the Assembled Gold Nanochains. *Biosens. Bioelectron.* **2015,** *67*, 472.

24. Patze, S.; Huebner, U.; Liebold, F.; Weber, K.; Cialla-May, D.; Popp, J., SERS as an Analytical Tool in Environmental Science: The Detection of Sulfamethoxazole in Water in the Nanomolar Range by Applying a Microfluidic Cartridge Setup. *Anal. Chim. Acta* **2017,** *949*, 1.

25. Radu, A. I.; Ryabchykov, O.; Bocklitz, T. W.; Huebner, U.; Weber, K.; Cialla-May, D.; Popp, J., Toward Food Analytics: Fast Estimation of Lycopene and Β-Carotene Content in Tomatoes Based on Surface Enhanced Raman Spectroscopy (SERS). *Analyst* **2016,** *141*, 4447.

26. Trautmann, S.; Aizpurua, J.; Götz, I.; Undisz, A.; Dellith, J.; Schneidewind, H.; Rettenmayr, M.; Deckert, V., A Classical Description of Subnanometer Resolution by Atomic Features in Metallic Structures. *Nanoscale* **2017,** *9* (1), 391-401.

27. Deckert-Gaudig, T.; Kurouski, D.; Hedegaard, M. A. B.; Singh, P.; Lednev, I. K.; Deckert, V., Spatially resolved spectroscopic differentiation of hydrophilic and hydrophobic domains on individual insulin amyloid fibrils. *Sci. Rep.* **2016,** *6* (1), 33575.

28. Deckert-Gaudig, T.; Kämmer, E.; Deckert, V., Tracking of Nanoscale Structural Variations on a Single Amyloid Fibril with Tip-Enhanced Raman Scattering. *J. Biophotoics.* **2012,** *5*, 215.

29. Stockle, R.; Suh, Y.; Deckert, V.; Zenobi, R., Nanoscale Chemical Analysis by Tip-Enhanced Raman Spectroscopy. *Chem. Phys. Lett.* **2000,** *318*, 131.

30. Hayazawa, N.; Inouye, Y.; Sekkat, Z.; Kawata, S., Metallized Tip Amplification of Near-Field Raman Scattering. *Opt. Commun.* **2000,** *183*, 333.

31. Hartschuh, A.; Anderson, N.; Novotny, L., Near-field Raman spectroscopy using a sharp metal tip. *Journal of Microscopy* **2003,** *210* (3), 234-240.

32. Chaigneau, M.; Picardi, G.; Ossikovski, R., Molecular arrangement in self-assembled azobenzene-containing thiol monolayers at the individual domain level studied through polarized near-field Raman spectroscopy. *Int. J. Mol.* **2011,** *12* (2), 1245-1258.

33. Jiang, N.; Chiang, N.; Madison, L. R.; Pozzi, E. A.; Wasielewski, M. R.; Seideman, T.; Ratner, M. A.; Hersam, M. C.; Schatz, G. C.; Van Duyne, R. P., Nanoscale Chemical Imaging of a Dynamic Molecular Phase Boundary with Ultrahigh Vacuum Tip-Enhanced Raman Spectroscopy. *Nano Lett.* **2016,** *16*, 3898.

34. Stadler, J.; Schmid, T.; Zenobi, R., Nanoscale Chemical Imaging of Single-Layer Graphene. *ACS Nano* **2011,** *5* (10), 8442-8448.

35. van Schrojenstein Lantman, E. M.; Deckert-Gaudig, T.; Mank, A. J. G.; Deckert, V.; Weckhuysen, B. M., Catalytic Processes Monitored at the Nanoscale with Tip-Enhanced Raman Spectroscopy. *Nat. Nanotechnol.* **2012,** *7*, 583.

36. Zhang, Z.; Deckert-Gaudig, T.; Deckert, V., Label-free monitoring of plasmonic catalysis on the nanoscale. *Analyst* **2015,** *140* (13), 4325-4335.

37. Treffer, R.; Lin, X.; Bailo, E.; Deckert-Gaudig, T.; Deckert, V., Distinction of Nucleobases - a Tip-Enhanced Raman Approach. *Beilstein J. Nanotechnol.* **2011,** *2*, 628.

38. Deckert-Gaudig, T.; Pichot, V.; Spitzer, D.; Deckert, V., High-Resolution Raman Spectroscopy for the Nanostructural Characterization of Explosive Nanodiamond Precursors. *ChemPhysChem* **2017,** *18* (2), 175-178.

39. Höppener, C.; Schacher, F. H.; Deckert, V., Multimodal Characterization of Resin Embedded and Sliced Polymer Nanoparticles by Means of Tip-Enhanced Raman Spectroscopy and Force–Distance Curve Based Atomic Force Microscopy. *Small* **2020**, 1907418.

2 Theoretical Background

Within this chapter the theoretical background of Raman spectroscopy in general, surface enhanced Raman spectroscopy (SERS) and tip enhanced Raman spectroscopy (TERS) is presented. Especially, intrinsic features of Raman scattering, SERS and TERS are examined in more detail since they form the basis for the presented spectra analyses.

2.1 Basics of Light-Molecule Interactions

To develop a deeper understanding about the mechanism of Raman scattering, it is useful to discuss shortly the basic principles of the interactions between light and matter. Basically, there exist various mechanisms of light-matter interactions. These mechanisms depend strongly on the energy of the incident light. Since Raman spectroscopy is exclusively undertaken with near ultra-violet (NUV), visible (VIS) or near infrared (NIR) light, only interactions between matter and light with wavelengths between 200 nm and 50000 nm (50000 cm^{-1} – 200 cm^{-1}) are presented. Furthermore, the here investigated composite systems consist solely of organic submicron and nanoparticles, thus the focus of the following introduction is on light-molecule interactions in the previously mentioned spectral range.

2.1.1 Molecular Energy Levels

Interactions between light and matter are typically connected with energy transfers. Therefore, it is of fundamental importance for the description of light-matter interactions to know how energy is distributed in molecules. Basically, the total molecular energy comprises of the summation of its electronic, vibrational, rotational, nuclear and translational energy: [1]

$$E_{tot} = E_{el} + E_{vib} + E_{rot} + E_{nuc} + E_{trans}\ . \qquad \text{Eq. 2.1}$$

Due to quantum mechanics, molecules cannot absorb all energy values. Like atoms, molecules have specific energy levels (often energy states) which can solely adopt discrete values. Excepted from this quantization is only the translational energy E_{trans}. Moreover, the occupation of the energy levels of the atom nuclei and thus E_{nuc} stays normally constant during interactions with light. Thus, it is not necessary to include E_{trans} and E_{nuc} into consideration for the description of molecular energy levels. This simplification is, in addition, permissible, since spectroscopic investigations deal only with the energy differences between certain energy levels and not with total energy level values.

Anyway, the main tool to describe quantum mechanically the behavior of atoms and molecules is the wave function ψ. This wave function describes distinctly the state of a quantum system although it has no physical meaning. To ascertain all possible energy levels a quantum mechanically system can adopt, the Hamiltonian $\hat{H}$ is applied on the wave function ψ resulting in the Schrödinger equation: [2]

$$\hat{H}\psi = E\psi. \qquad \text{Eq. 2.2}$$

All wave functions solving the Schrödinger equation are eigenfunctions of the Hamiltonian $\hat{H}$ and describe the adoptable quantum states. The energy eigenvalues E corresponding to the eigenfunctions represent the energy values of the quantum state, respectively energy level. The Hamiltonian $\hat{H}$ itself is built up by the sum of the operators of the kinetic energy $\hat{T}$ and potential energy $\hat{V}$: [2]

$$\hat{H} = \hat{T} + \hat{V}. \qquad \text{Eq. 2.3}$$

Therefore, the energy levels of atoms and further molecules can be calculated by the set-up of an appropriate Hamiltonian and the solution of the Schrödinger equation. If one applies this scheme to describe quantum mechanically the energy levels for one of the simplest real existing quantum mechanical systems the hydrogen atom, it turns out that some energy eigenvalues correspond to different eigenfunctions. These quantum states have equivalent energy levels and are called degenerated quantum states. To distinguish these quantum states, it is necessary to introduce four quantum numbers. These are the principal quantum number n describing the energy level of an electron, the azimuthal quantum number l giving the shape of the orbital, the magnetic quantum number m_l subdividing the orbital shape referring to its spatial orientation towards a freely chosen coordinate system axis. The spin quantum number m_s describes the electron spin within the orbital. The squares of the eigenfunctions solving the Schrödinger equation for a hydrogen atom give the probability density of the electron. The projection of the real part of the spherical harmonic of the wave functions onto a Cartesian coordinate system depict graphically the shapes of the orbitals. Table 2.1 summarizes the possible values of the quantum numbers. The calculations are not shown since the mathematical background is not of relevance for a better understanding of the later presented spectroscopic experiments and results. Interested readers are referred here to comprehensive standard works about quantum mechanical and molecular physics (e.g. references 1-3).

Table 2.1. Quantum numbers

Quantum numbers	**Values**	**Atom terms**
n	1, 2, 3, 4, 5, …	1, 2, 3, 4, 5, …
l	0	s
	1	p
	2, 3, 4, …	d, f, g, …
	n – 1	after f in alphabetic order
m_l	$-l$, …, -1, 0, +1, …, $+l$	e.g. p_x, p_y, p_z
m_s	- ½ , + ½	↓, ↑

The quantum numbers allow to describe each atomic electronic state which can be occupied within an atom and thus the electronic energy E_{el}. This changes if several atoms form chemical bonds and arrange each other to molecules with molecule orbitals. Since molecules consists from nature of at least two atoms, molecular total energy E_{tot} contains additionally vibrational energy E_{vib} and rotational energy E_{rot} proportions (compare Eq. 2.1). The vibrational energy

E_{vib} and rotational energy E_{rot} proportions arise from the higher amount of degrees of freedom which is provided by molecules compared to atoms. The total number of degrees of freedom f_{tot} of atoms or molecules is given as

$$f_{tot} = 3n\,, \qquad \text{Eq. 2.4}$$

respectively as

$$f_{tot} = f_{trans} + f_{vib} + f_{rot}\,, \qquad \text{Eq. 2.5}$$

where n represents the number of atoms, f_{trans} the translation degrees of freedom, f_{vib} the vibration degrees of freedom and f_{rot} the rotation degrees of freedom.[1] The amount of vibrational degrees of freedom f_{vib} and rotational degrees of freedom f_{rot} is next to the number of atoms related to the molecular arrangement. Thus, linear molecules provide more vibration degrees of freedom but less rotation degrees of freedom than nonlinear molecules with the same number of atoms. These differences are summed up in Table 2.2.

Table 2.2 Differences in degrees of freedom between linear and nonlinear molecules

degrees of freedom	**linear molecules**	**nonlinear molecules**
f_{trans}	3	3
f_{vib}	3n-5	3n-6
f_{rot}	2	3
f_{tot}	3n	3n

Each vibrational degree of freedom and rotational degree of freedom represents a single molecular vibration and rotation which can absorb (and emit) energy. Like the electronic energy

E_{el}, molecular vibrations and rotations can only absorb (and emit) certain energy values. Thus, also E_{vib} and E_{rot} are quantized. Molecular rotations are quantum mechanically treated as linear ridged rotators. However, since later presented Raman experiments are performed on solids only, molecular rotational energy levels are not further discussed. Anyway, molecular vibrations can be quantum mechanically approximated as harmonic oscillator. In accordance to classical mechanics, the quantum mechanical harmonic oscillator describes a particle, e.g. a molecule, in a potential of the general form

$$V(x) = \frac{1}{2}kx^2 = \frac{1}{2}m\omega^2x^2, \qquad \text{Eq. 2.6}$$

with k is the force constant, x is the particle position, m the mass of the particle and ω is the angular frequency.[3] Since molecule vibrations are in focus of this thesis, the particle position x is given as the normal coordinate q of a molecule vibration in the following. The normal coordinate q gives the relative position of all molecule atoms during the molecule vibration relative to their equilibrium positions (Figure 2.1, left). The vibration energy eigenstates of a quantum mechanical oscillator can be calculated by finding an appropriate Hamiltonian (Eq. 2.3) and solving the Schrödinger equation (Eq. 2.2). The kinetic energy operator of a particle is given as:[3]

$$\hat{T} = \frac{\hat{p}^2}{2m} = -\frac{\hbar^2}{m}\frac{d^2}{dq^2}. \qquad \text{Eq. 2.7}$$

Following Eq. 2.6 and Eq. 2.7, the Hamiltonian of a harmonic oscillator is

$$\hat{H} = -\frac{\hbar^2}{m}\frac{d^2}{dq^2} + \frac{m\omega^2}{2}q^2 \qquad \text{Eq. 2.8}$$

and the resulting Schrödinger equation is

$$\left[-\frac{\hbar^2}{m}\frac{d^2}{dq^2}+\frac{m\omega^2}{2}q^2\right]\psi(q)=E\psi(q). \quad \text{Eq. 2.9}$$

The solution of this differential equation gives the eigenfunctions of $\psi_v(q)$ of the harmonic oscillator which are the Hermite-functions

$$\psi_v(q)=\frac{\left(\frac{m\omega}{\hbar\pi}\right)^{\frac{1}{4}}}{\sqrt{2^v v!}}H_v\left(\sqrt{\frac{m\omega}{\hbar}}q\right)e^{\left(-\frac{m\omega}{2\hbar}q^2\right)} \quad \text{Eq. 2.10}$$

with the corresponding energy levels

$$E_v(q)=\hbar\omega(v+\tfrac{1}{2})\,.^{2} \quad \text{Eq. 2.11}$$

The harmonic oscillator eigenfunctions, especially their symmetries, are important for estimating if a vibration is Raman active or not and is discussed in more detail later within the semi quantum mechanical description of Raman scattering. The energy levels of the corresponding molecule vibration states are equally distributed with an energy difference of $\hbar\omega$ between two successive states. Furthermore, the zero-point energy of the vibrational ground state v_0 is $\hbar\omega/2$ and thus in accordance with the Heisenberg uncertainly principle (Figure 2.1, right). Anyway, the model of the quantum mechanical harmonic oscillator is not sufficient to describe the energy distribution of molecules in general. The harmonic oscillator provides an infinite parabolic potential resulting in the occurrence of vibrational energy states characterized by infinitely high energy levels. This is in contradiction to the natural behavior of molecules.

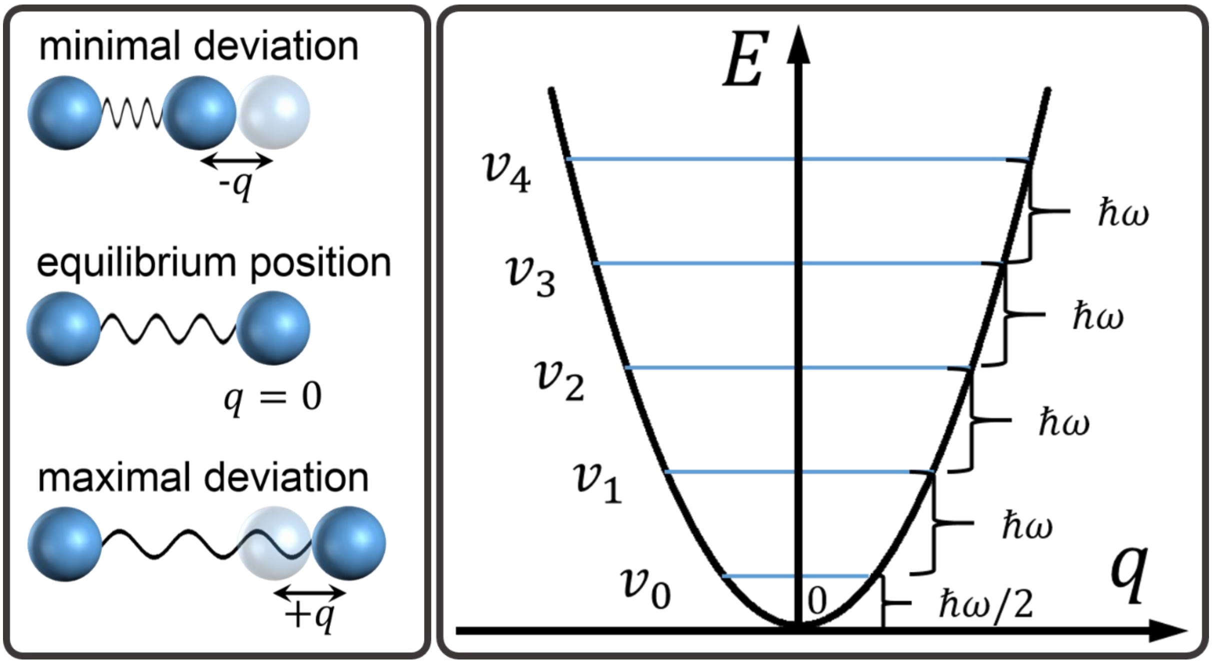

Figure 2.1. Left: The normal coordinate q defines the relative position of atoms during a molecular vibrations related to their equilibrium positions. Blue spheres represent any atoms. **Right:** Parabolic potential of the harmonic oscillator. Blue lines depict certain vibrational energy states v. The energy difference between two vibrational states is $\hbar\omega$. The vibrational ground state v_0 energy is $\hbar\omega/2$.

Higher vibration energy levels are related with higher minimal and maximal deflections of the normal coordinate q. The shorter the minimal deviation the stronger are the repulsive forces between the atomic nuclei. Accordingly, the atomic nuclei involved in the molecule vibration cannot arbitrarily near each other. On the other hand, the wider the maximal deviation the weaker are the molecular bond resulting in the dissociation of the molecule.[1] A more accurate quantum mechanical description of molecule vibrations is the anharmonic oscillator. The quantum mechanical anharmonic oscillator defines a maximal vibration state related with a maximal energy level, the dissociation energy (Figure 2.2). Furthermore, the energy differences between two successive vibrational states are not constant like they are in case of the harmonic oscillator; with increasing v the energy differences become smaller. However, this effect gains only increasing importance for higher vibrational states. Since only fundamental vibrational frequencies (v_0 to v_1) are investigated in the later presented Raman spectroscopy experiments, the quantum mechanical harmonic oscillator remains a sufficient tool to describe the results.

By “combing” the electronic energy states n and the vibrational energy states v an impression can be created how energy is distributed in molecules. Thus, every electronic state has subordinate vibrational states. Figure 2.2 depict schematically the energy distribution within molecules. Generally, the vibration energy states are further subdivided by the molecule rotation states. Since rotation transitions are not investigated in the following and to guarantee comprehensibility, molecule rotation states are not presented within Figure 2.2.

In conclusion, quantum mechanical considerations allow to describe the energy distribution within a molecule. Accordingly, solely discrete energy states can be occupied. The energy states are built up by electronic states subdivided by vibration states which are further subdivided by the rotation states. This approximated quantum mechanical model enable to describe transitions between the diverse energy states. An atom or a molecule undergoes such transitions *e.g.* by absorbing or emitting a photon. Next to the required photon energy, further conditions must be satisfied so that a transition is “allowed”. A simplified quantum mechanical explanation about photon absorption and emission is presented within the next sub-chapter.

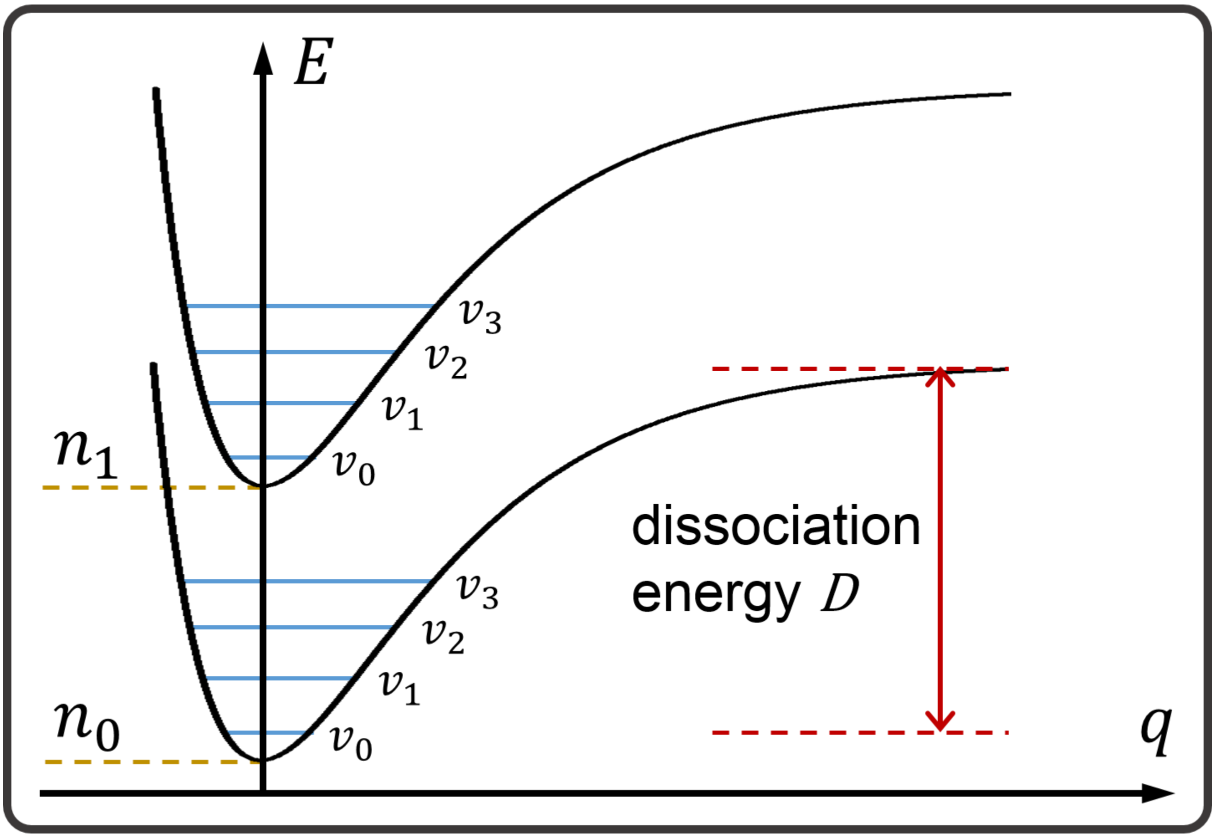

Figure 2.2 Simplified schematic representation of energy distribution within a molecule. The electron states n are subdivided by the vibration states v. The dissociation energy D gives the energy level where the maximum deviation of the normal coordinate q is too large so that the molecule cannot relax into its equilibrium position. As a consequence, the molecule dissociates.

2.1.2 Photon Absorption, Emission and Non-Radiative Relaxation

When a molecule interacts with electromagnetic radiation *e.g.* by absorbing or emitting a photon it can undergo an energy transition. Depending on the wavelength of the incident light, the transition can be electronic, vibrational or both. In case of wavelengths in the IR range (2500 nm – 50000 nm, 4000 cm^{-1} - 200 cm^{-1}), molecules typically experience vibration state transitions. If the wavelengths of the electromagnetic radiation are localized between the UV and the VIS range (200 nm – 800 nm, 50000 cm^{-1} – 12500 cm^{-1}), molecules may undergo an electronic state transition. This electronic state transitions can be connected with an additional vibration state transition. In order to induce a molecular energy transition, the energy of the absorbed photon must coincide with the energy differences between the initial state and the excited state. However, this is only half the story. Not every molecular transition, independently if it is of electronic or vibrational nature, is allowed. In case of molecular electronic transitions, the molecule orbital symmetry and the spin multiplicity influence if a transition is allowed or forbidden. The spin multiplicity ($2S+1$) gives the number of degenerated eigenstates related to the total spin angular momentum (simplified: number of unpaired electrons). In most of all cases, molecules have no unpaired electrons resulting in a spin multiplicity of one of the ground state. This configuration is called singlet *S*. However, some molecules have unpaired electrons (*e.g.* O_2). Accordingly, the spin multiplicity is unequal to one. If the spin multiplicity is two, it is called doublet; if it is three, the configuration is called triplet *T*. The change in spin multiplicity must be zero so that a transition is spin-allowed. In case of vibrational transitions, the symmetry of the molecule vibration in the ground and in the excited state gives information whether the transition is allowed or forbidden. A molecular energy state transition is quantum mechanically expressed by the transition moment integral

$$\mu = \int_{-\infty}^{+\infty} \psi_2^* \hat{o} \psi_1 \qquad \text{Eq. 2.12}$$

with ψ_2^* represents the complex-conjugate wave function of the final state, $\hat{o}$ the transition operator and ψ_1 the wave function of the initial state. In general, the wave functions are formed from the product of the electronic wave function and a wave function describing the positions of the atom nuclei within the molecule. However, electronic transitions normally do not appear in Raman spectroscopy (except for resonance Raman spectroscopy) and thus the electronic wave functions stay constant during vibrational transition. Therefore, a detailed consideration of the behavior of this proportion of the wave functions is not shown. Anyway, if the transition moment integral turns zero, the transition is called forbidden. However, solving the transition moment integral is not a trivial matter and can be only solved numerical for complex quantum mechanical system like molecules, especially if electronic and vibrational transitions occur simultaneously. Fortunately, the concrete solution of this integral is not required since symmetry determinations of the wave functions and the transition operators are already expedient. Thus, the integral turns zero if the symmetry of the transition function $\psi_1^*\hat{o}\psi_2$ is odd. Contrary, if the transition function is even, the transition function is unequal to zero and consequently the transition is allowed. The transition moment integral and the Raman transition selection rules are discussed in detail within the semi quantum mechanically description of Raman scattering.

In order to visualize the changes of the occupations of the energy states in a molecule while interacting with electromagnetic radiation, the Jablonski diagram has proven its worth. Accordingly, the Jablonski diagram illustrates in a simple manner all possible energy transitions a molecule can undergo as presented in Figure 2.3. If a molecule absorbs a photon satisfying the necessary requirements, the molecule undergoes an energy transition from its ground state to an excited state: $S_0v_0 \rightarrow S_xv_y$. In case of IR absorption (IR A, Figure 2.3), the molecule resists in its electronic ground state but are excited into an excited vibrational state: $S_0v_0 \rightarrow S_0v_y$. The transition $S_0v_0 \rightarrow S_0v_1$ is the fundamental transition which occurs most likely. Vibrational frequencies found in typical IR or Raman spectra correspond in general to the energy difference between $S_0v_0 \rightarrow S_0v_1$. If a molecule is excited from its vibrational ground state into a vibrational state >1, the transition is called overtone (*e.g.* $S_0v_0 \rightarrow S_0v_2$). A transition from an already excited vibrational state into a higher vibrational state is called hot transition (*e.g.* $S_0v_1 \rightarrow S_0v_2$). The relaxation from an excited vibrational state to the ground state (*e.g.* $S_0v_1 \rightarrow S_0v_0$) appears non-radiative, that means without an emission of a photon. The non-radiative relaxation are accomplished by the release of thermal energy.[1] If a molecule absorbs a photon from the UV-VIS range (UV-VIS A, Figure 2.3), an electronic state transition may take place which is often accompanied by an additional vibrational transition (*e.g.* $S_0v_0 \rightarrow S_1v_3$, Figure 2.3). The relaxation from such an excited state occurs first over a *non-radiative* *relaxation* to the vibrational ground state of the excited electronic state ($S_1 v_3 \rightarrow S_1 v_0$). The further relaxation from the excited electronic state to the electronic ground state depends strongly of the molecule characteristics. Three different relaxation mechanisms exist. The first is driven by the internal conversion (IC), a non-radiative transition. This transition takes place between an excited electronic state and the excited vibrational state of the electronic ground state (*e.g.* $S_1 v_0 \rightarrow S_0 v_7$, Figure 2.3). Hereby, the energy levels of both, the initial and the final state, must be equivalent, or in other words they must be degenerated eigenstates.[1] The final energy relaxation of this mechanism occur non-radiatively in the vibrational ground state of the electronic ground state (*e.g.* $S_0 v_7 \rightarrow S_0 v_0$, Figure 2.3). The second relaxation mechanism starts with an intersystem crossing (ISC), another non-radiative transition between the excited electronic singlet state and an excited vibrational state of a lower energy electronic triplet state (*e.g.* $S_1 v_0 \rightarrow T_1 v_2$, Figure 2.3). The ISC is followed by a non-radiative vibrational relaxation from the excited vibrational state to vibrational ground state of the electronic triplet state

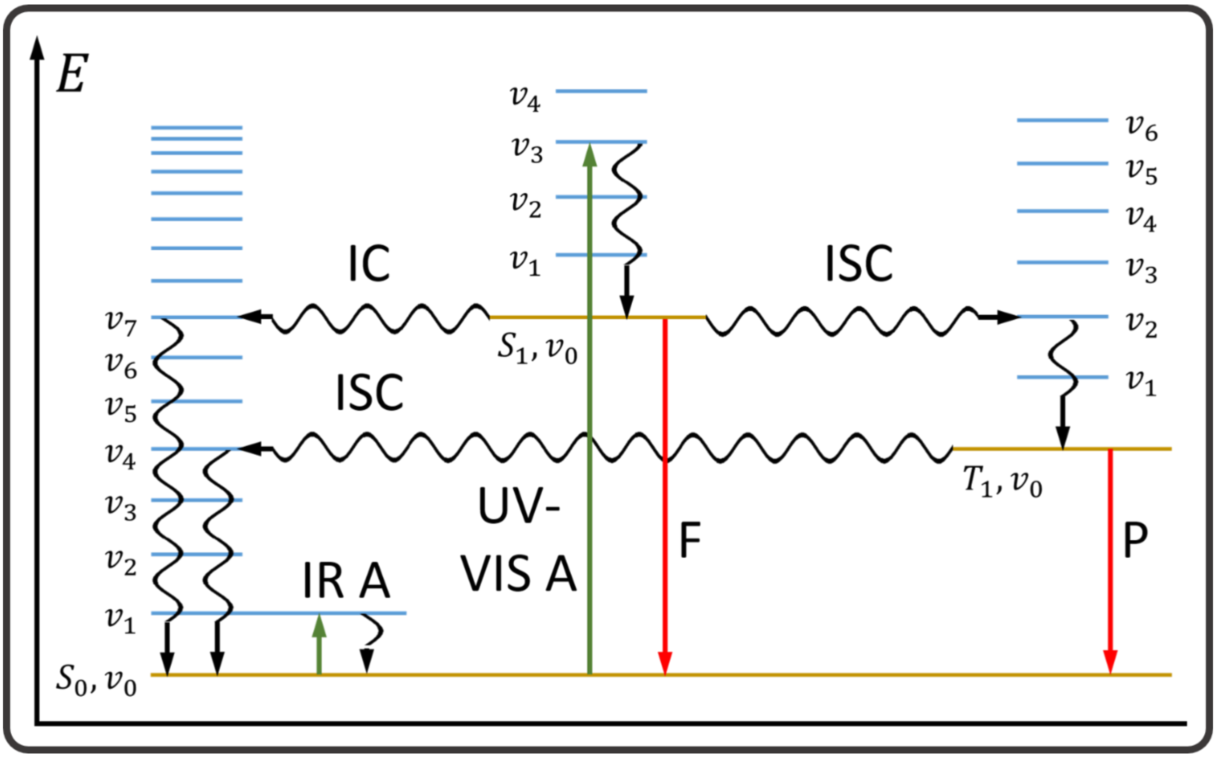

Figure 2.3. The Jablonski diagram illustrates the molecular energy states and the possible transitions. S_0: singlet ground state; S1: first excited singlet state; T_1: lowest triplet state; v_0: vibrational ground state; v_x: excited vibrational states; IR A: infrared absorption; UV-VIS: ultra-violet or visible light absorption; F: fluorescence; P: phosphorescence; IC: internal conversion; ISC: inter system crossing; arrows represent photonic processes; horizontal wave arrows depict non-radiative transitions; vertical wave arrows diagram non-radiative relaxation.[1]

(*e.g.* $T_1 v_2 \rightarrow T_1 v_0$). From here the molecule can undergo another ISC to an excited vibrational state of the electronic ground state (*e.g.* $T_1 v_0 \rightarrow S_0 v_4$) followed by non-radiative relaxation (*e.g.* $S_1 v_4 \rightarrow S_0 v_0$). However, the molecule can relax from the excited electronic triplet state to the ground state (*e.g.* $T_1 v_0 \rightarrow S_0 v_0$) also by emitting a photon. This radiative relaxation mechanism is called *phosphorescence* (P, Figure 2.3). The third relaxation mechanism from the excited electronic state to the electronic ground state (*e.g.* $S_1 v_0 \rightarrow S_0 v_0$) is the *fluorescence* (F, Figure 2.3). The relaxation appears here by emitting a photon with an energy corresponding to the energy difference between the excited and the ground state. Since the energy difference of the absorbed and the emitted photon is close to the energy differences between two vibrational states, fluorescence bands can occur in Raman spectra. These fluorescence bands appear sometimes extreme broad and intense so that an accurate spectral analysis becomes impossible.

2.2 Raman Scattering

The Raman effect is an inelastic scattering process of light at matter whereby the energy (respectively the wavelength or the angular frequency) of the scattered light is either decreased or increased (*Raman scattering*). The Raman effect was already predicted in 1923 by Adolf Smekal and quantum mechanically described by Kramer, Heisenberg and Dirac before it could be experimentally verified.[4-7] It took five more years after its prediction until Raman and Krishnan could observe and describe the Raman effect by investigations of organic liquids illuminated with sunlight.[8-13] Within the same year, Landsberg and Mandelstam observed the Raman effect in inorganic crystals independently from Raman and Krishnan.[14] Though the Raman effect was predicted, described and observed by various researchers, it is named after the Indian physicist Chandrasekhara Venkata Raman.

If a photon with an energy $h\nu_0$ which coincides not with the energy difference between two molecular energy states interacts with a molecule (or matter in general), the molecule can be excited in a virtual energy state V. The photon energy is hereby typically smaller than required for a molecular electronic transition (except for resonance Raman spectroscopy). Virtual states are short-lived, not stationary states of a molecule because they are not eigenfunctions of any operator.[15] Virtual states are an interesting research topic per se which do not have to be discussed in more detail here since a closer description is not necessary for Raman spectra analyses. Anyway, if a molecule is excited from its electronic and vibrational ground state to a virtual state by absorbing a photon ($S_0 v_0 \rightarrow V$), it immediately relaxes by emitting a photon. In most of the cases, the molecule relaxes back to its electronic and vibrational ground state ($V \rightarrow S_0 v_0$). Accordingly, the photon energy of the absorbed and the emitted photon is equal (Figure 2.4). This elastic scattering process is called *Rayleigh scattering*. Rayleigh scattering typically occurs with a probability of $10^{-4} – 10^{-3}$. However, with a possibility of $10^{-8} – 10^{-5}$ the molecule can also relax from the virtual state to the first excited vibrational state of the electronic ground state ($V \rightarrow S_0 v_1$). This inelastic scattering process is the *Stokes-scattering*. The energy difference between the absorbed and the emitted photon coincides hereby with the energy difference between the vibrational ground state and the first vibrational state (Figure **2.4**). If the molecule is stated in the first excited vibrational state of the electronic ground state before absorbing a photon ($S_0 v_1 \rightarrow V$), the molecule can relax to its vibrational and electronic ground states ($S_0 v_0 \rightarrow V$). Therefore, the energy of the emitted photon is increased by the energy

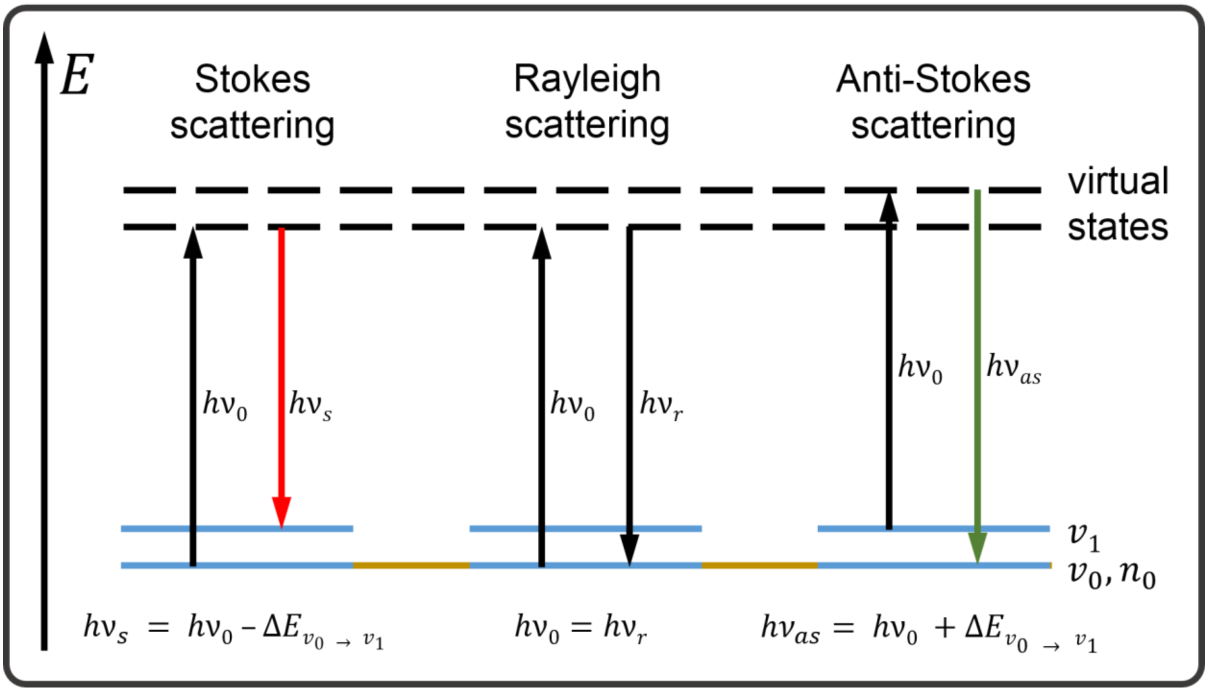

Figure 2.4. Schematic representation of the Raman effect. v_0 and v_1 represent the vibrational ground state and the first excited vibrational state of a molecule. Black arrows depict the energy $h\nu_0$ and $h\nu_r$ of an incident photon as well as the energy of a Rayleigh scattered photon. The red arrow represents the energy $h\nu_s$ of a Stokes scattered photon, the green arrow symbolizes the energy of an Anti-Stokes scattered photon $h\nu_{as}$.

difference between the vibrational ground state and the first excited vibrational state. This inelastic scattering process is called *Anti-Stokes scattering*. Since only less molecules are stated in excited vibrational states at room temperature, Anti-Stokes scattering occurs less probably than Stokes-scattering resulting in less frequency intensities in Raman spectra.

2.2.1 Classical Description of Raman scattering

In the following, a classical description of Raman scattering is developed since it is in most of the cases sufficient to interpret spectroscopic data.[7] Accordingly, the classical description of Raman scattering gives if a molecular vibration is Raman active or inactive. Furthermore, the vectorial consideration allows to draw conclusion about the intensity ratios of different molecular vibration depending on their orientation towards the electric field vector of the incident light. The following presented mathematical description is based on reference 7.

In classical theory, a dipole moment is induced in a molecule while interacting with electromagnetic radiation. The induced dipole moment oscillates with the same frequency as the incident light. The electromagnetic radiation created by the induced dipole spreads over the whole solid angle. The electric field vector $\vec{E}(t)$ of the incident light is

$$\vec{E}(t) = \vec{E}_0 \cos \omega_0 t \,, \qquad \text{Eq. 2.13}$$

with $\vec{E}_0$ is the directed amplitude of the electromagnetic wave and ω_0 is the angular frequency. The induced dipole moment $\vec{\mu}(t)$ is then given by vector relation

$$\vec{\mu}(t) = \tilde{\alpha}\vec{E}(t) \,. \qquad \text{Eq. 2.14}$$

The proportionality factor $\tilde{\alpha}$ is the polarizability of the molecule. The polarizability $\tilde{\alpha}$ is a second rank tensor assigning $\vec{E}(t)$ to $\vec{\mu}(t)$ thus it can be described as a 3x3 matrix (Figure 2.5, left). Generally, the polarizability is a measure for the deformability of the molecule orbitals in an external electric field. Since the polarizability is a second rank tensor, it can be illustrated as ellipsoids. Anyway, in order to simplify the mathematical description, the electric field vector $\vec{E}(t)$ is reduced on its z – component $E_z(t)$. Additionally, only the z – component of the induced dipole moment is discussed $\mu_z(t)$. By applying both simplifications the polarizability tensor is reduced to α_{zz} and thus Eq. 2.14 becomes a scalar relation resulting in

$$\mu_z(t) = \alpha_{zz} E_z(t) \,. \qquad \text{Eq. 2.15}$$

The simplification can be realized experimentally by using z – polarized light and a z – analyzer placed in front of the Raman spectrometer (Figure 2.5, right). The investigated molecule, here

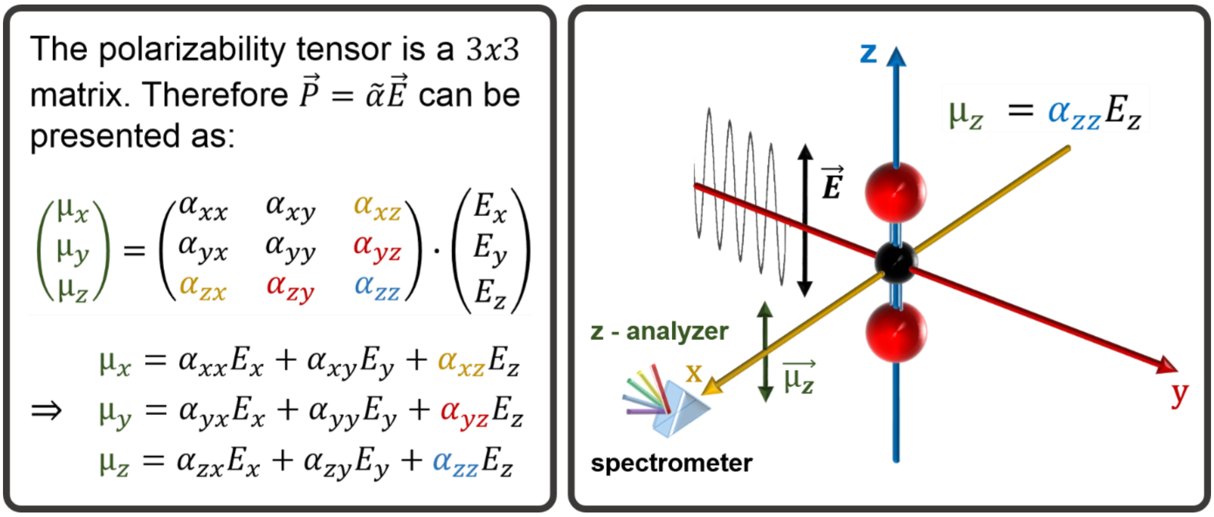

The polarizability tensor is a $3x3$ matrix. Therefore $\vec{P} = \tilde{\alpha}\vec{E}$ can be presented as:

$$\begin{pmatrix} \mu_x \\ \mu_y \\ \mu_z \end{pmatrix} = \begin{pmatrix} \alpha_{xx} & \alpha_{xy} & \alpha_{xz} \\ \alpha_{yx} & \alpha_{yy} & \alpha_{yz} \\ \alpha_{zx} & \alpha_{zy} & \alpha_{zz} \end{pmatrix} \cdot \begin{pmatrix} E_x \\ E_y \\ E_z \end{pmatrix}$$

$$\Rightarrow \begin{aligned} \mu_x &= \alpha_{xx}E_x + \alpha_{xy}E_y + \alpha_{xz}E_z \\ \mu_y &= \alpha_{yx}E_x + \alpha_{yy}E_y + \alpha_{yz}E_z \\ \mu_z &= \alpha_{zx}E_x + \alpha_{zy}E_y + \alpha_{zz}E_z \end{aligned}$$

Figure 2.5. Left: Matrix representation of the polarizability tensor $\tilde{\alpha}$ and vectorial description of the induced dipole moment $\vec{\mu}$. Coloured polarizability components participate at $\vec{\mu}$ if incident light is z – polarized. **Right:** Setup of the investigated theoretical scattering system. A CO_2 molecule is located in the origin of the scattering system and aligned parallel to the z- axis. The incident light is z – polarized; $\vec{E} \rightarrow E_z$. Only z – components of scattered light can pass the z – analyser and reach the detector; $\vec{\mu} \rightarrow \mu_z$. Accordingly, the polarizability tensor is reduced to α_{zz} and thus $\mu_z(t) = \alpha_{zz}E_z(t)$ is a scalar relation.

a CO_2 molecule, is centered at the origin of the Raman scattering system aligned along the z – axis of the scattering system. The z – analyzer and the Raman spectrometer are localized along the x – axis of the Raman scattering system. The indices describing the z – components in Eq. 2.15 are dropped within the following to guarantee comprehensibility

$$\mu(t) = \alpha E(t)\,. \qquad \text{Eq. 2.16}$$

Inserting of Eq. 2.13 results in

$$\mu(t) = \alpha E_0 cos(\omega_0 t)\,. \qquad \text{Eq. 2.17}$$

According to classical electrodynamics, a time-varying dipole moment emits electromagnetic radiation with the frequency of its own oscillation (Hertz'scher dipole). If the polarizability α is constant by meaning α is not a function of time, the induced dipole will re-emit an electromagnetic wave with the same angular frequency ω_0 than the incident light. Since the frequency and thus the wavelength of the incident and the emitted light are identic, Eq. 2.17 already describes the elastic *Rayleigh scattering*. Anyway, if a molecule (or each other scattering system) oscillates, the polarizability α changes depending on the relative positions of the molecule atoms to their equilibrium position. As already introduced in chapter 2.1.1, the relative molecule atom positions can be expressed with the normal coordinate q. Since molecular vibrations are innately periodic oscillations, the time-dependent normal coordinate $q(t)$ of a molecular vibration can be described as a harmonic oscillator

$$q(t) = q_0 cos(\omega_q t) \qquad \text{Eq. 2.18}$$

with q_0 is the maximal deviation from the equilibrium position (amplitude) and ω_q is the angular frequency of the molecular vibration. Since the polarizability depends on the molecule atom positions, it follows this oscillation and become a function of the normal coordinate $\alpha(q)$. Since the concrete form of the polarizability function is unknown, a Taylor series is applied to approximate the polarizability around the equilibrium position ($q = 0$). The atom position deviation during a molecular vibration are relatively small. Accordingly, only terms of first order must be considered resulting in

$$\alpha(q) = \alpha_0 + \left(\frac{\partial \alpha}{\partial q}\right)_0 q\,. \qquad \text{Eq. 2.19}$$

Eq. 2.18 in Eq. 2.19 gives

$$\alpha(q) = \alpha_0 + \left(\frac{\partial\alpha}{\partial q}\right)_0 q_0 cos\left(\omega_q t\right). \qquad \text{Eq. 2.20}$$

Inserting Eq. 2.20 in Eq. 2.17 results in the time-dependent dipole moment $\mu(\mathrm{t})$ of an oscillating molecule

$$\mu(t) = \left[\alpha_0 + \left(\frac{\partial\alpha}{\partial q}\right)_0 q_0 cos\left(\omega_q t\right)\right] E_0 cos(\omega_0 t). \qquad \text{Eq. 2.21}$$

This equation describes the emitted modified electromagnetic radiation. However, in the present form, Eq. 2.21 allows not to draw conclusions in which manner the emitted radiation is affected by the diverse scattering mechanisms (Rayleigh, Stokes or Anti-Stokes). Rearranging Eq. 2.21 with the trigonometry relation

$$cos\,A\,cos\,B = \frac{1}{2}[cos(A + B) + cos(A - B)] \qquad \text{Eq. 2.22}$$

Results finally in

$$\mu(t) = \alpha_0\, E_0 \cos(\omega_0 t) + \frac{1}{2}\left(\frac{\partial\alpha}{\partial q}\right)_0 q_0 E_0 \cos\left[\left(\omega_0 - \omega_q\right)t\right] + \frac{1}{2}\left(\frac{\partial\alpha}{\partial q}\right)_0 q_0 E_0 \cos\left[\left(\omega_0 + \omega_q\right)t\right]. \qquad \text{Eq. 2.23}$$

The influences of the diverse scattering mechanisms can directly be seen in the single addends of the rearranged time-dependent dipole moment $\mu(\mathrm{t})$. The first addend represents the Rayleigh scattering, the second addend gives the Stokes-scattering and the third describes the Anti-stokes

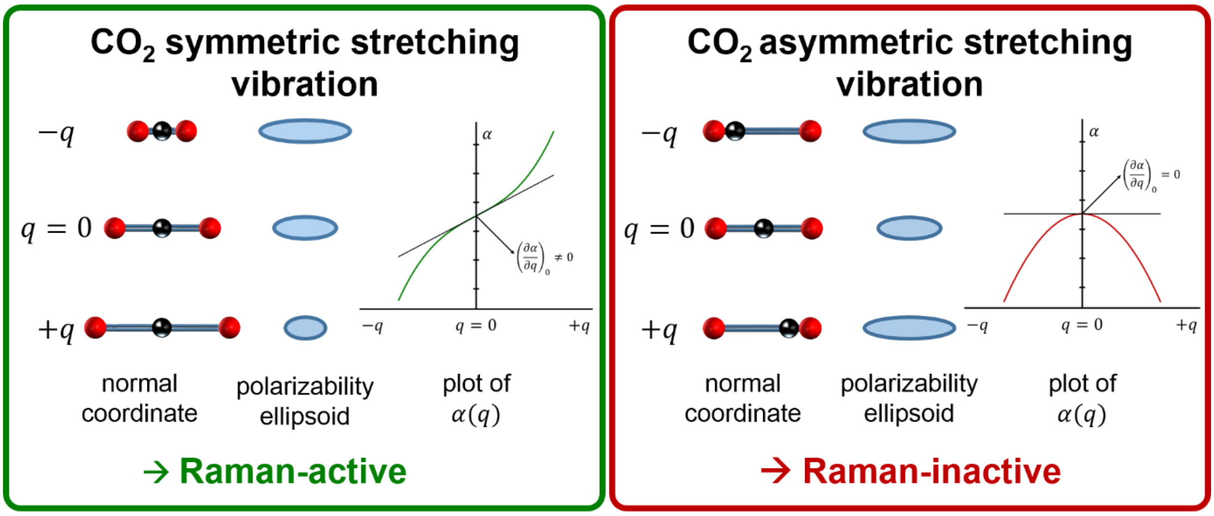

Figure 2.6. Left: Schematic representation of the CO_2 symmetric stretching vibration. This molecular vibration provides an alteration of the polarizability when oscillating through the equilibrium position. Accordingly, the vibration is Raman-active and occurs in the Raman spectrum. **Right:** Schematic representation of the CO_2 asymmetric stretching vibration. The polarizability does not alternate while oscillating through the equilibrium position. Thus, this vibration is Raman-inactive and do not appear within the Raman spectrum.

scattering. Moreover, it is obvious that the difference of the modified angular frequencies $\omega_0 \pm \omega_q$ correspond to the energy of the Stokes or Anti-stokes scattered photons ($E_p = \hbar\omega = h\nu$; $E_{v_0 \to v_1} = \hbar\omega_q$; compare Figure 2.4). However, the Stokes respectively the Anti-Stokes term provides additionally information whether a molecular vibration is Raman active or not. Therefore, the Stokes and Anti-Stokes terms disappear if the polarizability alteration while the molecule oscillates through its equilibrium position $(\partial\alpha/\partial q)_0$ is zero. Consequently, the molecular vibration would not appear in the Raman spectrum. In contrast, if $(\partial\alpha/\partial q)_0$ is unequal to zero, the Stokes and the Anti-Stokes terms participate to the time-dependent induced dipole moment $\mu(t)$ and thus the vibration can be find within the Raman spectrum. As an example, the CO_2 symmetric and asymmetric stretching vibrations are investigated (Figure 2.6). In case of the CO_2 symmetric stretching vibration, the polarizability alteration is unequal to zero while the molecule oscillates through its equilibrium position as visualized by the different polarizability ellipsoid shapes of $-q$ and $+q$ in Figure 2.6. Accordingly, the CO_2 symmetric stretching vibration is Raman-active. On the other hand, the CO_2 asymmetric stretching vibration provides no polarizability alteration while oscillating through the equilibrium position (same ellipsoid shapes of $-q$ and $+q$). Therefore, the CO_2 asymmetric stretching vibration is Raman-inactive. The intensity of Stokes or Anti-Stokes scattered photons in the Raman spectrum is directly proportional to the polarizability alteration. Since the polarizability is a measure of deformability of molecular orbitals and the shapes of molecule orbitals depend on the molecule conformations, changes of the molecule conformation can influence strongly the measured Raman intensity of a molecular vibration. Furthermore, the classical description of Raman scattering presents that also the orientations of the electric field vector of the incident light $\vec{E}$ and the normal coordinate q affect the Raman intensities. Thus, the highest Raman intensity is expected for a parallel alignment of $\vec{E}$ and q. On the other hand, if $\vec{E}$ and q are aligned perpendicular the Raman intensity will tend towards zero.

2.2.2 Semi-Quantum Mechanical Description

Principally, the scattering system and the electromagnetic field can be described quantum mechanically. However, a closer quantum mechanical description of the incident and emitted light is not necessary since only the changes of the scattering molecules are of interest. As already introduced in chapter 2.1.2, a molecule can solely undergo an energy transition, if the transition momentum integral

$$\mathrm{\mu} = \int_{-\infty}^{+\infty} \psi_2^* \hat{o} \psi_1 \qquad \text{Eq. 2.12}$$

is unequal to zero. This certainly also applies to Raman scattering. In case of Raman scattering, the transition operator $\hat{o}$ turns to the polarizability operator $\hat{\alpha}$ and the transition moment integral is given as $\alpha_{v_0 \to v_1}^{trans}$. Since only fundamental vibrational transition are investigated and thus only the vibrational proportion of the wave functions are of interest, the wave function of the vibrational ground state is called ϕ_0 and the wave function describing the first excited vibrational state is given as ϕ_1 in the following to avoid confusions with the total wave function ψ (compare chapter 2.1.1). Accordingly, the Raman transition momentum integral can be given as

$$\alpha_{v_0\rightarrow v_1}^{trans} = \int_{-\infty}^{+\infty} \phi_1^{*}\hat{\alpha}\phi_0 \,. \qquad \text{Eq. 2.24}$$

The vibrational wave functions ϕ_0 and ϕ_1 arise from the Schrödinger equation of the harmonic oscillator (Eq. 2.10) as presented within chapter 2.1.1:

$$\phi_0(q) = \left(\frac{m\omega}{\hbar\pi}\right)^{\frac{1}{4}} e^{\left(-\frac{m\omega}{2\hbar}q^2\right)} \qquad \text{Eq. 2.25}$$

$$\phi_1(q) = \frac{2}{\sqrt{2}}\pi^{\frac{1}{4}}\left(\frac{m\omega}{\hbar}\right)^{\frac{3}{4}} q e^{\left(-\frac{m\omega}{2\hbar}q^2\right)} \,. \qquad \text{Eq. 2.26}$$

From Eq. 2.24 - Eq. 2.26 it becomes obvious that a concrete solution of the transition momentum integral is a difficult task, especially since the normal coordinate q can be arbitrarily complicated for large molecules. Moreover, the concrete character of the polarizability operator $\hat{\alpha}$ is unknown. However, symmetry investigations of the vibrational wave functions and the operator are already sufficient to predict if a molecular vibration is Raman-active or -inactive. A molecular vibration is Raman-active if $\alpha_{v_0\rightarrow v_1}^{trans}$ is unequal to zero. Accordingly, the symmetry of the polarizability transition momentum function must be even so that $\alpha_{v_0\rightarrow v_1}^{trans} \neq 0$ (compare 2.1.2). In case of 1 – dimensional wave functions, the symmetry of the transition momentum integral could be easily determined by multiplying the parities (+1 for even functions, -1 for odd functions) of the single wave functions and the operator resulting in the parity of transition momentum integral function. If the parity of the transition momentum integral function is -1, the function symmetry is odd ($-f(-x) = f(x)$) and the integral turns zero. On the other hand, if the total parity is +1, the function symmetry is even ($-f(x) = f(x)$) resulting in a $\alpha_{v_0\rightarrow v_1}^{trans} \neq 0$. However, the variable of vibrational wave functions is the normal coordinate q. The normal coordinate q is formed from the x –, y – and z – coordinates of all molecule atoms resulting in a 3N – dimensional vector, where N represents the number of molecule atoms. Consequently, the vibrational wave functions are also 3N – dimensional making a symmetry investigation significantly more difficult. However, the normal coordinate q is related to the atom positions within the molecule and thus to the symmetry of the molecule. Therefore, the normal coordinate is a basis of an irreducible representation in the symmetry point group of the molecule. The product of the irreducible representations $\Gamma_{\phi_0 \hat{\alpha} \phi_1}$ of ϕ_0, $\hat{\alpha}$ and ϕ_1

$$\Gamma_{\phi_0 \hat{\alpha} \phi_1} = \Gamma_{\phi_0} \Gamma_{\hat{\alpha}} \Gamma_{\phi_1} \qquad \text{Eq. 2.27}$$

thus provides information about the symmetry of the polarizability transition momentum integral function. The polarizability transition momentum integral $\alpha_{v_0 \to v_1}^{trans}$ is solely unequal to zero if the product $\Gamma_{\phi_0 \hat{\alpha} \phi_1}$ contains the total symmetric irreducible representation of the symmetry point group of the molecule.[1] The symmetry of the vibrational wave functions are related to the occurrence of the normal coordinate within the wave function. The wave function of the vibrational ground state ϕ_0 contains the normal coordinate as q^2 only (Eq. 2.25). Consequently, ϕ_0 transforms always like the total symmetric irreducible representation of the point group. On the other hand, ϕ_1 contains additional to q^2 a linear factor q. Since q^2 results in a total symmetric transformation, the vibrational wave function ϕ_1 transforms always like q.[1] Finally, the polarizability operator $\hat{\alpha}$ transforms like the basic functions x^2, y^2, z^2, xy, xz, yz of the underlying symmetric point group. The correlation between $\alpha_{v_0 \to v_1}^{trans}$ and $\Gamma_{\phi_0 \hat{\alpha} \phi_1}$ is presented in the following by the examples of the CO_2 symmetric and asymmetric stretching vibrations. The CO_2 molecule provides a $D_{\infty h}$ symmetry. The CO_2 symmetric stretching vibration respectively its normal coordinate q transforms like the irreducible representation a_{1g} of the $D_{\infty h}$ point group, the CO_2 asymmetric stretching vibration transforms like the irreducible representation a_{1u}.[1] The character table of the $D_{\infty h}$ symmetry point group is presented in Figure **2.7**. The symmetric behavior of a molecular vibration can also be derived from the molecule symmetry but is not shown here. A detailed introduction to this topic is given in reference 1. Anyway, the wave function of the vibrational ground state ϕ_0 transforms always like the total symmetric representation of the underlying point group. In case of the $D_{\infty h}$ symmetry

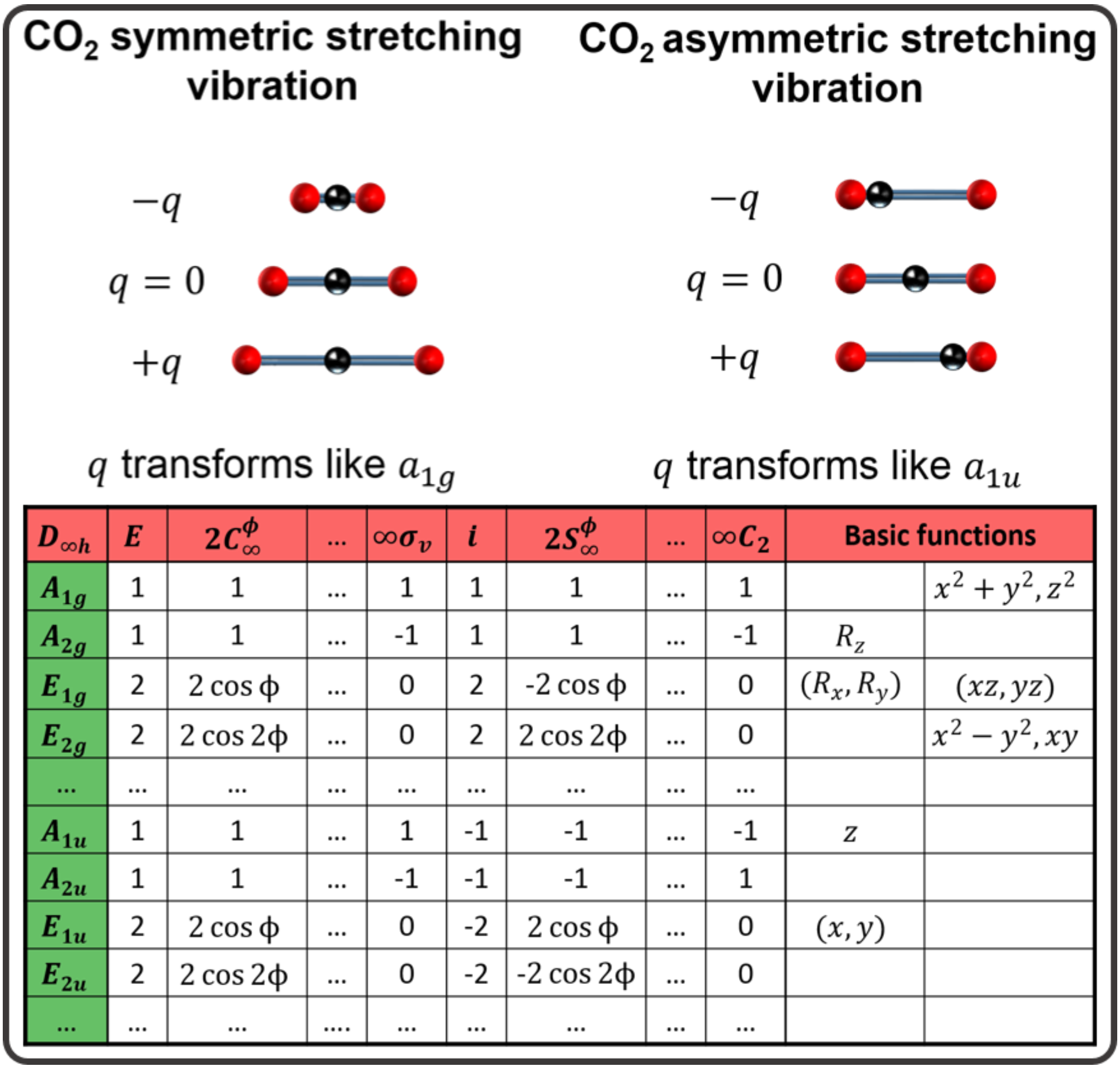

$D_{\infty h}$	E	$2C_{\infty}^{\phi}$	...	$\infty\sigma_v$	i	$2S_{\infty}^{\phi}$	...	∞C_2	Basic functions	
A_{1g}	1	1	...	1	1	1	...	1		x^2+y^2, z^2
A_{2g}	1	1	...	-1	1	1	...	-1	R_z	
E_{1g}	2	2 cos ϕ	...	0	2	-2 cos ϕ	...	0	(R_x, R_y)	(xz, yz)
E_{2g}	2	2 cos 2ϕ	...	0	2	2 cos 2ϕ	...	0		x^2-y^2, xy
...	...	...	...	...	...	...	...	...		
A_{1u}	1	1	...	1	-1	-1	...	-1	z	
A_{2u}	1	1	...	-1	-1	-1	...	1		
E_{1u}	2	2 cos ϕ	...	0	-2	2 cos ϕ	...	0	(x, y)	
E_{2u}	2	2 cos 2ϕ	...	0	-2	-2 cos 2ϕ	...	0		
...	...	...	....	...	...	...	...	...		

Figure 2.7. Top: Schematic representation of the CO₂ symmetric and asymmetric stretching vibrations. The normal coordinate q of the CO₂ symmetric stretching vibration transforms like a_{1g} of the $D_{\infty h}$ symmetry point group, the normal coordinate q of the CO₂ asymmetric stretching vibration transforms like a_{1u}. **Bottom:** Character table of the $D_{\infty h}$ symmetry point group.

point group, the total symmetric irreducible representation is a_{1u} (compare Figure **2.7**). The wave function of the first excited vibrational state ϕ_1 transforms like the normal coordinate of the vibration. Consequently, the wave function of the first excited vibrational state ϕ_1 of the CO₂ symmetric stretching vibration transforms like a_{1g} and the wave function of the first excited vibrational state ϕ_1 of the CO₂ asymmetric stretching vibration like a_{1u}. The components of the polarizability operator $\hat{\alpha}$ by meaning of the basic functions x^2, y^2, z^2, xy, xz, yz respectively their combinations transform like a_{1g}, e_{1g} and e_{2g} of the $D_{\infty h}$ symmetry point group. Therefore, the product of the irreducible representations $\Gamma_{\phi_0\hat{\alpha}\phi_1}$ for the CO$_2$ symmetric stretching vibration can be given as

$$\Gamma_{\phi_0\hat{\alpha}\phi_1} = a_{1g}\begin{pmatrix} a_{1g} \\ e_{1g} \\ e_{2g} \end{pmatrix} a_{1g} \qquad \text{Eq. 2.28}$$

$\Gamma_{\phi_0\hat{\alpha}\phi_1}$ can be solved by multiplying the values of each symmetry operation of the irreducible representation with the corresponding values of the other irreducible representations. This product results in a further irreducible presentation as presented for the CO$_2$ symmetric stretching vibration in Table 2.3 - Table 2.5.

Table 2.3. Calculation of the first component of $\Gamma_{\phi_0\hat{\alpha}\phi_1}$ of CO$_2$ symmetric stretching vibration

$D_{\infty h}$	E	$2C_\infty^\phi$	...	$\infty\sigma_v$	i	$2S_\infty^\phi$	...	∞C_2	$\Gamma_{\phi_0\hat{\alpha}\phi_1}$
a_{1g}	1	1	...	1	1	1	...	1	
a_{1g}	1	1	...	1	1	1	...	1	
a_{1g}	1	1	...	1	1	1	...	1	
Product	1	1	...	1	1	1	...	1	a_{1g}

Table 2.4. Calculation of the second component of $\Gamma_{\phi_0\hat{\alpha}\phi_1}$ of CO$_2$ symmetric stretching vibration

$D_{\infty h}$	E	$2C_\infty^\phi$	...	$\infty\sigma_v$	i	$2S_\infty^\phi$	...	∞C_2	$\Gamma_{\phi_0\hat{\alpha}\phi_1}$
a_{1g}	1	1	...	1	1	1	...	1	
e_{1g}	2	2 cos ϕ	...	0	2	-2 cos ϕ	...	0	
a_{1g}	1	1	...	1	1	1	...	1	
Product	2	2 cos ϕ	...	0	2	-2 cos ϕ	...	0	e_{1g}

Table 2.5. Calculation of the third component of $\Gamma_{\phi_0\hat{\alpha}\phi_1}$of CO_2 symmetric stretching vibration

$D_{\infty h}$	E	$2C_{\infty}^{\phi}$	...	$\infty\sigma_v$	i	$2S_{\infty}^{\phi}$	...	∞C_2	$\Gamma_{\phi_0\hat{\alpha}\phi_1}$
a_{1g}	1	1	...	1	1	1	...	1	
e_{2g}	2	2 cos 2ϕ	...	0	2	2 cos 2ϕ	...	0	
a_{1g}	1	1	...	1	1	1	...	1	
Product	2	2 cos 2ϕ	...	0	2	2 cos 2ϕ	...	0	e_{2g}

Finally, the product of the irreducible representations $\Gamma_{\phi_0\hat{\alpha}\phi_1}$ for the CO_2 symmetric stretching vibration can be given as

$$\Gamma_{\phi_0\hat{\alpha}\phi_1} = a_{1g}\begin{pmatrix} a_{1g} \\ e_{1g} \\ e_{2g} \end{pmatrix} a_{1g} = \begin{pmatrix} \boldsymbol{a_{1g}} \\ \boldsymbol{e_{1g}} \\ \boldsymbol{e_{2g}} \end{pmatrix} \qquad \text{Eq. 2.29}$$

The product contains the total symmetric irreducible representation a_{1g} of the $D_{\infty h}$ symmetry point group. Therefore, the polarizability transition moment integral $\alpha_{v_0\rightarrow v_1}^{trans}$ is unequal to zero and thus the CO_2 symmetric vibration is Raman-active. In case of the CO_2 asymmetric stretching vibration, the product of the irreducible representations $\Gamma_{\phi_0\hat{\alpha}\phi_1}$is

$$\Gamma_{\phi_0\hat{\alpha}\phi_1} = a_{1g}\begin{pmatrix} a_{1g} \\ e_{1g} \\ e_{2g} \end{pmatrix} a_{1u} = \begin{pmatrix} \boldsymbol{a_{1u}} \\ \boldsymbol{e_{1u}} \\ \boldsymbol{e_{2u}} \end{pmatrix} \qquad \text{Eq. 2.30}$$

$\Gamma_{\phi_0\hat{\alpha}\phi_1}$ do not contain the total symmetric representation a_{1g}. Thus, the CO_2 asymmetric stretching vibration is Raman-inactive.

Both, the classical as well as the quantum mechanical treatment of the Raman effect, lead to same results regarding the prediction if a molecular vibration is Raman-active or Raman-inactive. In contrast to the classical description, the (semi-)quantum mechanical treatment allow to draw conclusions about the Raman-activity regarding to the molecule symmetry. The symmetry of a molecule depends *inter alia* on the molecule conformation. Accordingly, molecular vibrations may be Raman-active or Raman-inactive for a given molecule conformation but can become Raman-active or Raman-inactive if the molecule adopt another conformation. This phenomenon can occur at organic crystal surfaces. Due to the crystal symmetry break at the surface, a molecule may adopt an energetic more favorable conformation as it does in the bulk. Consequently, the symmetry of the surface molecules differs from that of the bulk molecules which can result in the appearance or disappearance of molecular vibrations in the Raman spectrum.

2.3 Surface Enhanced Raman Spectroscopy

As already mentioned within the previous section, the possibility that a photon is Raman scattered at a molecule is $10^{-8} – 10^{-5}$ and thus very low. Furthermore, the scattered photon carries only the information of a single vibrational mode and it must find the way to the detector. For Raman spectra analyses, however, it is necessary that the spectra contain all molecular vibrations with sufficient intensities. To fulfill these requirements, a relatively large amount of substance is needed to guarantee that enough Raman scattered photons reach the detector. Single nano- or sub-micron particles do not provide enough molecules for this purpose even if the laser power and thus the number of photons interacting with the sample is drastically increased. Therefore, Raman investigations of single nanoparticles are not possible using standard Raman spectroscopy methods. Fortunately, an effect first observed by Fleischmann *et al.* in 1974 and further described by Jeanmaire *et al.* and Albrecht *et al*. allows to overcome this limitation.[16-18] It could be demonstrated that the Raman intensities are drastically increased if the molecules are adsorbed on rough silver surfaces. Up to now, however, it could be shown that also other nano structured (precious) metal surfaces like gold or platinum increase the Raman intensity. This effect has become famous as *surface enhanced Raman scattering* (SERS). The exact mechanism behind SERS is still being discussed but two theories have been manifested. These are based an electromagnetic enhancement on the one hand and on the other hand on a chemical enhancement. The basics of both theories are shortly presented in the following.

2.3.1 Electromagnetic Enhancement

The electromagnetic theory of SERS is based on an electric field enhancement provided by the metal nanostructures. If a metal surface is placed within the electric field of incident light, the valence electrons start to oscillate. In general, the collective oscillation of the valence electrons relative to the atom nuclei can be mathematically described as a quasi-particle called plasmon. In case of metal nanoparticles, the collective oscillation of the valence electrons is called localized surface plasmon (LSP). If a metal nanoparticle interacts with light, the valence electrons are forced towards the particle edges in opposite direction to the electric field vector of the incident light $\vec{E}_{in}$. Due to the displacement of the valence electrons with respect to the

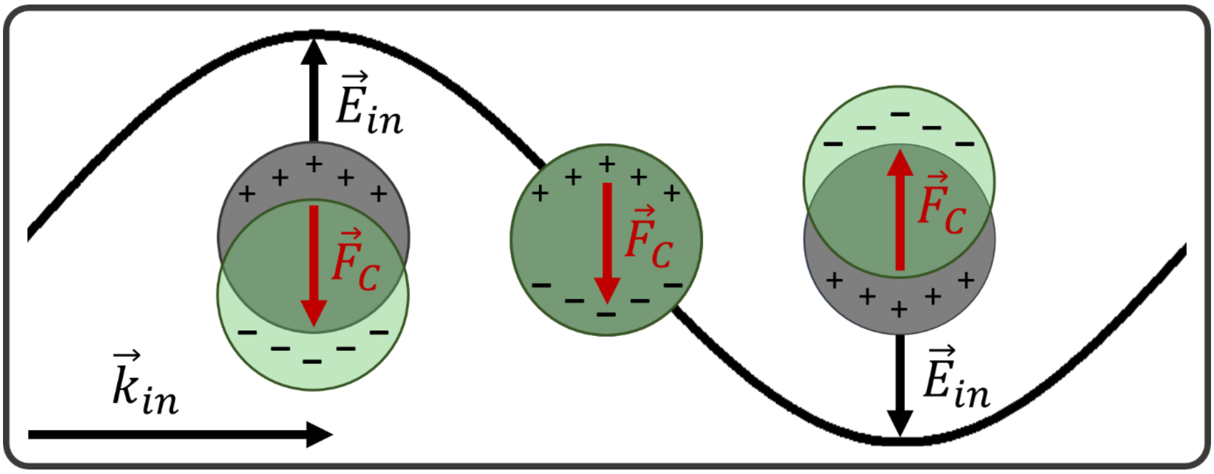

Figure 2.8. Schematic representation of the localized surface plasmon resonance (LSPR). If a metal nanoparticle interacts with electromagnetic radiation, the valence electrons are displaced relatively to the atomic nuclei towards the particle surface in opposite direction to the electric field vector $\vec{E}_{in}$. Because of the related charge separation, a restoring force due to Coulomb attractions occurs leading to a collective oscillation of the valence electrons. If the frequency of the electromagnetic radiation is in resonance with the oscillation frequency of the valence electrons (LSPR), an electric field is created at the particle surface parallel to $\vec{E}_{in}$.

atomic nuclei in the crystal lattice, a charge separation between positively charged atom nuclei and a negatively charged electrons occurs (Figure 2.8, left). Consequently, a restoring force $\vec{F}_C$ arises from Coulomb attraction.[19] This force induces an oscillation of the valence electrons. Because of the collective oscillation of the valence electrons, an electric field is created at the nanoparticle surface parallel towards the electric field vector $\vec{E}_{in}$ of the incident light. The intensity of this electric field is strongly enhanced compared to the intensity of the incident light. The strongest field enhancement occurs if the LSP of the metal nanoparticle oscillates in resonance with the incident light (localized surface plasmon resonance, LSPR). The LSPR frequency depends on material properties like the electron density, the effective electron mass and the size and shape of the charge distribution.[19] Besides material properties, also the size and shape of the nanoparticles influences the LSPR frequency.[19] The metal nanoparticle size, however, must be in the order of the penetration depth of the incident light and thus significantly smaller than its wavelength.[20] The LSPR frequencies can be experimentally determined via extinction (absorption) spectroscopy. Generally, the LSPR occurs as broad peak within such spectra. Thus, the LSPR of nanoparticles formed from given materials with given shapes and sizes occurs maximal at wavelengths related to the strongest optical extinctions in the extinction spectra. According to Mie-theory, the extinction spectrum E(λ) and thus the range of LSPR frequencies of spherical nanoparticles can be calculated by

$$E(\lambda) = \frac{24\pi^2 N a^3 \varepsilon_{out}^{\frac{3}{2}}}{\lambda\, ln(10)} \left[\frac{\varepsilon_i(\lambda)}{(\varepsilon_r(\lambda) + \chi\varepsilon_{out})^2 + \varepsilon_i(\lambda)^2}\right], \qquad \text{Eq. 2.31}$$

with λ is the wavelength of the incident light, N is the number of nanoparticles, a is the nanoparticle radius, ε_{out} is the dielectric constant of the environment, $\varepsilon_r(\lambda)$ and $\varepsilon_i(\lambda)$ are the real and imaginary components of the metal dielectric function $\varepsilon_{in}(\lambda)$ and χ is a shape factor which is 2 for spherical nanoparticles.[21-22] Both experimental results and theoretical calculation show that the LSPR wavelengths for silver and gold nanoparticles are in the VIS range. Due to this fact and their relative stability against oxidation, silver and gold nanostructures are typically used for SERS experiments.[22] Anyway, the electric field E_{out} at and close to the surface of a spherical nanoparticle excited by z – polarized light E_0 can be calculated using a quasi-statistic approximation allowing to replace Maxwell's equations of electrodynamics by the Laplace equation of electrostatics.[19, 22] Therefore, the electric field E_{out} surrounding the nanoparticle can be describes as

$$E_{out}(x,y,z) = E_0\vec{z} - \alpha E_0 \left[\frac{\vec{z}}{r^3} - \frac{3z}{r^5}(x\vec{x} + y\vec{y} + z\vec{z})\right], \qquad \text{Eq. 2.32}$$

with x, y and z are Cartesian coordinates, $\vec{x}$, $\vec{y}$ and $\vec{z}$ are the corresponding unit vectors, r is the radial distance and α is the polarizability of the metal nanoparticle. The polarizability α can be expressed as

$$\alpha = ga^3 \qquad \text{Eq. 2.33}$$

with

$$g = \frac{\varepsilon_{in} - \varepsilon_{out}}{(\varepsilon_{in} + 2\varepsilon_{out})} \, . \qquad \text{Eq. 2.34}$$

Following Eq. 2.32 it is obvious that E_{out} becomes solely larger than E_0 if the content of the square brackets is smaller than zero. This occurs only for very small radial distances implying a fast decay of the E_{out} with respect to the distance from the nanoparticle surface. Although, E_{out} rapidly decays with increasing radial distance, it is compared to E_0 drastically enhanced within a small volume. Thus, maximal enhancement factors E_{out}^2/E_0^2 for spherical silver nanoparticles with radii of 30 nm and 35 nm respectively are calculated to be 85 and 100.[19, 22] However, in SERS the Raman intensity enhancement is of interest and not only the field enhancement at the nanoparticle surface. The Raman intensity I_R is linear to the intensity of the electromagnetic field and thus

$$I_R \sim E_{out}^2 \qquad \text{Eq. 2.35}$$

If a molecule is placed within the enhanced electromagnetic field, a dipole oscillating with the same frequency is induced reemitting an electromagnetic wave. If Stokes-scattering (or Anti-Stokes-scattering) appears the reemitted wave is modified by the frequency of the molecular vibration (see Eq. 2.23). This reemitted wave can be additionally enhanced by inducing a LSPR in the metal nanoparticle leading to a further enhanced electric field $E_{out'}$.[23-24] Accordingly, the Raman intensity is proportional to the intensities of both enhanced fields:

$$I_R \sim E_{out}^2 E_{out'}^2 \qquad \text{Eq. 2.36}$$

If the frequencies respectively wavelengths difference of the incident and Stoke-scattered light is small, Eq. 2.36 can be approximated to

$$I_R \sim E_{out}^4. \qquad \text{Eq. 2.37}$$

This is known as E^4 enhancement or the fourth power of field enhancement at the nanoparticle surface.[22] If the wavelengths of Stoke-scattered light is shifted too strong so that it do not coincide with a LSPR, a further field enhancement will not occur resulting in a E^2 enhancement only. Consequently, Raman intensities occur weaker than for an E^4 enhancement. Anyway, due to the E^4 enhancement an approximated SERS enhancement factor EF can be formulated as follows

$$EF = \frac{E_{out}^4}{E_0^4}\ . \qquad \text{Eq. 2.38}$$

Following the previously presented approximations, theoretical enhancement factors for spherical silver nanoparticles can be calculated appearing within a range between $10^4 – 10^5$.[22] Higher-ordered structures can even reach theoretical enhancement factors of 10^8 and higher.[22, 25] The EFs can further be increased by placing molecules between metal nanoparticle aggregates reaching EFs of 10^{10}-10^{14} which allow single molecule investigations.[25-29] However, theoretical approximations deal normally with perfectly smooth nanostructure surfaces without any sub-structures. If sub-structures formed from single metal atoms are drawn under consideration, the field enhancement is significantly higher leading to theoretical maximal Raman intensity E^4 enhancements of 10^{12} directly at the sub-structure of silver nanoparticle surfaces as shown by Trautmann *et al.*[30] The strong field enhancement at the atomic sub-structures is explained as a consequence of an atomic lightning rod effect.[31-32] The lightning rod effect appears related to the LSPR at ellipsoid nanoparticles resulting in a stronger field enhancement at the ellipsoid tips.[33] Anyway, as already mentioned, the enhanced field is highly localized at the nanoparticle surface and decays rapidly with increasing distance.[34] The range of field enhancement was found to be less than 8 nm and 90 – 95 % of the maximum signal enhancement decreases within 10 nm.[34-40] The extreme field enhancement found at atomic sub-structures decays even faster. Thus, the magnitude of the field enhancement and Raman intensity enhancements can be found within a distance less than 1 nm from the atomic feature.[30] The field decay plays an important role for SERS investigations of sub-micro or nano composites. Since the magnitude of the enhanced field can be found within a range smaller than 1 nm, surface molecules will contribute mostly to the total Raman signal than molecules from the bulk. As already mentioned in chapter 2.2.2, surface molecules may adopt conformations differing from that in the bulk. On the one hand, different conformations may lead to different molecule symmetries resulting in the appearance or the disappearance of molecule vibrations within the Raman spectra. On the other hand, changes in molecular conformation can modify the molecular vibrational states resulting in slightly shifts of band positions in the Raman spectra. Also, Raman intensities can differ in SERS spectra compared to them in far-field Raman spectra. This is firstly related to the conformations, surface molecules may adopt, leading to an increase or decrease of the polarizability and thus to more or less intense peaks in the Raman spectra. Further, the orientation of the surface molecules of nanoparticles towards the field vector of the enhanced field influences the Raman intensity. In contrast to far-field Raman spectroscopy where a lot of possible alignments between scattering molecules and the electric field vector are summed up in one spectrum, SERS spectra contain less alignments. Due to these facts, SERS spectra can differ – sometimes strongly – from far-field Raman spectra. Anyway, the strong field enhancement and the resulting Raman intensity enhancement provided by the LSPR of metallic nanoparticles allow already Raman investigations of organic nanoparticles.

2.3.2 Chemical Enhancement

Although the electromagnetic enhancement gives with Raman intensity enhancements of $10^6 – 10^{10}$ the lion’s share in SERS, the theory of chemical enhancement should be shortly discussed. The chemical enhancement is with enhancement factors between 10^2 and 10^4 less effective than the electromagnetic enhancement, however, it provides intrinsic features recognizable in band position shifts and intensity changes in Raman spectra.[41] The theory of chemical enhancement can be subdivided into a *non-resonant chemical effect* and a *resonant charge transfer chemical effect*.[41-42] The non-resonant chemical effect is related to the molecule conformation which changes if a molecule is absorbed on a nanoparticle's surface. Like surface molecules of organic crystals as described in chapter 2.3.1, the conformation alteration of absorbed molecules can lead to slight shifts of band positions in Raman spectra. Moreover, the conformation change can magnify the polarizability of certain vibrational modes and thus increase the Raman intensities. The resonant charge transfer chemical effect is related to the *resonance Raman effect*. In contrast to the "normal" non-resonant Raman effect, the wavelength of the incident light coincides with the energy difference between the electronic ground to the first (or even higher) excited electronic state of the molecule (Figure 2.9, left). Since an electronic transition occurs more probable from the electronic ground state to an excited electronic state instead to a virtual state, the Raman intensities are enhanced.[15] However, only certain molecular vibrations are enhanced by the resonance Raman effect. Since electronic transitions accompany with structural changes of the molecule orbitals and of the electron density, only the Raman intensities of vibrations which are related with a change in bond length

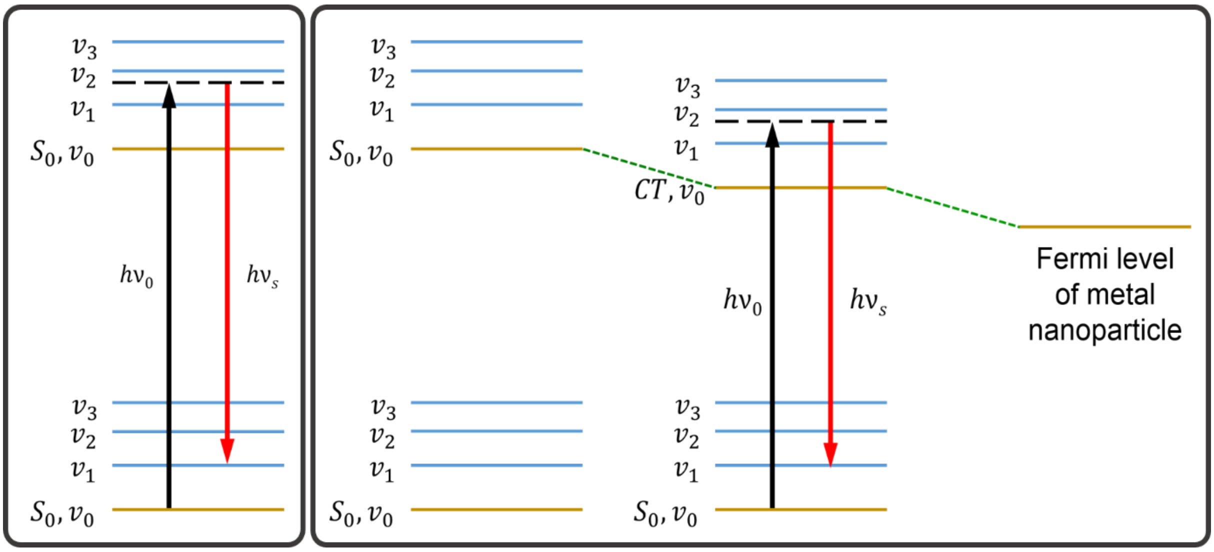

Figure 2.9. Left: Schematic representation of the resonance Raman effect. In contrast to the non-resonant Raman effect, the wavelength of the incident light coincides with the energy difference between the electric ground state and the first excited electronic state. Raman resonant vibrations appear more intense in Raman spectra. **Right:** Schematic representation of the resonant charge transfer chemical effect. A chemisorbed molecule forms a charge transfer (CT) state with the nanoparticle surface. If the wavelength of the incident light coincides with the energy difference between the electric ground state and the electronic CT state, the Raman intensities of certain molecular vibrations are enhanced (10^2 – 10^4).[41]

during the electronic excitation are enhanced.[43] In case of the resonant charge transfer chemical effect, molecules are chemisorbed at the nanoparticle surface. If the Fermi level of the nanoparticle is close to the energy level of the frontier orbitals of the molecule, they can form a metal-molecule (or molecule-metal) electronic charge transfer (CT) state (Figure 2.9, right).[41] If the wavelength of the incident light is in coincidence with the energy difference between the molecular ground state and the CT state, the Raman intensities of certain molecular vibrations can be enhanced as described above. Since the chemical enhancement is not inevitably related to a LSPR, it can appear also on non-metallic nanostructures.[44] Anyway, if metal nanoparticles like silver or gold nanoparticles are used for SERS, both the electromagnetic and the chemical enhancement can occur simultaneously.[25, 41]

2.4 Tip Enhanced Raman Spectroscopy

Although SERS allows Raman investigations of small amounts of samples like single nanoparticle, however, it does not provide information about size and morphology of the particles. To overcome this last limitation, SERS must be combined with a microscopic technique providing a spatial resolution allowing to depict single nanoparticles. Scanning probe microscopy (SPM) methods like atomic force microscopy (AFM) or scanning tunneling microscopy (STM) are perfectly suited for this purpose.[34, 45-47] The combination of both methods is called tip enhanced Raman spectroscopy (TERS) which was firstly performed by Stöckle *et al.* in 2000.[48] Since the experiments presented in chapter 3 and in chapter 4 were undertaken using AFM-TERS, only AFM-TERS measurement methods and setups are presented within this chapter. Anyway, to combine SERS with a SPM technique, the used probe tip must provide a plasmonic feature like a single silver or gold nanoparticle mounted at the tip apex or the sharp tip must consist completely of these materials to promote a lightning rod effect. Furthermore, the tip apex must be illuminated by a laser with a wavelength matching the LSPR of the plasmonic feature. Typically, silver tips are used for excitation wavelengths between 488 nm and 568 nm, whereas gold tips are used for wavelengths between 633 nm and 785 nm.[34] Moreover, the geometry of the TERS setup by meaning of the alignment between the illumination optics and the tip must be chosen so that the sample is placed within the enhanced electric field area at the silver or gold nanoparticle surface. Also, the SPM techniques have certain measurement modii providing specific advantages and disadvantages. The different TERS setup geometries, diverse TERS tip production procedures and TERS applications are presented in the following.

2.4.1 TERS Illumination Setups

Three different illumination geometries are typically used for AFM-TERS experiments. These are the *bottom-illumination*, the *side-illumination* and the *top-illumination setups*. Each illumination setup has its specific advantages and disadvantages regarding the field enhancement at the tip apex, the laser focus, the background signal and the character of the sample being examined. Anyway, the first TERS experiments were undertaken using the bottom-illumination setup.[34, 48-51] In this illumination mode, an inverse optical microscope

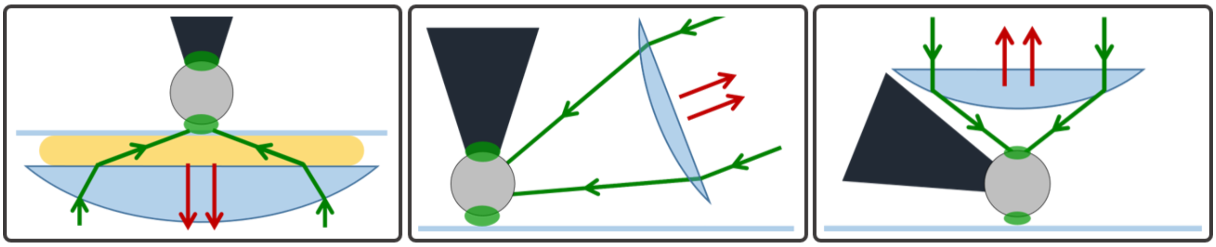

Figure 2.10. Schematic representation of different TERS illumination geometries. Green arrows depict the incident laser light; the red arrows depict Raman scattered light; the grey triangles and spheres represent the metal tips; green ellipses illustrate the enhanced field provided by LSPRs and the lightning rod effect; the blue circle segments represent optical lenses, the different lens sizes represent diverse numerical apertures (NA). **Left:** Bottom-illumination setup. **Middle:** Side-illumination setup. **Right:** Top-illumination setup.

equipped with an oil-immersion objective with a high numerical aperture (NA, typically 1.4 – 1.6) illuminates the sample from the bottom (Figure 2.10, left). Using high NA immersion-oil objectives involves two advantages. Firstly, these objectives generate small laser foci providing high laser intensities on the one hand and reducing far-field Raman signals to a minimum on the other hand.[34, 52] Secondly, high NA oil-objectives refract the incident light under a relatively large angle (compared to small NA) resulting in a total reflection of the outer parts of the laser beam at the glass substrate, creating an evanescent filed polarized parallel toward the tip axis. Due to the evanescent field and the strongly refracted laser beams, the enhanced electric field at the tip apex is mainly polarized along the tip axis and thus the excitation of Raman scattering of the sample beneath the tip is maximized. The field enhancement can be further increased in bottom-illumination setups by using radially polarized laser light.[34, 53-54] Raman scattered light is collected in back-reflection mode by the same immersion-oil objective as used for sample illumination. Since the excitation light and the Raman scattered light must travel through the sample, only transparent samples are accessible for TERS in bottom-illumination setups. Furthermore, the samples may not exceed a certain thickness because the evanescent field created at the glass substrate surface contributes mainly to the LSPR polarized along the tip axis.[55] Since evanescent fields do spread in the direction of the electric field vector, they decay strongly with respect to the distance from the surface. Thus, TERS samples should not be thicker than 100 – 150 nm (depending on the wavelength of the incident light). Although this limitation, the bottom-illumination is the most efficient setup for TERS investigations.[34] Due to its high efficiency, the bottom-illumination setup was used for structure investigations of organic nanoscale composites as presented within chapter 3 and 4.

In contrast to the bottom-illumination, side-illumination allows TERS investigations of opaque and thicker samples.[34, 56-61] As already indicated by the name, the incident light illuminates the TERS tip from the side and above the sample within an angle between 45° – 80° (Figure 2.10, middle).[34, 52, 62] Long working distance objectives with smaller NAs (0.28 – 0.7) have to be used in side-illumination since the objective cannot brought close enough to the tip to use short working distance objectives with higher NAs. Long working distance objectives provide broader focused laser spots. Furthermore, the angle between sample and illumination optics deforms the laser spot to an ellipse at the sample. Both, the broader laser focus and its elliptical character increase the laser spot size resulting in a higher contribution of far-field signals in the TERS spectra.[52] Furthermore, the increased spot size provided by long working distance objectives compared to short working distance objectives requires higher laser powers to receive equivalent results as in bottom-illumination setups. In contrast to bottom-illumination geometries, strongest field enhancements at the tip apex are obtained for using linear polarized light along the tip axis.[34, 54] Raman scattered light can be collected via the same objectives in back-reflection mode for all samples or in bottom-collection mode for transparent samples.[52]

As like as in side-illumination setups, also top-illumination setups allow TERS measurements on opaque samples. The illumination of the metal tip apex and the sample take place from above perpendicular to the sample surface (Figure 2.10, right).[52] Also here, long working distance objectives with small NAs (compared to bottom-illumination mode) are used.[63-64] This results in broader laser spots and thus in a higher contribution of far-field signals in TERS spectra. The far-field contribution is, however, smaller than for side-illumination setups since the incident light strikes the sample perpendicular forming a circular laser spot instead of angled resulting in an elliptical spot. Anyway, the components of the incident light being polarized perpendicular to sample (parallel to the tip axis) are less pronounced in bottom-illumination setups compared to bottom- and side illumination geometries. Hence, also the enhanced field at the tip apex is less polarized perpendicular to the sample leading to weaker TERS signals. Furthermore, special AFM-probes providing an angle between tip and tip holder should be used to reduce shadowing effects and thus further TERS signal losses.[34] Anyway, top-illumination setups can be easier integrated into standard AFM microscope systems compared to the other illumination geometries.[34]

In sake of completeness, it should be mentioned that a fourth, less commonly used setup exists, the parabolic mirror illumination. Here, the sample is illuminated from the bottom but in contrast to common bottom-illumination, a parabolic mirror focuses additionally the incident laser light onto the sample and the tip apex.[52, 65-67]

2.4.2 TERS Tip Preparation Methods

One of the most important (if not the most important) element in TERS is the tip. As already mentioned above, it must provide a plasmonic feature like a nanoparticle localized at the tip apex which fulfill the requirements so that a LSPR can be induced by the incident light. However, the sharp tip can also consist completely of a plasmonic material like silver and gold. In this case, the field enhancement at the tip apex is generated mainly by the lighting rod effect.[33, 45] Anyway, one of the most common methods to produce TERS active tips is undertaken by vacuum deposition of thin metal layers (< 50 nm) onto commercially available silicon or silicon-nitride AFM tips using thermal evaporation or sputtering techniques.[34, 48-50, 68-74] Vacuum deposition of silver or gold results in a metal coating onto the AFM tips characterized by the formation of metal islands. Due to the geometry of sharp AFM tips, a single silver respectively gold nanoparticle is formed at the tip apex. The formation of single silver or gold nanoparticles at the tip apex can be supported by a subsequent annealing of the metallized tips.[75-76] However, silver and especially gold nanoparticles do not adhere strongly to the silicon surface of the tips. Hence, if the metalized tips are exposed to mechanical stress, the nanoparticle positioned at the tip apex may get lost rendering the tip TERS inactive. This problem can be handled by coating the tips previously with an adhesive layer consisting of chromium or titanium. [52, 75-79] Next to vapor deposition techniques, AFM tip apexes can be equipped chemically with a single metal nanoparticle. Different chemical procedures are reported in literature including *inter alia* electrochemical deposition, electroless chemical deposition, silver mirror reactions and photoinduced reactions.[34, 52, 80-87] Furthermore, TERS active tips can be prepared by picking up gold nanoparticles previously coated with a glue from a flat substrate.[34, 52, 77, 88] Moreover, etching and focus ion beam milling procedures for TERS active tip preparation are also reported in literature.[89-102] Within this work, TERS active tips were produced by sputtering a thin layer of silver onto a commercially available AFM probe. Before silver sputtering, the AFM tips were previously coated with a titanium adhesion layer. Afterwards, TERS tips were annealed to promote the formation of a single silver nanoparticle at the tip apex. This procedure is described in more detail within chapter 3 and 4.

2.4.3 Special Features of TERS

Since TERS is in principle the combination of SERS and AFM, the same special features are expected to occur in TERS spectra like in SERS spectra. In contrast to SERS, however, where a various number of metal nanoparticles are localized within the laser spot and thus recorded spectra contain information of all molecules close or in direct contact to these nanoparticles' surfaces, only a single nanoparticle providing the necessary field enhancement is placed in the laser focus in TERS. Accordingly, the intrinsic features are more prominent in TERS than in SERS. Especially the orientation between the investigated molecules and the direction of the enhanced field which is mainly aligned along the tip axis in bottom-illumination setups influences strongly TERS spectra. Thus, molecular vibrational modes aligned parallel to the tip axis are maximally enhanced.[34] *Vice versa*, vibrational modes aligned perpendicular to the polarization of the enhanced field are less or even not enhanced and may miss in TERS spectra. This phenomenon is observable at in-plane modes of molecules lying flat on the substrate.[34, 38, 103-106] The orientation of vibrational modes towards the polarization of the enhanced field is for example of pivotal importance in TERS investigations of nanoscale co-crystals as shown and described in more detail within chapter 3. Although, presented TERS experiments are exclusively performed in non-contact AFM mode and thus the TERS tip is normally not in direct contact to the sample surface, tip-sample interactions may further influence TERS spectra. Hence, temporal fluctuations in Raman band intensities and positions are reported assigned to molecular diffusions and orientation changes during the measurements.[34, 92, 107-109] If the tip should "accidently" touch the sample, the sample surface can be deformed and chemical interactions between the tip and sample molecules may arise. Both, the surface deformation and chemical interactions can cause further changes in molecular orientation and conformation leading to modified selection rules and alternating Raman spectra.[34, 110-112] Since the enhanced field arises of a single metal nanoparticle (or of the apex of a sharp metal tip) and due to the rapid field decay, TERS provides a high spatial resolution (< 1 nm).[30, 113-114] Hence, only vibrational modes of a few surface molecules contribute to TERS spectra of organic nanoparticles. As already described (see chapter 2.2.2 and 2.3.1), molecular conformations of surface molecules are supposed to be different than that in the bulk. Thus, TERS spectra of nanoscale organic crystals can differ strongly from conventional far-field Raman spectra as presented in the following chapters.

2.5 References

1. Engelke, F., *Aufbau der Moleküle: Eine Einführung*. Springer-Verlag: 2013.
2. Schwabl, F., *Quantenmechanik (QM I)*. Springer Nature: 2007; Vol. 7.
3. Pietschmann, H., *Quantenmechanik verstehen*. Springer Nature: 2003.
4. Smekal, A., Zur Quantentheorie der Dispersion. *Naturwissenschaften* **1923,** *11* (43), 873-875.
5. Kramers, H. A.; Heisenberg, W., Über die Streuung von Strahlung durch Atome. *Zeitschrift für Physik* **1925,** *31* (1), 681-708.
6. Dirac, P. A. M., The quantum theory of dispersion. *Proceedings of the Royal Society of London. Series A, Containing Papers of a Mathematical and Physical Character* **1927,** *114* (769), 710-728.
7. Kiefer, W., Raman-Spektroskopie. In *Spektroskopie amorpher und kristalliner Festkörper*, Springer: 1995; pp 117-147.
8. Raman, C.; Krishnan, K., Molecular spectra in the extreme infra-red. *Nature* **1928,** *122*, 278.
9. Raman, C.; Krishnan, K., Polarisation of scattered light-quanta. *Nature* **1928,** *122*, 169.
10. Raman, C.; Krishnan, K., The negative absorption of radiation. *Nature* **1928,** *122*, 12-13.
11. Raman, C. V., A change of wave-length in light scattering. *Nature* **1928,** *121*, 619.
12. Raman, C. V.; Krishnan, K. S., A new type of secondary radiation. *Nature* **1928,** *121*, 501-502.
13. Raman, C. V.; Krishnan, K. S., The optical analogue of the Compton effect. *Nature* **1928,** *121*, 711.
14. Landsberg, G.; Mandelstam, L., Eine neue Erscheinung bei der Lichtzerstreuung in Krystallen. *Naturwissenschaften* **1928,** *16* (28), 557-558.
15. Long, D. A., *The Raman Effect: A Unified Treatment of the Theory of Raman Scattering by Molecules*. Wiley: 2002.
16. Fleischmann, M.; Hendra, P. J.; McQuillan, A. J., Raman Spectra of Pyridine Adsorbed at a Silver Electrode. *Chem. Phys. Lett.* **1974,** *26*, 163.
17. Jeanmaire, D. L.; Van Duyne, R. P., Surface Raman Spectroelectrochemistry Part I. Heterocyclic, Aromatic, and Aliphatic Amines Adsorbed on the Anodized Silver Electrode. *J. Electroanal. Chem. Interfacial Electrochem.* **1977,** *84*, 1.

18. Albrecht, M. G.; Creighton, J. A., Anomalously Intense Raman Spectra of Pyridine at a Silver Electrode. *J. Am. Chem. Soc.* **1977,** *99*, 5215.

19. Kelly, K. L.; Coronado, E.; Zhao, L. L.; Schatz, G. C., The optical properties of metal nanoparticles: The influence of size, shape, and dielectric environment. *J. Phys. Chem. B* **2003,** *107* (3), 668-677.

20. Sönnichsen, C. Plasmons in Metal Nanostructures. Dissertation, Ludwig-Maximilians University of Munich, 2001.

21. Mie, G., Beiträge zur Optik trüber Medien, speziell kolloidaler Metallösungen. *Annalen der Physik* **1908,** *330* (3), 377-445.

22. Stiles, P. L.; Dieringer, J. A.; Shah, N. C.; Van Duyne, R. P., Surface-enhanced Raman spectroscopy. *Annu. Rev. Anal. Chem.* **2008,** *1*, 601-626.

23. Wang, D. S.; Kerker, M., Enhanced Raman scattering by molecules adsorbed at the surface of colloidal spheroids. *Phys. Rev. B: Condens. Matter* **1981,** *24* (4), 1777-1790.

24. Kerker, M.; Wang, D.-S.; Chew, H., Surface enhanced Raman scattering (SERS) by molecules adsorbed at spherical particles: errata. *Appl. Opt.* **1980,** *19* (24), 4159-4174.

25. Langer, J.; Jimenez de Aberasturi, D.; Aizpurua, J.; Alvarez-Puebla, R. A.; Auguié, B.; Baumberg, J. J.; Bazan, G. C.; Bell, S. E. J.; Boisen, A.; Brolo, A. G.; Choo, J.; Cialla-May, D.; Deckert, V.; Fabris, L.; Faulds, K.; García de Abajo, F. J.; Goodacre, R.; Graham, D.; Haes, A. J.; Haynes, C. L.; Huck, C.; Itoh, T.; Käll, M.; Kneipp, J.; Kotov, N. A.; Kuang, H.; Le Ru, E. C.; Lee, H. K.; Li, J.-F.; Ling, X. Y.; Maier, S. A.; Mayerhöfer, T.; Moskovits, M.; Murakoshi, K.; Nam, J.-M.; Nie, S.; Ozaki, Y.; Pastoriza-Santos, I.; Perez-Juste, J.; Popp, J.; Pucci, A.; Reich, S.; Ren, B.; Schatz, G. C.; Shegai, T.; Schlücker, S.; Tay, L.-L.; Thomas, K. G.; Tian, Z.-Q.; Van Duyne, R. P.; Vo-Dinh, T.; Wang, Y.; Willets, K. A.; Xu, C.; Xu, H.; Xu, Y.; Yamamoto, Y. S.; Zhao, B.; Liz-Marzán, L. M., Present and Future of Surface-Enhanced Raman Scattering. *ACS Nano* **2020,** *14* (1), 28-117.

26. Kneipp, K.; Wang, Y.; Kneipp, H.; Perelman, L. T.; Itzkan, I.; Dasari, R. R.; Feld, M. S., Single Molecule Detection Using Surface-Enhanced Raman Scattering (SERS). *Phys. Rev. Lett.* **1997,** *78*, 1667.

27. Nie, S.; Emory, S. R., Probing Single Molecules and Single Nanoparticles by Surface-Enhanced Raman Scattering. *Science* **1997,** *275*, 1102.

28. Xu, H.; Aizpurua, J.; Käll, M.; Apell, P., Electromagnetic Contributions to Single-Molecule Sensitivity in Surface-Enhanced Raman Scattering. *Phys. Rev. E: Stat. Phys., Plasmas, Fluids, Relat. Interdiscip. Top.* **2000,** *62*, 4318.

29. Yamamoto, Y. S.; Ozaki, Y.; Itoh, T., Recent Progress and Frontiers in the Electromagnetic Mechanism of Surface-Enhanced Raman Scattering. *J. Photochem. Photobiol., C* **2014,** *21*, 81.

30. Trautmann, S.; Aizpurua, J.; Götz, I.; Undisz, A.; Dellith, J.; Schneidewind, H.; Rettenmayr, M.; Deckert, V., A Classical Description of Subnanometer Resolution by Atomic Features in Metallic Structures. *Nanoscale* **2017,** *9* (1), 391-401.

31. Benz, F.; Schmidt, M. K.; Dreismann, A.; Chikkaraddy, R.; Zhang, Y.; Demetriadou, A.; Carnegie, C.; Ohadi, H.; de Nijs, B.; Esteban, R.; Aizpurua, J.; Baumberg, J. J., Single-Molecule Optomechanics in Picocavities. *Science* **2016,** *354*, 726.

32. Barbry, M.; Koval, P.; Marchesin, F.; Esteban, R.; Borisov, A. G.; Aizpurua, J.; Sánchez-Portal, D., Atomistic Near-Field Nanoplasmonics: Reaching Atomic-Scale Resolution in Nanooptics. *Nano Lett.* **2015,** *15*, 3410.

33. Liao, P.; Wokaun, A., Lightning rod effect in surface enhanced Raman scattering. *J. Chem. Phys.* **1982,** *76* (1), 751-752.

34. Deckert-Gaudig, T.; Taguchi, A.; Kawata, S.; Deckert, V., Tip-Enhanced Raman Spectroscopy – From Early Developments to Recent Advances. *Chem. Soc. Rev.* **2017,** *46*, 4077.

35. Yano, T.-a.; Ichimura, T.; Taguchi, A.; Hayazawa, N.; Verma, P.; Inouye, Y.; Kawata, S., Confinement of enhanced field investigated by tip-sample gap regulation in tapping-mode tip-enhanced Raman microscopy. *Appl. Phys. Lett.* **2007,** *91* (12), 121101.

36. Hartschuh, A.; Sánchez, E. J.; Xie, X. S.; Novotny, L., High-Resolution Near-Field Raman Microscopy of Single-Walled Carbon Nanotubes. *Physical Review Letters* **2003,** *90* (9), 095503.

37. Roth, R. M.; Panoiu, N. C.; Adams, M. M.; Osgood, R. M.; Neacsu, C. C.; Raschke, M. B., Resonant-Plasmon Field Enhancement from Asymmetrically Illuminated Conical Metallic-Probe Tips. *Opt. Express* **2006,** *14* (7), 2921-2931.

38. Jiang, N.; Foley, E.; Klingsporn, J.; Sonntag, M.; Valley, N.; Dieringer, J.; Seideman, T.; Schatz, G.; Hersam, M.; Van Duyne, R., Observation of multiple vibrational modes in ultrahigh vacuum tip-enhanced Raman spectroscopy combined with molecular-resolution scanning tunneling microscopy. *Nano letters* **2012,** *12* (10), 5061-5067.

39. Pettinger, B.; Domke, K. F.; Zhang, D.; Schuster, R.; Ertl, G., Direct Monitoring of Plasmon Resonances in a Tip-Surface Gap of Varying Width. *Phys. Rev. B: Condens. Matter* **2007,** *76* (11).

40. Pashaee, F.; Hou, R.; Gobbo, P.; Workentin, M. S.; Lagugné-Labarthet, F., Tip-Enhanced Raman Spectroscopy of Self-Assembled Thiolated Monolayers on Flat Gold Nanoplates Using Gaussian-Transverse and Radially Polarized Excitations. *J. Phys. Chem. C* **2013,** *117* (30), 15639-15646.

41. Pilot, R.; Signorini, R.; Durante, C.; Orian, L.; Bhamidipati, M.; Fabris, L., A Review on Surface-Enhanced Raman Scattering. *Biosensors* **2019,** *9* (2), 57.

42. Jensen, L.; Aikens, C. M.; Schatz, G. C., Electronic Structure Methods for Studying Surface-Enhanced Raman Scattering. *Chem. Soc. Rev.* **2008,** *37*, 1061.

43. Hirakawa, A. Y.; Tsuboi, M., Molecular Geometry in an Excited Electronic State and a Preresonance Raman Effect. *Science* **1975,** *188* (4186), 359-361.

44. Kim, J.; Jang, Y.; Kim, N.-J.; Kim, H.; Yi, G.-C.; Shin, Y.; Kim, M. H.; Yoon, S., Study of Chemical Enhancement Mechanism in Non-plasmonic Surface Enhanced Raman Spectroscopy (SERS). *Frontiers in Chemistry* **2019,** *7* (582).

45. Bailo, E.; Deckert, V., Tip-Enhanced Raman Scattering. *Chem. Soc. Rev.* **2008,** *37* (5), 921-930.

46. Binnig, G.; Quate, C. F.; Gerber, C., Atomic Force Microscope. *Physical Review Letters* **1986,** *56* (9), 930-933.

47. Binnig, G.; Rohrer, H.; Gerber, C.; Weibel, E., Surface Studies by Scanning Tunneling Microscopy. *Physical Review Letters* **1982,** *49* (1), 57-61.

48. Stockle, R.; Suh, Y.; Deckert, V.; Zenobi, R., Nanoscale Chemical Analysis by Tip-Enhanced Raman Spectroscopy. *Chem. Phys. Lett.* **2000,** *318*, 131.

49. Hayazawa, N.; Inouye, Y.; Sekkat, Z.; Kawata, S., Metallized Tip Amplification of Near-Field Raman Scattering. *Opt. Commun.* **2000,** *183*, 333.

50. Hayazawa, N.; Inouye, Y.; Sekkat, Z.; Kawata, S., Near-field Raman imaging of organic molecules by an apertureless metallic probe scanning optical microscope. *Journal of Chemical Physics* **2002,** *117* (3), 1296-1301.

51. Hartschuh, A.; Anderson, N.; Novotny, L., Near-field Raman spectroscopy using a sharp metal tip. *Journal of Microscopy* **2003,** *210* (3), 234-240.

52. Gibson, K. F.; Kazarian, S. G., Tip-enhanced Raman Spectroscopy. *Encyclopedia of Analytical Chemistry*.

53. Hayazawa, N.; Ishitobi, H.; Taguchi, A.; Tarun, A.; Ikeda, K.; Kawata, S., Focused Excitation of Surface Plasmon Polaritons Based on Gap-Mode in Tip-Enhanced Spectroscopy. *Jpn. J. Appl. Phys.* **2007,** *46* (12), 7995-7999.

54. Kazemi-Zanjani, N.; Vedraine, S.; Lagugné-Labarthet, F., Localized enhancement of electric field in tip-enhanced Raman spectroscopy using radially and linearly polarized light. *Opt. Express* **2013,** *21* (21), 25271-25276.

55. Furukawa, H.; Kawata, S., Local Field Enhancement with an Apertureless Near-Field-Microscope Probe. *Opt. Commun.* **1998,** *148* (4-6), 221-224.

56. Anderson, M. S., Locally enhanced Raman spectroscopy with an atomic force microscope. *Appl. Phys. Lett.* **2000,** *76* (21), 3130-3132.

57. Hayazawa, N.; Tarun, A.; Inouye, Y.; Kawata, S., Near-field enhanced Raman spectroscopy using side illumination optics. *J. Appl. Phys.* **2002,** *92* (12), 6983-6986.

58. Mehtani, D.; Lee, N.; Hartschuh, R. D.; Kisliuk, A.; Foster, M. D.; Sokolov, A. P.; Maguire, J. F., Nano-Raman spectroscopy with side-illumination optics. *J. Raman Spectrosc.* **2005,** *36* (11), 1068-1075.

59. Lee, N.; Hartschuh, R.; Mehtani, D.; Kisliuk, A.; Maguire, J.; Green, M.; Foster, M.; Sokolov, A., High contrast scanning nano-Raman spectroscopy of silicon. *J. Raman Spectrosc.* **2007,** *38* (6), 789-796.

60. Liu, Z.; Wang, X.; Dai, K.; Jin, S.; Zeng, Z.-C.; Zhuang, M.-D.; Yang, Z.-L.; Wu, D.-Y.; Ren, B.; Tian, Z.-Q., Tip-enhanced Raman spectroscopy for investigating adsorbed nonresonant molecules on single-crystal surfaces: tip regeneration, probe molecule, and enhancement effect. *J. Raman Spectrosc.* **2009,** *40* (10), 1400-1406.

61. Marquestaut, N.; Talaga, D.; Servant, L.; Yang, P.; Pauzauskie, P.; Lagugné-Labarthet, F., Imaging of single GaN nanowires by tip-enhanced Raman spectroscopy. *J. Raman Spectrosc.* **2009,** *40* (10), 1441-1445.

62. Stadler, J.; Schmid, T.; Zenobi, R., Developments in and practical guidelines for tip-enhanced Raman spectroscopy. *Nanoscale* **2012,** *4* (6), 1856-1870.

63. Berweger, S.; Raschke, M. B., Signal limitations in tip-enhanced Raman scattering: the challenge to become a routine analytical technique. *Analytical and Bioanalytical Chemistry* **2010,** *396* (1), 115-123.

64. Stadler, J.; Schmid, T.; Zenobi, R., Nanoscale chemical imaging using top-illumination tip-enhanced Raman spectroscopy. *Nano letters* **2010,** *10* (11), 4514-4520.

65. Steidtner, J.; Pettinger, B., High-resolution microscope for tip-enhanced optical processes in ultrahigh vacuum. *Review of Scientific Instruments* **2007,** *78* (10).

66. Stanciu, C.; Sackrow, M.; Meixner, A. J., High NA particle- and tip-enhanced nanoscale Raman spectroscopy with a parabolic-mirror microscope. *Journal of Microscopy* **2008,** *229* (2), 247-253.

67. Debus, C.; Lieb, M. A.; Drechsler, A.; Meixner, A. J., Probing highly confined optical fields in the focal region of a high NA parabolic mirror with subwavelength spatial resolution. *Journal of Microscopy* **2003,** *210* (3), 203-208.

68. Bailo, E.; Deckert, V., Tip-Enhanced Raman Spectroscopy of Single RNA Strands: Towards a Novel Direct-Sequencing Method. *Angew. Chem. Int. Ed.* **2008,** *47* (9), 1658-1661.

69. Hayazawa, N.; Yano, T.; Watanabe, H.; Inouye, Y.; Kawata, S., Detection of an individual single-wall carbon nanotube by tip-enhanced near-field Raman spectroscopy. *Chemical Physics Letters* **2003,** *376* (1-2), 174-180.

70. Deckert-Gaudig, T.; Richter, M.; Knebel, D.; Jähnke, T.; Jankowski, T.; Stock, E.; Deckert, V., A Modified Transmission Tip-Enhanced Raman Scattering (TERS) Setup Provides Access to Opaque Samples. *Appl. Spectrosc.* **2014,** *68* (8), 916-919.

71. Yeo, B. S.; Zhang, W.; Vannier, C.; Zenobi, R., Enhancement of Raman signals with silver-coated tips. *Appl. Spectrosc.* **2006,** *60* (10), 1142-1147.

72. Hayazawa, N.; Yano, T.-a.; Kawata, S., Highly reproducible tip-enhanced Raman scattering using an oxidized and metallized silicon cantilever tip as a tool for everyone. *J. Raman Spectrosc.* **2012,** *43* (9), 1177-1182.

73. Yang, Y.; Li, Z.-Y.; Nogami, M.; Tanemura, M.; Huang, Z., The controlled fabrication of "Tip-On-Tip" TERS probes. *RSC Advances* **2014,** *4* (9), 4718-4722.

74. Asghari-Khiavi, M.; Wood, B. R.; Hojati-Talemi, P.; Downes, A.; McNaughton, D.; Mechler, A., Exploring the origin of tip-enhanced Raman scattering; preparation of efficient TERS probes with high yield. *J. Raman Spectrosc.* **2012,** *43* (2), 173-180.

75. Hübner, J.; Deckert-Gaudig, T.; Glorian, J.; Deckert, V. K.; Spitzer, D., Surface Characterization of Nanoscale Co-Crystals Enabled through Tip Enhanced Raman Spectroscopy. *Nanoscale* **2020**, *18*, 10306-10319.

76. Hübner, J.; Pichot, V.; Lobry, E.; Deckert-Gaudig, T.; Deckert, V.; Spitzer, D., *Formation Mechanism of Anisotropic RDX-TNT Core-Shell Nanoparticles and their Influence onto Nanodiamond Detonation Syntheses*. 2020.

77. Park, C.-G.; Kim, J.-Y.; Lee, E.-B.; Choi, H.-K.; Park, W.-H.; Kim, J.-W.; Kim, Z.-H., Tip-Enhanced Raman Scattering with a Nanoparticle-Functionalized Probe. *Bulletin of the Korean Chemical Society* **2012,** *33* (5), 1748-1752.

78. Kim, T.; Jeon, K.-S.; Heo, K.; Kim, H. M.; Park, J.; Suh, Y. D.; Hong, S., Multilayered nano-prism vertex tips for tip-enhanced Raman spectroscopy and imaging. *Analyst* **2013,** *138* (19), 5588-5593.

79. Weber-Bargioni, A.; Schwartzberg, A.; Cornaglia, M.; Ismach, A.; Urban, J. J.; Pang, Y.; Gordon, R.; Bokor, J.; Salmeron, M. B.; Ogletree, D. F., Hyperspectral nanoscale imaging on dielectric substrates with coaxial optical antenna scan probes. *Nano letters* **2011,** *11* (3), 1201-1207.

80. Yang, L. K.; Huang, T. X.; Zeng, Z. C.; Li, M. H.; Wang, X.; Yang, F. Z.; Ren, B., Rational Fabrication of a Gold-Coated AFM TERS Tip by Pulsed Electrodeposition. *Nanoscale* **2015,** *7*, 18225.

81. Huang, T. X.; Huang, S. C.; Li, M. H.; Zeng, Z. C.; Wang, X.; Ren, B., Tip-Enhanced Raman Spectroscopy: Tip-Related Issues. *Anal. Bioanal. Chem.* **2015,** *407*, 8177.

82. Wang, R.; Wang, J.; Hao, F.; Zhang, M.; Tian, Q., Tip-enhanced Raman spectroscopy with silver-coated optical fiber probe in reflection mode for investigating multiwall carbon nanotubes. *Appl. Opt.* **2010,** *49* (10), 1845-1848.

83. Barsegova, I.; Lewis, A.; Khatchatouriants, A.; Manevitch, A.; Ignatov, A.; Axelrod, N.; Sukenik, C., Controlled fabrication of silver or gold nanoparticle near-field optical atomic force probes: Enhancement of second-harmonic generation. *Appl. Phys. Lett.* **2002,** *81* (18), 3461-3463.

84. Coluccio, M. L.; Francardi, M.; Gentile, F.; Candeloro, P.; Ferrara, L.; Perozziello, G.; Di Fabrizio, E., Plasmonic 3D-structures based on silver decorated nanotips for biological sensing. *Optics and Lasers in Engineering* **2016,** *76*, 45-51.

85. Wang, J. J.; Saito, Y.; Batchelder, D. N.; Kirkham, J.; Robinson, C.; Smith, D. A., Controllable method for the preparation of metalized probes for efficient scanning near-field optical Raman microscopy. *Appl. Phys. Lett.* **2005,** *86* (26), 1-3.

86. Wang, J.; Saito, Y.; Batchelder, D.; Kirkham, J.; Robinson, C.; Smith, D., Controllable method for the preparation of metalized probes for efficient scanning near-field optical Raman microscopy. *Appl. Phys. Lett.* **2005,** *86* (26), 263111.

87. Umakoshi, T.; Yano, T.-a.; Saito, Y.; Verma, P., Fabrication of Near-Field Plasmonic Tip by Photoreduction for Strong Enhancement in Tip-Enhanced Raman Spectroscopy. *Applied Physics Express* **2012,** *5* (5), 052001.

88. Kalkbrenner, T.; Ramstein, M.; Mlynek, J.; Sandoghdar, V., A single gold particle as a probe for apertureless scanning near-field optical microscopy. *Journal of Microscopy* **2001,** *202* (1), 72-76.

89. Hartschuh, A.; Qian, H.; Meixner, A. J.; Anderson, N.; Novotny, L., Nanoscale optical imaging of single-walled carbon nanotubes. *Journal of Luminescence* **2006,** *119-120* (SPEC. ISS.), 204-208.

90. Neacsu, C. C.; Dreyer, J.; Behr, N.; Raschke, M. B., Scanning-probe Raman spectroscopy with single-molecule sensitivity. *Phys. Rev. B: Condens. Matter* **2006,** *73* (19).

91. Paulite, M.; Blum, C.; Schmid, T.; Opilik, L.; Eyer, K.; Walker, G. C.; Zenobi, R., Full Spectroscopic Tip-Enhanced Raman Imaging of Single Nanotapes Formed from β-Amyloid(1–40) Peptide Fragments. *ACS Nano* **2013,** *7* (2), 911-920.

92. Zhang, W.; Yeo, B. S.; Schmid, T.; Zenobi, R., Single molecule tip-enhanced Raman spectroscopy with silver tips. *J. Phys. Chem. C* **2007,** *111* (4), 1733-1738.

93. Wang, X.; Liu, Z.; Zhuang, M.-D.; Zhang, H.-M.; Wang, X.; Xie, Z.-X.; Wu, D.-Y.; Ren, B.; Tian, Z.-Q., Tip-enhanced Raman spectroscopy for investigating adsorbed species on a single-crystal surface using electrochemically prepared Au tips. *Appl. Phys. Lett.* **2007,** *91* (10), 101105.

94. Ren, B.; Picardi, G.; Pettinger, B., Preparation of gold tips suitable for tip-enhanced Raman spectroscopy and light emission by electrochemical etching. *Review of Scientific Instruments* **2004,** *75* (4), 837-841.

95. Chen, J.; Yang, W.; Dick, K.; Deppert, K.; Xu, H. Q.; Samuelson, L.; Xu, H., Tip-enhanced Raman scattering of p-thiocresol molecules on individual gold nanoparticles. *Appl. Phys. Lett.* **2008,** *92* (9), 093110.

96. Roy, D.; Williams, C. M.; Mingard, K., Single crystal gold tips for tip-enhanced Raman spectroscopy. *J. Vac. Sci. Technol. B* **2010,** *28* (3), 631-634.

97. Kharintsev, S. S.; Noskov, A. I.; Hoffmann, G. G.; Loos, J., Near-field optical taper antennas fabricated with a highly replicable ac electrochemical etching method. *Nanotechnology* **2010,** *22* (2), 025202.

98. Xu, G.; Liu, Z.; Xu, K.; Zhang, Y.; Zhong, H.; Fan, Y.; Huang, Z., Constant current etching of gold tips suitable for tip-enhanced Raman spectroscopy. *Review of Scientific Instruments* **2012,** *83* (10), 103708.

99. Kharintsev, S.; Alekseev, A.; Vasilchenko, V.; Kharitonov, A.; Salakhov, M., Electrochemical design of plasmonic nanoantennas for tip-enhanced optical spectroscopy and imaging performance. *Opt. Mater. Express* **2015,** *5* (10), 2225-2230.

100. Kharintsev, S.; Alekseev, A.; Loos, J., Etchant-based design of gold tip apexes for plasmon-enhanced Raman spectromicroscopy. *Spectrochim. Acta A* **2017,** *171*, 139-143.

101. Taminiau, T. H.; Moerland, R. J.; Segerink, F. B.; Kuipers, L.; van Hulst, N. F., λ/4 Resonance of an Optical Monopole Antenna Probed by Single Molecule Fluorescence. *Nano Letters* **2007,** *7* (1), 28-33.

102. Maouli, I.; Taguchi, A.; Saito, Y.; Kawata, S.; Verma, P., Optical antennas for tunable enhancement in tip-enhanced Raman spectroscopy imaging. *Applied Physics Express* **2015,** *8* (3), 032401.

103. Deckert-Gaudig, T.; Rauls, E.; Deckert, V., Aromatic Amino Acid Monolayers Sandwiched between Gold and Silver: A Combined Tip-Enhanced Raman and Theoretical Approach. *J. Phys. Chem. C* **2010,** *114* (16), 7412-7420.

104. Stadler, J.; Schmid, T.; Zenobi, R., Nanoscale Chemical Imaging of Single-Layer Graphene. *ACS Nano* **2011,** *5* (10), 8442-8448.

105. Opilik, L.; Payamyar, P.; Szczerbiński, J.; Schütz, A. P.; Servalli, M.; Hungerland, T.; Schlüter, A. D.; Zenobi, R., Minimally Invasive Characterization of Covalent Monolayer Sheets Using Tip-Enhanced Raman Spectroscopy. *ACS Nano* **2015,** *9* (4), 4252-4259.

106. Jiang, N.; Chiang, N.; Madison, L. R.; Pozzi, E. A.; Wasielewski, M. R.; Seideman, T.; Ratner, M. A.; Hersam, M. C.; Schatz, G. C.; Van Duyne, R. P., Nanoscale Chemical Imaging of a Dynamic Molecular Phase Boundary with Ultrahigh Vacuum Tip-Enhanced Raman Spectroscopy. *Nano Lett.* **2016,** *16*, 3898.

107. Singh, P.; Deckert-Gaudig, T.; Schneidewind, H.; Kirsch, K.; van Schrojenstein Lantman, E. M.; Weckhuysen, B. M.; Deckert, V., Differences in single and aggregated nanoparticle plasmon spectroscopy. *Phys. Chem. Chem. Phys.* **2015,** *17* (5), 2991-2995.

108. Agapov, R. L.; Malkovskiy, A. V.; Sokolov, A. P.; Foster, M. D., Prolonged Blinking with TERS Probes. *J. Phys. Chem. C* **2011,** *115* (18), 8900-8905.

109. Domke, K. F.; Zhang, D.; Pettinger, B., Enhanced Raman spectroscopy: Single molecules or carbon? *J. Phys. Chem. C* **2007,** *111* (24), 8611-8616.

110. Watanabe, H.; Ishida, Y.; Hayazawa, N.; Inouye, Y.; Kawata, S., Tip-Enhanced Near-Field Raman Analysis of Tip-Pressurized Adenine Molecule. *Phys. Rev. B: Condens. Matter* **2004,** *69* (15), 155418-1-155418-11.

111. Hayazawa, N.; Watanabe, H.; Saito, Y.; Kawata, S., Towards Atomic Site-Selective Sensitivity in Tip-Enhanced Raman Spectroscopy. *J. Chem. Phys.* **2006,** *125*, 244706.

112. Ichimura, T.; Watanabe, H.; Morita, Y.; Verma, P.; Kawata, S.; Inouye, Y., Temporal Fluctuation of Tip-Enhanced Raman Spectra of Adenine Molecules. *J. Phys. Chem. C* **2007,** *111* (26), 9460-9464.

113. Deckert-Gaudig, T.; Kämmer, E.; Deckert, V., Tracking of Nanoscale Structural Variations on a Single Amyloid Fibril with Tip-Enhanced Raman Scattering. *J. Biophotoics.* **2012,** *5*, 215.

114. Deckert-Gaudig, T.; Kurouski, D.; Hedegaard, M. A. B.; Singh, P.; Lednev, I. K.; Deckert, V., Spatially resolved spectroscopic differentiation of hydrophilic and hydrophobic domains on individual insulin amyloid fibrils. *Sci. Rep.* **2016,** *6* (1), 33575.

3 Surface Characterization of Nanoscale Co-Crystals Enabled through Tip Enhanced Raman Spectroscopy

Before the first TERS structure investigations of nanoscale composites could be performed, an appropriate measurement mode had to be found. During the first TERS measurements on single compound nanoparticles, it turned out already that contact AFM measurement methods are not suited for this purpose. Due the direct contact between tip and sample, nanoparticles or particle fragments were often picked up contaminating the TERS tip. Hence, Raman signals were recorded at positions were no nanoparticle could be found in AFM scans. Accordingly, the dynamic non-contact mode was chosen for TERS measurements. Furthermore, a reproducible tip production procedure had to be found. Both, the measurement mode and the tip production procedure are presented in more detail in the following. After these “teething problems” could be eliminated successfully, the first nanoscale composite, a co-crystal consisting of CL-20 and HMX, could be investigated. Since this co-crystal was the first co-crystal ever characterized by TERS and thus no reference data existed, it figured out a challenging task. Anyway, TERS investigations gave new insights into the surface composition of these nano co-crystals allowing to draw conclusions about their reaction behavior. Moreover, a simplified 3D approximation of vibrational normal coordinates could be introduced enabling predictions about the intensity ratio of normal modes in TERS spectra.

(This chapter is published at: Hübner, J.; Deckert-Gaudig, T.; Glorian, J.; Deckert, V. K.; Spitzer, D., Surface Characterization of Nanoscale Co-Crystals Enabled through Tip Enhanced Raman Spectroscopy. *Nanoscale* **2020**, *18*, 10306-10319, DOI: 10.1039/D0NR00397B)

3.1 Abstract

Atomic Force Microscopy coupled with Tip Enhanced Raman Spectroscopy (AFM-TERS) was applied to obtain information about structure and surface composition of single nano co-crystals. For this purpose, a co-crystalline system consisting of 2,4,6,8,10,12-Hexanitro-2,4,6,8,10,12-hexaazatetracyclo-[5.5.0.0^{3,11}.0^{5,9}]-dodecane (CL-20) and 1,3,5,7-Tetranitro-1,3,5,7-tetrazocane (HMX) in a molar ratio of 2:1 (CL-20/HMX) were chosen. CL-20/HMX nano-plates were prepared by Spray Flash Evaporation. To ensure co-crystallinity and nanostructure, powder X-Ray Diffraction and AFM investigations were performed. Results demonstrate that coherence lengths and particle dimensions are on a similar level though coherence lengths appear shorter than measured particle dimension. According to this fact, defects inside the nano co-crystals are minimized. The co-crystallinity was additionally proven by confocal Raman spectroscopy. Here, marker bands for pristine CL-20 and HMX were chosen which appear in the CL-20/HMX spectrum in an intensity ratio of ~ 2.5:1 (CL-20:HMX). Afterwards surface investigations of single CL-20/HMX nano-plates were performed by AFM-TERS. Due to the surface sensitivity of TERS, these experiments reveal that the ratio of the Raman intensities between CL-20 and HMX inverts at CL-20/HMX nano-plate surfaces. Therefore, it is concluded that nano co-crystal surfaces consist of molecular layers of HMX. A theoretical approximation of the normal coordinates of the investigated marker vibrations supports this conclusion, since it can exclude the occurrence of the intensity ratio inversion because of the given orientation between CL-20/HMX nano-plates and the Raman scattering system. Based on this finding, an impact ignition mechanism is proposed enabling to explain the close impact sensitivity values of β-HMX and CL-20/HMX.

3.2 Introduction

Co-crystals are crystal systems built up from two or more chemical compounds.[1] Due to different intermolecular interactions like hydrogen bonding, van der Waals forces or π-π stacking chemical compounds can align in a specific manner during the crystallization process which is energetically more favored than single compound crystals. These co-crystals often differs in their physical properties *e.g.* solubility, melting point and mechanical properties from their origin single compounds.[2] Hence co-crystals have found their usage in chemical industry like the pharmaceutic sector. Here, for example, adding specific co-formers can improve the rate of dissolution of active pharmaceutical ingredient and thus accelerate the pharmaceutic effects.[2-3] Next to pharmaceutic industry co-crystallization has been also started to be applied for engineering of energetic materials. Especially in this field it is necessary to combine two properties which often behave diametrically opposed. These properties are safety characteristics like impact or friction sensitivity and a high energy release. One of these compounds showing a very pronounced diametrical behavior between energetic performance and stability is 2,4,6,8,10,12-Hexanitro-2,4,6,8,10,12-hexaazatetracyclo[5.5.0.$0^{3,11}$.$0^{5,9}$]dodecane (CL-20). CL-20 is one of the most energy-rich known organic explosives which was firstly synthesized by Nielsen in 1987.[4-5] Unfortunately, CL-20 is not only characterized by its high detonation velocity but also by its relatively high sensitivity against impact and friction. Next to diverse methods like adding of binders, nano-structuring, or micro-capsulation to or of CL-20 crystals, co-crystallization of CL-20 with diverse inert or even energetic co-formers could successfully decrease sensitivites.[6-12] One of the most promising of these compounds is a co-crystal between CL-20 and the energetic cyclic nitroamine 1,3,5,7-Tetranitro-1,3,5,7-tetrazocane (HMX) in a molar ratio of 2 : 1 (CL-20/HMX) which was firstly synthesized by Bolton *et al.* in 2012.[13] CL-20/HMX demonstrates perfectly the synergy between its single components; thus the co-crystal shows a higher detonation velocity than pure HMX which is close to CL-20 and nearly the sensitivity values of HMX.[13-15] Additional downsizing onto sub-micron or nano-scale of CL-20/HMX co-crystal improves further the sensitivity. Here, An *et al.* could show that nano CL-20/HMX particles are even less sensitive than pristine HMX.[16] However, up to now it is not completely understood how the co-crystal structure effects on performance and sensitivity.

A dispersion-corrected density functional theory (DFT-D) study undertaken by Liu *et al.* reveals that the CL-20/HMX co-crystal is more compressible than its pristine compounds.[17]

Though the increased compressibility can explain the improved sensitivity for structure defect-free single crystals it does not include the influences of defect sites in micro or nano-structured CL-20/HMX powders leading to the formation of hot-spots. Since crystal surfaces are defect sites per se, crystal morphology and surface condition participate strongly to the sensitivities of energetic materials especially if they are nano-structured.[18-20] Therefore, a detailed study of these parameters might give a deeper insight into the impact sensitivity of nano CL-20/HMX co-crystals. Next to its extraordinary pyrotechnical characteristics CL-20/HMX was chosen additionally as the co-crystal sample system of this study since its structure properties are already well investigated.

The method of choice for this purpose is Tip-Enhanced Raman Spectroscopy (TERS) based on Atomic Force Microscopy (AFM; combined: AFM-TERS). AFM-TERS combines the lateral resolution of AFM with the advantages of Surface Enhanced Raman Spectroscopy. Hereby the apex of an AFM tip is equipped with a silver or gold nanoparticle. This modified tip is then brought close to the sample surface and becomes irradiated by a laser. The irradiation leads to a strong electric field enhancement close to the particle surface which rapidly decays within a few nanometers.[21-24] This strong field enhancement allows to perform Raman spectroscopy on small amounts of substances like single nanoparticles, molecular monolayer or even single molecules.[25-30] Furthermore, the fast decay of the field enhancement makes TERS to an extremely surface sensitive measurement method. AFM-TERS enables a simultaneous recording of the sample height and the corresponding Raman spectrum at single measurement points. These point measurements can be assembled to a topographic and spectrographic map depicting particle morphology and composition. Hereby lateral resolutions < 1 nm can be reached.[21] A further reason making TERS a perfectly suited tool for surface or structure investigations of nano energetic materials is the relatively low energy input compared to common techniques like electron microscopy which is necessary since organic molecules especially energetic organic molecules tend to dissociate under the electron beam. The suitability of AFM-TERS for investigations of energetic nano-composites could be already demonstrated by structure determination of RDX/TNT core/shell and patchy nanoparticles.[31-32]

In this work investigated CL-20/HMX nano co-crystals were synthesized by the Spray Flash Evaporation process. This process was invented at the NS3E lab and enables the continuous production of organic nanoparticles which are used in pharmaceutic and energetic sector.[33-34] During the process a pressurized solution of one or more components is sprayed through a heated hollow cone nozzle into an evacuated reaction chamber. The strong pressure drop forces an immediate evaporation of the solvent leading to the release of the desired nanoparticles. These particles are collected in a filter system. Due to the composition of the precursor solution a wide variety of nano-structured products can be obtained. If the precursor solution consists only of a solvent and a single solved compound, the SFE reactor acts as a recrystallizer providing single compound submicron- or nanoparticles.[15, 35-36] If two or more compounds are solved in the precursor solution the obtained products depend strongly on the intermolecular interactions. Nano-structured products can occur *e.g.* as uncoupled but physically perfectly mixed single compounds, core/shell nanoparticles or nano co-crystals.[15, 31, 37-39] One of these nano co-crystals systems which can be produced by SFE is the already introduced CL-20/HMX co-crystal. Synthesis details, X-Ray powder diffraction- (XRPD), AFM, Raman- and AFM-TERS investigations of this nano co-crystal system are presented in the following sections.

3.3 Experimental Section

3.3.1 Chemicals

2,4,6,8,10,12-hexanitro-2,4,6,8,10,12-hexaazaisowurtzitane crystallized in ϵ phase (ϵ-CL-20) and the β – polymorph of 1,3,5,7-tetranitro-1,3,5,7-tetrazocane (β-HMX) were purchased by EURENCO (Massy, France). ϵ-CL-20 and β-HMX were dried for 6h at 50 °C in a vacuum drying oven before further use. Acetone (CHROMASOLV®) was sourced by Sigma-Aldrich (Munich, Germany) and used without further purification.

3.3.2 Preparation of CL-20 γ – Polymorph

The γ – polymorph of CL-20 (γ-CL-20) was fabricated by forcing a thermal induced phase transition from the ϵ – phase into the γ – phase. Therefore ~ 10 mg of dried ϵ-CL-20 were evenly spread onto a microscope glass slide. Afterwards the prepared slide was heated in an oven for 3h by 160 °C. A comparable route is described by Thiboutot *et al.*[40]

3.3.3 Preparation of CL-20 β – Polymorph

The CL-20 β – polymorph (β-CL-20) was synthesized using the Spray Flash Evaporation (SFE) process which is described in more detail elsewhere.[33-34] Figure 3.1 depicts a photography of the lab version of a SFE reactor as well as a flow chart of the set-up. For β-CL-20 synthesis, 3.14 g (7.2 mM) of dry ϵ-CL-20 were dissolved in 200 mL acetone. This solution was given into the solution storage tank of the SFE device. For the spraying process an 80 µm hollow cone nozzle was used, which was heated up to 160 °C. The pressure in front of the nozzle was set to 40 bar. The pressure behind the nozzle inside the reaction chamber amounted 8 - 15 mbar during the process. After the complete β-CL-20 acetone solution was sprayed, the final product was collected from the walls of the filter system as a white-yellowish powder.

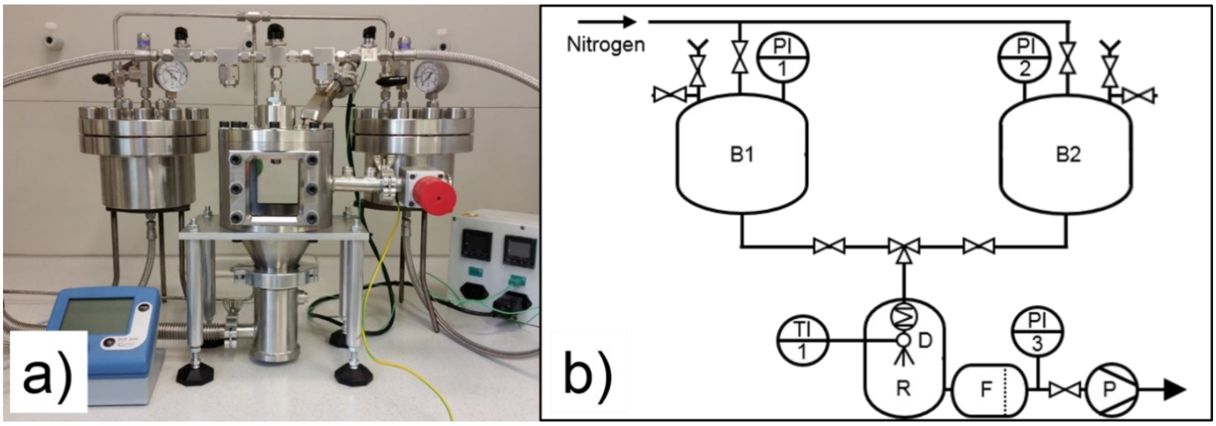

Figure 3.1. a) Photography of a lab version SFE - reactor. **b)** Flow-chart of SFE setup. B1, B2: solvent and solution tank; R: reaction chamber; D: hollow cone nozzle, F: filter, P: vacuum pump; PI: pressure sensor; TI: temperature sensor.

3.3.4 Preparation of CL-20/HMX (2:1) Co-Crystal

CL-20/HMX co-crystals were synthesized using SFE process as well. For performed synthesis, a 2 wt.% solution of 2.4 g (5.4 mM) ϵ-CL-20 and 0.80 (2.7 mM) β-HMX in 200 ml acetone were prepared and transferred into the SFE solution tank. During the synthesis procedure same nozzle size, temperature and pressure settings were used as like as for β-CL-20 synthesis.

3.3.5 TERS Tip Preparation

AppNano ACCESS-NC AFM-probes (Mountain View, USA) were used for TERS-active tip production. Since the tips of the used probes are mounted onto the cantilever at an angle of 120° (Figure 3.2.a), the probes were fixed onto a 30° prism template to generate a perpendicular arrangement between the tip and the sputtering target. This template was installed in the vacuum chamber of an HHV Auto 306 (Bangalore, India) argon plasma sputtering system at a distance of 10 cm from the sputtering target. In a first step, 3 nm of titanium were deposited onto the tip at a deposition rate of 0.5 Å/s. Titanium is used as an adhesive promoter between the native oxide layer of the Si - tip and silver. Afterwards the Si/Ti - tips were coated with a 25 nm layer of silver (sputtering rate 0.5 Å/s). Finally, the Si/Ti/Ag - tips were annealed on a heating plate for 1 min at 300 °C under an argon atmosphere. The SEM image in Figure 3.2.b) shows the

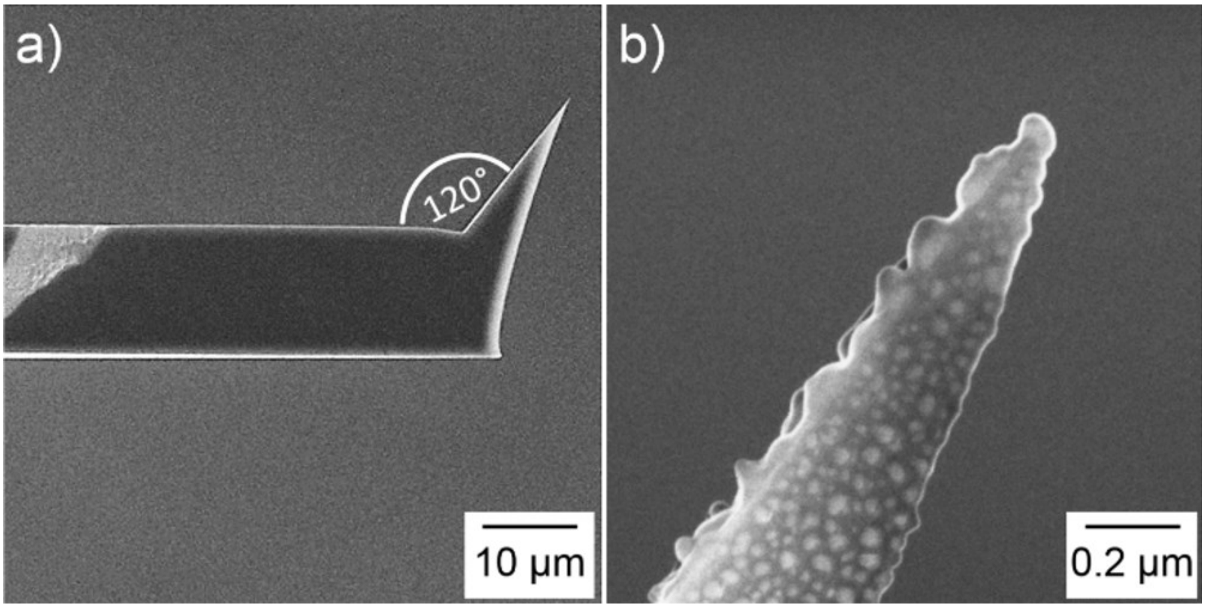

Figure 3.2. a) Untreated AFM probe (AppNano Access-NC). The tip is mounted onto the cantilever at an angle of 120°. **b)** Annealed Ti/Ag coated Si – tip.

successful formation of a single Ag nanoparticle on the tip apex after the manufacturing procedure.

3.3.6 Analysis Methods

X-ray powder diffraction (XRPD) analysis in Bragg–Brentano geometry was performed on a Bruker AXS Advance D8 (Karlsruhe; Germany) X-ray powder diffractometer using Cu-K_α radiation (λ= 1.54 Å). The acceleration voltage amounts 40 kV and the operating current is 40 mA. The step size for all scans was set to 0.0148° (2 θ). The loose powder samples were measured on a rotated sample holder. Coherence length L_{hkl} was calculated from the full width at half- maximum (FWHM) of single diffraction peaks by using the well- known Scherrer equation assuming Gaussian shaped peaks that were fitted with OriginPro 2015 (version b9.2.214). A crystal shape model was simulated with VESTA (version 3.4.4) by using obtained coherence lengths.

Atomic force microscopy (AFM) was carried out on an AIST-NT CombiScope^{TM}-1000SPM atomic force microscope (Novato, USA) in non-contact mode. All samples were applied onto glass cover slides, by depositing a spatula's tip between two 2 cm x 2 cm cover glasses. The sample is spread on the glass surface through pressureless rubbing of the two glass slides against each other. All measurements were undertaken with AppNano ACCESS-NC Si - probes (Mountain View, USA) (Figure 3.2.a).

Confocal far-field Raman spectroscopy and microscopy were undertaken on a HORIBA Jobin Yvon (Kyoto, Japan) LabRam HR evolution confocal Raman microscope. For this purpose, pristine CL-20, HMX and n-CL-20/HMX were applied onto glass slides as described above. Sample excitation for single point spectra was provided by linear polarized illumination light from a 532 nm diode laser with an adjusted output power of 13.5 mW at an acquisition time of 3 s per spectrum. Raman maps along the substrate plane (xy-plane) were recorded with same laser and output power. The acquisition time amounted 0.5 s per spectrum at a step size of 250 nm for these maps. The laser light was focused onto the sample through a 100x, 0.9 NA objective. Raman scattered photons were collected by the same objective. Scattered light passed an edge filter, a confocal aperture with a diameter adjusted to 200 nm and a diffraction grating with 300 lines/mm before hitting a deep cooled CCD camera (- 60°C). Confocal Raman maps were calculated and depicted using LabSpec Spectroscopy Suite 6.4.4. (HORIBA; Paris, France).

Tip Enhanced Raman Spectroscopy (TERS) spectra and maps, based on AFM, were recorded on a combination between the above described AFM microscope and confocal Raman microscope. The confocal Raman microscope acts in this combination as light source and spectrometer. All measurements were performed in bottom-illumination mode (transmission mode). Incident linear polarized laser light (532 nm) is focused onto the tip apex by a 100x, 1.4 NA oil-immersion objective. Precise positioning of the AFM-tip relatively to the focused laser spot is undertaken by objective scans inside xy - and xz – plane of the scattering system. Figure **3.3** depicts schematically the experimental setup. All samples were prepared as described within AFM section above. The acquisition time amounted 0.2 s per measurement point. Step sizes of measurement points differ depending on the scanning area. They are given within the captions of the corresponding TERS maps.

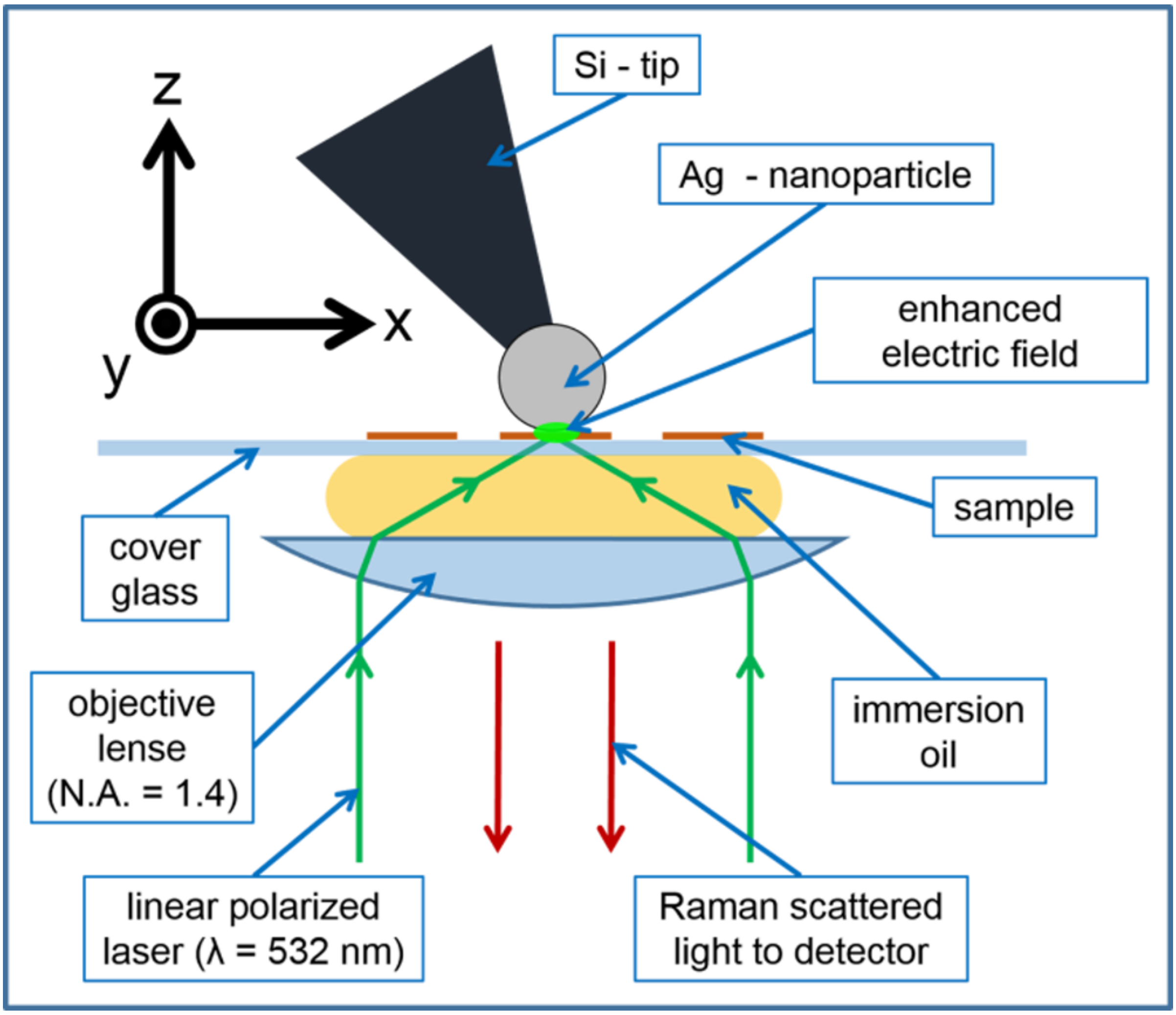

Figure 3.3. Schematic representation of the experimental setup.

3.3.7 Simulation of Molecular Normal Modes

Molecular normal modes were computed through computational chemical calculations using Gaussian 16.[41] The use of density functional theory (DFT) with a B3LYP-6-31G(d,p) basis set was chosen since it is suitable for quite large systems such as CL-20. DFT B3LYP-6-31G(d,p) relevancy for energetic materials was demonstrated by Osmont *et al.*[42] For each studied molecules, the most stable geometry was obtained from the minimization of the ground state energy. All vibrational frequencies were checked to be positive.

3.4 Results and Discussion

3.4.1 XRPD and AFM

After SFE synthesis the final product was collected as a dry, ultra-fine, white-yellowish powder (n-CL-20/HMX). XRPD patterns were recorded to investigate the crystal structure of n-CL-20/HMX. Obtained XRPD pattern shows same Bragg reflex positions as simulated XRPD diffractogram from single crystal X-ray diffraction results of CL-20/HMX monoclinic co-crystals (molar ratio CL-20 : HMX 2 : 1) undertaken by Bolton *et al*. Figure 3.4 compares XRPD patterns of synthesized n-CL-20/HMX and literature data in the relevant data range between 10° and 40° (2θ).[13] In this crystal system layers of HMX alternate with bilayers of CL-20 in [300] – direction. The conformation of HMX corresponds to the chair conformation which is also found in the β – polymorph of HMX. CL-20 molecules are present in pairs, whereby one takes on the conformation seen in the β – polymorph of pure CL-20 while the other adopt the conformation which is present in the γ – polymorph.[13] No additional signals appear in the n-CL-20/HMX diffractogram indicating a complete conversion of pristine CL-20 and HMX into CL-20/HMX. Additionally, the crystal morphology of single nano-crystals was simulated by calculated coherence lengths (table in Figure 3.4). The plate shape of this simulated CL-20/HMX nano co-crystal is shown in Figure 3.5d. AFM investigations were aimed to gain insight into size and structure of n-CL-20/HMX particles. n-CL-20/HMX forms angular plates with heights of ~29 nm. Their lengths and widths range between 100 nm and 400 nm. Figure **3.5**.a) depicts an agglomerate of two of these nano-crystals. These particles are well representing the general appearance of n-CL-20/HMX, since similar particles are found in all AFM measurements (further AFM maps can be found in the supporting information). The detected heights of 29 nm correspond with the calculated coherence length in [300] – direction. Moreover, the measured particle morphology resembles strongly to the simulated shapes, though particle dimensions in the substrate plane are three to four times bigger. These differences hint towards crystal structure defects. A possible explanation for these defect sites is a non-classical growth mechanism of the nano-sized CL-20/HMX plates *via* oriented aggregation. In this case a classical formation of primary nanoparticles with the simulated dimensions is the first step. Afterwards these primary particles accumulate along similar crystal faces and aggregate to the measured secondary n-CL-20/HMX particles. A comparable formation of hierarchal superstructured ZnO submicron particles has been

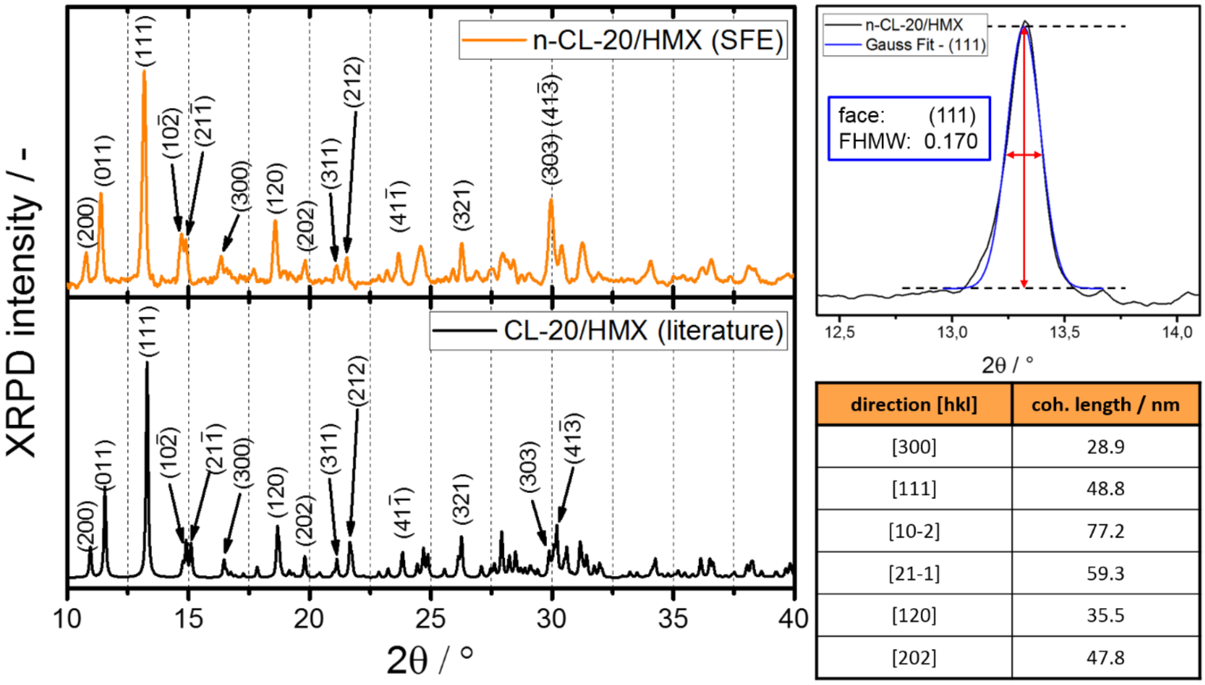

direction [hkl]	coh. length / nm
[300]	28.9
[111]	48.8
[10-2]	77.2
[21-1]	59.3
[120]	35.5
[202]	47.8

Figure 3.4. *Upper left:* Relevant section of n-CL-20/HMX XRPD pattern between 10° and 40°. *Bottom left:* Simulated XRP diffractogram of single crystal X-Ray diffraction results of CL-20/HMX taken from ref. 1. Bragg reflexes of n-CL-20/HMX appear at same positions as reference CL-20/HMX reflexes. *Upper right:* Gaussian fitted (111) – reflex. *Bottom right:* Calculated coherence length of crystal faces determining the crystal morphology.

described in detail by Klaumünzer *et al.*[43] Since HR-TEM investigations were not possible due to dissociation of CL-20/HMX triggered by the relatively high energy input through the electron beam, a direct evidence of the suggested building mechanism cannot be given here. However, particle heights can be aligned to the crystallographic [300] – direction regarding to results of AFM and XRPD. Contrary, Ghosh *et al.* assign the crystal height of platelet macro CL-20/HMX crystals to crystallographic [111] – direction because of weakest short contacts between the molecules in this crystallographic direction.[14] These weak short contacts lead to the slowest growing rate in this direction and hence to a domination of the crystal morphology by (111) – planes. On the other hand, Ghosh *et al.* used a slow evaporation rate of 1 mL/min to grow CL-20/HMX crystal with a size around 200 µm, this slow evaporation method is hardly comparable to the ultra-fast SFE process. Therefore, other crystallographic planes can determine n-CL-20/HMX nano-plate morphology due to massive differences in thermodynamic and kinetic circumstances during the co-crystal growth process. Furthermore, the height of the simulated nano-crystal is extended in [300] – direction and measured AFM heights and calculated coherence lengths in [300] – direction coincide perfectly. Moreover, this alignment is flanked by TERS measurements which are presented and discussed later. The predominance of the (111) - reflex in XRPD pattern is supposed to arise due to agglomeration of n-CL-20/HMX nano-plates along their (300) surfaces leading to alignments of (111) – planes parallel towards the substrate plane. Thus, main interfaces between n-CL-20/HMX nano-plates consists of layers of pure CL-20 or HMX in consideration of the present monoclinic crystal structure. An approximation of the surface areas of a typical nano-plate (a = 30 nm, b = 300 nm, c = 400 nm) reveals that 85 % of particle surfaces are built up by these single compound layers.

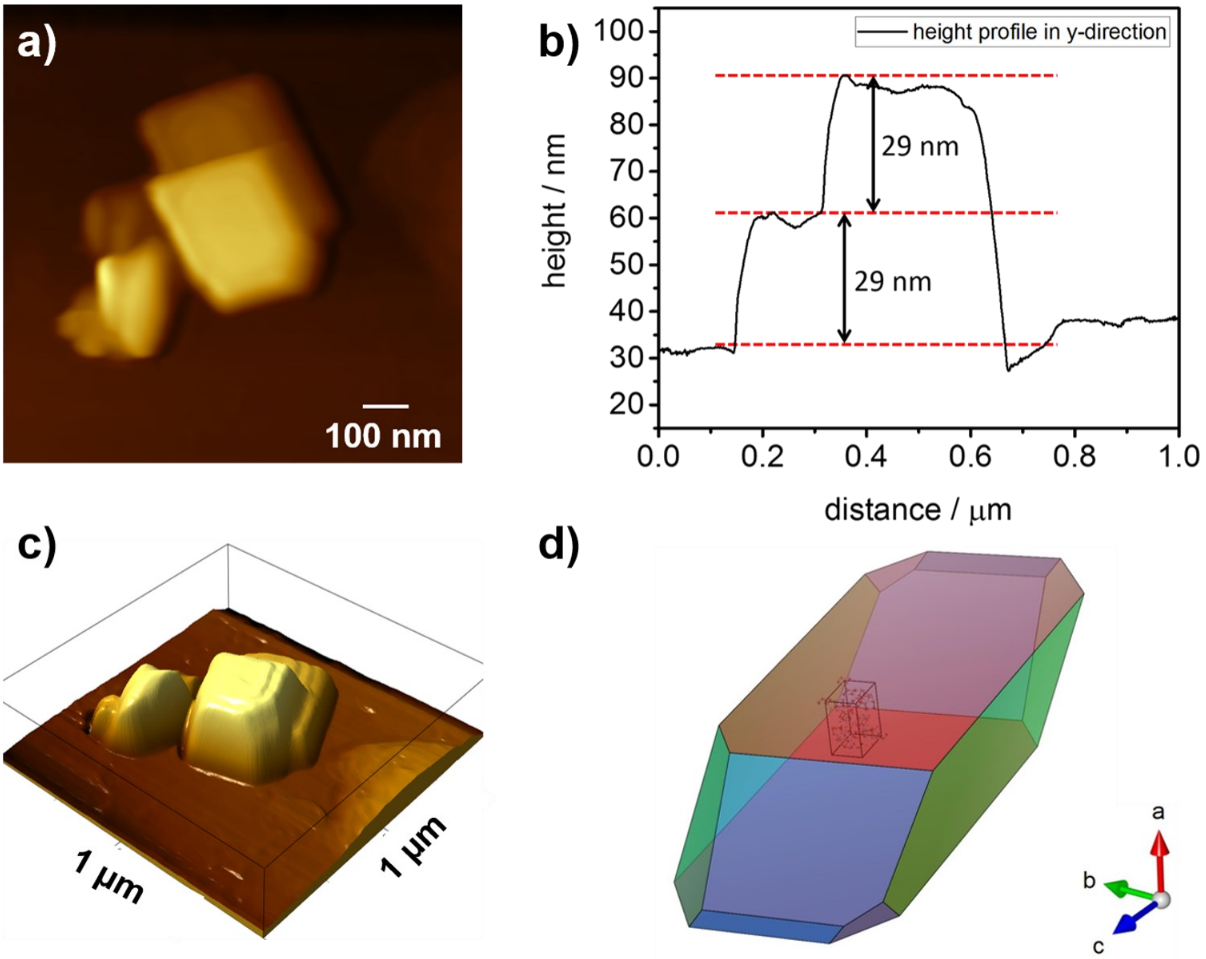

Figure 3.5. a) AFM topographic maps of n-CL-20/HMX co-crystals. **b)** Height profile of particles shown in a) along y – direcFigure 3.6tion. **c)** 3D image of a). **d)** Crystal morphology simulated by using crystal faces and corresponding coherence lengths from XPRD data. Calculated and measured shapes resemble strongly one another. Moreover, particle heights fit to coherence length in [300] – direction. Particles sizes in crystallographic bc – plane are larger than corresponding coherence length. This may be caused by crystal structure defects occurring due to oriented attachment of primary nanoparticles to regarding n-CL-20/HMX plates.

3.4.2 Confocal Far-field Raman Spectroscopy and Microscopy

Far-field Raman spectra of β-CL-20, γ-CL-20, β-HMX and n-CL-20/HMX were recorded to receive an overview how vibrational modes of pure compounds, contribute to the n-CL-20/HMX co-crystal Raman spectrum (Figure **3.7**). Reference β-CL-20, γ-CL-20 and β-HMX spectra were compared with literature and are clearly identifiable as named polymorphs.[44-46] Also the far-field Raman spectrum of n-CL-20/HMX shows the characteristic signature of the 2:1 CL-20/HMX co-crystal.[14] Tables of the respective vibrational frequencies and assignments of β-CL-20, γ-CL-20, β-HMX and CL-20/HMX can be found in the supporting information. In order to analyze the contributions of single compounds in the n-CL-20/HMX spectrum, marker bands were selected for CL-20 and β-HMX from the acquired Raman data sets. These marker bands ideally appear at wavenumbers where no signals can be detected in the spectra of the other compounds, with a view to distinguish the contribution of CL-20 and HMX to the n-CL-20/HMX spectrum. CL-20 can be found in two different conformations in the co-crystal, thus NO_2 asymmetric stretching vibrations were chosen as CL-20 marker bands because they appear at nearly same positions in β-CL-20 (1595 cm^{-1}, literature: 1593 cm^{-1}), γ-CL-20 (1598 cm^{-1}, literature: 1600 cm^{-1}) and n-CL-20/HMX (1602 cm^{-1}) spectra.[14, 45] Moreover, in the region between 1580 cm^{-1} and 1620 cm^{-1} no vibrational mode is found in pristine β-HMX far-field Raman spectrum. Thus, the broad peak at 1600 cm^{-1} in n-CL-20/HMX spectrum can be clearly assigned to NO_2 asymmetric stretching vibrations of the diverse CL-20 conformations. The NO_2 asymmetric stretching vibrations of the two CL-20 conformations broaden in the n-CL-20/HMX Raman spectrum compared to the same vibration in the spectra of pristine CL-20 polymorphs because of a superposition of single NO_2 asymmetric stretching vibrations of both conformations. Furthermore, no signals appear in the region between 1400 cm^{-1} and 1500 cm^{-1} in β-CL-20 and γ-CL-20 spectra. As a consequence, the CH_2 out of plane wagging vibration of β-HMX localized at 1416 cm^{-1} (literature: 1418 cm^{-1} – 1422 cm^{-1}) was selected as the HMX marker band.[46-48] This vibrational mode is detected slightly blue-shifted at 1417 cm^{-1} and broadened in the n-CL-20/HMX Raman spectrum. Shift and broadening are explainable by the different chemical environment in the CL-20/HMX co-crystal system compared to the β-HMX polymorph leading to various interactions between H atoms of HMX and $–NO_2$ functional groups of CL-20. Marker bands appear in the CL-20/HMX spectrum with an intensity ratio of ~ 2.5:1 (CL-20/HMX). Confocal far-field Raman maps were recorded to investigate if CL-20 and HMX marker bands are equally

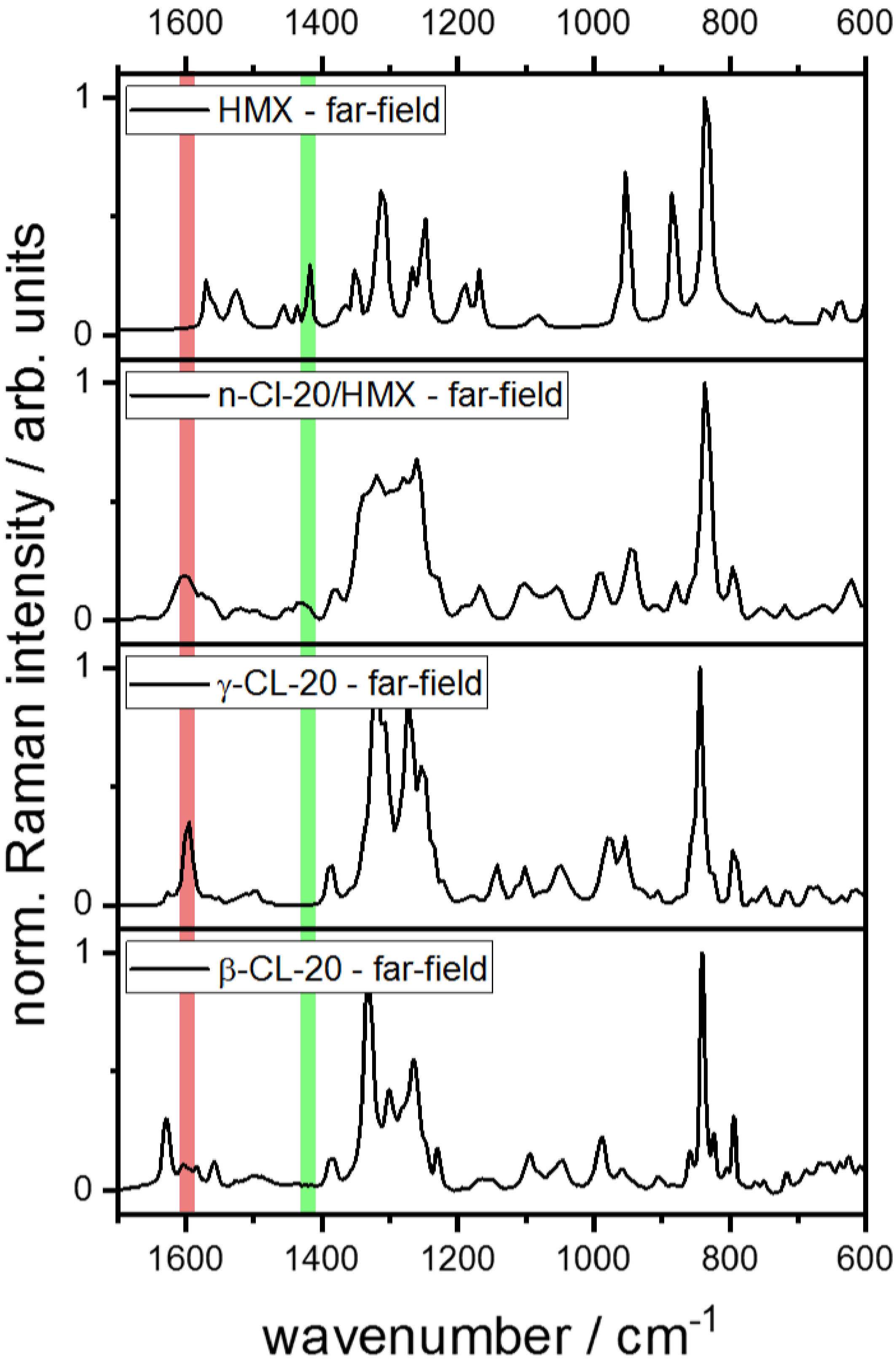

Figure 3.7. Far-field Raman spectra of β-CL-20, γ-CL-20, n-CL-20/HMX and β-HMX between 1700 cm^{-1} and 600 cm^{-1}. Marker bands of CL-20 (β-CL-20: 1595 cm^{-1}, γ-CL-20: 1598 cm^{-1}, O-N-O asymmetric stretching vibration, red) and HMX (1417 cm^{-1}, CH_2 wagging vibration, green) were chosen to indicate the contribution of pristine compounds in n-CL-20/HMX TERS maps. Raman intensities are normalized to improve comparability.

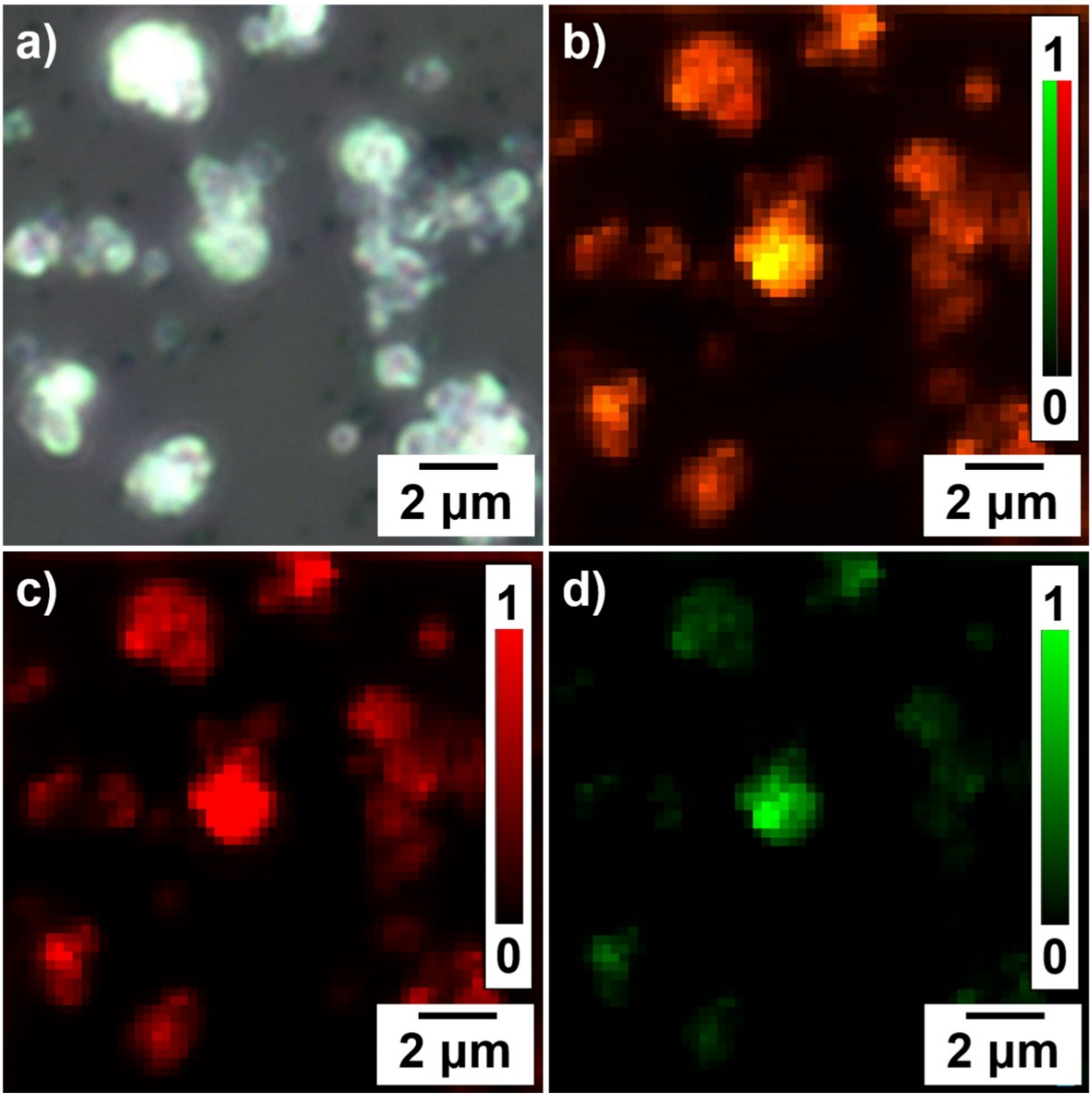

Figure 3.8. a) Optical microscopic images of n-CL-20/HMX agglomerates. **b) - d)** Confocal Raman maps n-CL-20/HMX agglomerates shown in a). The scanned area amounts 15 µm x 15 µm at a measurement step size of 250 nm. Raman intensities are normalized in all shown maps. **b)** Marker bands of CL-20 (O-N-O asymmetric stretching vibration; 1602 cm^{-1}; red) and HMX (CH_2 wagging vibration; 1416 cm^{-1}; green), are depicted superimposed. Generally, if both signals show same intensity, superpositions are illustrated in yellow. Since the intensity of CL-20 marker band doubles the intensity of HMX marker band in CL-20/HMX Raman spectrum, CL-20 dominates consequently resulting in a more reddish appearance. **c)** Confocal Raman maps of CL-20 marker band (1602 cm^{-1}) colored in red. **d)** Confocal Raman maps of HMX marker band (1416 cm^{-1}) colored in green.

distributed over the whole sample. Figure 3.8.a) illustrates a 15 µm x 15 µm optical microscopic image of n-CL-20/HMX agglomerates. Figure 3.8.c) shows the corresponding confocal Raman maps of the CL-20 O-N-O asymmetric stretching vibration marker band colored in red, Figure 3.8.d) displays in green the HMX CH_2 wagging vibration. Color intensities of shown Raman maps were calculated by the areas under the selected peaks. Thus, the brightness in which diverse scanning areas appear in the confocal Raman maps is directly proportional to the area under the selected peaks. To ensure comparability of calculated peak areas, same wavenumber differences limiting the peak areas have to be chosen for both marker bands. In case of the CL-20 marker band area a wavenumber range between 1585 cm^{-1} and 1615 cm^{-1} are chosen and for the HMX marker band a range between 1404 cm^{-1} and 1434 cm^{-1} was selected. This means a wavenumber difference $\Delta\tilde{\nu}$ of 30 cm^{-1} for both compounds enabling a direct comparability of the brightness in which chosen marker signals appear. CL-20 marker band intensities (Figure 3.8.c) are significantly larger than HMX marker band intensities (Figure 3.8.d). This trend is also recognizable in Figure 3.8.b) presenting an intensity superposition of both vibrational modes. In case of superposition maps two signals with same intensity would be displayed in yellow. Since the intensity of CL-20 Raman marker band is on average 2.5 times larger than the intensity of HMX marker band in n-CL-20/HMX agglomerates, they appear orange in superimposed far-field Raman maps. If HMX marker band intensity would surpass CL-20 marker band intensity, corresponding pixels would appear greenish to green within the Raman maps. Anyway, recorded far-field spectra, respectively maps, demonstrate that the intensity difference between CL-20 and HMX marker bands occur independently from the orientation of the crystal towards the polarization of the incident light and the measurement geometry. For sure, far-field Raman spectrometry represent an integral measurement method and thus all molecular orientations are represented summarized in the spectra. But the flat morphology of n-CL-20/HMX co-crystals is supposed to lead to an orientated agglomeration at least parallel towards their crystallographic bc – plane. These oriented agglomerates are randomly arranged towards the electric field vector $\vec{E}$ of the incident laser light. Figure 3.9.a) and b) illustrate two of these possible arrangements of n-CL-20/HMX agglomerates. Since all investigated n-CL-20/HMX agglomerates appear in orange in the far-field Raman maps, it can be concluded, that the arrangement of the agglomerates does not strongly influence the intensity ratio of the marker bands. The consideration about the relationship between the Raman intensity ratio and the crystal orientation towards the Raman

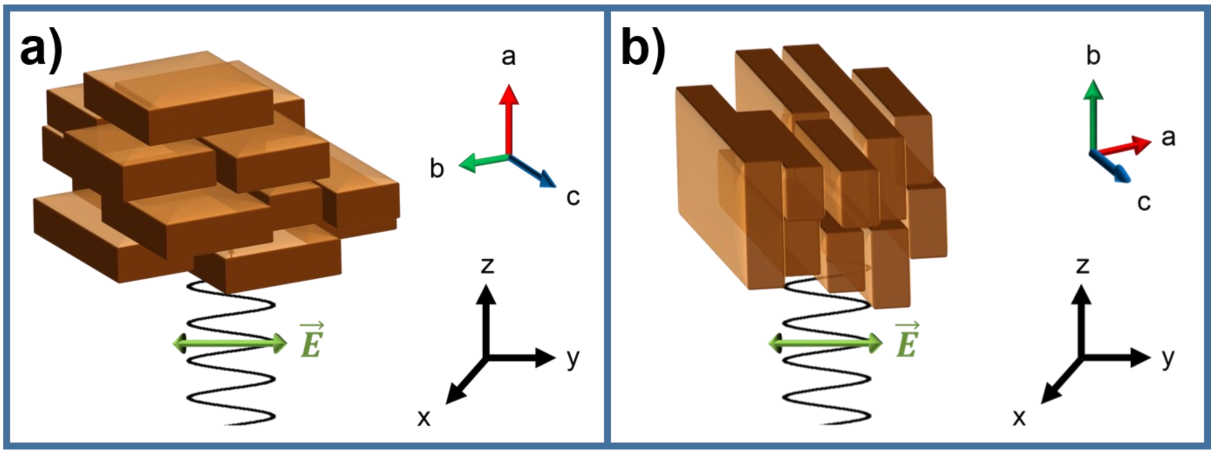

Figure 3.9. Oriented agglomerates of n-CL-20/HMX nano-plates. **a)** Crystallographic bc – plane lies in xy – plane of the Raman scattering system. **b)** Here the crystallographic bc – plane is aligned perpendicular to the xy – plane of the scattering system. Incident laser light in z-direction is linear polarized thus the orientation of the electric field vector $\vec{E}$ towards the crystallographic axes depends only on the orientation of n-CL-20/HMX agglomerates.

scattering system is necessary here, since orientation of crystallographic axes, molecules and thus vibrational modes is randomly distributed in far-field Raman spectroscopy but plays a key role for the interpretation of near-field TERS data. Furthermore, the Raman mapping results underline the purity of the SFE process which was already elucidated by XRPD measurements.

3.4.3 Tip Enhanced Raman Spectroscopy

Since XRPD results demonstrate that the main surface area of n-CL-20/HMX consists of single CL-20 or HMX layers, TERS analysis were performed to investigate if the surface composition in [300] – direction alternates between CL-20 and HMX in consideration of their molar ratio or if a specific molecular layer is favored. Contrary to XRPD and far-field Raman spectroscopy TERS is perfectly suited for this purpose due to its strong surface sensitivity. During TERS measurements only single n-CL-20/HMX nano-plates were analyzed because of two reasons. Firstly, a higher yield of Raman scattered photons is expected because of the minimization of crystal defects and particle height. Secondly, a semi-orientation of n-CL-20/HMX particles is known in consideration of XRPD and AFM results. Here, the crystallographic bc-planes of single n-CL-20/HMX nano-plates are always aligned parallel towards the substrate surface defined as xy-plane of the scattering system. This semi-orientation simplifies the spectra evaluations extremely as shown in the following. Anyway, all relevant CL-20 and β-HMX vibrational modes appear evenly distributed in TERS spectra over all particles, although they appear slightly shifted and differ in their intensities (Figure 3.10). The shifts may appear because of the missing molecular layer at the particle surface leading to a change of intermolecular interactions such as Van-der-Waals forces or hydrogen – bonds. The lack of these interactions leads to changes in molecular arrangements to the energetically most favorable conformation.[30] Consequently different arrangements influence the polarizabilities and the energy levels of the vibrational states implying a shift of the detected normal modes. Also interactions between the Ag nanoparticle located at the tip apex and the surface molecules have been shown to influence the band positions.[25] However, the detectability of all vibrational modes clarifies that TERS can demonstrate the co-crystallinity of nanoparticles due to the even distribution of Raman signals over all measured particles. Moreover, all TERS spectra contain CL-20 and HMX marker bands (1602 $\mathrm{cm^{-1}}$; 1416 $\mathrm{cm^{-1}}$). If no co-crystal formation but the formation of other hierarchical arranged nano-particle would occur (*e.g.* core/shell particles), superimposed CL-20 and HMX far-field Raman spectra could be misinterpreted as CL-20/HMX co-crystal signature due to the less surface sensitivity of far-field Raman spectroscopy. Contrary to far-field Raman TERS is able to identify these particle arrangements due to its surface sensitivity demonstrated recently on RDX/TNT core/shell nano-particles.[31] This renders TERS a powerful tool for the investigation of co-crystalline systems, especially if it is not possible to grow these new co-crystals to a necessary size for single crystal X-ray diffraction. By using SFE process which is designed for recrystallization on the sub-micro and nano-scale, this necessary size will not be reached. On the other hand, it is supposed that this rapid crystallization process may force two (or more) compounds into specific co-crystal arrangements which they would not adopt in slow crystallization processes. Though, such a nano co-crystal growth may occur, integral methods like XRPD and far-field Raman spectroscopy may lead to wrong assumptions because signal superpositions or the arising of new signals can be misinterpreted as new co-crystal structures. However, as already mentioned TERS spectra differ from far-field Raman spectra not only in slight band positions shifts but also in intensity changes. One particular reason for this effect is the fixed orientation of the investigated molecules towards the electric field vector of the enhanced electric field at the Ag nanoparticle surface. Contrary to far-field Raman spectroscopy where signals are averaged over various molecular orientations, TERS investigations are by nature on single n-CL-20/HMX nano-plates. Thus, TERS experiments are rather comparable to single crystal far-field Raman

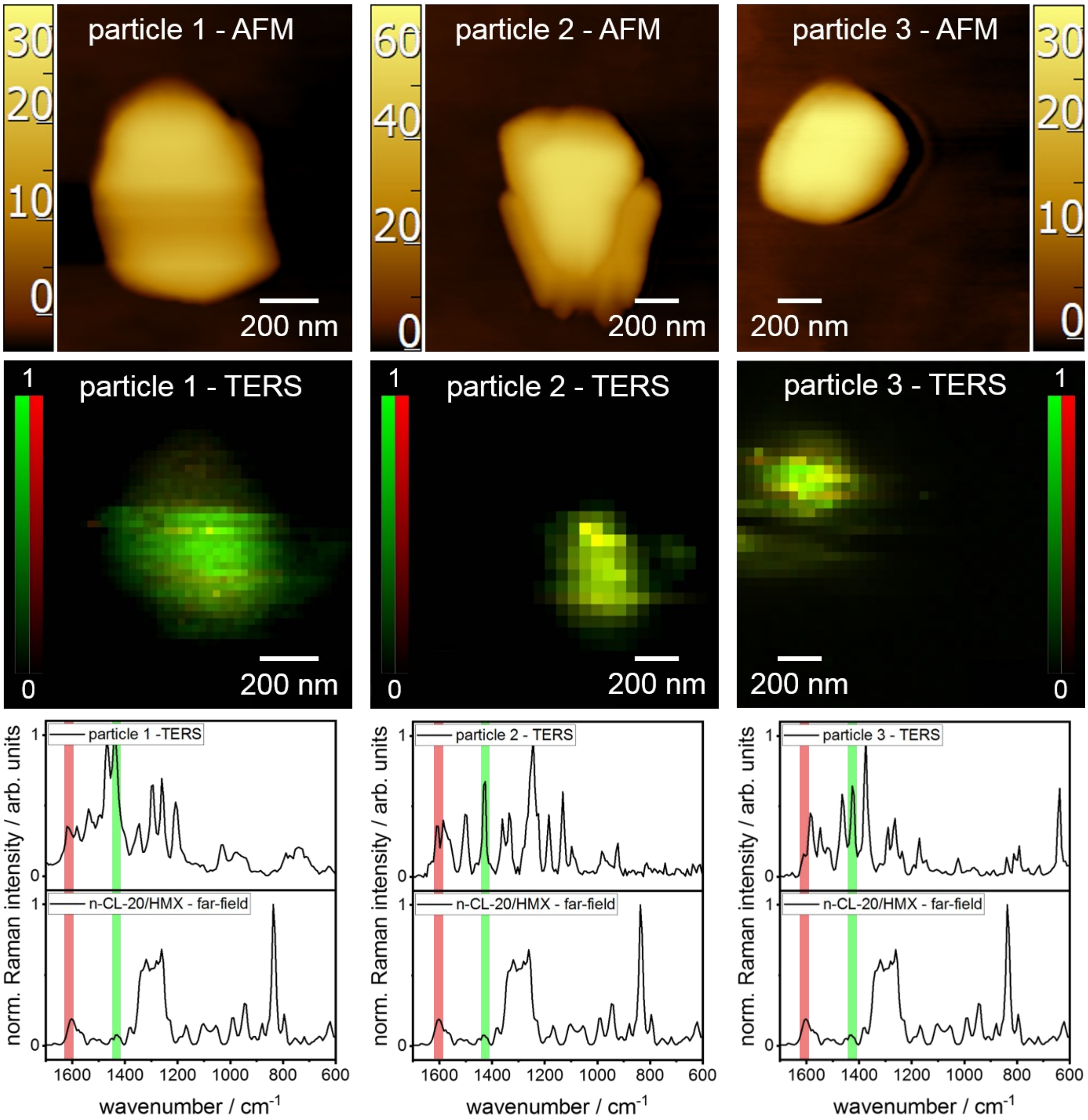

Figure 3.10. AFM topography images, TERS maps and corresponding spectra of n-CL-20/HMX nano-plates. TERS spectra represent the average over all TERS spectra on the particle surfaces. At all measured surface areas an intensity inversion between CL-20 and HMX marker bands occur. TERS maps and TERS spectra are normalized for better comparability. AFM topography images were recorded after TERS mapping. **Step sizes:** particle_1 20 nm, particle_2 and particle_3 50 nm.

or single molecule TERS investigations with arbitrary but fixed orientations.[49] Due to the experimental setup the longitudinal field (along z – axis, Figure 3.11. c) and d)) provides the main contribution with respect to the localized surface plasmon resonance and hence normal modes with stronger vibrational components perpendicular to the substrate plane (xy – plane) appear more intense in TERS spectra.[22, 27, 50-51] If one compares the intensity ratio between the CL-20 ONO asymmetric stretching vibration and the HMX CH_2 wagging vibration, an inversion of the intensity ratio from ~ 2.5 : 1 to ~ 1 : 1.5 (CL-20 : HMX) on average is recognizable within TERS spectra compared to far-field Raman-spectra. This inversion is illustrated in the TERS maps in Figure 3.10. In relation to the far-field Raman maps shown above, intensities of the CL-20 marker band are depicted in red in these TERS maps while the intensities of the HMX marker band are depicted in green. Due to the intensity ratio inversion from CL-20 marker band towards HMX marker band which can be recognized by comparing intensities of far-field and TERS spectra (Figure 3.10), surfaces of n-CL-20/HMX nano-plates appear green-yellowish to green instead of red-orange in TERS maps. This is indeed interesting and unexpected, since none of the investigated n-CL-20/HMX agglomerates show such an intensity ratio inversion in far-field Raman maps. As described above it is assumed that n-CL-20/ HMX nano-plates aggregate semi-orientated parallel towards their crystallographic bc – planes. Thus, it is highly likely that one of this agglomerates will be arranged in a manner that the bc – planes of single n-CL-20/HMX nano-plates are aligned parallel towards the substrate plane, respectively the xy – plane of the scattering system. Thus, the measured intensity ratio inversion should not arise due to a specific orientation.

3.4.4 Approximated Normal Coordinate Analysis

To verify this presumption, an approximated qualitative investigation of the arrangement between the n-CL-20/HMX nano-plates and the present TERS scattering system is necessary at this point. For this purpose, approximations of the normal coordinates of the investigated normal modes of β-CL-20, γ-CL-20 and β-HMX have to be found in a first step. This approximation is formed by the following three assumptions. Firstly, the norms of the vectors play only a subordinate role here, since only their orientations towards the electric field of the incident light are of interest. Thus, they are normalized. Secondly, only atoms showing a relatively strong derivation from their equilibrium position are to be considered in this approximation. Thirdly, all x – , y – and z – components of the 3N dimensional normal coordinates, where N represents the number of the investigated oscillating atoms, can be summed up - resulting in a three-dimensional vector - since the assumption is not focused on the emitted electromagnetic field. Therefore, the detected Raman intensities of the investigated normal modes depend on the orientation of this simplified normal coordinate vector towards the electric field vector of the linear polarized incident light as shown later. The oscillation directions of the molecular fragments involved in the investigated vibrations were computed by a DFT calculation. In case of the ONO asymmetric stretching vibrations of the CL-20 polymorphs, the N atoms oscillate oppositely to the O atoms of the NO_2 functional groups. This oscillation takes place in a plane formed by the involved N and O atoms. Additionally, the atomic deviations during the oscillation are equal in all NO_2 groups. Therefore, a vector $\vec{q}_{m;\beta\text{-}CL\text{-}20}$, respectively $\vec{q}_{m;\gamma\text{-}CL\text{-}20}$, starting at one O atom and pointing to the other O atom of the same functional group is able to describe qualitatively the oscillation of this NO_2 group. Hence, the approximated normal coordinates $\vec{q}_{0;\beta\text{-}CL\text{-}20}$ and $\vec{q}_{0;\gamma\text{-}CL\text{-}20}$ arise from

$$\vec{q}_{0;\beta\text{-}CL\text{-}20} = \sum_{m=1}^{4} \vec{q}_{m;\beta\text{-}CL\text{-}20} \qquad \text{Eq. 3.1}$$

and

$$\vec{q}_{0;\gamma\text{-}CL\text{-}20} = \sum_{m=1}^{4} \vec{q}_{m;\gamma\text{-}CL\text{-}20} \,. \qquad \text{Eq. 3.2}$$

The directions of the single vectors $\vec{q}_{n;\beta\text{-}CL\text{-}20;xy}$ and $\vec{q}_{n;\gamma\text{-}CL\text{-}20;xy}$ are represented as yellow arrows in Figure 3.11. a). It should be mentioned that only the four marked NO_2 functional groups contribute to the investigated CL-20 normal modes. Resulting CL-20 normal coordinates were normalized and added:

$$\vec{q}_{0;CL\text{-}20} = \frac{1}{n_{\beta\text{-}CL\text{-}20}} \vec{q}_{0;\beta\text{-}CL\text{-}20} + \frac{1}{n_{\gamma\text{-}CL\text{-}20}} \vec{q}_{0;\gamma\text{-}CL\text{-}20} \,, \qquad \text{Eq. 3.3}$$

where $n_{\beta\text{-}CL\text{-}20}$ and $n_{\gamma\text{-}CL\text{-}20}$ represent the normalization factors of $\vec{q}_{0;\beta\text{-}CL\text{-}20}$ and $\vec{q}_{0;\gamma\text{-}CL\text{-}20}$. Normalization was done to ensure a comparability between CL-20 and HMX normal modes. The summation of $\vec{q}_{0;\beta\text{-}CL\text{-}20}$ and $\vec{q}_{0;\gamma\text{-}CL\text{-}20}$ is necessary due to the molar ratio of 2:1 between CL-20 and HMX in the CL-20/HMX co-crystal system.

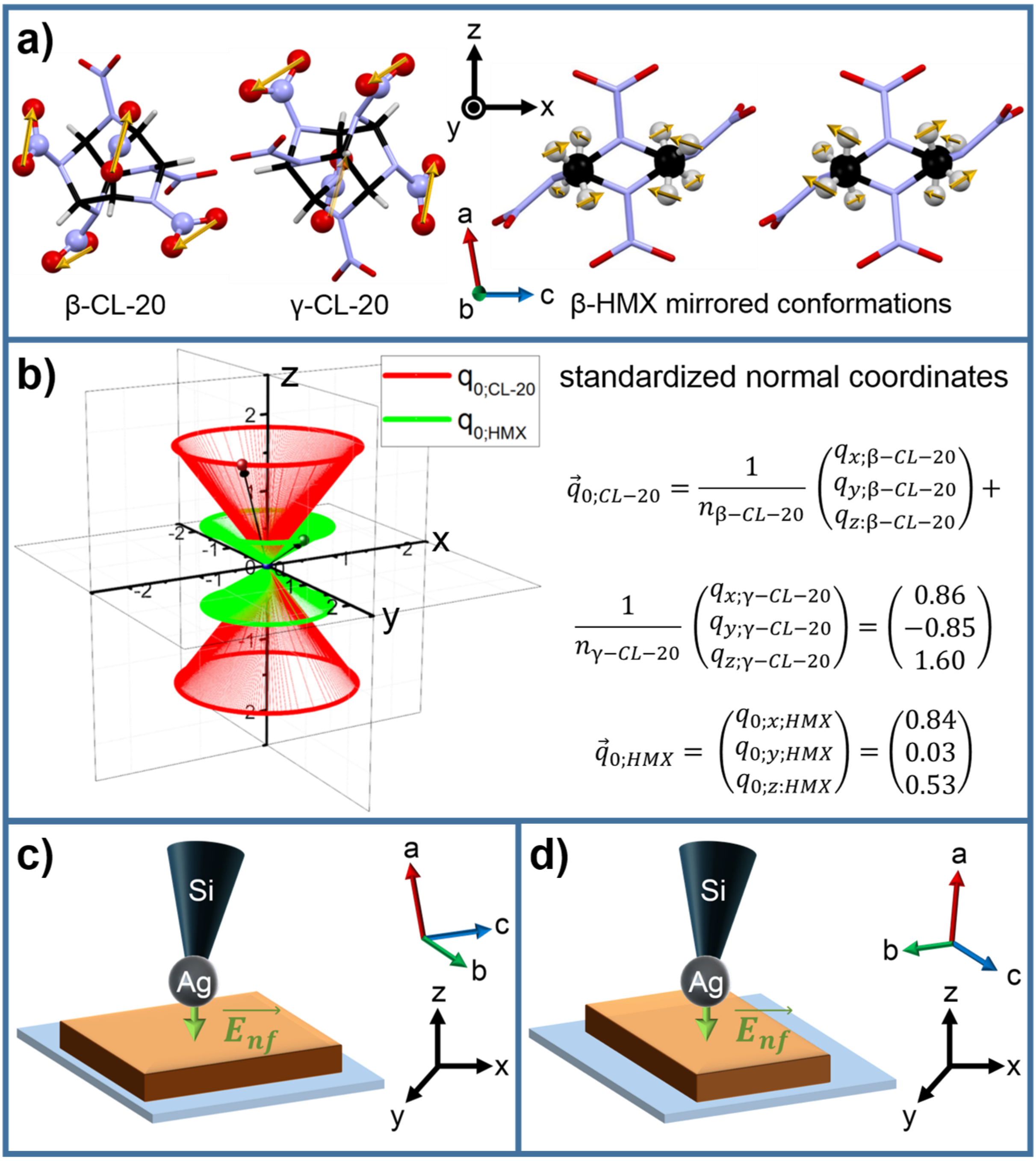

Figure 3.11. a) Orientations and conformations of β-CL-20, γ-CL-20 and β-HMX mirrored conformations in the CL-20/HMX co-crystal lattice. Yellow arrows represent the approximated single vector components of the approximated normal coordinates. **b)** Approximated normal coordinates; $\vec{q}_{0;CL-20}$ is depicted in red, $\vec{q}_{0;HMX}$ is depicted in green. Since the crystallographic bc – plane is aligned parallel towards the xy – plane, all possible orientations between the normal coordinates and the electric field vector $\vec{E}_{nf}$ can be illustrated as cones around the z – axis. Therefore, the present semi-orientation does not affect the Raman intensity ratio in TERS, since the angles included by the normal coordinates and the z – axis ($\vec{E}_{nf}$) remains unchanged in all possible alignments. **c)** and **d)** two possible arrangements of the semi-orientated scattering system. The crystallographic bc – plane is always aligned parallel to the xy – plane of the scattering system. The electric field vector $\vec{E}_{nf}$ of the near-field located one the Ag nanoparticle at the tip apex is approximated perpendicular towards the xy – plane.

In case of the HMX CH_2 wagging vibration, the path which is covered by the H atoms can be described as a circular segment around the central C atom. Accordingly, the movement of the plane defined by the C and H atoms from the equilibrium position to the maximal derivation position can be expressed approximately by the normal vector $\vec{q}_{m;HMX}$ of this plane at the equilibrium position. In case of the investigated HMX normal mode opposite CH_2 groups oscillating in the same direction (Figure 3.11.a). Additionally, the derivation of all groups from their equilibrium position are identical. HMX molecules in CL-20/HMX co-crystals appear in two conformations which act like mirror images along the crystallographic bc – plane. Regarding these facts, the approximation of the normalized $\vec{q}_{0;\,\beta\text{-}HMX}$ can be expressed as

$$\vec{q}_{0;\beta\text{-}HMX} = \frac{1}{2}\left(\frac{\sum_{m=1}^{4}\vec{q}_{m;\beta\text{-}HMX-1}}{n_{\beta-HMX-1}} + \frac{\sum_{m=1}^{4}\vec{q}_{m;\beta\text{-}HMX-2}}{n_{\beta-HMX-2}}\right). \qquad \text{Eq. 3.4}$$

The approximated vectors $\vec{q}_{0;\,CL-20}$ and $\vec{q}_{0;\,\beta\text{-}HMX}$ are shown in Figure 3.11.b). The detailed calculations of these vectors are provided within the supporting information. Due to the semi-orientated scattering system the crystallographic ac – plane can be aligned in every possible direction inside the xy – plane of the scattering system. Therefore all possible orientations of $\vec{q}_{0;\,CL-20}$ and $\vec{q}_{0;\,\beta\text{-}HMX}$ in the scattering system can be depicted as circles around the z – axis (Figure 3.11.b). The cones shown in Figure 3.11.b) represent furthermore the changes of the approximated normal coordinates over time. As already mentioned above, the z – component of the electric field vector $\vec{E}_{nf}$ (nf = near field) is the main source of $\vec{E}_{nf}$ and hence $\vec{E}_{nf}$ can be approximated to

$$\vec{E}_{nf} = \begin{pmatrix} 0 \\ 0 \\ E_{z;nf} \end{pmatrix}. \qquad \text{Eq. 3.5}$$

Due to the Stokes term of the classical interpretation of the Raman scattering

$$\frac{1}{2}\left(\frac{\partial\hat{\alpha}}{\partial q}\right)_0 \vec{q}_0\, \vec{E}_0 \cos\,(\omega_0 - \omega_R)t \qquad \text{Eq. 3.6}$$

the measured Raman intensity is proportional to the absolute value of the scalar product between the normal coordinate $\vec{q}_{0;\,CL-20}$, respectively $\vec{q}_{0;\,\beta\text{-}HMX}$, and the electric field vector $\vec{E}_{nf}$:

$$I_{CL-20} \sim \left|\vec{E}_{nf} \cdot \vec{q}_{0;CL-20}\right| = \left|E_{z;nf} \cdot q_{0;z;CL-20}\right| \qquad \text{Eq. 3.7}$$

$$I_{HMX} \sim \left|\vec{E}_{nf} \cdot \vec{q}_{0;HMX}\right| = \left|E_{z;nf} \cdot q_{0;z;HMX}\right| . \qquad \text{Eq. 3.8}$$

From this correlations it is apparent that only the z – components $q_{0;z;CL-20}$ and $q_{0;z;HMX}$ of the approximated normal coordinates contributes to the scalar products. These z – components are constant for each possible parallel orientation of the crystallographic bc – plane inside the xy – plane of the scattering system. Therefore, the theoretical approximation of the intensity ratios can be finally given as:

$$\frac{I_{CL-20}}{I_{HMX}} = \frac{\left|E_{z;nf} \cdot q_{0;z;CL-20}\right|}{\left|E_{z;nf} \cdot q_{0;z;HMX}\right|} = \frac{\left|q_{0;z;CL-20}\right|}{\left|q_{0;z;HMX}\right|} = \frac{1.60}{0.53} \approx \frac{3}{1} \ . \qquad \text{Eq. 3.9}$$

Accordingly, as already assumed from far-field Raman data, the intensity ratio inversion of the marker bands within the TERS spectra of n-CL-20/HMX nano-plates is very unlikely to occur because of the (semi-)orientated scattering system.

3.4.5 Surface Composition of CL-20/HMX Nano-Plates

Next to the molecular arrangement towards the TERS scattering system, the distance between the Ag nanoparticle at the tip apex and the sample surface influences strongly the Raman intensities. This dependency arises from the rapid decrease of the localized enhanced field at the tip apex as a function of the distance. Experimental studies and simulations have shown that the decay of the majority of the field enhancement occurs at a distance less than 8 nm – 10 nm from the surface of the Ag nanoparticle.[21-24] Furthermore, TERS experiments presented here were recorded in non-contact mode (see experimental section). In this dynamic AFM mode, the tip oscillates with a certain frequency and amplitude over the sample surface. Thus, the distance between the tip apex and the n-CL-20/HMX nano-plates surfaces varies constantly during the measurement. Regarding this fact, measured signal intensities represent a weighted average over all particle-surface distances during the acquisition time. Trautmann *et al.* could show *via* electrodynamic simulations that the average Raman enhancement strongly depends on the closest distance between Ag nanoparticle and sample surface at dynamic AFM modes. Further they could demonstrate that the main field enhancement is localized within a distance less than 2 nm from the particle surface (green spheres in Figure 3.12).[21] In case of single n-CL-20/HMX nano-plates surfaces parallel to the xy – plane of the scattering system always consists of pure HMX or CL-20 layers (see XRPD and AFM section). Accordingly, the tip – surface distance represents always the distance between the tip apex and a specific molecular layer. Therefore, the distance between the next molecular layer and the tip apex is always around a third of the height of the crystallographic unit cell h_{unit}

$$h_{unit} = \frac{1}{3} a \cos\beta = \frac{1}{3} \cdot 1.63\, nm \cdot \cos 9.23° = 0.54\, nm \qquad \text{Eq. 3.10}$$

larger than the tip-surface distance.[13] Regarding this fact, the surface layer is always located in a field region showing a stronger Raman enhancement than the second molecular layer (Figure **3.12**). This difference leads to a significantly stronger enhancement of the actual surface layer and hence to stronger Raman intensities of this layer. Thus, the Raman intensity inversions between the CL-20 and HMX marker bands from ~2.5:1 to ~1.5:1 (CL-20 : HMX) in the TERS spectra can be explained by HMX as the surface finishing layer. Since the intensity inversion

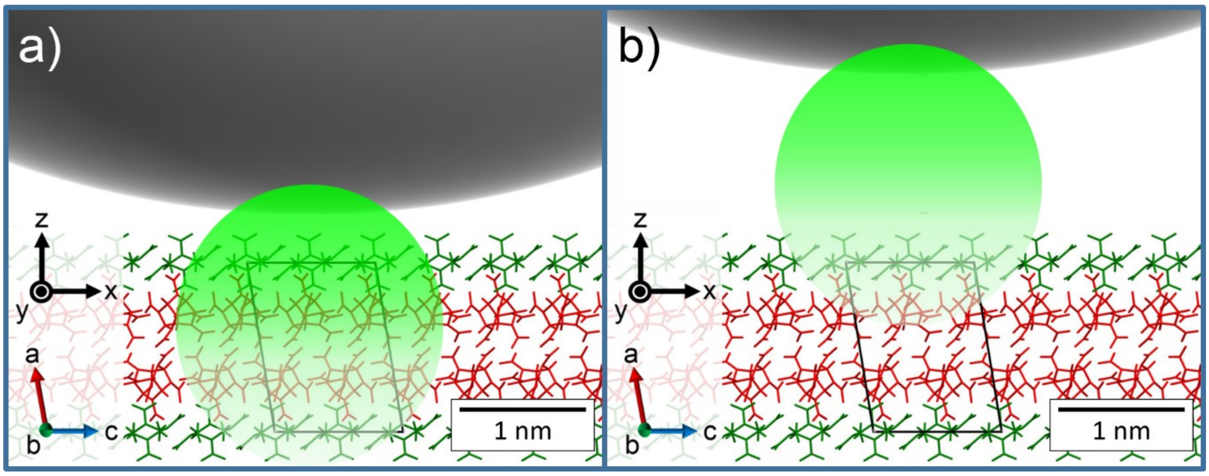

Figure 3.12. Schematic representation of a dynamic non-contact TERS measurement of n-CL-20/HMX. The grey sphere represents the TERS active Ag nanoparticle. The green circle symbolizes the localized enhanced field at the tip apex. **a)** Closest distance between TERS active Ag – tip and particle surface. **b)** TERS active Ag – tip is moving upwards. **a)** and **b)** During the whole TERS measurements the HMX surface layer is always located in an electric field region showing a stronger Raman enhancement. Thus, the HMX marker band appears more intense in TERS spectra.

arises at each measured n-CL-20/HMX nano-plate surface, it is assumed that an HMX surface finishing is energetically favored. This assumption is explicable by the molecular structure of HMX. Contrary to the CL-20 cage structure, HMX is a cyclic nitroamine and hence it is easier to deform. Regarding this HMX should be able to adopt an energetically more favorable conformation than CL-20. Therefore, surface energy of CL-20/HMX nano-plates is minimized through an HMX surface finishing.

3.4.6 Proposed Mechanism for Ignition by Impact

The HMX surface finishing may contribute to explain why the impact sensitivity of CL-20/HMX is much closer to HMX than to CL-20 (Table 3.1).[13-15] Up to now it is assumed that the relative low impact sensitivity of CL-20/HMX arises inter alia due to an enhanced compressibility of the co-crystal system compared to its pure compounds. This increased compressibility was shown by a DFT-D study undertaken by Liu *et al.*[17] Therefore, input impact energy are able to dissipate easier over the crystal lattice and thus more energy is needed to overcome the bond-dissociation energies of CL-20 and HMX. Moreover, a profusely electron delocalization between the O atoms of the nitro functional groups and adjoining H atoms is suggested to participate in the mechanical stability.[17]

Table 3.1. Impact sensitivities of CL-20/HMX, ϵ-CL-20 and β-HMX measured by various groups

Impact sensitivity CL-20/HMX	Impact sensitivity ϵ-CL-20	Impact sensitivity β-HMX	Reference
h_{50} = 55 cm	h_{50} = 29 cm	h_{50} = 55 cm	Bolton *et al.*[13]
h_{50} = 43 cm - 48 cm	h_{50} = 25 cm - 28 cm	h_{50} = 45 cm - 50 cm	Gosh *et al.*[14]
1.5 Joule	n/a	1.6 Joule	n-CL-20/HMX [15]

However, this assumption deals solely with perfect defect free crystals and does not include defect sides or crystal surfaces. Due to the nanostructure of n-CL-20/HMX, the nano-plates exhibit only a few crystal defects but a relatively high surface area because of the high surface to volume ratio (see AFM and XPRD measurements). These surfaces consist approximately to 85% of HMX (see XRPD and AFM section). Next to the (300) – faces also the other crystal lattice planes defining the particle surfaces (or internal defect sides) are very likely finished by an HMX molecular layer because of the surface energy minimization due to the more easily deformable HMX molecule. However, TERS investigations of these inclined planes including a theoretical approximation are significantly more difficult, since also the xy – components of the enhanced electric field at the Ag nanoparticle surface must be considered. Anyway, since the compressibility of the CL-20/HMX co-crystal system is higher than those of its pristine compounds, a higher amount of impact energy should be necessary to induce the dissociation of CL-20 and HMX in the co-crystal as in its pure compounds. However, impact sensitivity experiments were not able to validate this assumption.[13-15] Therefore, it should be considered that at the measured impact energies an ignition of CL-20/HMX does not take place in the bulk material. Thus, the following mechanism is proposed. In a first step input impact energy which still can be absorbed by compression of the CL-20/HMX co-crystal but sufficient to ignite pure β-HMX and thus β-CL-20 and γ-CL-20 compresses n-CL-20/HMX. During the relaxation of the compressed crystal input impact energy is converted into thermal energy dissipating over the crystal lattice. If the amount of the dissipating thermal energy while reaching the HMX determined particles surface (or structural defect) is still high enough to overcome the dissociation energy of HMX, HMX molecules will dissociate, since a further dissipation of the thermal energy is hindered. The released heat of reaction induces the dissociation of neighboring HMX and CL-20 leading to a chain-reaction and finally to the combustion of the CL-20/HMX co-crystal. Thus, the ignition by impact is spread from the surfaces respectively structure defects towards the inside of the bulk material by starting with dissociation of HMX surface molecules. However, the measured sensitivities against impact values are subjacent to this of β-HMX. This fact can be explained by the conformation – or better conformations, since different surface faces should lead to different HMX conformations – adapted by surfaces HMX molecules. The adapted conformations will lead to a surface energy minimization but should be energetically less favored than that of pure β-HMX. Furthermore, energy transfers between compressed air and HMX surfaces may contribute to the impact ignition mechanism. For the sake of completeness, it should be mentioned that An *et al.* show a less sensitivity against impact of nano sub-structured CL-20/HMX micro particles.[16] This improved sensitivity may be caused by the underlying 3D-networks and a possible interaction between these networks and included air. Anyway, the proposed mechanism would explain the nearly similar impact sensitivities of CL-20/HMX and HMX without contradiction to previously found theoretical and experimental data.

3.5 Conclusion

The paper shows the successful synthesis of CL-20/HMX nano-plates *via* the Spray Flash Evaporation process. XRPD prove impeccably the co-crystallinity of n-CL-20/HMX and AFM investigations demonstrates the nanostructure of n-CL-20/HMX nano-plates. Furthermore far-field Raman maps support the XPRD results and demonstrate besides a complete conversion of pristine CL-20 and HMX into n-CL-20/HMX. Marker bands for HMX and CL-20 were chosen from far-field Raman spectroscopy data with the premise that no signal appears at these wavenumbers at the other pristine compound Raman spectrum. In far-field spectra the CL-20 marker band (NO_2 asymmetric stretching vibrations localized at 1600 cm^{-1}) appears with an around 2.5 times higher intensity as the HMX marker band (CH_2 out of plane wagging vibration, localized at 1416 cm^{-1}). The intensity ratio of these marker bands inverts to a ratio of around 1.5 : 1 (HMX to CL-20) in TERS spectra which strongly hints to an HMX determined surface of n-CL-20/HMX. To ensure this assumption, an approximated normal coordinate analysis was undertaken, since the intensity ratio inversion could occur due to a specific arrangement of n-CL-20/HMX nano-plates towards the Raman scattering system. Therefore, the movements of the atoms involved in the investigated normal modes were simulated with a DFT method. Only atoms with strong derivations from their equilibrium position were drawn under consideration by expressing their movements as 3D dimensional vectors leading to simplified 3N dimensional normal coordinates. Since only the interactions between the incident light and the normal modes and not the emitted field are of interest for this purpose, the x-, y- and z – components of these 3N dimensional normal coordinates were summed up and normalized resulting in 3D normalized vectors. This simplification demonstrates that under the given orientation the intensity of CL-20 marker vibration should triple the intensity of HMX marker vibration which is close to the measured ratio. Thus, the intensity ratio inversion arises most likely from an HMX surface finishing, since HMX surface molecules are always located in a higher enhanced field region during the dynamic AFM-TERS measurements. In consideration of this finding an impact ignition mechanism is proposed enabling to explain the close sensitivity values of HMX and CL-20/HMX in spite of a higher compressibility of CL-20/HMX.

In conclusion, this study demonstrates again the extraordinary possibilities that lie behind TERS. It was possible to figure out co-crystallinity on single nanoscale co-crystals. This is of analytical interest, for example, if synthesized nano co-crystals are not present in sufficient amounts to perform more common analytical methods like XRPD. Moreover, we could show that TERS enables surface investigations of nano (co-) crystalline particles which may help to receive a better understanding of co-crystal formation and co-crystal design for specific applications.

3.6 Supporting Information

3.6.1 AFM Topographic Mappings of n-CL-20/HMX Nano-Plates

In the following further AFM topographic maps of n-CL-20/HMX nano-plates recorded in non-contact mode are presented. n-CL-20/HMX nano-plates occur as single particles as well as agglomerates along their crystallographic bc-axis. Figure 3.13 shows one of these agglomerates. The substructure of single nano-plates can be identified easily from the AFM topographic image. n-CL-20/HMX agglomerates can be randomly orientated towards the scattering system. Therefore, only single CL-20/HMX nano-plates were investigated via AFM-TERS in this study. Figure 3.14 depict a selection of different single and agglomerated CL-20/HMX nano-plates to demonstrate that these structures appear in the whole sample.

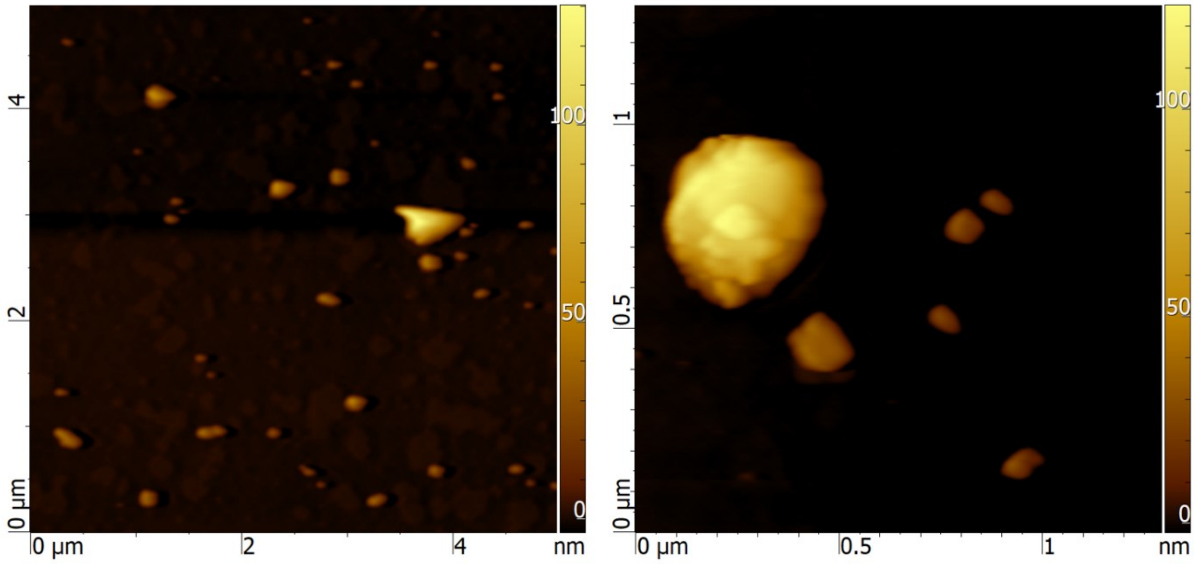

Figure 3.13. Left: AFM topographic mappings of several n-CL-20/HMX nano-plates. Single nano-plates show a height of ~30 nm. n-CL-20/HMX nano-plates built up agglomerates along their crystallographic bc-planes. **Right:** Single n-CL-20/HMX nano-plates and a CL-20/HMX nano-plate agglomerate.

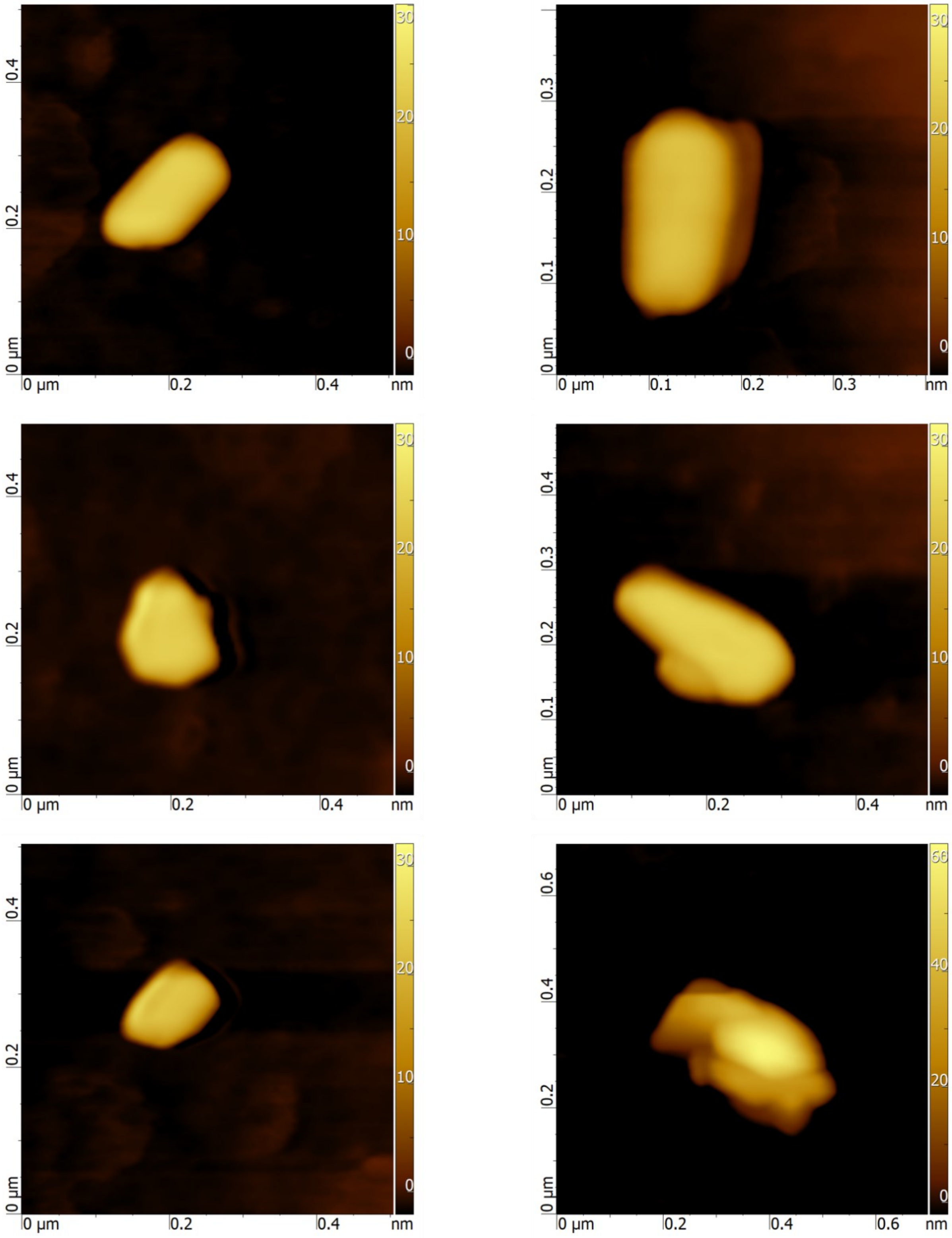

Figure 3.14. Selection of single and agglomerated n-CL-20/HMX nano-plates.

3.6.2 Raman Active Vibrational Frequencies and Assignments

In the following Raman spectra and tables of Raman active vibrational frequencies of β-CL-20, γ-CL-20, β-HMX, CL-20/HMX as well as their assignments are presented.

β-CL-20

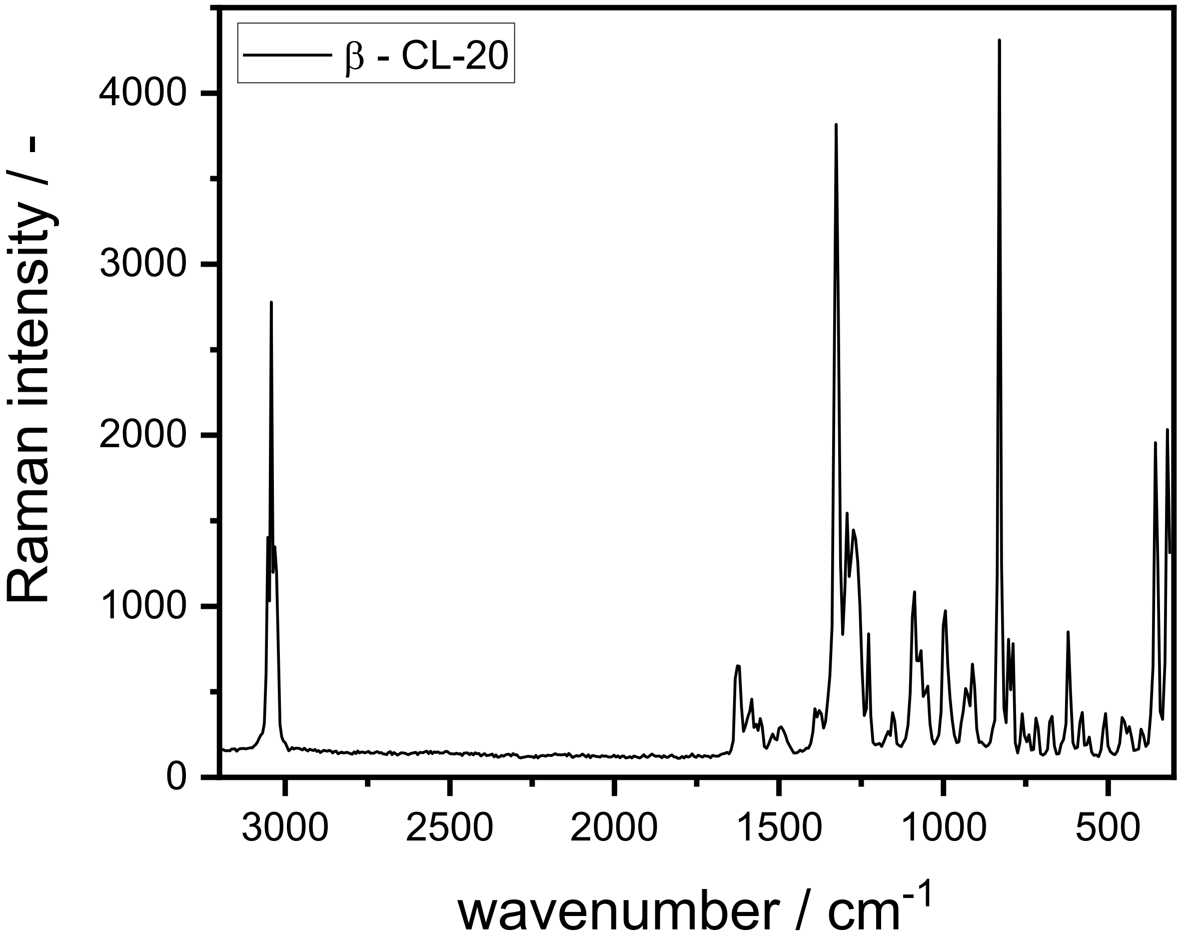

Figure 3.15. Raman spectrum of β-CL-20 in a spectral range between 3200 cm^{-1} and 300 cm^{-1}.

Table 3.2. Raman frequencies and their assignments of β-CL-20.

Raman frequencies of β-CL-20		
Experiment / cm^{-1}	**Literature / cm^{-1} [45]**	**Assignments [45]**
320 m	319 m	cage def, CNN bend
356 m	353, 369 w	cage def, N-NO_2 bend
400 vw	398 vw	N-NO_2 bend
436 vw	435 vw	N-NO_2 bend

457 vw	456 vw	N-NO$_2$ bend
507 vw	511 vw	NNO bend
557 vw	560 vw	cage def
579 vw	583 vw	cage def
621 w	621 w	cage def
670 vw	673 vw	NO bend
719 vw	718 vw	NO bend, NNO$_2$ bend
740 vw	744 vw	ONO bend
761 vw	762 vw	ONO bend
789 w	791w	ONO bend
803 w	803 w	ONO bend
830 vs	832 s	ring CH wag
913 w	912 w	ring str, ring CH wag
933 vw	932, 944 w	ring str, ring CH wag
994 w	982, 999 w	NN str
1048 vw	1052 vw	NN str
1068 w	1071 vw	NN str
1088 m	1093 w	NN str
1155 vw	1154 vw	CH bend
1228 w	1229 w	CH bend, NO str sym
1274 m	1276 m	CH bend, NO str sym
1293 m	1295 w	CH bend, NO str sym
1326 vs	1328 s	CH bend
1378 vw	1377 vw	CH bend
1391 vw	1390 vw	CH bend
1494 vw	1496 vw	CH bend
1557 vw	1557 vw	ONO str asym
1570 vw	1570 vw	ONO str asym
1582 w	1585 w	ONO str asym
1595 w	1593 w	ONO str asym
1626 m	1631 w	ONO str asym
3027 m	3027 w	CH str
3032 m	3036 m	CH str
3043 s	3045 s	CH str
3053 m	3056 m	CH str

β-CL-20 marker vibration (1595 cm^{-1}; ONO asymmetric stretching)) is marked in red. **Notes:** vs – very strong, s – strong, m – medium, w – weak, vw – very weak; asym – asymmetric, sym – symmetric, bend – bending, def – deformation, str – stretching, wag – wagging *γ-CL-20*

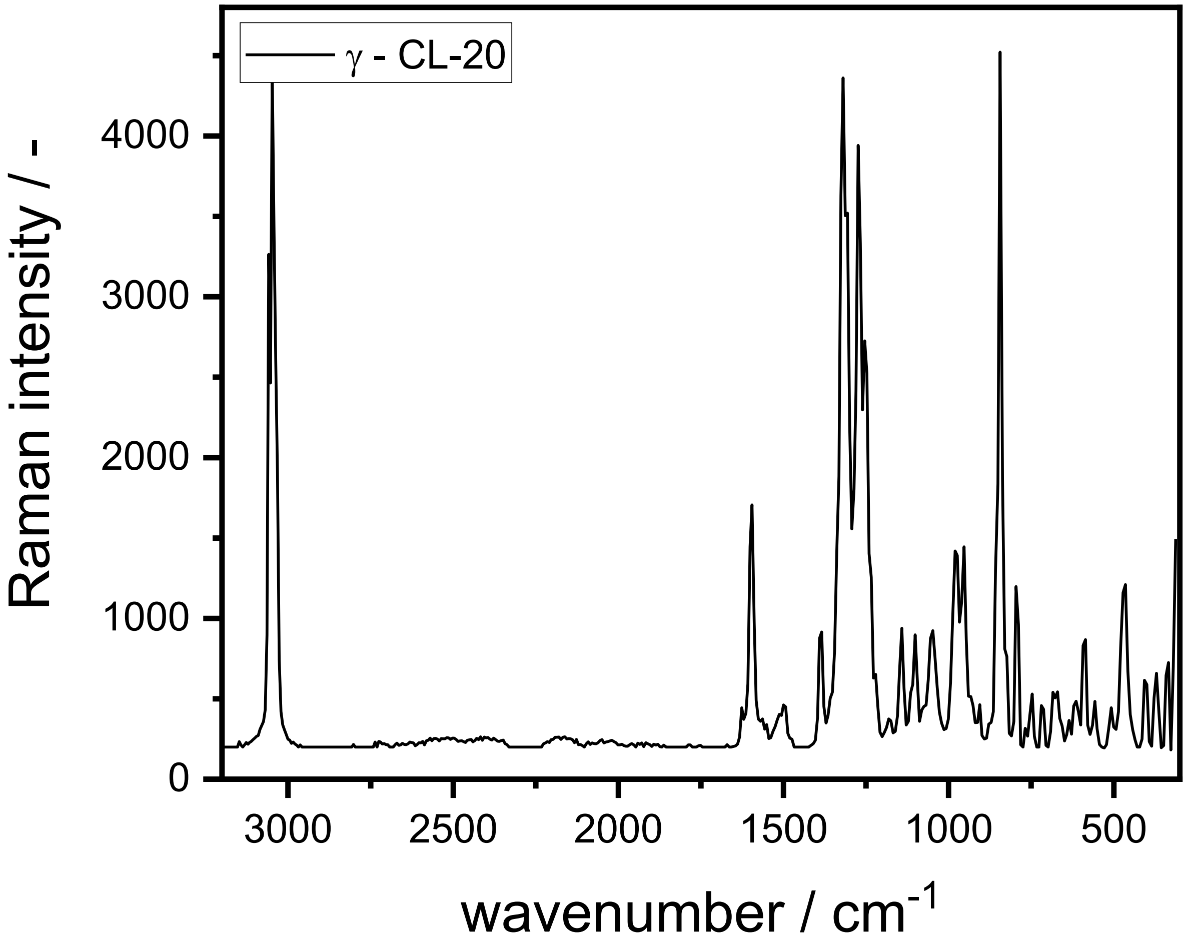

Figure 3.16. Raman spectrum of γ-CL-20 in a spectral range between 3200 cm^{-1} and 300 cm^{-1}.

Table 3.3. Raman frequencies and their assignments of γ-CL-20.

Raman frequencies of γ-CL-20		
Experiment / cm^{-1}	**Literature / cm^{-1} [45]**	**Assignments [45]**
312 m	318 m	cage def
334 w	340 vw	cage def
370 w	366 w	cage def
406 w	406 w	N-NO_2 bend
464 m	470, 479 vw	N-NO_2 bend
508 vw	512 w	N-NO_2 bend
557 vw	560 vw	N-NO_2 bend
585 w	592 w	cage def
614 vw	613, 619 w	cage def
635 vw	639 vw	cage def
684 w	686 vw	ONO bend

719 vw	718 w	ONO bend
747 w	750 vw	ONO bend
768 vw	770 vw	ONO bend
795 m	795, 807 w	ONO bend
823 w	827 vw	ONO bend
844 vs	846 m	ring CH wag
858 m	858 m	ring CH wag
878 vw	877 w	ring CH wag
906 vw	909	ring CH wag
933 w	935 vw	ring str, ring CH wag
953 m	956 w	ring str, ring CH wag
981 m	978 w	ring str, ring CH wag
1048 w	1055 w	ring str, NN str
1102 w	1105 w	NN str
1142 w	1145 m	CH bend, ring str
1182 vw	1179 w	CH bend, ring str
1221 w	1220 vw	CH bend
1234 m	1238 w	CH bend
1254 s	1254 m	CH bend, NO str sym
1273 s	1273 m	CH bend, NO str sym
1306 s	1310	CH bend, NO str sym
1319 vs	1324 s	CH bend, NO str sym
1338 m	1336 w	CH bend, NO str sym
1384 w	1389 w	CH bend
1500 vw	1498 vw	ONO str asym
1551 vw	1554 vw	ONO str asym
1563 vw	-	ONO str asym
1598 m	1600 m	ONO str asym
1627 vw	-	ONO str asym
3032 m	3034 s	CH str
3048 vs	3043, 3050 s	CH str
3059 s	3061 m	CH str

γ-CL-20 marker vibration (1598 cm^{-1}; ONO asymmetric stretching)) is marked in red. **Notes:** vs – very strong, s – strong, m – medium, w – weak, vw – very weak; asym – asymmetric, sym – symmetric, bend – bending, def – deformation, str – stretching, wag – wagging *β-HMX*

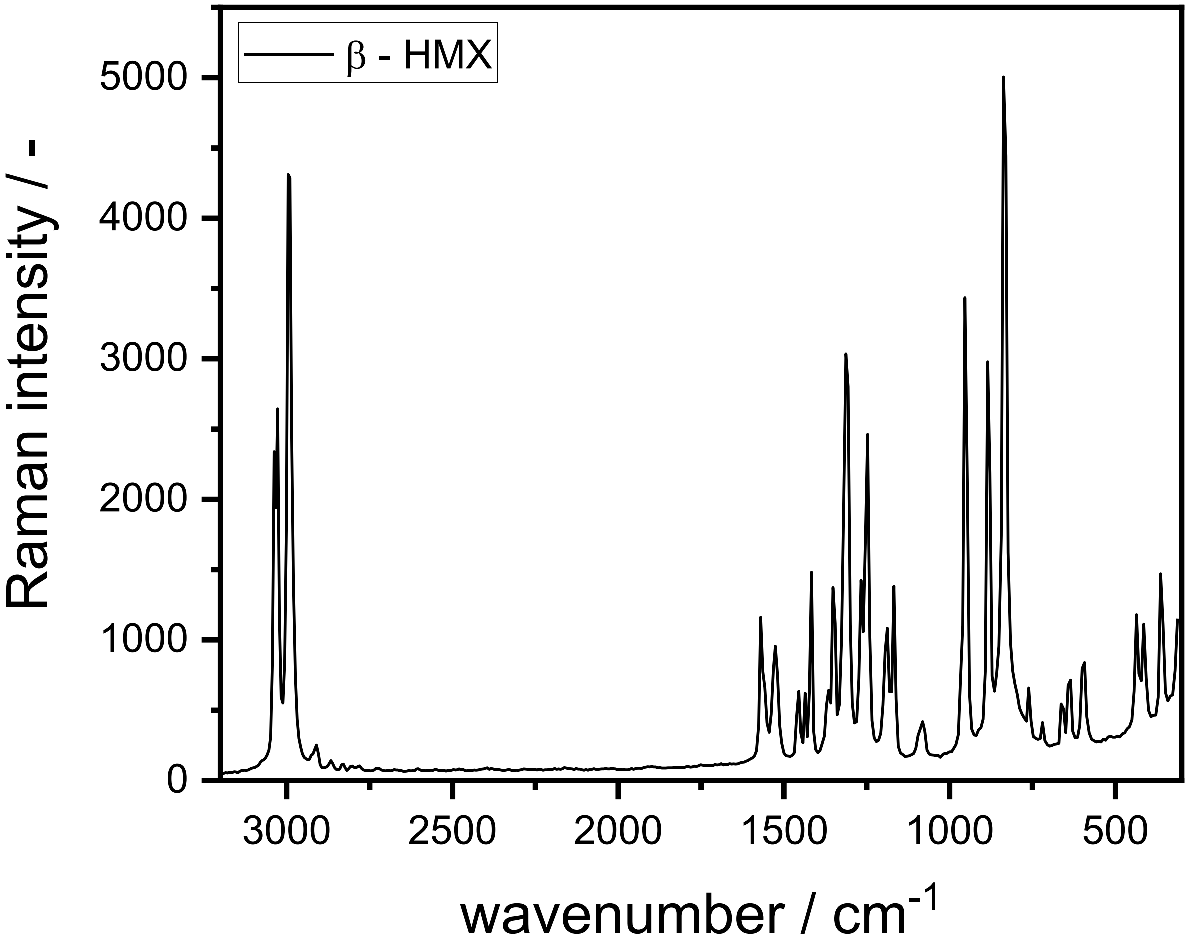

Figure 3.17. Raman spectrum of β-HMX in a spectral range between 3200 cm^{-1} and 300 cm^{-1}.

Table 3.4. Raman frequencies and their assignments of β-HMX.

Raman frequencies of β-HMX		
Experiment / cm^{-1}	**Literature / cm^{-1} [46-47]**	**Assignments [47]**
364 m	342	CN str, NN str, NCN bend
414 m	412	NNO bend, NNC bend
436 m	432	CNC bend, NNC bend
593 w	597	NNO bend
635 w	638	NNO bend, NN str
664 w	662	NNO bend, NN str
720 vw	721	ONO bend, CN str
761 v	759	ONO wag
837 vs	834	NC_2 str sym

885 s	881	NNC_2 str sym
954 s	950	NN str, CH_2 rock
967 w	965	CNN str asym, CH_2 rock
1082 vw	1090	NNC_2 str asym
1168 m	1168	CNN str asym, CH_2 rock
1188 m	1190	NC_2 str asym
1248 s	1248	NC_2 str asym
1267 m	1268	NO_2 str sym
1313 s	1312	CH_2 twist
1352 m	1350	CH_2 twist
1365 w	1368	CH_2 wag
1417 m	1418	CH_2 wag
1436 w	1438	HCH bend
1455 w	1460	HCH bend
1526 w	1532	NO_2 str asym
1570 m	1558	NO_2 str asym
2995 vs	2992	CH_2 str sym
3027 s	3028	CH_2 str asym
3038 s	3037	CH_2 str asym

β-HMX marker vibration (1417 cm^{-1}; CH_2 wagging) is marked in green. Notes: vs – very strong, s – strong, m – medium, w – weak, vw – very weak; asym – asymmetric, sym – symmetric, bend – bending, rock – rocking, str – stretching, twist – twisting, wag – wagging

CL-20/HMX (2:1) co-crystal

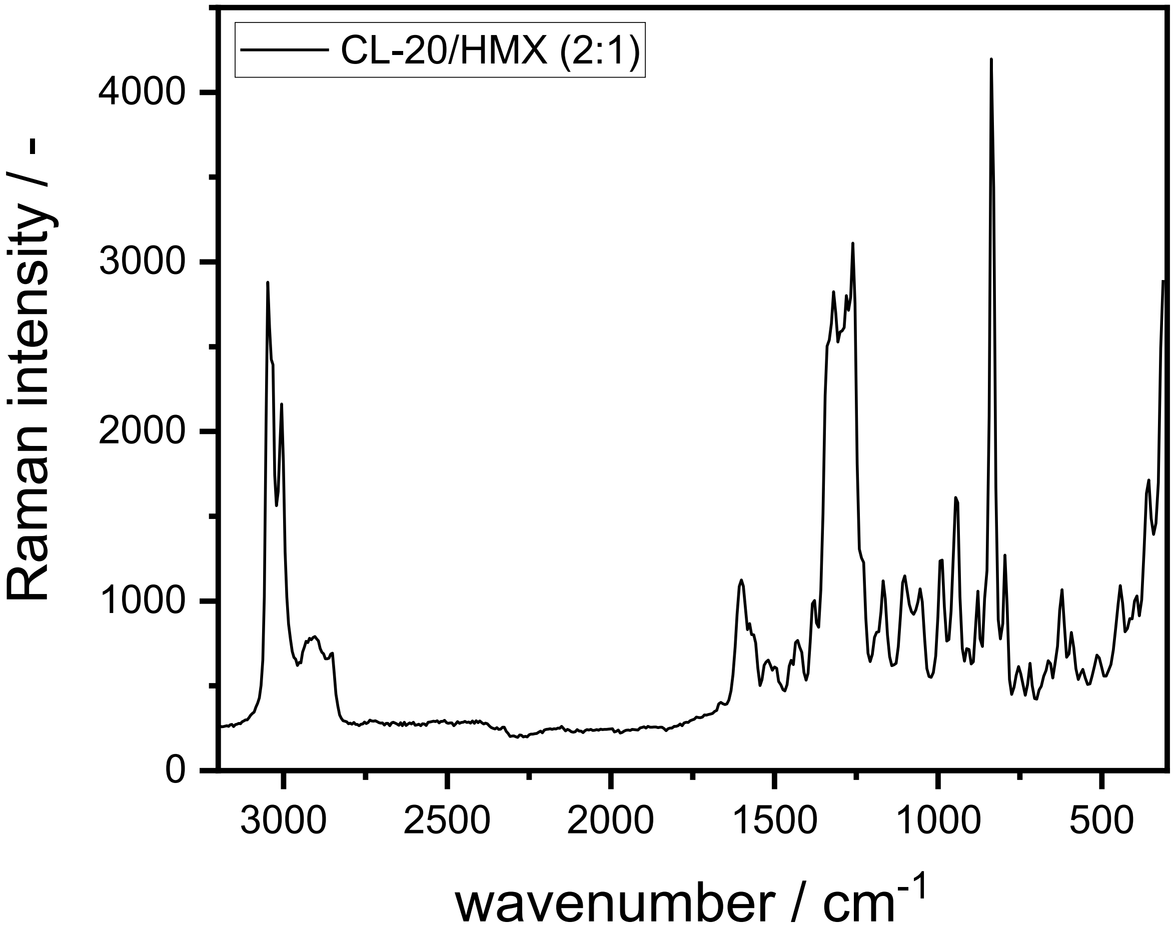

Figure 3.18. Raman spectrum of CL-20/HMX co-crystal (2:1) in a spectral range between 3200 cm^{-1} and 300 cm-^{1}.

Table 3.5. Raman frequencies and their assignments of CL-20/HMX.

Raman frequencies of CL-20/HMX (2:1)		
Experiment / cm^{-1}	**Literature / cm^{-1} (experimental) [14]**	**Assignments [14]**
356 m	360.4 w	**HMX**: ring def, CNC bend; **CL-20:** cage def
393 w	395.3 w	**CL-20:** CNC bend, N-NO$_2$ bend
414 w	415.1 w	**HMX:** NCN bend, N-NO$_2$ bend
443 w	441.1 m	**CL-20:** CNC bend, N-NO$_2$ bend

515 vw	515.9 w	**CL-20:** NCN bend, N-NO_2 bend, cage def
557 vw	560.5 w	**CL-20:** CNC bend, N-NO_2 bend
593 w	591.5 m	**CL-20:** cage def, CNC bend N-NO_2, bend
621 w	622.8 w	**CL-20:** cage def, N-NO_2 bend
656 w	658.2 w	**HMX:** cage def, ONO bend, CNC bend
664 w	665.7 vw	HMX: cage def, ONO bend, CNC bend
719 w	719.3 w	**CL-20:** cage def, N-NO_2 bend, CCN bend, **HMX:** ring def, CNC bend, ONO bend
754 w	755.8 w	**CL-20:** CCN bend, ONO bend
795 w	793.3 w	**HMX:** CNC bend, ONO bend
837 vs	835.4 vs	**CL-20:** ONO bend, NCN bend
858 w	856.0 m	**CL-20:** ONO bend, C-C str, N-N str
879 w	878.6 m	**HMX:** CNC str, N-N str, ONO bend
913 vw	908.3 w	**CL-20:** CNC str, CNC bend
947 m	942.1 m	**CL-20:** C-C str , N-N str
994 m	989.8 m	**CL-20:** C-C str, N-N str, ONO bend
1055 w	1053.7 m	**CL-20:** N-N str, ONO bend, CH wag
1102 m	1102.4 m	**CL-20:** NN tors, CH wag
1168 m	1167.2 m	**CL-20:** CNC str asym
1228 m	1230.3 m	**HMX:** CNC str asym
1260 s	1257.3 s	**CL-20:** CH wag; **HMX:** CNC str, ONO str
1280 s	1281.2 s	**CL-20:** CNC str asym, ONO str sym
1300 s	1301.7 s	**CL-20:** CH wag, ONO str sym
1320 s	1321.5 s	**CL-20:** CH bend, N-N str, ONO str sym
1340 s	1342.3 s	**CL-20:** CH wag, CN str, ONO str sym
1346 s	1353.1 w	CL-20: CH bend

1378 w	1372.8 w	**CL-20:** CH bend; **HMX:** CH_2 wag, ONO str sym, N-N str
1417 w	1413.9 w	**HMX:** CH_2 wag
1430 w	1432.4 m	**CL-20:** CH bend, CNC str
1500 vw	1505.8 w	**HMX:** CH_2 bend
1519 w	1517.2 w	**HMX:** CH_2 bend
1531 vw	1528.6 m	**HMX:** CH_2 bend
1563 w	1562.7 m	**HMX:** ONO str asym
1576 w	1575.8 m	**HMX:** ONO str asym
1595 m	1597.6 m	**CL-20:** ONO str asym
1602 m	1604.2 m	**CL-20:** ONO str asym
1608 m	1615.1 w	**CL-20:** ONO str asym
3006 s	3006.5 s	**HMX:** CH str
3016 s	3016.4 m	**HMX:** CH str
3032 s	3033.6 s	**CL-20:** CH str
3048 s	3050.8 vs	**CL-20:** CH str
3059 m	3059.3 m	**CL-20:** CH str

CL-20 marker vibration (1602cm^{-1}; ONO asymmetric stretching)) is marked in red, HMX marker vibration (1417 cm^{-1}, CH_2 wagging) is marked in green. **Notes:** vs – very strong, s – strong, m – medium, w – weak, vw – very weak; asym – asymmetric, sym – symmetric, bend – bending, rock – rocking, tors – torsion, str – stretching, twist – twisting, wag – wagging

3.6.3 Calculation of Approximated 3D Normal Coordinates

In a first step x-, y- and z-coordinates from all atoms which are involved mainly at the investigated molecular vibration were extracted from crystallographic data published by Bolton et al.[13] These atoms are depicted and numbered in Figure 3.19. As already described within the paper, the N atoms of the NO_2 functional groups of CL-20 oscillate oppositely to the O atoms. Furthermore, the atomic derivations from their equilibrium position are the same for all involved NO_2 groups. Thus, the vectors $\vec{q}_{m;\beta\text{-}CL\text{-}20}$, respectively $\vec{q}_{m;\gamma\text{-}CL\text{-}20}$, describe approximately the oscillation of the NO_2 group. These vectors are presented as yellow arrows in Figure 3.19. The directions of these vectors correspond to the direction of movement of the

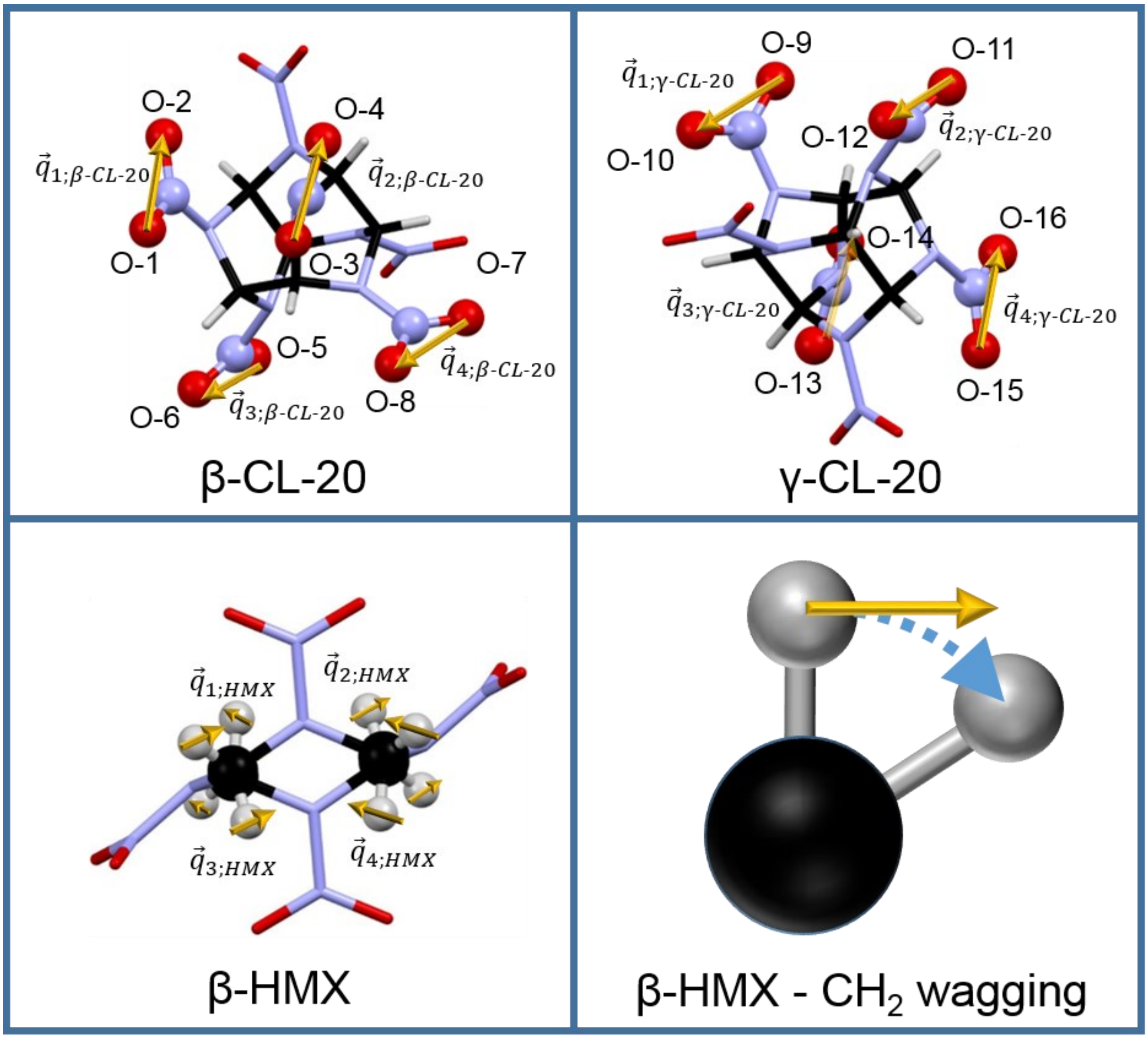

Figure 3.19. Atoms involved in the investigated normal modes. Yellow arrows represent vectors describing approximately oscillation directions of single functional groups.

individual N atoms during the oscillation. These directions were determined by simulated molecular vibrations computed with Gaussian 16.

The summation of $\vec{q}_{m;\beta\text{-}CL\text{-}20}$ and $\vec{q}_{m;\gamma\text{-}CL\text{-}20}$ leads to the approximated normal coordinates $\vec{q}_{0;\beta\text{-}CL\text{-}20}$ and $\vec{q}_{0;\gamma\text{-}CL\text{-}20}$ of the ONO asymmetric stretching vibrations of the CL-20 polymorphs. Since the Cartesian coordinates of crystallographic data do not correspond with that of the Raman scattering system, they had to be transformed. Calculations and number values of $\vec{q}_{0;\beta\text{-}CL\text{-}20}$ and $\vec{q}_{0;\gamma\text{-}CL\text{-}20}$ are summed up in Table 3.6 respectively Table **3.7**.

Table 3.6. Calculation and number values of $\vec{q}_{0;\beta\text{-}CL\text{-}20}$

β-CL-20					
O-1		**O-2**		$\vec{q}_{1;\beta\text{-}CL\text{-}20}$	
x	12.245	**x**	14.052	**x**	1.807
y	6.907	**y**	5.850	**y**	-1.057
z	-4.246	**z**	-3.616	**z**	0.630
O-3		**O-4**		$\vec{q}_{2;\beta\text{-}CL\text{-}20}$	
x	11.561	**x**	13.450	**x**	1.889
y	9.040	**y**	8.479	**y**	-0.561
z	-1.344	**z**	-0.427	**z**	0.917
O-5		**O-6**		$\vec{q}_{3;\beta\text{-}CL\text{-}20}$	
x	9.328	**x**	8.866	**x**	-0.462
y	2.188	**y**	3.918	**y**	1.730
z	-2.549	**z**	-3.797	**z**	-1.248
O-7		**O-8**		$\vec{q}_{4;\beta\text{-}CL\text{-}20}$	
x	9.420	**x**	8.725	**x**	-0.695
y	5.985	**y**	7.270	**y**	1.285
z	1.867	**z**	0.255	**z**	-1.612
$\vec{q}_{0;\beta\text{-}CL\text{-}20}$		**crystal axis**	**projection**	$\vec{q}_{0;\beta\text{-}CL\text{-}20}$ **(in Raman scattering system)**	
x	2.539	**a**	**z → x**	**x**	1.397
y	1.397	**b**	**x → y**	**y**	-1.313
z	-1.313	**c**	**y → z**	**z**	2.539

Table 3.7. Calculation and number values of $\vec{q}_{0;\gamma\text{-}CL\text{-}20}$

γ-CL-20					
O-9		**O-10**		$\vec{q}_{1;\gamma\text{-}CL\text{-}20}$	
x	8.129	**x**	7.427	**x**	-0.702
y	3.647	**y**	4.858	**y**	1.211
z	0.511	**z**	-1.172	**z**	-1.683
O-11		**O-12**		$\vec{q}_{2;\gamma\text{-}CL\text{-}20}$	
x	7.479	**x**	7.018	**x**	-0.461
y	6.018	**y**	7.748	**y**	1.730
z	3.797	**z**	2.549	**z**	-1.248
O-13		**O-14**		$\vec{q}_{3;\gamma\text{-}CL\text{-}20}$	
x	2.896	**x**	4.785	**x**	1.889
y	1.457	**y**	0.896	**y**	-0.561
z	0.427	**z**	1.344	**z**	0.917
O-15		**O-16**		$\vec{q}_{4;\gamma\text{-}CL\text{-}20}$	
x	2.293	**x**	4.100	**x**	1.807
y	4.086	**y**	3.029	**y**	-1.057
z	3.616	**z**	4.246	**z**	0.630
$\vec{q}_{0;\gamma\text{-}CL\text{-}20}$		**crystal axis**	**projection**	$\vec{q}_{0;\gamma\text{-}CL\text{-}20}$ **(in Raman scattering system)**	
x	2.533	**a**	**z → x**	x	1.323
y	1.323	**b**	**x → y**	y	-1.384
z	-1.384	**c**	**y → z**	z	2.533

In case of the HMX CH_2 wagging vibration the path which is covered by the H is a circular segment around the central C atom. This movement can be described mathematically by a partially rotation of a plane defined by C and H atoms of a CH_2 functional group around the C atom. Thus the direction of this movement can be expressed approximately by the normal vector $\vec{q}_{m;HMX}$ of this plane at the equilibrium position (Figure 3.19, bottom right). The direction of these vectors and thus their algebraic signs are depicted in Figure 3.19 (bottom left). Here again the summation of $\vec{q}_{m;HMX}$ gives the approximated normal coordinate $\vec{q}_{0;HMX}$ of the HMX CH_2 wagging vibration. Since HMX molecules in β conformation appear as image and mirror image inside the CL-20/HMX co-crystal $\vec{q}_{0;HMX}$ has to be split into $\vec{q}_{0;HMX-1}$ and $\vec{q}_{0;HMX-2}$. The calculation and the number values of $\vec{q}_{0;HMX-1}$ and $\vec{q}_{0;HMX-2}$ can be found in Table 3.8 and Table 3.9. The approximated normal coordinate of both HMX conformations can be expressed as the average of $\vec{q}_{0;HMX-1}$ and $\vec{q}_{0;HMX-1}$:

Table 3.8. Calculation and number values of $\vec{q}_{0;HMX-1}$

β-HMX-1 (along b-axis)			
$\vec{q}_{1;HMX-1}$		$\vec{q}_{2;HMX-1}$	
x	-0.293	x	0.324
y	-0.531	y	0.444
z	0.795	z	0.835
$\vec{q}_{3;HMX-1}$		$\vec{q}_{4;HMX-1}$	
x	0.324	x	-0.293
y	0.444	y	-0.531
z	0.835	z	0.795
$\vec{q}_{0;HMX-1}$		**crystal axis**	**projection**
x	1.234	**a**	**z → x**
y	1.950	**b**	**x → y**
z	0.080	**c**	**y → z**
$\vec{q}_{0;HMX-1}$ **(in Raman scattering system)**			
x	0,080		
y	1,234		
z	1,950		

Table 3.9. Calculation and number values of $\vec{q}_{0;HMX-1}$

β-HMX-2 (along b-axis)			
$\vec{q}_{1;HMX-2}$		$\vec{q}_{2;HMX-2}$	
x	0.293	x	-0.324
y	0.531	y	-0.444
z	-0.795	z	-0.835
$\vec{q}_{3;HMX-2}$		$\vec{q}_{4;HMX-2}$	
x	-0.324	x	0.293
y	-0.444	y	0.531
z	-0.835	z	-0.795
$\vec{q}_{0;HMX-2}$		**crystal axis**	**projection**
x	1.234	**a**	**z → x**
y	1.950	**b**	**x → y**
z	0.080	**c**	**y → z**
$\vec{q}_{0;HMX-2}$ **(in Raman scattering system)**			
x	1.950		
y	0.080		
z	1.234		

The approximated normal coordinate of both HMX conformations can be expressed as the average of $\vec{q}_{0;HMX-1}$ and $\vec{q}_{0;HMX-1}$:

$$\vec{q}_{0;\beta\text{-}HMX} = \frac{1}{2}\left(\frac{\sum_{m=1}^{4}\vec{q}_{m;\beta\text{-}HMX-1}}{n_{\beta-HMX-1}} + \frac{\sum_{m=1}^{4}\vec{q}_{m;\beta\text{-}HMX-2}}{n_{\beta-HMX-2}}\right) = \begin{pmatrix}1.950\\0.080\\1.234\end{pmatrix}. \qquad \text{Eq. 3.11}$$

In order to ensure a comparability of the approximated normal modes, $\vec{q}_{0;\beta\text{-}CL\text{-}20}$, $\vec{q}_{0;\gamma\text{-}CL\text{-}20}$ and $\vec{q}_{0;\beta\text{-}HMX}$ are finally standardized. The standardization of the approximated normal mode vectors is depicted in Table 3.10.

Table 3.10. Standardization of approximated normal mode vectors

Standardization of $\vec{q}_{0;\beta\text{-}HMX}$				
$\vec{q}_{0;\beta\text{-}CL-20}$			**standardized $\vec{q}_{0;\beta\text{-}CL-20}$**	
x	1.397	**factor:**	**x**	0.44
y	-1.313	3.182	**y**	-0.41
z	2.539		**z**	0.80
Standardization of $\vec{q}_{0;\beta\text{-}HMX}$				
$\vec{q}_{0;\gamma\text{-}CL\text{-}20}$			**standardized $\vec{q}_{0;\gamma\text{-}CL\text{-}20}$**	
x	1.323	**factor:**	**x**	0.42
y	-1.384	3.175	**y**	-0.44
z	2.533		**z**	0.80
Standardization of $\vec{q}_{0;\beta\text{-}HMX}$				
$\vec{q}_{0;\beta\text{-}HMX}$			**standardized $\vec{q}_{0;\beta\text{-}HMX}$**	
x	1.950	**factor:**	**x**	0.84
y	0.080	2.309	**y**	0.03
z	1.234		**z**	0.53

3.7 References

1. Aitipamula, S.; Banerjee, R.; Bansal, A. K.; Biradha, K.; Cheney, M. L.; Choudhury, A. R.; Desiraju, G. R.; Dikundwar, A. G.; Dubey, R.; Duggirala, N., Polymorphs, Salts and Cocrystals: What's in a Name? *Cryst. Growth Des.* **2012,** *12* (5), 2147-2152.

2. Braga, D.; Grepioni, F.; Maini, L.; Polito, M., Crystal Polymorphism and Multiple Crystal Forms. In *Molecular networks*, Springer: 2009; pp 87-95.

3. Vishweshwar, P.; McMahon, J. A.; Bis, J. A.; Zaworotko, M. J., Pharmaceutical Co-Crystals. *J. Pharm. Sci.* **2006,** *95* (3), 499-516.

4. Meyer, R.; Köhler, J.; Homburg, A., *Explosives, 6th, completely revised ed*. Wiley-VCH Verlag: 2007.

5. Nielsen, A. T. Caged Polynitramine Compound. US5693794A, 1987.

6. Li, J.; Brill, T. B., Nanostructured Energetic Composites of CL-20 and Binders Synthesized by Sol Gel Methods. *Propellants Explos. Pyrotech.* **2006,** *31* (1), 61-69.

7. Bayat, Y.; Zeynali, V., Preparation and Characterization of Nano-CL-20 Explosive. *J. Energ. Mater.* **2011,** *29* (4), 281-291.

8. Guo, X.; Ouyang, G.; Liu, J.; Li, Q.; Wang, L.; Gu, Z.; Li, F., Massive Preparation of Reduced-Sensitivity Nano CL-20 and Its Characterization. *J. Energ. Mater.* **2015,** *33* (1), 24-33.

9. Yang, Z.; Ding, L.; Wu, P.; Liu, Y.; Nie, F.; Huang, F., Fabrication of RDX, HMX and CL-20 Based Microcapsules Via In Situ Polymerization of Melamine–Formaldehyde Resins with Reduced Sensitivity. *Chem. Eng. J.* **2015,** *268*, 60-66.

10. Millar, D. I.; Maynard-Casely, H. E.; Allan, D. R.; Cumming, A. S.; Lennie, A. R.; Mackay, A. J.; Oswald, I. D.; Tang, C. C.; Pulham, C. R., Crystal Engineering of Energetic Materials: Co-Crystals of CL-20. *CrystEngComm* **2012,** *14* (10), 3742-3749.

11. Zhang, C.; Xue, X.; Cao, Y.; Zhou, J.; Zhang, A.; Li, H.; Zhou, Y.; Xu, R.; Gao, T., Toward Low-Sensitive and High-Energetic Co-Crystal II: Structural, Electronic and Energetic Features of CL-20 Polymorphs and the Observed CL-20-Based Energetic–Energetic Co-Crystals. *CrystEngComm* **2014,** *16* (26), 5905-5916.

12. Bolton, O.; Matzger, A. J., Improved Stability and Smart-Material Functionality Realized in an Energetic Cocrystal. *Angewandte Chemie* **2011,** *123* (38), 9122-9125.

13. Bolton, O.; Simke, L. R.; Pagoria, P. F.; Matzger, A. J., High Power Explosive with Good Sensitivity: A 2:1 Cocrystal of CL-20:HMX. *Cryst. Growth Des.* **2012,** *12* (9), 4311-4314.

14. Ghosh, M.; Sikder, A. K.; Banerjee, S.; Gonnade, R. G., Studies on CL-20/HMX (2: 1) Co-crystal: A New Preparation Method, Structural and Thermo Kinetic Analysis. *Cryst. Growth Des.* **2018,** *18* (7), 3781-3793.

15. Klaumünzer, M.; Hübner, J.; Spitzer, D., Production of Energetic Nanomaterials by Spray Flash Evaporation. *World Academy of Science, Engineering and Technology, International Journal of Chemical, Molecular, Nuclear, Materials and Metallurgical Engineering* **2016,** *10* (9), 1079-1083.

16. An, C.; Li, H.; Ye, B.; Wang, J., Nano-CL-20/HMX Cocrystal Explosive for Significantly Reduced Mechanical Sensitivity. *J. Nanomater.* **2017,** *2017*.

17. Liu, Z.; Wu, Q.; Zhu, W.; Xiao, H., Insights into the Roles of Two Constituents CL-20 and HMX in the CL-20:HMX Cocrystal at High Pressure: A DFT-D Study. *RSC Advances* **2015,** *5* (43), 34216-34225.

18. Klaumünzer, M.; Pessina, F.; Spitzer, D., Indicating Inconsistency of Desensitizing High Explosives Against Impact through Recrystallization at the Nanoscale. *J. Energ. Mater.* **2016**, 1-10.

19. Hübner, J.; Klaumünzer, M.; Comet, M.; Martin, C.; Vidal, L.; Schäfer, M.; Kryschi, C.; Spitzer, D., Insights into Combustion Mechanisms of Variable Aluminum-Based Iron Oxide/-Hydroxide Nanothermites. *Combust. Flame* **2017,** *184*, 186-194.

20. Klaumünzer, M.; Hübner, J.; Spitzer, D.; Kryschi, C., Surface Functionalization and Electrical Discharge Sensitivity of Passivated Al Nanoparticles. *ACS Omega* **2017,** *2* (1), 52-61.

21. Trautmann, S.; Aizpurua, J.; Götz, I.; Undisz, A.; Dellith, J.; Schneidewind, H.; Rettenmayr, M.; Deckert, V., A Classical Description of Subnanometer Resolution by Atomic Features in Metallic Structures. *Nanoscale* **2017,** *9* (1), 391-401.

22. Deckert-Gaudig, T.; Taguchi, A.; Kawata, S.; Deckert, V., Tip-Enhanced Raman Spectroscopy–From Early Developments to Recent Advances. *Chem. Soc. Rev.* **2017**.

23. Roth, R. M.; Panoiu, N. C.; Adams, M. M.; Osgood, R. M.; Neacsu, C. C.; Raschke, M. B., Resonant-Plasmon Field Enhancement from Asymmetrically Illuminated Conical Metallic-Probe Tips. *Opt. Express* **2006,** *14* (7), 2921-2931.

24. Pettinger, B.; Domke, K. F.; Zhang, D.; Schuster, R.; Ertl, G., Direct Monitoring of Plasmon Resonances in a Tip-Surface Gap of Varying Width. *Phys. Rev. B: Condens. Matter* **2007,** *76* (11), 113409.

25. Watanabe, H.; Ishida, Y.; Hayazawa, N.; Inouye, Y.; Kawata, S., Tip-Enhanced Near-Field Raman Analysis of Tip-Pressurized Adenine Molecule. *Phys. Rev. B: Condens. Matter* **2004,** *69* (15), 155418-1-155418-11.

26. Ichimura, T.; Watanabe, H.; Morita, Y.; Verma, P.; Kawata, S.; Inouye, Y., Temporal Fluctuation of Tip-Enhanced Raman Spectra of Adenine Molecules. *J. Phys. Chem. C* **2007,** *111* (26), 9460-9464.

27. Deckert-Gaudig, T.; Rauls, E.; Deckert, V., Aromatic Amino Acid Monolayers Sandwiched Between Gold and Silver: A Combined Tip-Enhanced Raman and Theoretical Approach. *J. Phys. Chem. C* **2009,** *114* (16), 7412-7420.

28. Sonntag, M. D.; Klingsporn, J. M.; Garibay, L. K.; Roberts, J. M.; Dieringer, J. A.; Seideman, T.; Scheidt, K. A.; Jensen, L.; Schatz, G. C.; Van Duyne, R. P., Single-molecule tip-enhanced Raman spectroscopy. *J. Phys. Chem. C* **2011,** *116* (1), 478-483.

29. Klingsporn, J. M.; Jiang, N.; Pozzi, E. A.; Sonntag, M. D.; Chulhai, D.; Seideman, T.; Jensen, L.; Hersam, M. C.; Duyne, R. P. V., Intramolecular Insight Into Adsorbate–Substrate Interactions via Low-Temperature, Ultrahigh-Vacuum Tip-Enhanced Raman Spectroscopy. *J. Am. Chem. Soc.* **2014,** *136* (10), 3881-3887.

30. Bailo, E.; Deckert, V., Tip-Enhanced Raman Spectroscopy of Single RNA Strands: Towards a Novel Direct-Sequencing Method. *Angew. Chem. Int. Ed.* **2008,** *47* (9), 1658-1661.

31. Deckert-Gaudig, T.; Pichot, V.; Spitzer, D.; Deckert, V., High-Resolution Raman Spectroscopy for the Nanostructural Characterization of Explosive Nanodiamond Precursors. *ChemPhysChem* **2017,** *18* (2), 175-178.

32. Hübner, J.; Pichot, V.; Guillevic, M.; Spitzer, D., Structure Investigation of Energetic Nanocomposites Produced by Spray Flash Evaporation via AFM-TERS. In *ICORS*, South Korea, 2018.

33. Risse, B.; Hassler, D.; Spitzer, D. Preparation of Nanoparticles by Flash Evaporation. US20150000846A1, 2015.

34. Risse, B.; Spitzer, D.; Hassler, D.; Schnell, F.; Comet, M.; Pichot, V.; Muhr, H., Continuous Formation of Submicron Energetic Particles by the Flash-Evaporation Technique. *Chem. Eng. J.* **2012,** *203*, 158-165.

35. Risse, B.; Schnell, F.; Spitzer, D., Synthesis and Desensitization of Nano-β-HMX. *Propellants Explos. Pyrotech.* **2014,** *39* (3), 397-401.

36. Sève, A.; Pichot, V.; Schnell, F.; Spitzer, D., Trinitrotoluene Nanostructuring by Spray Flash Evaporation Process. *Propellants Explos. Pyrotech.* **2017,** *42* (9), 1051-1056.

37. Blas, L.; Klaumünzer, M.; Pessina, F.; Braun, S.; Spitzer, D., Nanostructuring of Pure and Composite-Based K6 Formulations with Low Sensitivities. *Propellants Explos. Pyrotech.* **2015,** *40* (6), 938-944.

38. Pichot, V.; Comet, M.; Risse, B.; Spitzer, D., Detonation of Nanosized Explosive: New Mechanistic Model for Nanodiamond Formation. *Diamond Relat. Mater.* **2015,** *54*, 59-63.

39. Spitzer, D.; Risse, B.; Schnell, F.; Pichot, V.; Klaumünzer, M.; Schaefer, M., Continuous Engineering of Nano-Cocrystals for Medical and Energetic Applications. *Sci. Rep.* **2014,** *4*.

40. Thiboutot, S.; Brousseau, P.; Ampleman, G.; Pantea, D.; Cote, S., Potential Use of CL-20 in TNT/ETPE-Based Melt Cast Formulations. *Propellants Explos. Pyrotech.* **2008,** *33* (2), 103-108.

41. Frish, M.; Trucks, G.; Schlegel, H.; Scuseria, G.; Robb, M.; Cheeseman, J.; Scalmani, G.; Barone, V.; Mennucci, B.; Petersson, G., Gaussian 09 (Revision A. 1). *Gaussian Inc.: Wallingford, CT* **2009**.

42. Osmont, A.; Catoire, L.; Gökalp, I.; Yang, V., Ab Initio Quantum Chemical Predictions of Enthalpies of Formation, Heat Capacities, and Entropies of Gas-Phase Energetic Compounds. *Combust. Flame* **2007,** *151* (1-2), 262-273.

43. Klaumünzer, M.; Distaso, M.; Hübner, J.; Mačković, M.; Spiecker, E.; Kryschi, C.; Peukert, W., ZnO Superstructures Via Oriented Aggregation Initiated in a Block Copolymer Melt. *CrystEngComm* **2014,** *16* (8), 1502-1513.

44. Goede, P.; Latypov, N. V.; Östmark, H., Fourier Transform Raman Spectroscopy of the Four Crystallographic Phases of α, β, γ and ε 2, 4, 6, 8, 10, 12-Hexanitro-2, 4, 6, 8, 10, 12-hexaazatetracyclo-[5.5. 0.05, 9.03, 11]-dodecane (HNIW, CL-20). *Propellants Explos. Pyrotech.* **2004,** *29* (4), 205-208.

45. Ghosh, M.; Venkatesan, V.; Sikder, N.; Sikder, A. K., Quantitative Analysis of α-CL-20 Polymorphic Impurity in ε-CL-20 Using Dispersive Raman Spectroscopy. *Cent. Eur. J. Eenerg. Mat.* **2013,** *10*.

46. Brand, H. V.; Rabie, R. L.; Funk, D. J.; Diaz-Acosta, I.; Pulay, P.; Lippert, T. K., Theoretical and Experimental Study of the Vibrational Spectra of the α, β, and δ Phases of

Octahydro-1, 3, 5, 7-tetranitro-1, 3, 5, 7-tetrazocine (HMX). *The Journal of Physical Chemistry B* **2002,** *106* (41), 10594-10604.

47. Goetz, F.; Brill, T., Laser Raman Spectra of Alpha.-, Beta.-, Gamma.-, and Delta-octahydro-1, 3, 5, 7-tetranitro-1, 3, 5, 7-tetrazocine and Their Temperature Dependence. *J. Phys. Chem.* **1979,** *83* (3), 340-346.

48. Iqbal, Z.; Bulusu, S.; Autera, J. R., Vibrational Spectra of β-Cyclotetramethylene Tetranitramine and some of Its Isotopic Isomers. *J. Chem. Phys.* **1974,** *60* (1), 221-230.

49. Bailo, E.; Deckert, V., Tip-Enhanced Raman Scattering. *Chem. Soc. Rev.* **2008,** *37* (5), 921-930.

50. Hayazawa, N.; Saito, Y.; Kawata, S., Detection and Characterization of Longitudinal Field for Tip-Enhanced Raman Spectroscopy. *Appl. Phys. Lett.* **2004,** *85* (25), 6239-6241.

51. Furukawa, H.; Kawata, S., Local Field Enhancement with an Apertureless Near-Field-Microscope Probe. *Opt. Commun.* **1998,** *148* (4-6), 221-224.

4 Formation Mechanism of Anisotropic RDX/TNT Core/Shell Nanoparticles and their Influence onto Nanodiamond Detonation Syntheses

Since it could be shown that TERS provides new insights into the structure and the surface composition of nanoscale composites, different composite nanoparticles consisting of RDX and TNT with varying mass ratios were analyzed. These so called hexolite mixtures are used as precursor for nanodiamond detonation syntheses. TERS investigations were performed aimed to elucidate the structural composition of the hexolite particles. It could be figured out that the hexolite composite are formed by anisotropic patchy or core/shell nanoparticles with an RDX core and a TNT shell. From these findings, a formation mechanism could be derived allowing a deeper understanding of the kinetics within in the SFE process. More interestingly, since TERS structure determination allowed to link the hexolite precursor structures and arrangements with the resulting nanodiamond sizes, a nanodiamond formation mechanism could be derived.

(This chapter is published at: Hübner, J.; Pichot, V.; Lobry, E.; Deckert-Gaudig, T.; Deckert, V.; Spitzer, D., Formation Mechanism of Anisotropic RDX-TNT Core-Shell Nanoparticles and their Influence onto Nanodiamond Detonation Syntheses, *chemrxiv.org,* **2020**, DOI: 10.26434/chemrxiv.12005625.v1)

4.1 Abstract

Mixtures of RDX and TNT or hexolite mixtures are well known precursors for nanodiamond detonation syntheses. In this study, diverse nanoscale hexolite mixtures varying in mass ratios of RDX and TNT are synthesized via Spray Flash Evaporation. The hexolite mixtures are characterized by confocal Raman spectroscopy and tip-enhanced Raman spectroscopy (TERS) to obtain information about their molecular structure composition. The marker bands of pristine RDX and TNT enable the identification and distinction of both compounds in the Raman spectra. Confocal Raman spectroscopy indicates an intermixture of RDX and TNT molecules on the nanoscale since both marker bands are detected in all spectra. TERS investigations of single hexolite particles reveal that the particle surfaces are mainly composed of TNT. The comparison of confocal Raman and TERS results suggests that (depending on the mass ratio) hexolite particles are either inhomogeneous patchy RDX/TNT nanoparticles or anisotropic RDX/TNT core/shell nanoparticles. A building mechanism to explain the formation/growth of those nanoparticles is derived from the spectroscopic data and the dynamics of the SFE process. Finally, a correlation between the TNT shell thickness, the symmetry of the anisotropic hexolite precursor nanoparticles, and the resulting nanodiamond sizes is discussed in detail.

4.2 Introduction

Since the first detonation synthesis of nanodiamonds in the USSR back in the 1960s, nanodiamonds have become a focal point of interest in various fields of science and industries.[1-2] Functionalized nanodiamonds found their use *inter alia* in biomedical approaches as non-toxic compounds for biomedical imaging or as drug and gene delivery agents.[3-8] In addition to the medical approaches, nanodiamonds are used in electronic, chemical, material and energetic applications.[9-13] Probably due to the broad field of application and the constantly growing demand for nanodiamonds, research increasingly aims at gaining insights into the mechanism of nanodiamond formation in detonation syntheses.[14-22] A detailed knowledge of the building mechanism is crucial for the adaption of nanodiamond sizes and size distribution associated with their application. Furthermore, especially the structure of the precursor material influences strongly the resulting nanodiamonds. Pichot *et al.* demonstrated that nanoscale RDX and TNT (hexolite) precursor particles result in the formation of nanodiamonds characterized by smaller mean sizes and narrower size distribution as obtained by employing micron sized precursor materials.[23-24] Using nanostructured RDX and TNT precursor particles, they obtained nanodiamonds defined by particle mean sizes between 2.8 nm - 4.2 nm depending on the precursor compositions. Since the precursor structure affects strongly the resulting nanodiamonds different nanoscale hexolite mixtures of various RDX and TNT mass ratios are investigated in this study. All presented nano hexolites were produced by Spray Flash Evaporation (SFE). This technique allows the continuous production of organic submicron- and nanoparticles.[25-26] During the SFE process a preheated and pressurized solution containing one (or more) different components is sprayed through a hollow cone nozzle into a permanently evacuated reaction chamber. The strong pressure and temperature difference in front and behind the nozzle implement an immediate evaporation of the dissolved micro droplets resulting in the release of submicron or nanoparticles. Depending on the composition of the dissolved precursors a huge variety of submicron or nanoscale particles can be obtained.[23-24, 26-32]

However, the characterization of SFE-produced hexolite composites turned out to be quite difficult using common measurement methods for several reasons. On the one hand, electron microscopy and energy dispersive X-ray spectroscopy failed to determine the structure and composition of single hexolite particles although these techniques allow structure analysis of other energetic materials.[33] Due to the thermal instability of RDX and TNT, hexolite, nanoparticles tend to dissociate under the electron beam. Other standard methods like infrared and far-field Raman spectroscopy or X-ray diffraction may provide molecular and crystallographic information but due to the lack of an adequate sensitivity and resolution, the characterization of single nanoparticles remain impossible. Furthermore, X-ray photoelectron spectroscopy (XPS) failed to investigate structures and chemical compositions of SFE-produced hexolite mixtures since nanostructured TNT sublimates rapidly under the high vacuum conditions of XPS. Thus, AFM-based tip-enhanced Raman spectroscopy (TERS) was chosen for hexolite nanoparticle characterization since it provides ultrahigh sensitivity and spatial resolution at a low energetic load on the sample (compared to electron microscopy methods). In AFM-TERS a common cantilever tip is coated with silver (or gold) nanoparticle and irradiated with a laser wavelength that matches the plasmon resonance of the nanoparticles. The incident laser light causes a collective oscillation of the conductive electrons within the silver nanoparticle. This so called localized surface plasmon resonance (LSPR) leads to an enhancement of the electrical field close to the silver particle surface, which rapidly decays within a few nanometers.[34-37] The strong field enhancement enables spectroscopic investigations of nanoparticles, molecular monolayers and even single molecules.[32-33, 38-44] Furthermore, Deckert-Gaudig et al. successfully analyzed hexolite RDX/TNT core/shell nanoparticles with TERS.[44] In this contribution, the synthesis and characterization of diverse SFE produced anisotropic RDX/TNT core/shell nanoparticles and inhomogeneous RDX/TNT nanoparticles are presented. Furthermore, a building mechanism of these nanoparticles including the spectroscopic data and the dynamics of the SFE process is proposed. Finally, the influence of the precursor structure onto the resulting nanodiamonds is discussed in detail.

4.3 Experimental Section

4.3.1 Chemicals

1,3,5-Trinitro-1,3,5-triazine (RDX; M = 222.12 g/mol) and 2-Methyl-1,3,5-trinitrobenzene (TNT; M = 227.13 g/mol) were purchased by EURENCO (Massy, France). Both explosives were dried in a vacuum drying oven for 6h at 50 °C before further use. Acetone (for HPLC, ≥99.9%) was sourced by Sigma-Aldrich (Munich, Germany) and used without further purification.

4.3.2 Production of Hexolite Mixtures

Diverse hexolite mixtures were produced via Spray Flash Evaporation (SFE) which is described in detail elsewhere.[25, 29] A flow chart of the SFE setup as well as a photography of the used SFE reactor are depicted in Figure 4.1. For hexolite mixture production 2 wt.% solutions of various RDX and TNT mass fractions in 500 mL acetone were prepared. Thus, the mass of RDX plus TNT amounted 8.2 g in each solution. The amounts of RDX and TNT for each hexolite mixture solution are summed up in Table 4.1.

Table 4.1. Mass and amount of substance of RDX and TNT for each hexolite mixture

hexolite mass fraction (RDX/TNT)	**RDX**		**TNT**	
	mass / g	**amount of substance / mmol**	**mass / g**	**amount of substance / mmol**
80/20	6.5	29.3	1.7	7.3
60/40	4.9	22.1	3.3	14.3
40/60	3.3	14.7	4.9	21.6
20/80	1.7	7.5	6.5	28.6

Each solution was given into the solution storage tank of the vertical SFE – reactor. A pressure of 40 bar was applied onto the solution storage tank. Afterwards the RDX-TNT-acetone solutions were sprayed through a preheated ruby hollow cone nozzle (160°C) with a diameter of 200 µm into the permanently evacuated atomization chamber. During the spraying, the

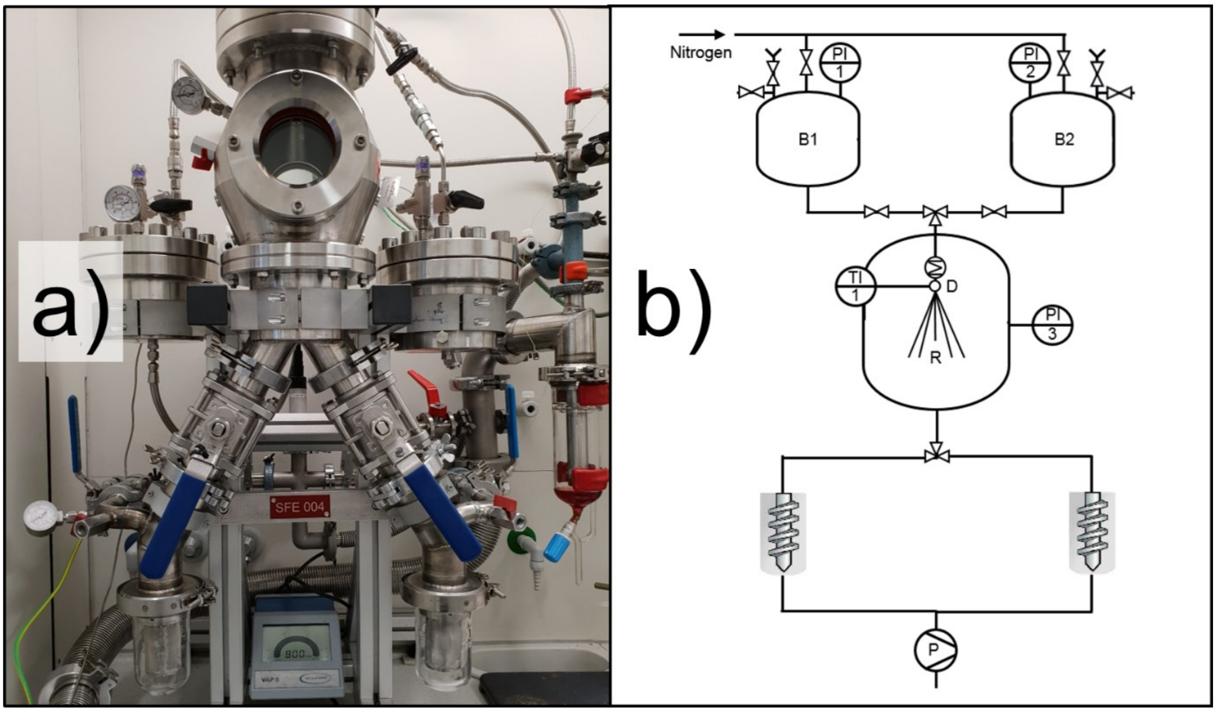

Figure 4.1. a) Photography of a medium sized vertical SFE - reactor. **b)** Flow-chart of SFE setup. Final product is collected with axial cyclones (marked in grey). B1, B2: solvent and solution tank; R: reaction chamber; D: hollow cone nozzle, P: vacuum pump; PI: pressure sensor; TIC: temperature sensor.

pressure inside the reaction chamber amounted 2 – 5 mbar. Final hexolite products were collected as white-yellowish powders whereby the yellowish shade increases slightly with the amount of TNT. In Table 4.1 the hexolite mixtures are named by the mass ratios of RDX and TNT and the first number gives the percentage of RDX and the second one the percentage of TNT (e.g. 80/20).

4.3.3 Production of Physically Mixed Hexolite Reference Samples

A reference sample using a 60/40 hexolite mixture was prepared through physical mixing. 60 mg of RDX nanoparticles and 40 mg of TNT nanoparticles were transferred into a porcelain mortar and mixed carefully and pressureless with a porcelain pestle. Pure RDX and TNT nanoparticles were also prepared via SFE. In a first step 8.2 g (36.7 mmol) RDX, respectively 8.2 g (35.9 mmol) TNT were solved in acetone in order to obtain 4 wt.% solutions. Recrystallization of pure RDX and pure TNT were performed using the same SFE set-up and settings as described above.

4.3.4 TERS Tip Preparation

AppNano ACCESS-NC AFM-probes (Mountain View, USA) were used for TERS experiments. AFM probes were mounted onto a 30° prism template to generate a perpendicular arrangement between the tip and the sputtering target, since the tips are mounted onto the cantilever at an angle of 120° (Figure 4.2.a). The prism template was inserted into the vacuum chamber of an HHV Auto 306 (Bangalore, India) argon plasma sputtering device at a distance of 10 cm from the sputtering target. Initially, 5 nm of titanium were deposited onto the tips with a deposition rate of 0.5 Å/s. Titanium acts as an adhesive promoter between the native oxide layer of the Si tip and Ag. Afterwards the Si-Ti tips were coated with a 25 nm silver layer (sputtering rate 0.5 Å/s). Finally, the TERS tips were annealed in a muffle furnace for 2.5 min at 320 °C and stored under Ar and used within two days. The SEM image in Figure 4.2.b) shows the successful formation of a single Ag nanoparticle on the tip apex in the described procedure.[32]

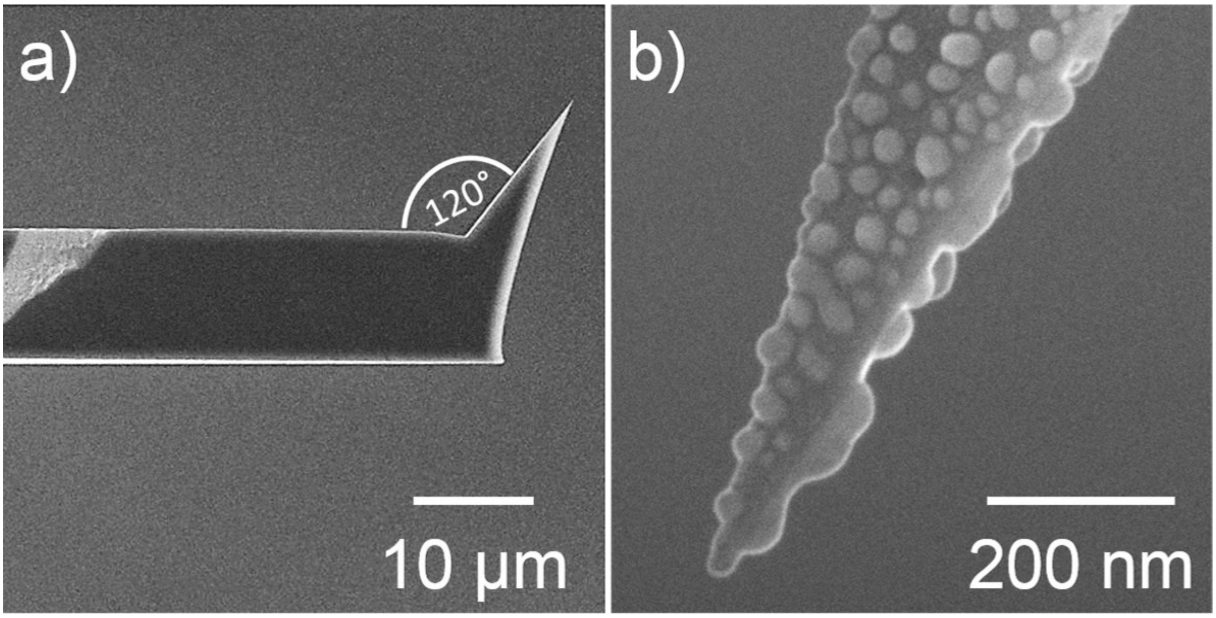

Figure 4.2. a) Pristine AppNano Access-NC AFM probe. The tip is mounted onto the cantilever at an angle of 120°. **b)** Si – tip sputtered with a 5 nm layer of Ti and a 25 nm layer of Ag. After the sputtering process the tips were annealed in a muffle furnace.

4.3.5 Nanodiamond Detonation Syntheses

Each SFE-produced hexolite mixture was pressed to cylinders with lengths and diameters of 15.8 mm at room temperature for 10 minutes. These cylinders were cemented afterwards with pyrotechnic glue. The cylindrical explosive charges were transferred into a water-filled pocket before firing in a detonation tank. Obtained nanodiamonds were dried via rotation evaporation.

4.3.6 Analysis Methods

Confocal far-field Raman spectroscopy investigations were performed with a HORIBA (Kyoto, Japan) LabRam HR evolution confocal Raman microscope. In the experiment a spatula's tip of the diverse hexolite mixtures was applied to a glass slide. Single point spectra were obtained by sample excitation with a linear polarized illumination light from a 532 nm diode laser with an adjusted output power of 13.5 mW at an acquisition time of 3 s per spectrum. Raman mappings across the substrate were recorded with the same laser and output power. The acquisition time was set to 0.5 s per spectrum with a step size of 250 nm for these mappings. The laser light was focused onto the sample through a 100x, 0.9 NA objective. Raman scattered photons were collected with the same objective in back reflection geometry. Scattered light passed an edge filter, a confocal aperture with a diameter adjusted to 100 nm and a diffraction grating with 300 lines/mm before entering a deep cooled CCD camera (- 60°C). Confocal Raman maps were calculated and depicted using LabSpec Spectroscopy Suite 6.4.4. (HORIBA; Kyoto, Japan).

Atomic Force Microscopy (AFM) size distribution measurements of all SFE-produced hexolite mixtures and nanodiamonds were performed with an AIST-NT CombiScope$^{\mathrm{TM}}$-1000SPM Atomic Force Microscope (Novato, USA) in non-contact mode. The amplitude of the cantilever vibration was set to 10 nm. All measurements were performed with AppNano ACCESS-NC AFM-probes (Mountain View, USA). The size of all AFM topographic images was 5 µm x 5 µm with a resolution of 256 x 256 measurements points and a scanning rate of 0.6 Hz. 200 nanoparticles of each SFE-produced hexolite mixture and 200 nanodiamonds of each hexolite precursor were measured. Samples were prepared by depositing a spatula's tip of the diverse hexolite mixtures or nanodiamonds between two 2 cm x 2 cm cover slips. The sample was spread on the glass surface through pressureless rubbing of the two glass slides against each other.

Tip Enhanced Raman Spectroscopy (TERS) surface maps were recorded with a combination of the AFM microscope and the confocal Raman microscope described above. The confocal Raman microscope acts in this combination as light source and spectrometer. All measurements were performed in non-contact AFM mode with an amplitude of 10 nm and samples were illuminated from the below (transmission mode). Incident linear polarized laser light (532 nm) was focused onto the tip with by a 100x, 1.4 NA oil-immersion objective. The precise positioning of the AFM-tip in the focused laser spot was achieved by objective scans perpendicular and parallel towards the AFM-TERS tip. A typical square-shaped TERS surface map consists of 100 (10 x 10) single TERS spectra. The acquisition time was 3 s per measurement point at a laser power on the sample of 54 µW. Step sizes between the measurement points depend on the size and surface area of the investigated nanoparticle and varied between 2-5 nm. The same samples were used for TERS investigations as for AFM size distribution measurements.

High Resolution Transmission Electron Microscopy (HR-TEM) images of obtained nanodiamonds were recorded on a JEOL ARM2000F (Tokio, Japan) microscope with a nominal point resolution of 0.8 Å at Scherzer defocus. The microscope was operated at 200 kV acceleration voltage.

4.4 Results and Discussion

4.4.1 Distinction of RDX and TNT via Far- and Near-Field Raman Spectroscopy

In a first step, far-field Raman spectra of pristine RDX and TNT were recorded to obtain information about the structure composition of hexolite mixtures. Marker bands of each compound were chosen from these spectra. These marker band were detected in wavenumber regions were the other compound did not show a signal. The distinguishability of RDX and TNT molecules was already demonstrated in an earlier work and the same RDX and TNT marker bands were chosen.[44] The RDX marker band at 882 cm^{-1} can be assigned to the ring breathing vibration.[44-47] The TNT marker band between 1358-1371 cm^{-1} can be assigned to three NO_2 symmetric stretching vibrations.[44, 48-49] Figure 4.3 shows the Raman spectra of RDX and TNT with marker bands highlighted in green respectively red. The complete Raman spectra and the assignment are given in the Supporting Information. In confocal far-field Raman experiments maps were recorded of each hexolite mixture to obtain a first insight into the structure compositions. TERS was performed to investigate morphology, size and structure composition of the hexolite mixtures on the nanoscale. Due to its surface sensitivity, TERS is perfectly suited for surface characterization of composite nano materials as already demonstrated on 60/40 hexolite nanoparticles and on CL-20/HMX nano co-crystals in previous studies.[32, 44] TERS surface maps each containing 100 TERS spectra (10 x 10 spectra) with step sizes between 2 nm -5 nm (depending on the nanoparticle size) were recorded. 15 nanoparticles of each hexolite mixture were investigated. Thus, differences between far-field Raman spectra and TERS spectra of hexolite nanoparticles allowed to conclude on the distinct arrangement of RDX and TNT molecules in the particles.

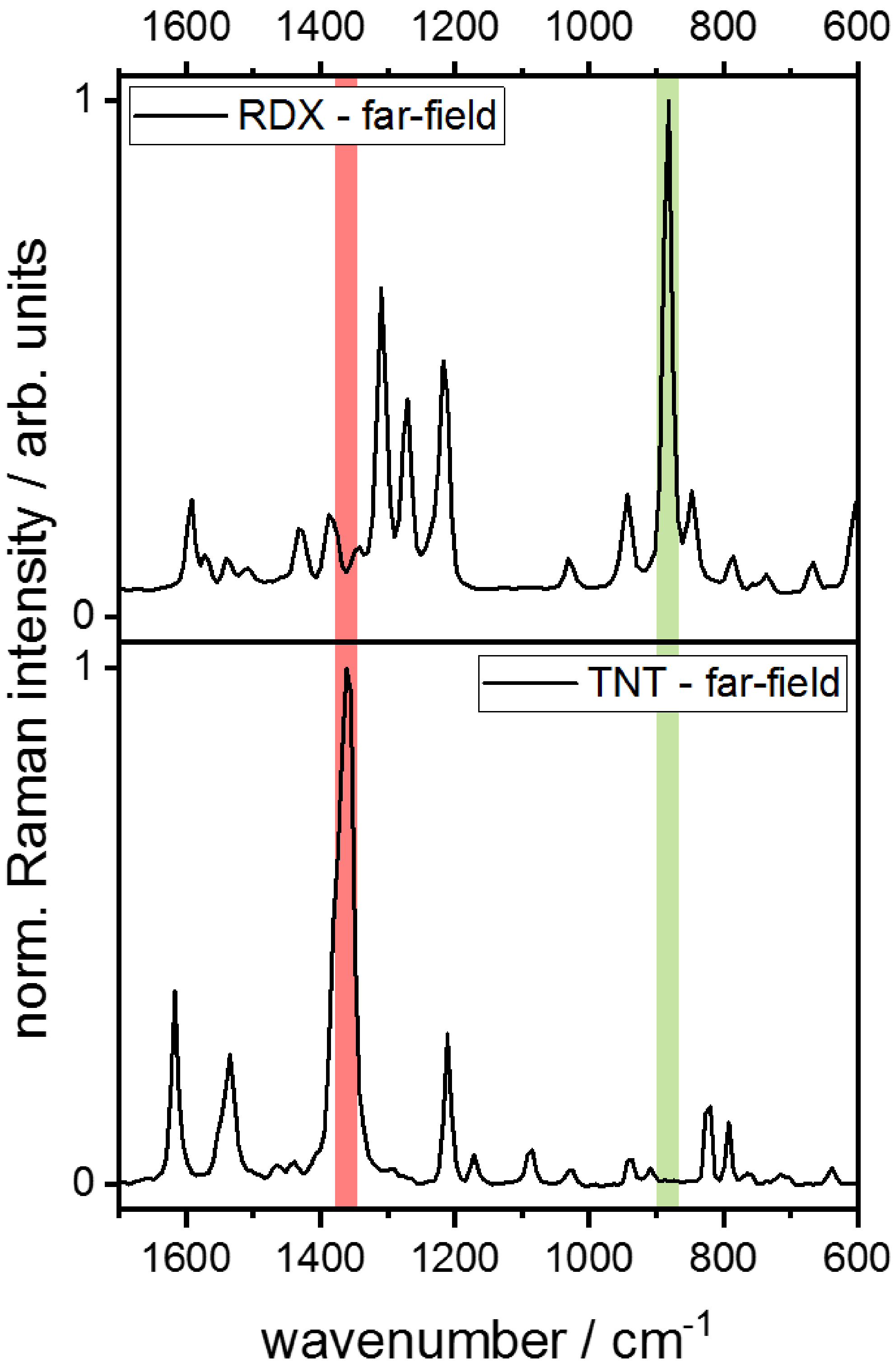

Figure 4.3. Far-field Raman spectra of RDX and TNT nanoparticles in the range between 1700 cm^{-1} and 600 cm^{-1}. The RDX marker band (882 cm^{-1}; ring breathing) is highlighted in green. The TNT marker band (1358 cm^{-1} - 1371 cm^{-1}; three NO_2 symmetric stretching vibrations) is marked in red.

4.4.2 Physically Mixed 60/40 Hexolite

Physically mixed 60/40 hexolite (p-60/40) was received as white-yellowish powder. Confocal Raman maps of this powder were recorded to provide insight into the intermixture of RDX and TNT nanoparticles. Figure 4.4 shows a microscope image and the corresponding confocal Raman map of p-60/40. These confocal Raman maps were recorded pixel-wise. The Raman intensity of the RDX marker band in the single spectra is shown in green and the Raman intensity of TNT is shown in red. If both marker bands were detected simultaneously, the band intensities are superimposed and appear as light green over yellow to dark orange pixels. Evidently, the confocal Raman maps demonstrate that RDX and TNT nanoparticles consist of microscale agglomerates without a further intermixture on the nanoscale. In order to visualize this finding Figure 4.4.a) und Figure 4.4.b) present only the intensity of RDX respectively TNT marker band. Even though confocal far-field Raman maps already exclude a nanoscale intermixture of RDX and TNT nanoparticles, TERS measurements were performed on single nanoparticles to verify this result and to receive reference data for TERS investigation of SFE produced nano hexolite mixtures. As expected, only pure RDX and pure TNT nanoparticles could be identified in the TERS spectra. Generally, TERS spectra differ from far-field Raman spectra by several features. Thus, slight shifts of band positions and differences in Raman intensities of same vibrational modes are evident in TERS spectra (Figure 4.4). are evident in TERS spectra (Figure 4.4). Since TERS is a surface sensitive detection technique, the orientation of molecules on the probed particles plays an important role. The surface molecules are supposed to have different molecular environments due to the crystal symmetry break at the particle's surface. This environmental change is associated with a change of intermolecular interactions.[32] The different molecular arrangements result in slight changes of the molecular energy levels and thus, molecular vibrations can be detected with slightly shifted band positions in TERS spectra.[50] This phenomenon is comparable with Raman frequency shifts in Raman spectra of different organic crystal polymorphs.[51-53] Furthermore, interactions between surface molecules and the silver coated tip may contribute to a band position shift as described above.[38, 54] In contrast, the far-field Raman spectra of the bulk material contain averaged information from all molecule orientations. Discrepancies of Raman intensities of same vibrational modes between far- and near-field Raman spectra can be explained by the orientation between illuminated molecules towards the electric field vector of the enhanced electric field. In general normal modes appear more intense if the vibrational direction and the electric field vector are

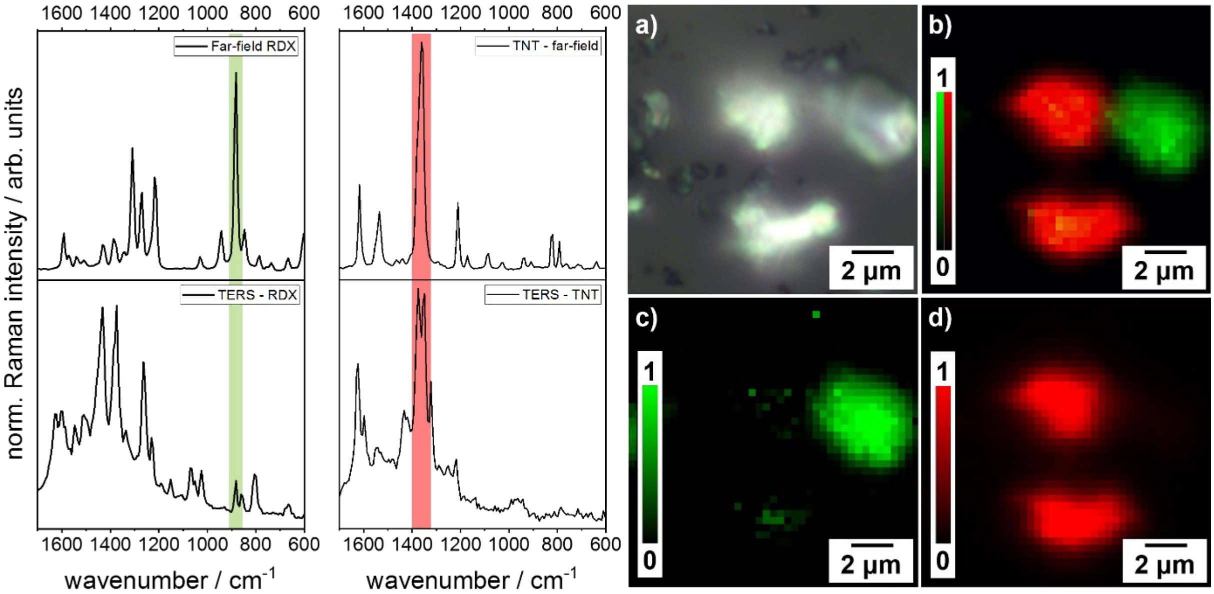

Figure 4.4. Left: Far-field Raman and TERS spectra of pristine RDX and TNT. **Right:** Confocal Raman microscopy maps of physically mixed 60/40 hexolite particles. A better comparability of the Raman intensities was achieved by normalization. **a)** Microscope image of p-60/40 nano hexolite particles. **b)** Corresponding confocal Raman map of superimposed RDX (882 cm^{-1}; ring breathing, NNO_2 stretching) and TNT (1358 cm^{-1} - 1371 cm^{-1}; three NO_2 symmetric stretching vibrations) marker band Raman intensities. **c)** Confocal Raman map of RDX marker band Raman intensities. **d)** Confocal Raman map of TNT marker band Raman intensities.

aligned parallel.[35, 40, 55-56] However, TERS spectra of p-60/40 nanoparticles contain all relevant peaks of RDX or TNT and can be consequently easily assigned to the specific compound (Figure 4.4). The RDX marker band is detected between 870-890 cm^{-1} in TERS spectra of RDX nanoparticles. Also, the TNT marker band is well identifiable in a wavenumber range between 1350 cm^{-1} and 1375 cm^{-1}. The shape of this broad peak can differ in TERS spectra compared to far-field Raman spectra since it contains several symmetric NO_2 stretching vibrations which can be enhanced differently due to specific orientations as described above. In contrast to nano hexolite mixtures produced by SFE only six particles p-60/40 were investigated by TERS, since a molecular intermixture of RDX and TNT could be already excluded by confocal Raman microscopy. Thus, a statistical more reliable investigation was not necessary at this point. However, three RDX and three TNT nanoparticles could be clearly identified by TERS.

4.4.3 80/20 SFE Hexolite Mixture

The ultrafine yellowish 80/20 hexolite powder produced by SFE (SFE-80/20) contains nanoparticles with a mean size of 65.7 nm ± 27.6 nm. The particle mean sizes of all investigated hexolite mixtures were determined via AFM microscopy and are presented in the Supporting Information. In contrast to physically mixed nano hexolite p-60/40 particles, not a single Raman spectrum containing only RDX or TNT signals could be found within SFE-80/20 confocal Raman maps. These measurements reveal that the particles are composed of a RDX/TNT mixture arrangement. The Raman mapping results are given in Figure 4.5. Especially confocal Raman maps showing only RDX and TNT marker band, respectively, (Figure 4.5.c) and d) indicate the presence of either of the compounds. On the other hand, TERS

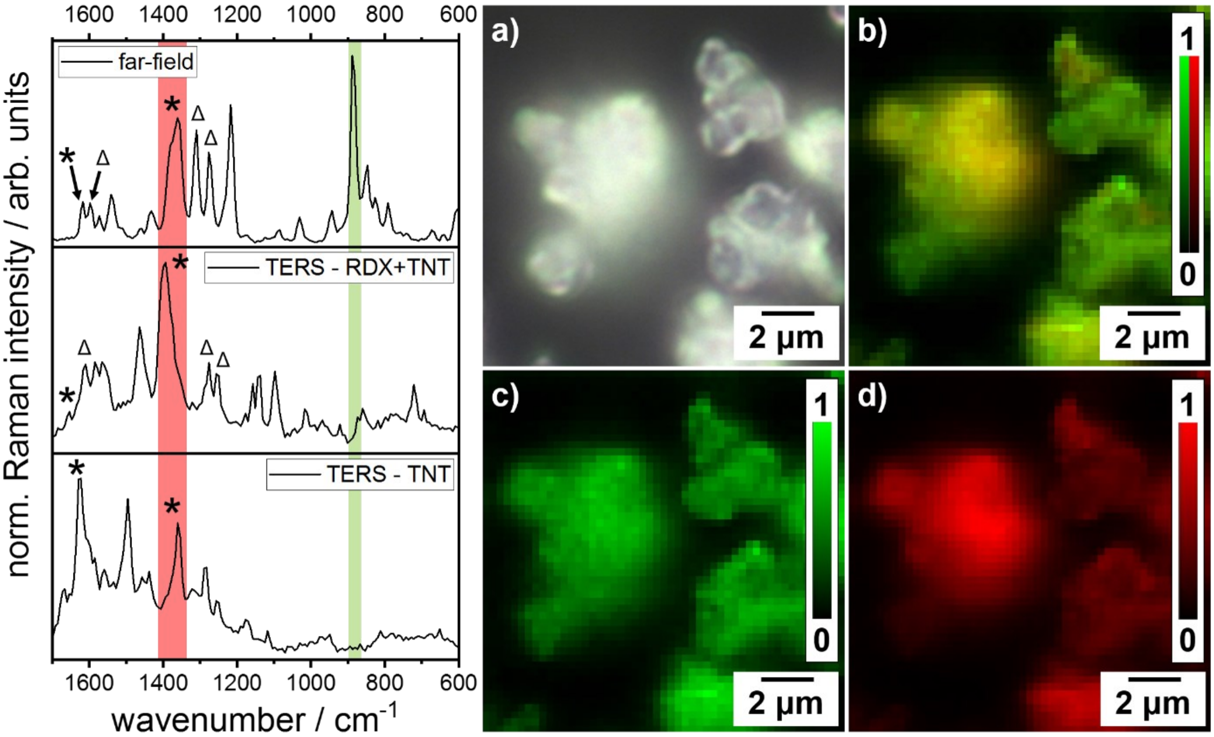

Figure 4.5. Left: Far-field Raman and TERS spectra of 80/20 hexolite powder produced by SFE. Typical TERS spectra show either both RDX (882 cm^{-1}; ring breathing) and TNT (1358 cm^{-1} - 1371 cm^{-1}; three NO_2 symmetric stretching vibrations) marker bands or only the TNT marker band. Δ indicate the N-NO_2 stretching vibration and the NO_2 asymmetric stretching vibration of RDX; * indicate the investigated NO_2 stretching vibrations of TNT. **Right:** Confocal Raman microscopy maps of SFE-80/20. Raman intensities are normalized for a better comparability. **a)** Microscope image of physically SFE-80/20 nano hexolite. **b)** Corresponding confocal Raman map of superimposed RDX and TNT marker band Raman intensities. **c)** Confocal Raman map of RDX marker band Raman intensities. **d)** Confocal Raman map of TNT marker band Raman intensities.

spectra of the SFE-80/20 nanoparticle surface maps indicate either a RDX/TNT mixture or pure TNT. In other words, 13 of 15 TERS surface maps of investigated SFE-80/20 nanoparticle surfaces contain RDX and TNT marker bands whereby 2 of 15 TERS spectra show only the TNT marker band. If the band positions of the NO_2 modes in RDX and TNT in the TERS spectra containing both marker vibrations are compared with those of pristine RDX and TNT in the far-field Raman spectra band position shifts are recognizable (see Table 4.2). Since some NO_2 modes of RDX and TNT overlap in the TERS spectra, only clearly assignable vibrational modes are used for detailed analysis. In RDX two N-NO_2 stretching vibrations are localized at 1270 cm^{-1} and 1309 cm^{-1}, respectively, and one NO_2 is localized at 1592 cm^{-1} in SFE-80/20 far field spectra. The RDX N-NO_2 stretching vibrational modes appear slightly shifted within a wavenumber range between 1256 cm^{-1} and 1283 cm^{-1} respectively 1296 cm^{-1} and 1322 cm^{-1} in SFE-80/20 TERS spectra. The RDX NO_2 asymmetric vibration can be found between 1585 cm^{-1} and 1622 cm^{-1}. The TNT marker band containing three clearly identifiable Raman active NO_2 symmetric stretching vibrations (between 1358 cm^{-1} and 1371 cm^{-1} in far-field Raman spectra) appears shifted between 1354 cm^{-1} and 1399 cm^{-1} in TERS spectra. The TNT NO_2 asymmetric stretching vibration localized at 1617 cm^{-1} in far-field Raman spectra is shifted between 1617 cm^{-1} and 1653 cm^{-1} in near-field TERS spectra. Generally, RDX N-NO_2 vibrations appear with a shift of ± 14 cm^{-1} less shifted than the RDX NO_2 asymmetric stretching vibration, which are detected within + 30 cm^{-1}. The TNT symmetric and asymmetric stretching vibrations show a wavenumber shift of up to 31 cm^{-1} and 36 cm^{-1}, respectively. Described shifts are supposed to appear due to intermolecular interactions between the NO_2 functional groups of RDX on the one hand and NO_2 functional groups of TNT on the other hand. Since the RDX N-NO_2 vibrations seem to be less affected by these interactions than the RDX NO_2 asymmetric stretching vibration, it is supposed that negatively charged oxygen atoms of the RDX NO_2 functional groups interact electrostatically with positively charged nitrogen atoms of the TNT NO_2 functional groups. If the electrostatic interaction would appear between the positively charged nitrogen atoms of the RDX NO_2 functional group and the negatively charged oxygen atoms of the TNT NO_2 functional groups, shifts of RDX N-NO_2 stretching vibrations are expected stronger than shifts of TNT and RDX NO_2 stretching vibrations. The described intermolecular electrostatic interactions force RDX respectively TNT molecules in specific molecular arrangements which differ from their arrangements in the bulk material. Thus, vibrational modes are slightly shifted in the TERS spectra compared to far-field Raman spectra.

Table 4.2. Band positions of NO_2 vibrational modes of RDX and TNT detected in the far-field Raman and TERS spectra

vibration [ref. 44-46, 48-49]	**far-field Raman wavenumber / cm^{-1}**	**TERS wavenumber / cm^{-1}**
RDX: N-NO_2 str	1270	1256 - 1283
RDX: N-NO_2 str	1309	1296 - 1322
RDX: NO_2 asym str	1541	1527 - 1546
RDX: NO_2 asym str	1573	1565 - 1584
RDX: NO_2 asym str	1592	1585 - 1622
TNT: 3x NO_2 sym str	1358 - 1371	1354 - 1399
TNT: NO_2 asym str	1534	1540 - 1546
TNT: NO_2 asym str	1553	1559 - 1572
TNT: NO_2 asym str	1617	1617 - 1653

asym: asymmetric; sym: symmetric; str: stretching; investigated RDX vibrations are marked in green; investigated TNT vibrations are marked in red

Since only RDX/TNT mixed surfaces and pure TNT surfaces could be identified within the TERS spectra, it is concluded that TNT nano-patches grow on RDX particle surfaces in the SFE process. This assumption is supported by the lower solubility of RDX in acetone than TNT. Thus, in SFE RDX nanoparticles are formed followed by the attachment of TNT molecules.[44]

4.4.4 60/40 SFE Hexolite Mixture

60/40 hexolite (SFE-60/40) nanoparticles produced in SFE were collected as a yellowish powder. SFE-60/40 are composed of spherical nanoparticles with a mean size of 32.2 nm ± 12.3 nm. Confocal Raman microscopy of SFE-60/40 points to a similar RDX/TNT mixture found for SFE-80/20. The TERS experiments show that none of the 15 investigated SFE-60/40 nanoparticles surfaces is built up by RDX only. In contrast to SFE-80/20, the TERS surface investigations of SFE-60/40 particles reveal that 10 of 15 nanoparticle surfaces consist of TNT

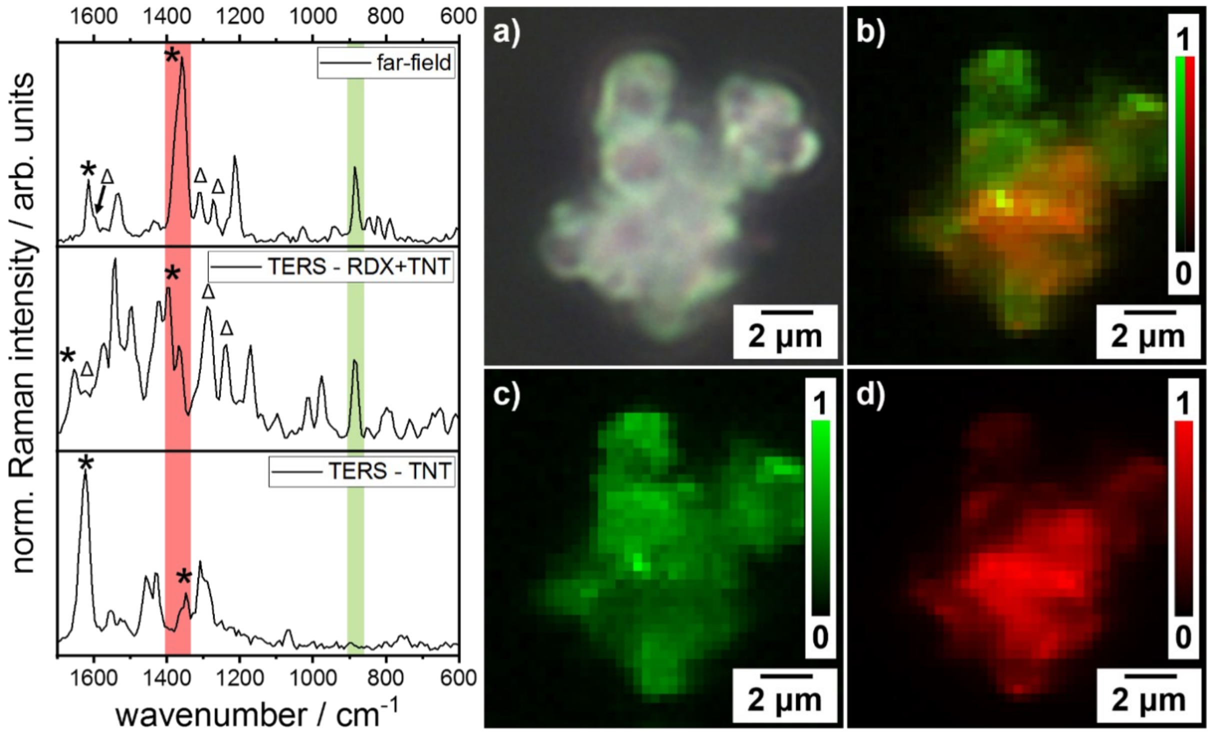

Figure 4.6. Left: Far-field Raman and TERS spectra of 60/40 hexolite powder produced by SFE. Typical TERS spectra show either both RDX (882 cm^{-1}; ring breathing) and TNT (1358 cm^{-1} - 1371 cm^{-1}; three NO$_2$ symmetric stretching vibrations) marker bands or only the TNT marker band. Δ indicate the N-NO$_2$ stretching vibration and the NO$_2$ asymmetric stretching vibration of RDX; * indicate the investigated NO$_2$ stretching vibrations of TNT. **Right:** Confocal Raman microscopy maps of SFE-60/40. Raman intensities are normalized for a better comparability. **a)** Microscope image of physically SFE-60/40 nano hexolite. **b)** Corresponding confocal Raman map of superimposed RDX and TNT marker band Raman intensities. **c)** Confocal Raman map of RDX marker band Raman intensities. **d)** Confocal Raman map of TNT marker band Raman intensities.

only whereas 5 of 15 TERS maps of SFE-60/40 surfaces contain both RDX and TNT marker bands. Similar results were earlier reported by Deckert-Gaudig *et al.* using a different TERS setup.[44] The authors demonstrated that the surfaces of 5 out of 8 SFE-60/40 nanoparticles were dominated by a TNT contribution. RDX and TNT marker bands were found in 3 of 8 SFE-60/40 TERS maps. By comparing far-field Raman and TERS spectra it was concluded that RDX cores were encapsulated by TNT shells. In the case of SFE-60/40 TERS maps showing RDX and TNT marker bands it is supposed that the thickness of the TNT shells is only a few nanometers. Thus, vibrations of TNT surface molecules and RDX molecules close to particle surfaces are identified in the TERS spectra. TERS spectra containing both RDX and TNT marker bands show similar band position shifts as already discussed in the SFE-80/20 section above and point to similar RDX-TNT intermolecular interactions. A typical TERS spectrum containing only TNT signals and a typical TERS spectrum with RDX and TNT marker bands in SFE-60/40 nanoparticles are shown in Figure 4.6.

4.4.5 40/60 SFE Hexolite Mixture

RDX/TNT (SFE-40/60) hexolite particles with a 40/60 weight ratio was produced via SFE as ultrafine yellowish powder. The nanoparticles have a mean size of 29.4 nm ± 11.8 nm. All far-field Raman spectra of SFE-40/60 show RDX and TNT marker bands (see Figure 4.7). The TERS analysis reveals that 12 of 15 investigated SFE-40/60 particle surfaces contain a TNT

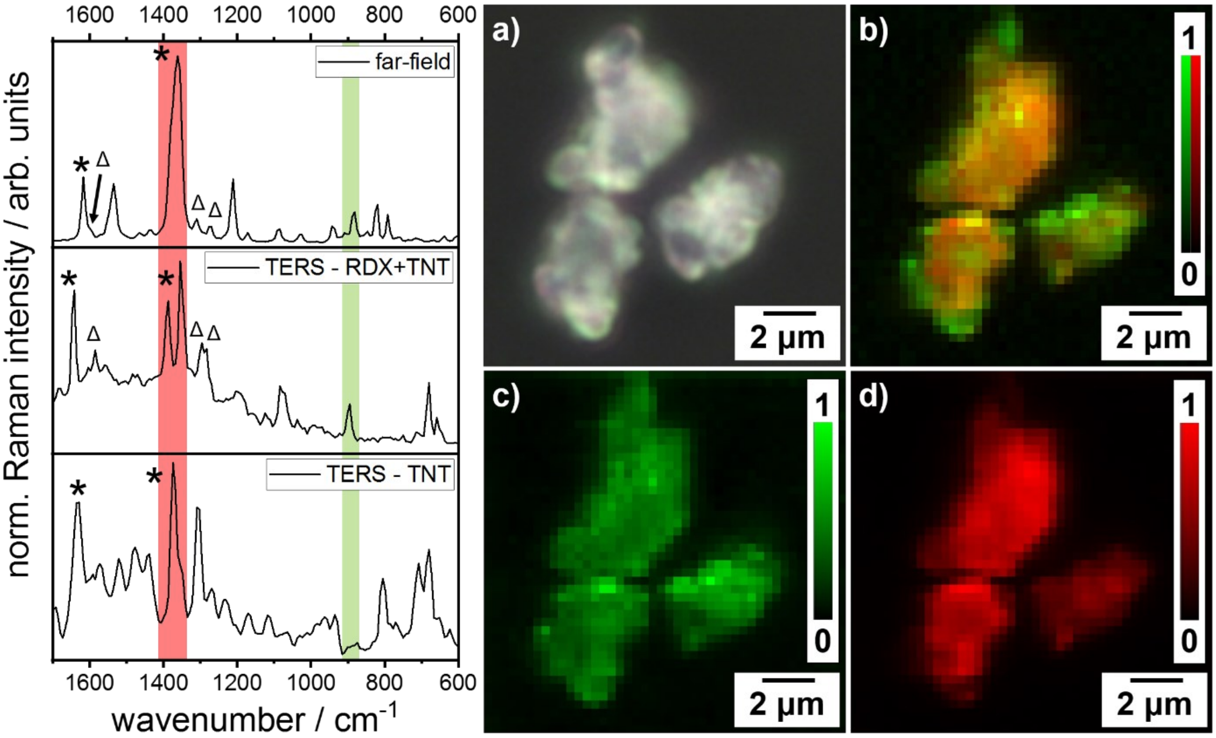

Figure 4.7. Left: Far-field Raman and TERS spectra of 40/60 hexolite powder produced by SFE. Typical TERS spectra show either both RDX (882 cm^{-1}; ring breathing) and TNT (1358 cm^{-1} - 1371 cm^{-1}; three NO_2 symmetric stretching vibrations) marker bands or only the TNT marker band. Δ indicate the N-NO_2 stretching vibration and the NO_2 asymmetric stretching vibration of RDX; * indicate the investigated NO_2 stretching vibrations of TNT. **Right:** Confocal Raman microscopy maps of SFE-40/60. Raman intensities are normalized for a better comparability. **a)** Microscope image of physically SFE-40/60 nano hexolite. **b)** Corresponding confocal Raman map of superimposed RDX and TNT marker band Raman intensities. **c)** Confocal Raman map of RDX marker band Raman intensities. **d)** Confocal Raman map of TNT marker band Raman intensities.

shell. In contrast, 3 out of 15 TERS maps show RDX and TNT marker bands. At first glance, these results appear unexpected since an increased amount of TNT is supposed to form thicker TNT shells around the RDX cores. As a result, RDX molecules should be undetectable by the electromagnetic field at the TERS tip apex. However, 3 out of 15 TERS maps demonstrate the presence of RDX molecules localized close to or even on SFE-40/60 nanoparticle surfaces. At this point, the formation of isotropic formed hierarchically ordered RDX/TNT core/shell nanoparticles appeared rather implausible. However, the mixed RDX/TNT TERS spectra show the same band position shifts of RDX and TNT NO_2 modes indicating similar intermolecular interactions between RDX and TNT molecules at the particle surfaces. A typical TERS spectrum showing only TNT signals and a typical TERS spectrum containing RDX and TNT marker bands of SFE-40/60 nanoparticles are given in Figure 4.7.

4.4.6 20/80 SFE Hexolite Mixture

A 20/80 hexolite mixture (SFE-20/80) was collected as an ultrafine yellowish powder composed of nanoparticles with a mean size of 59.7 nm ± 23.8 nm. In agreement with the far-field Raman measurements of the other SFE hexolite mixtures, all far-field Raman spectra contain RDX and TNT marker bands. The confocal Raman map given in Figure 4.8 illustrates these results by the pixel-wise superpositions of RDX and TNT marker bands intensities. TERS maps reveal that 13 out of 15 SFE-20/80 nanoparticle surfaces are formed of TNT only. TERS spectra from 2 out of 15 SFE-20/80 hexolite nanoparticles contain RDX and TNT marker bands. Although SFE-20/80 contains four times more TNT than RDX, RDX molecules are still detectable in the TERS spectra. This observation strengthens the assumption that SFE produced hexolite mixtures are not formed by isotropic RDX/TNT core/shell nanoparticles. Similar band position shifts of RDX and TNT NO_2 functional group vibrations could be identified within SFE-20/80 TERS spectra as like in TERS spectra of the other hexolite composite nanoparticles. An example TERS spectrum containing both RDX and TNT marker bands and an example TERS spectrum including only TNT marker bands are presented in Figure 4.8. Since the number of surfaces containing TNT only increases proportionally with the TNT mass fraction while the RDX marker band can still be detected in some TERS spectra of each measured hexolite mixture, an anisotropic RDX/TNT core/shell formation is suggested. The proposed building mechanism of such anisotropic core/shell nanoparticles will be discussed in detail in the next section.

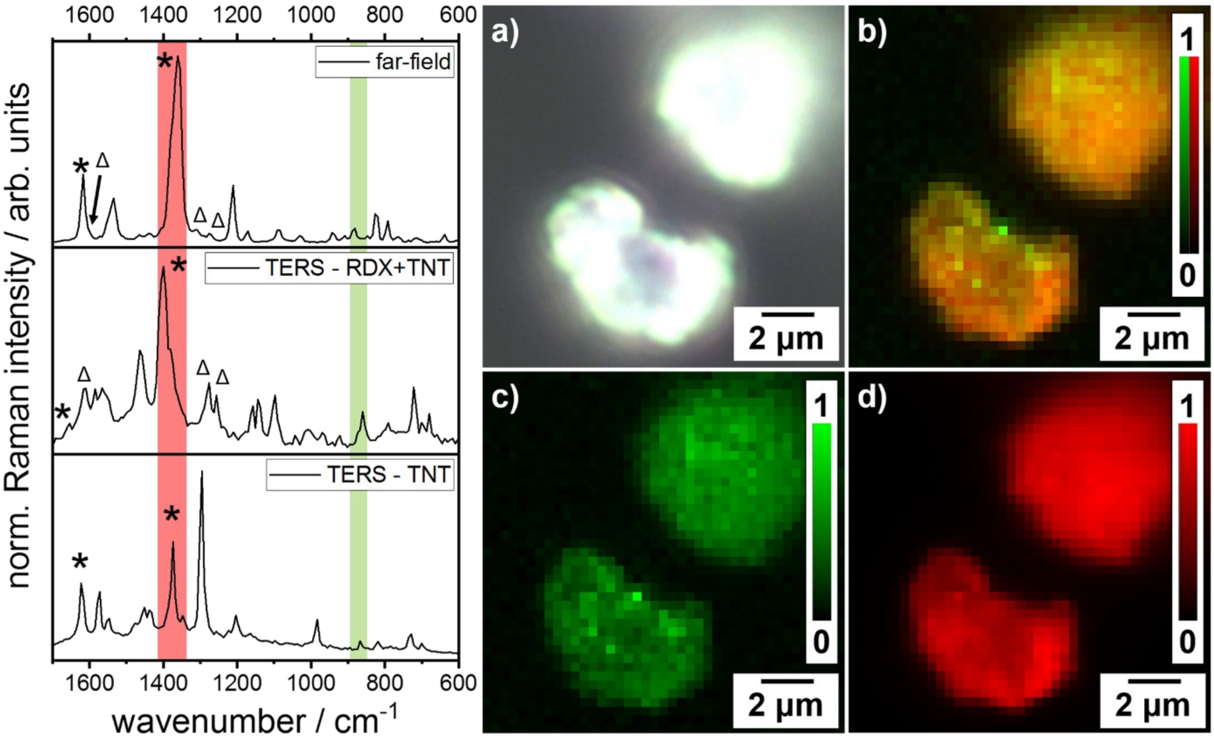

Figure 4.8. Left: Far-field Raman and TERS spectra of 20/80 hexolite powder produced by SFE. Typical TERS spectra show either both RDX (882 cm^{-1}; ring breathing) and TNT (1358 cm^{-1} - 1371 cm^{-1}; three NO_2 symmetric stretching vibrations) marker bands or only the TNT marker band. Δ indicate the N-NO_2 stretching vibration and the NO_2 asymmetric stretching vibration of RDX; * indicate the investigated NO_2 stretching vibrations of TNT. **Right:** Confocal Raman microscopy maps of SFE-20/80. Raman intensities are normalized for a better comparability. **a)** Microscope image of physically SFE-20/80 nano hexolite. **b)** Corresponding confocal Raman map of superimposed RDX and TNT marker band Raman intensities. **c)** Confocal Raman map of RDX marker band Raman intensities. **d)** Confocal Raman map of TNT marker band Raman intensities.

4.4.7 Building Mechanism of Hierarchically Structured SFE Hexolite Nanoparticles

The combination of AFM, confocal Raman microscopy and TERS results provide insights into the size, morphology and molecular composition of different hexolite mixtures. The smallest nanoparticle mean size of 29.4 nm ± 11.8 nm was found for SFE-40/60 hexolite nanocomposites. Particle mean sizes increase with increasing the mass fraction of RDX or TNT within the hexolite precursor solutions. Thus, SFE-80/20 nanoparticles having a diameter of 65.7 nm ± 27.6 nm provide the largest particle mean size. SFE-60/40 shows a particle mean size of 32.3 nm ± 12.3 nm and SFE-20/80 a mean size of 59.7 nm ± 23.8 nm. The dependence of particle mean sizes is presented as a function of the RDX mass fraction in Figure 4.9.a). Since all recorded far-field Raman spectra of each SFE produced hexolite mixtures contain RDX and TNT marker bands, confocal far-field Raman microscopy and spectroscopy demonstrates that RDX and TNT molecules are mixed on the nanoscale during the SFE process. Furthermore, TERS surface analysis demonstrates that not a single nanoparticle of all SFE produced hexolite nanoscale composites contains RDX only. Thus, TERS maps of all measured hexolite particles point either to surface covered by TNT only or to a mixture of RDX and TNT. The number of particles covered by TNT only increases with an increase of the TNT mass fraction. In contrast, the number of hexolite nanoparticle surfaces formed by RDX and TNT decreases consistently with an increased TNT mass fraction (Figure 4.9.b). Moreover, frequency shifts of NO_2 vibrations are detectable in TERS spectra containing both RDX and TNT marker bands. These shifts point towards an interaction between the NO_2 substituents in RDX and TNT.

In order to describe the building mechanism of the diverse hexolite mixtures it is necessary to briefly consider the dynamics of the SFE process. During the SFE process a pressured acetone solution is sprayed through a hollow cone nozzle into a permanently evacuated reaction chamber. By passing the hollow cone nozzle the precursor solution is accelerated and transformed into a fine spray characterized by droplets with a mean size of 2.6 µm ± 0.8 µm (measured 6 mm behind the nozzle, measurement details are presented in the Supporting Information). Leaving the hollow cone nozzle, parts of acetone droplet surfaces are in contact with the ruby surface of the nozzle. It is supposed that at these interfaces the free electron pairs of the carbonyl group in acetone form hydrogen bonds with hydrogen atoms of hydroxide ions determining the ruby surface. Since only localized areas of the acetone droplets surfaces interact with the nozzle surface, droplets are accelerated inhomogeneously while leaving the nozzle. It is supposed that at these interfaces the free electron pairs of the carbonyl functional groups of acetone molecules form hydrogen bonds with hydrogen atoms of hydroxide ions determining the ruby surface. Since only localized areas of the acetone droplets surfaces interact with the nozzle surface, droplets are accelerated inhomogeneously while leaving the nozzle. Because of the inhomogeneous acceleration and turbulences within the SFE atomization chamber, acetone droplets start to spin (Figure 4.9). Additionally, to the translational and angular acceleration forced by the nozzle, acetone droplets are continuously accelerated while passing the reaction chamber due to the flow provided by the vacuum pump. During the whole SFE processes the droplet size shrinks consistently until the solvent is completely evaporated (see Supporting Information, S3). Thus, the droplets act as accelerated dynamic micro reactors in the SFE process. For a better comprehensibility the building mechanisms for patchy SFE-80/20 nanoparticles and SFE-60/40, SFE-40/60, SFE-20/80 core/shell nanoparticles are described firstly without considering the acceleration of the dynamic micro-reactor droplets.

Directly after the injection of the hexolite solution droplets into the evacuated reaction chamber, the concentrations of RDX and TNT molecules within these microscale droplets are still the same as it is in the previously prepared acetone solutions. The continuous evaporation of acetone during SFE process and the related droplet shrinking results in a consistent increase of the RDX and TNT concentrations within the microscale droplets until the solution is supersaturated with RDX molecules. The supersaturation level of RDX molecules within the hexolite solution droplets is reached first since RDX exhibits with 6.8 g in 100 g acetone a six-time less solubility than TNT with 42.4 g per 100 g acetone at room temperature.[44] Following the classical theory of nucleation and crystallization, RDX molecules organizes to nuclei while the concentrations of RDX and TNT molecules further increase (Figure **4.9**.c).[57] These RDX nuclei grow to RDX nanoparticles. The growth of RDX nuclei to RDX nanoparticles appear due to the attaching of solved RDX molecules onto RDX nuclei, the aggregation of various RDX nuclei and nanoparticles and further due to Ostwald ripening. The driving force behind the nuclei growth and aggregation to nanoparticles is the minimization of surface energy which is realized by decreasing the surface-area-to-volume ratio. Anyway, nucleation and crystallization of RDX occurs first in all produced hexolite nano-composites independent of the used RDX and TNT mass fractions within the precursor solution. Due to further shrinking of

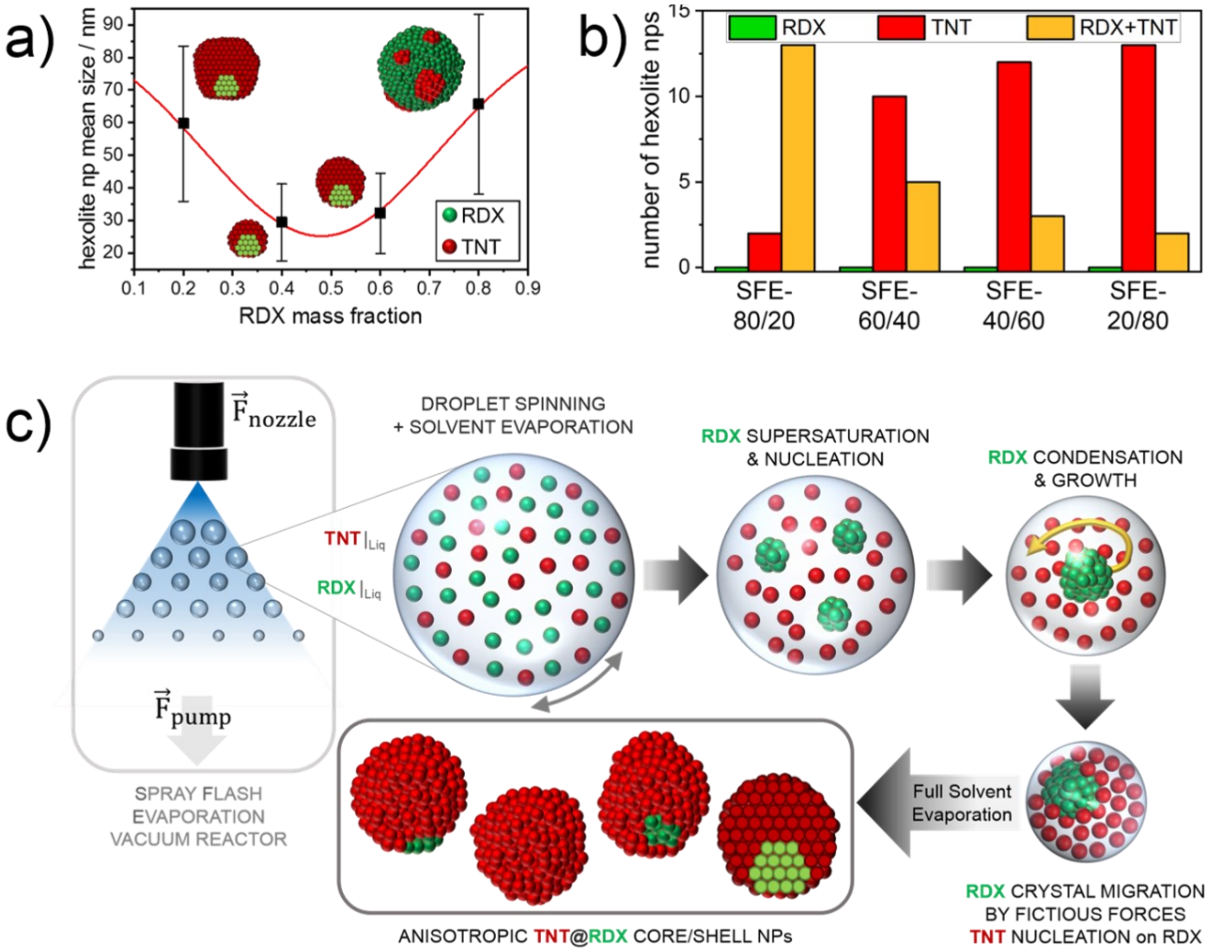

Figure 4.9. a) Mean sizes of anisotropic hexolite core/shell nanoparticles (SFE-80/20, SFE-60/40, SFE-40/60) and patchy hexolite sub-micron particles (SFE-20/80) as a function of the RDX mass fraction inside the precursor solutions. Green spheres represent RDX molecules; red spheres symbolize TNT molecules. Anisotropic hexolite core/shell nanoparticles are depicted as cross sections aimed to visualize its core/shell structure. **b)** Numbers of anisotropic hexolite nanoparticles and patchy nano particles providing RDX only, TNT only and RDX/TNT mixed surfaces. **c)** Flowchart of the supposed anisotropic RDX/TNT core/shell nanoparticle building mechanism.

the droplets and the related increase of RDX and TNT concentrations within the droplets the point of supersaturation of TNT in the solution is reached in the next step. Consequently, TNT molecules start to nucleate on top of RDX nanoparticle surfaces acting as nucleation seeds. As discussed within the SFE-80/20 section, the physisorption of at least the first layer of TNT molecules onto RDX nanoparticles surfaces is supposed to be initiated by electrostatic interactions between positively charged nitrogen atoms and negatively charged oxygen atoms of the NO_2 functional groups of both RDX and TNT molecules. Further TNT molecules grow onto this first TNT spots during the continued SFE process leading to the formation of the investigated TNT shells or TNT patches until the complete acetone is evaporated and the hexolite nanoparticles can be collected within the filter system (Figure **4.9**.c). However, due to the different RDX and TNT mass fractions used within the precursor solutions, hexolite nano-composites differ in size and arrangement. While mainly TNT only determined surfaces could be identified in TERS surface maps of SFE-60/40, SFE-40/60 and SFE-20/80 hexolite nanoparticles, TERS maps of SFE-80/20 surfaces contain dominantly both RDX and TNT marker bands. As already mentioned before, these results indicate the formation of RDX/TNT core/patches or Janus like nanoparticles for SFE-80/20. Contrary, SFE-60/40, SFE-40/60 and SFE-20/80 nano-composites are formed by hierarchal ordered nanoparticles providing a RDX/TNT core/shell character. Since the nucleation and crystallization of RDX occurs first, a certain amount of TNT molecules is needed to cover the primary RDX nanoparticles completely with a TNT shell. In case of SFE-80/20, the point of TNT supersaturation within the dynamic micro reactor droplets is reached later compared to the other hexolite systems due the relatively low TNT mass fraction (20 %). Thus, RDX molecules are allowed to organize themselves to larger primary particles within the droplets before TNT molecules start to adsorb onto RDX nanoparticle surfaces. Since symmetric and asymmetric stretching vibrations of NO_2 functional groups of TNT appear less shifted within TERS spectra of TNT only determined hexolite surfaces, it is supposed that intermolecular interactions between TNT molecules within the TNT shell and the TNT patches are rather comparable with the intermolecular interactions in TNT crystals. Thus TNT molecules are supposed to grow preferred onto previously adsorbed TNT molecules instead of uncoated RDX surfaces since intermolecular TNT-TNT interactions (electrostatic interactions between NO_2 functional groups and π-π stacking) should appear stronger than TNT-RDX interactions (electrostatic interactions between NO_2 functional groups only) leading to a reduction of surface and Gibbs free energy. The mechanism of these island or patch formations might be comparable with the Vollmer-Weber growth describing the formation of adatom clusters due to stronger adatom-adatom interactions than adatom-surface interactions.[58] Anyway, larger mean sizes of RDX primary particles result in the described SFE-80/20 patchy or Janus like particle structure since the amount of TNT molecules is insufficient to guarantee a complete surface coating. Contrary, SFE-60/40, SFE-40/60 and SFE-20/80 hexolite mixture provide a sufficient TNT content to form RDX/TNT core/shell particles. In accordance to the building mechanism of SFE-80/20 patchy nanoparticles, the formation of primary RDX nanoparticles takes place in a first step within these systems. These primary RDX nanoparticles appear smaller than for SFE-80/20 due to the lower mass fraction of RDX within the hexolite precursor solutions allowing a complete TNT surface coverage. While the TNT concentration increases within the droplets due to the related droplet size shrinking, RDX cores are coated with a TNT shell following the previously described mechanism. Additionally, further RDX core growths are quenched by the TNT encapsulations. Up to now, the presented reaction mechanism allows to explain the occurrence of different particle structure and sizes. However, the building mechanism does not include an explanation why TERS surface maps of RDX/TNT core/shell nanoparticles still include RDX signals even if the mass fraction of TNT amounts 80 % yet. Estimations of the RDX core diameters and the TNT shell thicknesses reveal that a typical SFE-60/40 core/shell nanoparticle provides a RDX core with a diameter of 26.7 nm and a TNT shell thickness of 2.7 nm. SFE-40/60 is formed by an RDX core with a diameter of 29.4 nm and a 4.1 nm thick TNT shell. The diameter of the RDX core of a typical SFE-20/80 nanoparticle amounts 59.7 nm and the TNT shell thickness amounts 12.9 nm. The estimations are based on the particle mean sizes of the diverse hexolite nano-composites and the densities of crystalline RDX and TNT. The results are summarized in Table 4.3. The detailed calculations are given within the Supporting Information.

Table 4.3. Estimated RDX core diameters and TNT shell thicknesses for isotropic hexolite core/shell nanoparticles

mass fraction ratio (RDX/TNT)	**particle mean size**	**RDX core diameter**	**TNT shell thickness**
60/40	32.2 nm	26.7 nm	2.7 nm
40/60	29.4 nm	21.2 nm	4.1 nm
20/80	59.7 nm	34.0 nm	12.9 nm

Due to the rapid field decay of the enhanced electric field generated by the LSPR of the silver nanoparticle localized at the AFM tip apex, the appearance of RDX signals within TERS spectra is at least very unlikely for SFE-60/40 and SFE-40/60 *de facto* impossible for SFE-20/80 (Figure 4.10.a).[34] Therefore the contribution of RDX Raman active frequencies to diverse TERS spectra must be related to the position of the RDX cores within the hexolite RDX/TNT core/shell nanoparticles. As mentioned before, the previous building mechanism describes the hexolite nano-composite formation without considering the translational and angular accelerations of the droplets in the SFE atomization chamber. Without these accelerations it can be assumed that RDX primary nanoparticles would be located randomly within the bulk of the droplets without stronger movements until the complete evaporation of acetone is finished resulting in the formation of isotropic RDX/TNT core/shell nano-spheres with a centered RDX core. However, during SFE process droplets are accelerated due to the release of the pressurized precursor solution into the evacuated atomization chamber through a hollow cone nozzle, the interactions of acetone droplet surface molecules with the nozzle surface while leaving the nozzle, turbulences in the atomization chamber and the flow generated by the vacuum pump. The first steps of the hexolite core/shell nanoparticle building mechanism by means of RDX superstation and nucleation within the micron sized droplets take place as already described for the non-accelerated case. After the phase change of solved RDX into solid RDX nuclei and the aggregation of these RDX nuclei into primary RDX nanoparticles, the acceleration of the droplets starts to influence the formation of the hierarchical order hexolite nanoparticles. Due to the translational accelerations (by nozzle and pump, Figure **4.9**.c) of the shrinking dynamic micro reactor droplets, a fictitious force affects the RDX primary nanoparticles pushing them back towards the edge of the droplets. This fictitious force is qualitatively the same fictitious force which presses a passenger into the seat of a car while the car is accelerated. Additionally, the inhomogeneous acceleration of the droplet while leaving the nozzle and turbulences within the SFE crystallization chamber induce a spin of the acetone micro droplets. This droplet spin is described by an angular acceleration of the droplet around itself. Consequently, a centrifugal force affects the RDX primary nanoparticles within the droplet pushing them towards the edge of the acetone droplet (Figure **4.9**.c). The combination of both effects forces RDX primary particles to looping motions starting in the droplet bulk and ending at the droplet surface. Similar looping motions and particle migrations are described by Chung for the motion of coal particles inside accelerated n-hexane respectively methanol micro droplets.[59] During the RDX nanoparticle migration the droplet sizes decrease continuously leading to TNT supersaturation and TNT nucleation on top of the RDX nanoparticles as already described for the non-accelerated case. Since the RDX core particles are localized close to or at the edges of the acetone droplets during the growth of the TNT shell, the formation of hexolite core/shell nano-spheres processes anisotropic (Figure **4.9**.c). Consequently, RDX cores are not centered in the middle of hexolite core/shell nanoparticles but are localized near or at the particle edges. Due to the varying RDX mass fractions within the different hexolite precursor solutions,

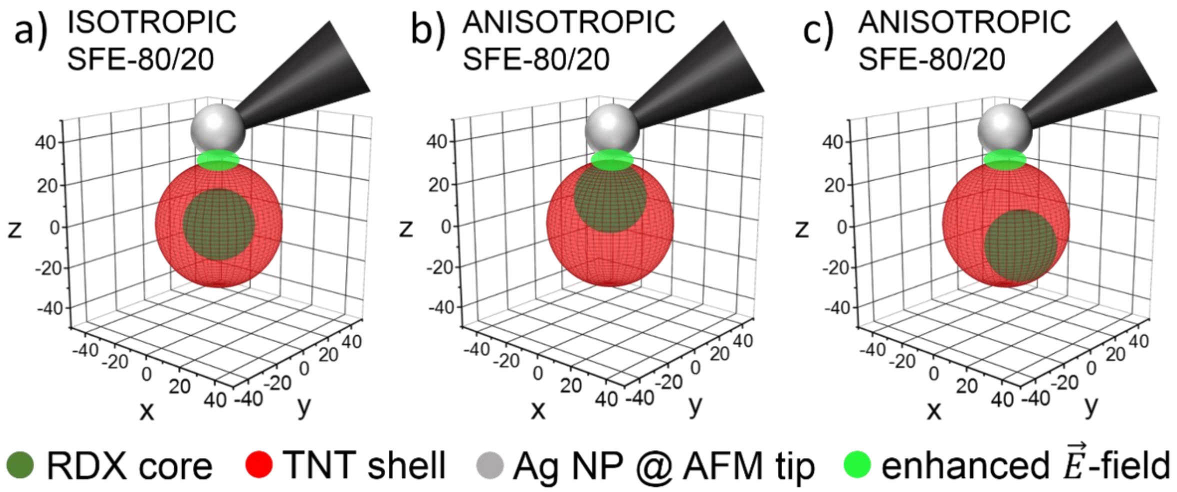

Figure 4.10. Different alignments of SFE-80/20 RDX/TNT core/shell particles towards the silver particle mounted at the AFM tip apex. Axis units are given in nm. **a)** Isotropic SFE-80/20 RDX/TNT core/shell nanoparticle. Due to the closed TNT shell only TNT Raman active frequencies would occur in TERS spectra. **b)** Anisotropic SFE-80/20 RDX/TNT core/shell nanoparticle. The RDX core is aligned towards the silver nanoparticle localized at the AFM tip apex. RDX or RDX and TNT Raman active frequencies appear in TERS spectra. **c)** Anisotropic SFE-80/20 RDX/TNT core/shell nanoparticle. The RDX core is not localized in the enhanced electric field of the silver nanoparticle. Only TNT Raman active frequencies appear in TERS spectra
.

kinetics of RDX nucleation and RDX core growths differ. RDX nucleation and RDX nanoparticle growth occur earlier the higher the RDX mass fraction. Accordingly, RDX primary nanoparticles are less affected by the fictitious forces the less the RDX mass fraction. Thus, a complete migration of RDX nanoparticles towards the droplets edges might not takes place for smaller RDX mass fraction hexolite systems. Therefore, it is expected that the RDX cores of SFE-20/80 and SFE-40/60 appear more centered inside hexolite nanoparticles. On the other hand, SFE-60/40 nanoparticles provide RDX cores which are located closer to the particle edges than to the particle centers. However, all of these arrangements cause nanoparticles providing partially thicker and thinner TNT shell areas. Thus, particle surface areas formed by RDX only or by RDX covered with a thin TNT layer occur. These RDX or RDX/TNT determined surface areas result in the presence of RDX Raman active frequencies within some TERS spectra of SFE-60/40, SFE-40/60 and SFE-20/80 TERS surface maps. Due to the anisotropic RDX/TNT core/shell nanoparticle morphology the number of TERS spectra containing RDX signals decreases with the increase of the TNT mass fraction within the hexolite mixtures. An increase of the TNT mass fraction leads to smaller RDX cores and thicker TNT shells. Therefore, the surface area of a hexolite nanoparticle formed by RDX respectively RDX and TNT decreases. Consequently, the possibility that the particle aligns in a manner towards the silver coated AFM tip so that the RDX determined surface area contributes to the TERS spectra decreases and thus less RDX and RDX/TNT determined surfaces are found (Figure 4.10).

4.4.8 Influence of the Hexolite Precursor Size and Structure onto the Resulting Nanodiamonds

Reaction products of the detonation syntheses of SFE produced hexolite mixtures were collected as dark-grey ultrafine powders after drying. In order to ascertain if nanodiamonds were formed during the detonation syntheses, reaction products of each SFE produced hexolite nanoparticles were investigated via HR-TEM and TERS. HR-TEM images of each sample demonstrates clearly the formation of nanodiamonds. Figure 4.11 (right) depicts a sample HR-TEM image of nanodiamonds synthesized from SFE-40/60 (ND-40/60). TERS spectra of nanodiamonds contain the broad graphitic G – and D – bands localized at ~1600 cm^{-1}

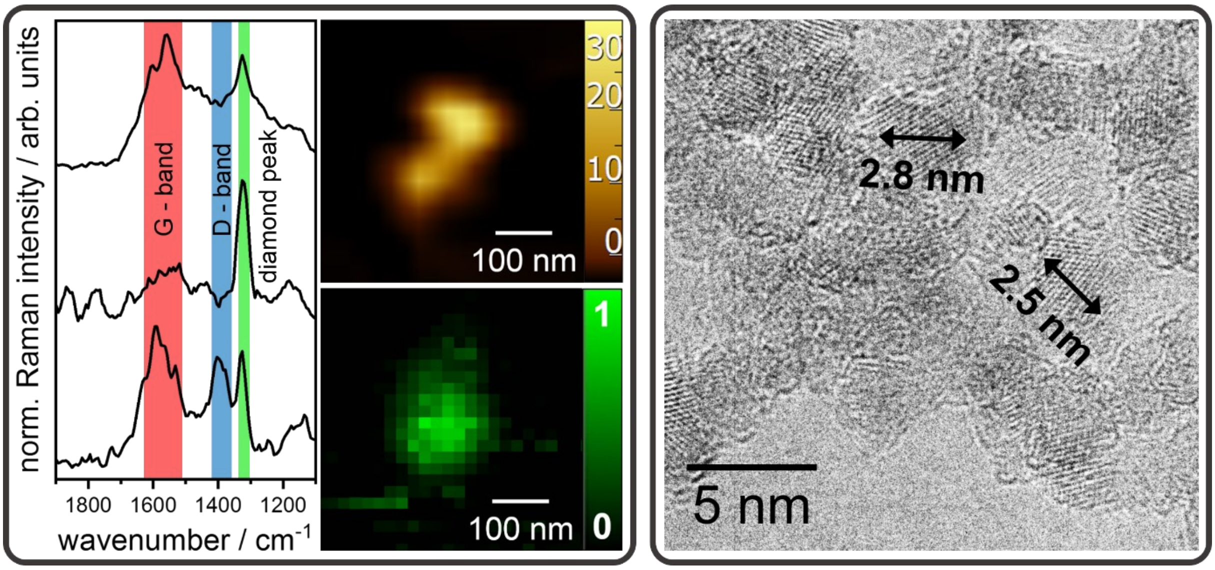

Figure 4.11. Left: TERS spectra of certain nanodiamonds synthesized from SFE-40/60 contain graphitic G – and D – bands (~1600 cm^{-1}, 1400 cm^{-1}) as well as the diamond peak (1325 cm^{-1}). The shift of the diamond peak from 1333 cm^{-1} to 1325 cm^{-1} hints onto a nanodiamond size < 10 nm. The AFM topographic map and the corresponding TERS map depict an agglomerate of nanodiamonds synthesized from SFE-40/60. **Right:** HR-TEM image of nanodiamonds synthesized from SFE-40/60.

respectively ~1400 cm^{-1} and the diamond band at 1325 cm^{-1}. The occurrence of the graphitic G – and D – bands within the TERS spectra points to the formation of a graphitic layer on the nanodiamond surfaces. The shift of the diamond vibration from 1333 cm^{-1} to the measured 1325 cm^{-1} hints to nanodiamond sizes below 10 nm. Presented TERS results are in good agreement with a recently published study undertaken by Ali *et al.*[60] Since TERS measurements are performed innately on single particles the exact position of the G – and D – bands may varying between single spectra as well as the intensities of these bands and the intensity of the diamond vibration. AFM topographic maps were recorded to determine the nanodiamond means sizes and size distribution. These investigations reveal that nanodiamonds resulting from SFE-40/60 provide with 3.6 nm ± 0.04 nm the smallest mean size and the narrowest size distribution. Detonation of SFE-20/80 leads to nanodiamonds (ND-20/80) with a particle mean size of 3.7 nm ± 0.08 nm, nanodiamonds synthesized from SFE-60/40 (ND-60/40) show a mean size of 4.1 nm ± 0.04 nm. SFE-80/20 result with 6.1 nm ± 0.2 nm in the largest nanodiamond mean size (ND-80/20). Nanodiamond means sizes and their evolution are summed up in Figure 4.12 as a function of the RDX mass ratio within the precursor SFE-produced hexolite nano-composites. It has already been reported that the hexolite precursor particle sizes influences strongly the mean size and the size distribution of the resulting nanodiamonds. Pichot *et al.* describe a correlation between the size reduction of the precursor material from the micro- onto the nanoscale and a related decrease of nanodiamond mean sizes.[23-24] Different hexolite and octolite (mixture of HMX and TNT) nano compounds with varying mass fraction of RDX and TNT respectively HMX and TNT are compared with micro structured hexolite and octolite mixtures in these studies. Both hexolite and octolite nano-composites were also prepared by SFE using similar settings as in the present work (see experimental section). They could demonstrate that the mean sizes of obtained nanodiamonds occur up to 50% smaller for nanostructured hexolite precursor compared to the micro structured precursors by same RDX and TNT mass fractions. Due to the lack of an accurate measurement technique which enables the investigation of the molecular arrangements of single particles on the nanoscale, they had to assume that RDX and TNT nanoparticles appear uncoupled and nearly homogeneous distributed within the pressed hexolite pellets which were prepared for nanodiamond detonation synthesis. Due to the assumed homogenous distribution of RDX and TNT particles, they proposed that the combustion reaction products of RDX (or HMX) form a diffusion barrier due to the RDX detonation pressure around single TNT nanoparticles (or more precisely the

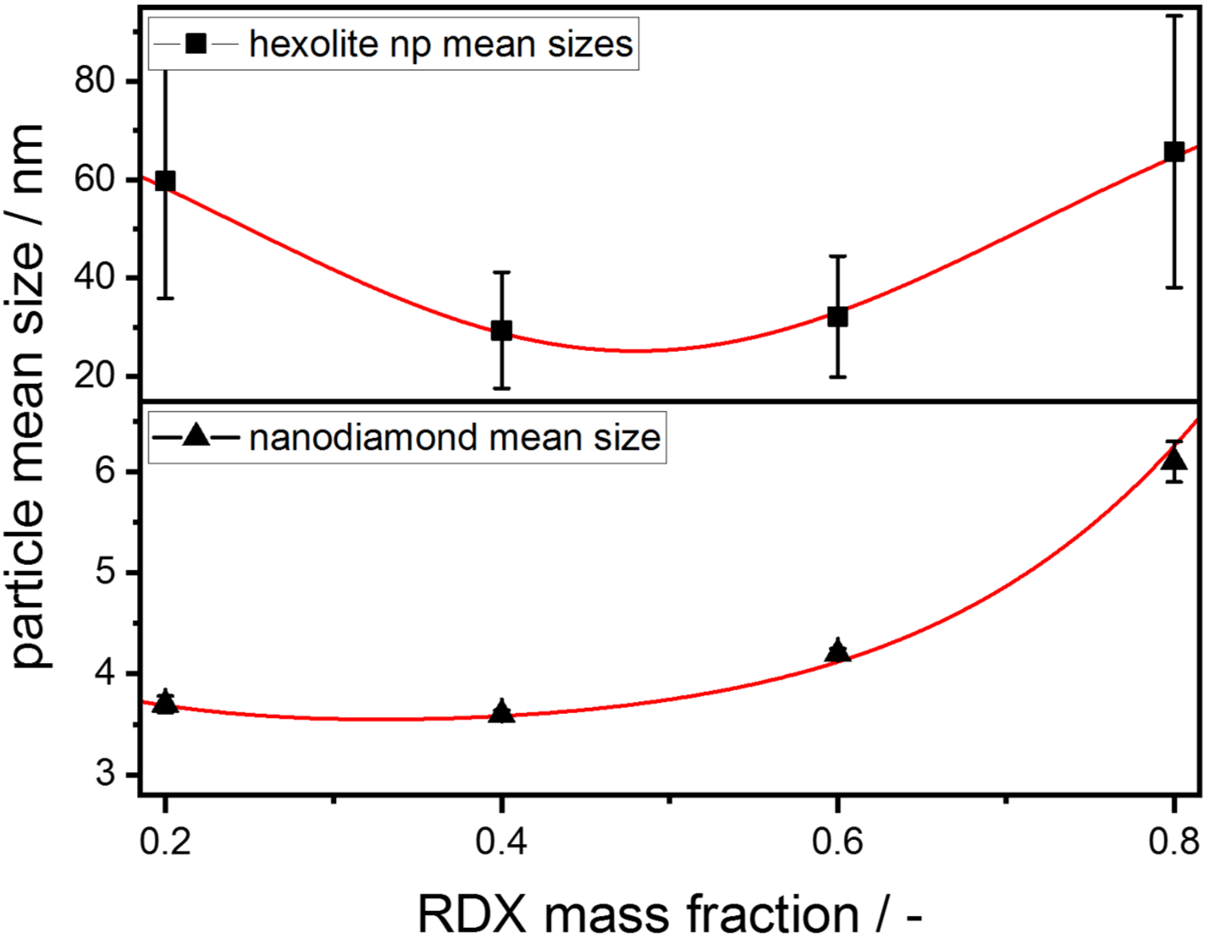

mass fraction ratio (RDX/TNT)	80/20	60/40	40/60	20/80
d_{hex}	65.7 nm ± 27.6 nm	32.2 nm ± 12.3 nm	29.4 nm ± 11.8 nm	59.7 nm ± 23.8 nm
d_{nd}	6.1 nm ± 0.20 nm	4.2 nm ± 0.05 nm	3.6 nm ± 0.04 nm	3.7 nm ± 0.08 nm

Figure 4.12. Evolution of hexolite RDX/TNT core/shell nanoparticles and evolution of detonation synthesized nanodiamond mean sizes as a function of the RDX mass fraction within the hexolite precursor nano-composite.

reaction products of the TNT nanoparticle) leading to a diffusion zone which is much smaller than the diffusion zone calculated for 1 nm nanodiamond nuclei.[20] Consequently, the amount of carbon atoms arising from TNT molecules which are mainly involved in the nanodiamond formation depends on the TNT nanoparticle diameter. Smaller TNT nanoparticles imply smaller diffusion zones which include less amounts of carbon atoms resulting generally in a decrease of nucleation sites and thus in smaller nanodiamonds. However, TERS investigations could show that SFE produced hexolite mixtures appear as anisotropic RDX/TNT core/shell particles and not as uncoupled RDX and TNT nanoparticles as presumed. Furthermore, here presented nanodiamonds do not follow this trend completely. Nanodiamonds resulting from the detonation of SFE-20/80 show a larger particle mean size than nanodiamonds produced from SFE-60/40 although SFE-60/40 core/shell nanoparticles provide a smaller particle mean size than SFE-20/80 nanoparticles. Consequently, the building mechanism proposed by Pichot *et al.* has to be slightly reconsidered.

For this purpose, an ideal case which is defined by monodispersed isotropic RDX/TNT core/shell nanoparticles forming a hexagonal close-packed precursor material after pressing is discussed first (Figure 4.13). After ignition and detonation, RDX reaction products are accelerated from the particle centers outwards whereas TNT reaction products are accelerated both towards the particle center and away from the particle center. The migration of RDX and TNT reaction products is driven by their specific detonation pressures. Depending on the RDX and TNT mass fractions which define the RDX core diameter and the TNT shell thickness, the competing migration effects can be dominated either by the RDX detonation pressure or by the TNT detonation pressure. Generally, RDX providing a higher detonation pressure than TNT. In case of RDX detonation pressure domination, TNT reaction products are forced into the center of a tetrahedron while RDX reaction products form a spherical diffusion barrier around it. If TNT detonation pressure dominates the competing migration effects due to a relatively low RDX mass fraction, RDX reaction products are forced to spherical diffusion barriers around the center of a tetrahedron. The tetrahedrons arise from the hexagonal close-packing of the material and represents the smallest repetitive area. The sites of the tetrahedron are defined by the connection lines between the centers of two neighboring isotropic hexolite particles. Thus, four times a fourth of the TNT reaction products of one single hexolite core/shell particles contributes to one diffusion zone. Anyway, depending on whether the RDX or TNT detonation pressure dominates, different thermodynamic circumstances regarding the pressure and the temperature prevail within the diffusion zones. Since in case of the RDX detonation pressure dominance the TNT reaction products are forced towards the tetrahedron centers, pressure and temperature are higher within these resulting diffusion zones than for diffusion zones formed in a TNT dominated system. Higher pressures and temperatures promote a more complete conversion of carbon atoms into nanodiamonds leading consequently to larger nanodiamond diameters. Contrary, smaller pressure and temperature values result in a less amount of carbon

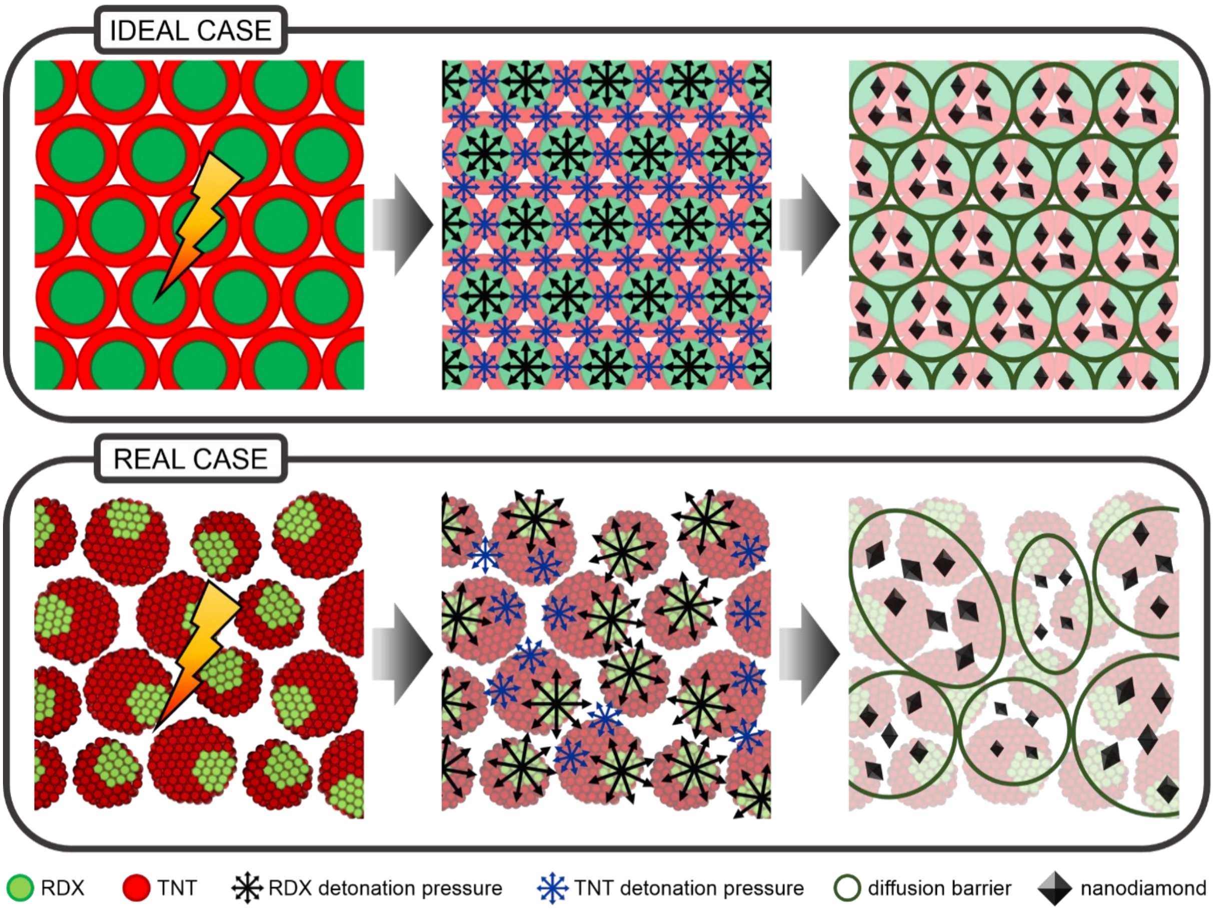

Figure 4.13. Top: Supposed building mechanism of nanodiamonds under ideal conditions presented as 2D cross sections. The hexolite precursor are built up by hexagonal close-packed isotropic RDX/TNT core/shell nanoparticles. Due to the higher detonation pressure of RDX compared to TNT and the high symmetry of the precursor, RDX reactions products form spherical diffusion barriers after detonation. Inside the diffusion zone nanodiamonds are formed from TNT carbon atoms. In the ideal case, all diffusion zones have the identic size and contain the same amount carbon atoms and nucleation sites. Thus, the same amount of monodispersed nanodiamonds are formed within the diffusion zones. Consequently, the nanodiamond size depends only on the TNT shell thickness in the ideal case. **Bottom:** Supposed building mechanism of nanodiamonds under real conditions presented as 2D cross sections. SFE-produced anisotropic core/shell nanoparticles are packed dense. Due to the size distribution of the hexolite precursor particles a perfect hexagonal close-packing is not possible. The random arrangement of the anisotropic core/shell particles leads to the formation of more ellipsoid diffusion zones of slightly differing sizes. Consequently, diffusion zones contain different amounts of carbon atoms and nucleation sites. Therefore, synthesized nanodiamonds provide slightly different sizes leading to a nanodiamonds size distribution. Thus, nanodiamond mean sizes and size distribution depend on the TNT shell thickness, the hexolite precursor particle size, the hexolite particle size standard deviation and on the level of anisotropy within the precursor structure.

atoms forming nanodiamonds and thus in smaller nanodiamond mean sizes. However, due to the high symmetry of ideal packed and perfectly monodispersed isotropic hexolite core/shell particles, the size of the diffusion zones and the thermodynamic circumstances within one diffusion zone is constant for all diffusion zones by a given RDX respectively TNT mass fraction. Consequently, the number of nucleation sites within the diffusions zones appears also constant and finally the number and sizes of obtained nanodiamonds within one diffusion zone (Figure **4.13**). Therefore, the nanodiamond size depend only on the RDX mass fraction and the TNT shell thickness in the ideal case. Following the suggested mechanism for the ideal case it becomes obvious that the correlation between precursor particle size and nanodiamond size proposed by Pichot et al. remains untouched since it is not germane for estimating the nanodiamond size if the TNT carbon atoms which form the nanodiamonds arises from a single TNT nanoparticle or of four fourth RDX/TNT core/shell nanoparticles. However, under real conditions the hexolite precursor material consist of anisotropic core/shell particles exhibiting a size distribution. Due to the size distribution, a perfect symmetrical hexagonal close-packing is not accomplishable even if a dense packing of the hexolite precursor material is undertaken before detonation synthesis (see Experimental section). Moreover, the anisotropy of the core/shell precursor particles (by meaning of the RDX core is not centered in the middle of the particle) causes a further decrease of the symmetry within the precursor structure. The symmetry decrease leads to formation of diffusion zones respectively diffusion barriers with more ellipsoid character and different dimensions (Figure 4.13). As a consequence, the thermodynamic and kinetic circumstances as well as the amount of TNT carbon atoms within the single diffusion zones differ leading to a varying number of nucleation sites. This results in slightly different nanodiamond sizes and thus in a nanodiamond size distribution. Consequently, the nanodiamond mean size d_{nd} of the obtained nanodiamonds depends not only on the RDX mass fraction ω_{RDX} and the TNT shell thickness d_{TNT} but also on the parameters defining the symmetry of the precursor material. These parameters are the hexolite precursor particle mean size d_{hex}, the hexolite precursor size standard deviation s_{hex} and the level of anisotropy a_{hex} within the precursor structure. Thus d_{nd} can be assumed by the following correlation:

$$d_{nd} \sim \omega_{RDX} d_{TNT} + d_{TNT}\left(a_{hex} + \frac{|s_{hex}|}{d_{hex}}\right) \qquad \text{Eq. 4.1}$$

The level of anisotropy is defined as the distance between the hexolite particle center and the center of the corresponding RDX core $d_{hex \to RDX}$ divided by the hexolite particle mean radius r_{hex}:

$$a_{hex} = \frac{d_{hex \to RDX}}{r_{hex}} \qquad \text{Eq. 4.2}$$

The described correlation presented in Eq. 4.1 allows an interpretation of the nanodiamond mean sizes and size distributions of the presented detonation synthesized nanodiamonds. ND-80/20 provides with 6.1 nm ± 0.2 nm the largest particle means size and the broadest size distribution. Due to the formation of patchy or Janus particles, the level of anisotropy a_{hex} of SFE-80/20 nanoparticles has the highest value of all investigated hexolite nano-mixtures because $d_{hex \to RDX}$ is nearly equal to r_{hex} (compare Figure 4.9.a). Furthermore d_{TNT} – which is in case of SFE-80/20 more a TNT patch diameter than a shell thickness – is supposed to be relatively large since TNT solely form patches at single spots at the RDX surface. Additionally, the formation of patchy particles causes a reduction of the symmetry within the precursor charge compared to core/shell particles. Moreover, SFE-80/20 provides the broadest size distribution and thus the highest particle size standard deviation reducing further the symmetry of the precursor charge. Finally, SFE-80/20 contains the highest RDX mass fraction promoting higher temperatures and pressures inside the diffusion zones leading to a more complete conversation of carbon atoms to nanodiamonds and thus to lager nanodiamond mean sizes. In contrast to ND-80/20, nanodiamonds formed from RDX/TNT core/shell nanoparticles (ND-60/40, ND-40/60, ND-20/80) exhibit significant smaller particle mean sizes and narrower size distributions. ND-60/40 shows with 4.2 nm ± 0.05 nm the largest particle mean size of all nanodiamonds synthesized from core/shell nanoparticles although the SFE-60/40 hexolite nanoparticles provide a relatively small mean size and TNT shell thickness. However, as already discussed at the building mechanism section above, RDX nucleates earlier the higher the RDX mass fractions. Consequently, RDX cores are more affected by the fictitious forces leading to a complete or nearly complete migration of the primary RDX nanoparticles towards the acetone droplet edges before TNT nucleation starts. As a consequence, SFE-60/40 shows a higher level of anisotropy a_{hex} than SFE-40/60 and SFE-20/80 and thus a higher reduction of the precursor symmetry. Additionally, the relatively high RDX mass fraction supports the carbon atom to diamond conversion leading to larger nanodiamond mean sizes as discussed above. On the other hand, ND-20/80 exhibit a mean size of 3.7 nm ± 0.08 nm though the SFE-20/80 precursor shows a larger core/shell nanoparticle means size and a larger TNT shell thickness d_{TNT}. Since this hexolite mixture includes the lowest RDX mass fraction SFE-20/80 particles should provide the smallest level of anisotropy of all presented hexolite mixtures. The lowest RDX mass fraction results further in the lowest temperature and pressure values inside the diffusion zones of all hexolite materials. Consequently, a less amount of carbon atoms converts into nanodiamonds leading to smaller nanodiamond mean sizes. Due to the smaller mean size of ND-20/80 compared to ND-60/40, the symmetry parameters, especially the level of anisotropy a_{hex}, seem to affect the nanodiamond mean size at least as strong as the TNT shell thickness d_{TNT} and the RDX mass fraction ω_{RDX}. Anyway, the smallest nanodiamond mean size including the narrowest size distribution could be found at ND-40/60 with 3.6 ± 0.04 nm. The SFE-40/60 hexolite precursor presents a thicker TNT shell but a less level of anisotropy a_{hex} than SFE-60/40. Contrary, SFE-40/60 is defined by a thinner TNT shell but a higher level of anisotropy than SFE-20/80. Since the level of anisotropy a_{hex} and the TNT shell thickness d_{TNT} within an anisotropic hexolite core/shell nanoparticle should be as small as possible in order to receive the smallest nanodiamonds (Eq. 4.1) but both parameters behave inversely proportional to each other (due to the varying RDX mass fractions), SFE-40/60 seems to provide the best mixture between its TNT shell thickness d_{TNT} and its level of anisotropy a_{hex}.

4.5 Conclusion

Different hexolite mixtures with various RDX/TNT mass ratios were produced via Spray Flash Evaporation and investigated with AFM, confocal far-field Raman spectroscopy and TERS. The combination of these techniques gave insight into the sizes of the produced hexolite particles and into the arrangements of RDX and TNT molecules within single particles on the nanoscale. It was demonstrated that SFE-80(RDX)/20(TNT) is built up by patchy RDX/TNT nanoparticles while SFE-60/40, SFE-40/60 and SFE-20/80 form anisotropic RDX/TNT core/shell nanoparticles. The anisotropy of the particles, which depends on the RDX/TNT mass ratio, expresses a non-centered RDX core appearing closer to the hexolite nanoparticle edges. A building mechanism for the different SFE produced hexolite mixtures based on the experimental results and the dynamics of the SFE process is proposed. Due to the higher solubility, RDX nanoparticles are formed first during SFE process. Driven by fictitious forces, RDX nanoparticles migrate towards acetone droplet edges while TNT grows onto RDX nanoparticle surfaces. Since RDX nanoparticles are not centered in the droplet, hexolite nanoparticle formation occur anisotropic.

The influence of the hexolite precursor structure on the size and the distribution of the resulting nanodiamonds was discussed in detail. It is proposed that the TNT shell thickness, the symmetry reduction by meaning of the level of anisotropy (position of the RDX core center related to the hexolite particle center) and the precursor size distribution determine the resulting nanodiamond mean size. Further studies are necessary to verify the correlation between these parameters and the nanodiamond mean size. For this purpose, more RDX/TNT mass ratios have to be investigated to find the perfect relationship between TNT shell thickness and the anisotropy level within the RDX/TNT core/shell nanoparticles. This way, the size distribution of nanodiamonds produced from the detonation of hexolite mixtures could be further reduced.

4.6 Supporting Information

4.6.1 Raman Active Vibrational Frequencies and Assignments

1,3,5-Trinitro-1,3,5-triazinane (RDX)

In the following measured Raman active frequencies of pristine 1,3,5-Trinitro-1,3,5-triazinane (RDX) are presented, assigned and compared with literature.

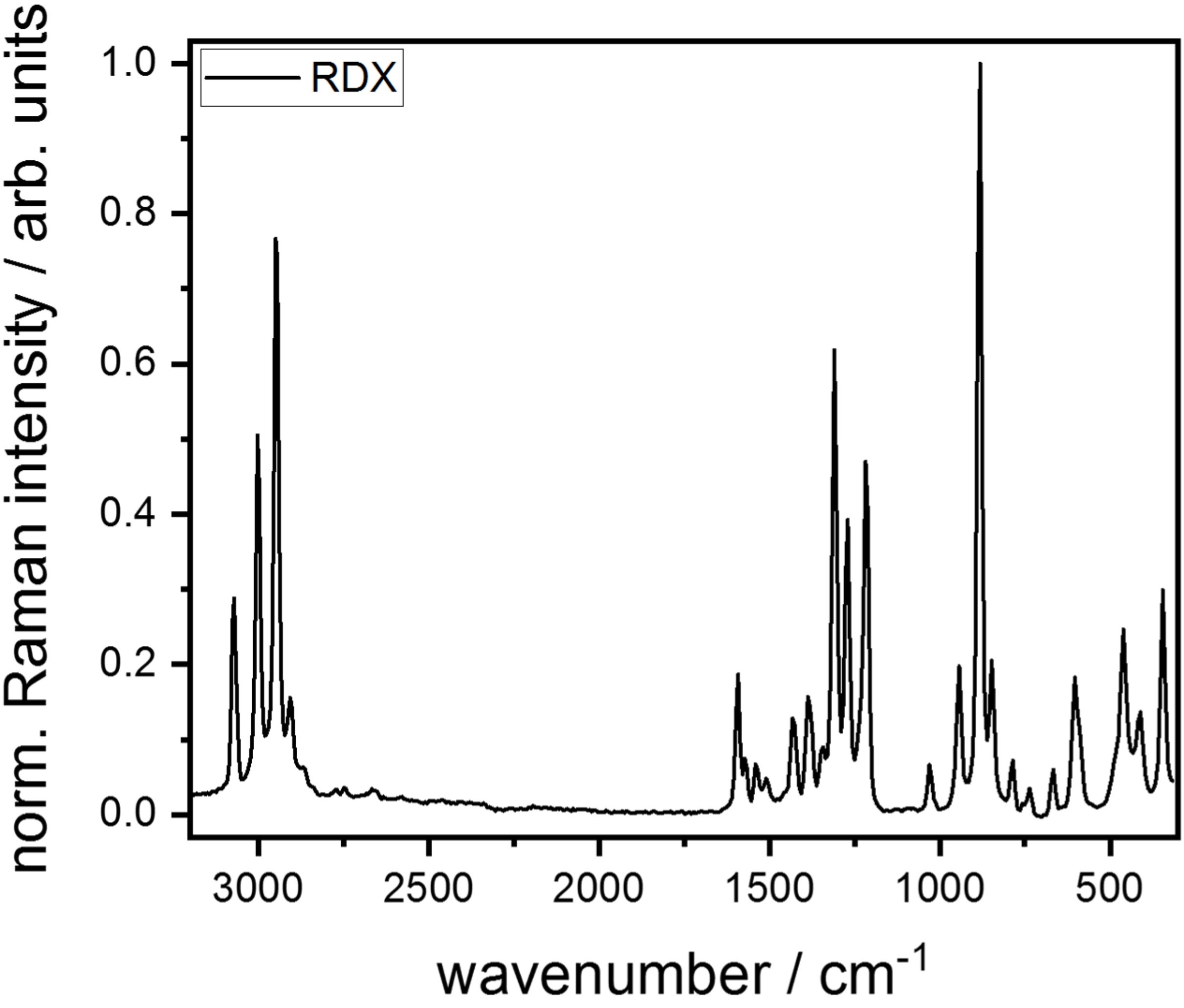

Figure 4.14. Raman spectrum of RDX in a spectral range between 3200 cm^{-1} and 300 cm^{-1}.

Table 4.4. Raman frequencies and their assignments of RDX

Raman frequencies of RDX		
Experiment / cm^{-1}	**Literature / cm^{-1} [47]**	**Assignments [44, 46-47]**
345 m	347	ring twist
410 w	415	ring bend
461 m	464	ring bend, N-N str
489 vw	488	ring twist, NO_2 sci
589 w	588	ring twist
603 w	607	ring rock
667 vw	670	ring bend
736 vw	739	N-NO_2 umb
757 vw	757	ring bend, NO_2 sci
785 vw	788	C-N str, NO_2 sci
847 m	848	N-N str, NO_2 sci
882 vs	885	ring breath
943 w	945	N-N str
1024 vw	1023	CH_2 rock
1031 vw	1031	N-C str
1218 m	1215	N-C str
1270 w	1273	N-NO_2 str sym
1309 s	1309	CH_2 twist, N-NO_2 str
1346 vw	1346	CH_2 wag
1377 w	1377	CH_2 twist
1387 w	1388	CH_2 wag
1432 w	1436	CH_2 sci
1458 vw	1460	CH_2 sci
1509 vw	1508	CH_2 sci
1541 vw	1542	NO_2 str asym
1573 vw	1573	NO_2 str asym
1592 w	1595	NO_2 str asym
2907 w	2906	C-H str
2949 vs	2949	C-H str
3003 s	3003	C-H str
3072 m	3067	C-H str
3077 m	3075	C-H str

RDX marker band vibration (882 cm-1; ring breathing) is marked in green. Notes: vs – very strong, s – strong, m – medium, w – weak, vw – very weak; asym – asymmetric, bend – bending, breath – breathing, rock – rocking, sci – scissoring, sym – symmetric, , str – stretching, twist – twisting, umb – umbrella, wag – wagging

2-Methyl-1,3,5-trinitrobenzene (TNT)

In the following measured Raman active frequencies of pristine 2-Methyl-1,3,5-trinitrobenzene (TNT) are summed up, assigned and compared with literature.

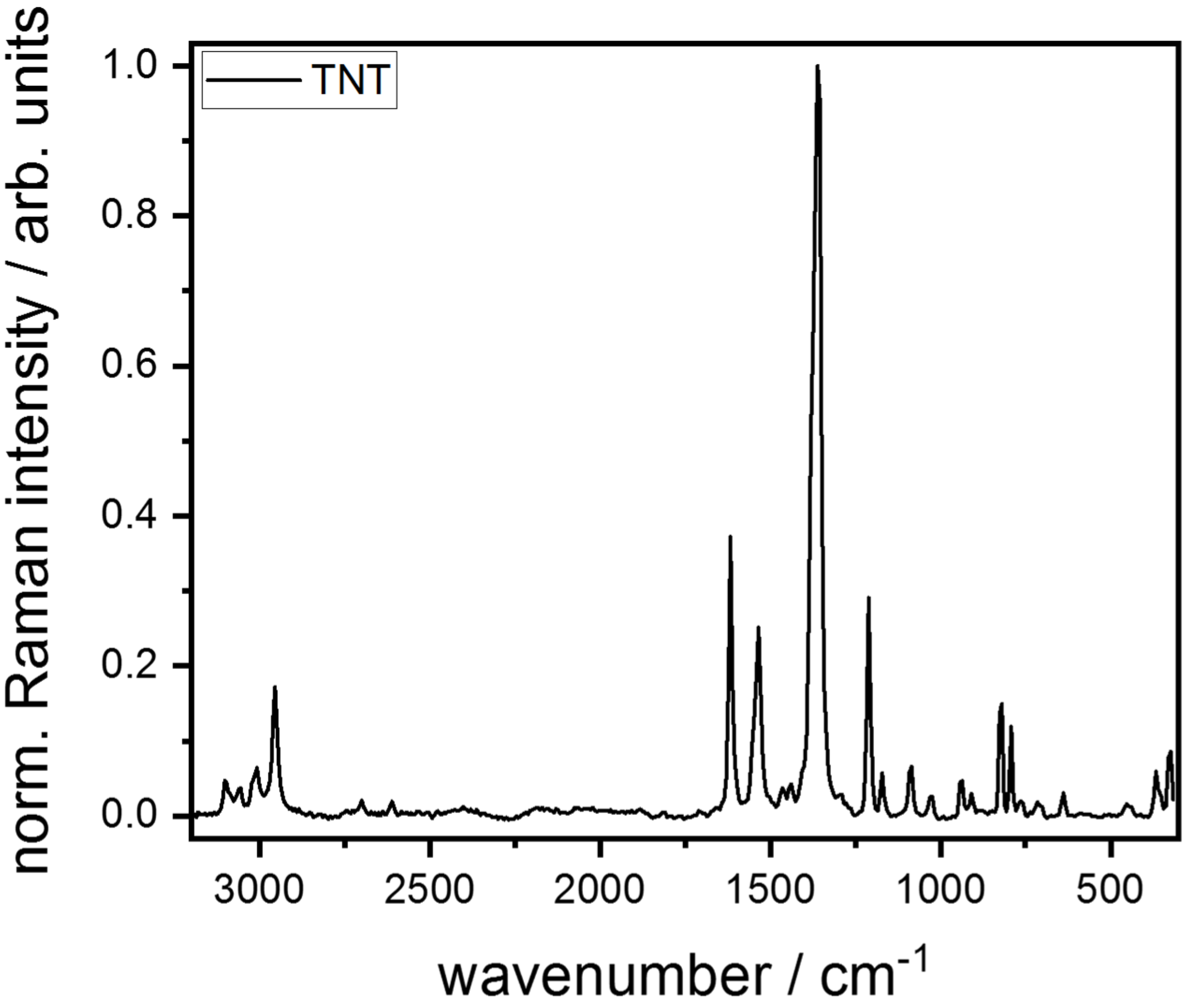

Figure 4.15. Raman spectrum of RDX in a spectral range between 3200 cm^{-1} and 300 cm^{-1}.

Table 4.5. Raman frequencies and their assignments of TNT

Raman frequencies of TNT		
Experiment / cm^{-1}	**Literature / cm^{-1} [49]**	**Assignments [44, 49]**
323 w	326	C-N tors, ring bend
352 vw	355	ring bend
367 w	366	CH_3 def, ring bend
439 vw	442	C-CH_3 wag

453 vw	457	ring tors
638 vw	639	ring bend
701 vw	704	ring tors
716 vw	717	4 NO_2 bend
736 vw	736	ring bend, 2,6-NO_2 sci
764 vw	760	2,4,6 NO_2 bend, ring tors
792 m	792	ring bend, C-CH_3 str, 2,4,6-NO_2 sci
819 m	822	2,4,6 NO_2 sci, ring bend
908 vw	907	2,4,6 NO_2 sci, ring bend, C-N str
936 w	939	C-H (ring) bend
1024 vw	1025	CH_3 def
1085 w	1086	C-H (ring) bend
1171 w	1170	C-C (ring) bend, 2,4,6 C-N str, C-CH_3 str
1211 s	1210	ring breath
1290 vw	1292	ring str
1358 vs	1359	4 NO_2 sym str, C-N str
1365 vs	1365	2,6 NO_2 sym str, C-N str
1371 vs	1375	2,4,6 NO_2 sym str, C-N str
1383 s	1381	CH_3 umb
1407 w	1403	ring str
1438 vw	1438	ring str, CH_3 def
1445 vw	1446	CH_3 def
1465 vw	1466	CH_3 def
1534 s	1533	4 NO_2 asym str, ring str
1553 m	1551	2,4,6 NO_2 asym str
1617 s	1618	2,6 asy str, ring str
2955 m	-	C-H (methyl) str
3008 w	-	C-H (ring) str
3056 vw	-	C-H (ring) str
3103 vw	-	C-H (ring) str

TNT marker band vibrations (1358 cm^{-1} - 1371 cm^{-1}; three NO_2 symmetric stretching vibrations) is marked in red. Notes: vs – very strong, s – strong, m – medium, w – weak, vw – very weak; asym – asymmetric, bend – bending, breath – breathing, def – deformation, rock – rocking, sci – scissoring, sym – symmetric, str – stretching, tors – torsion, twist – twisting, umb – umbrella, wag – wagging

4.6.2 Size Distributions of SFE-Produced Hexolite Composites

Particle size distributions of all SFE produced hexolite nanocomposites were estimated by Atomic Force Microscopy. For this purpose, the heights of 200 nanoparticles of each hexolite mixture were measured. The results, the fitted size distributions and the particle mean sizes (d_{hex}) of each hexolite sample are presented in Figure 4.17. Figure 4.17.a) (and b) depicts an example AFM topographic map of SFE-40/60 nanoparticles which is typical for hexolite size distribution AFM measurements. Particles with relatively large heights were measured individually by using smaller scan areas and less scan rates to ensure if they consist of single nanoparticles or if they are single submicron particles. If these individual AFM scans could clearly identify agglomerates these particles were not counted. Contrary, if an agglomeration of single nanoparticles could not be proven, the particle was considered within the statistics. An AFM topographic map of one of these typical agglomerates (SFE-20/80) is depicted in **Figure 4.17**.c) (and d). The height profile shows unambiguously that the scanned agglomerate is formed by several single nanoparticles.

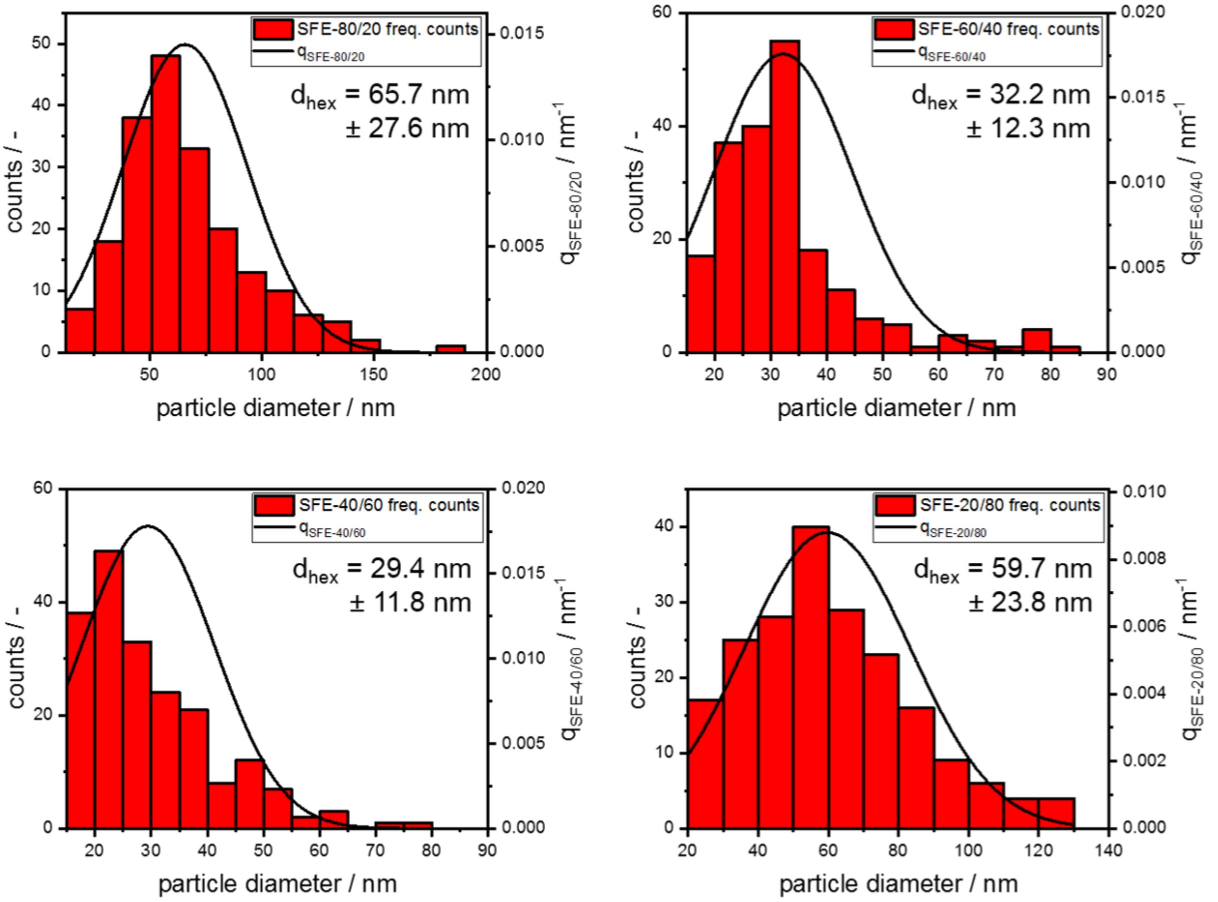

Figure 4.16. Size distribution of SFE-produced hexolite nanoparticles.

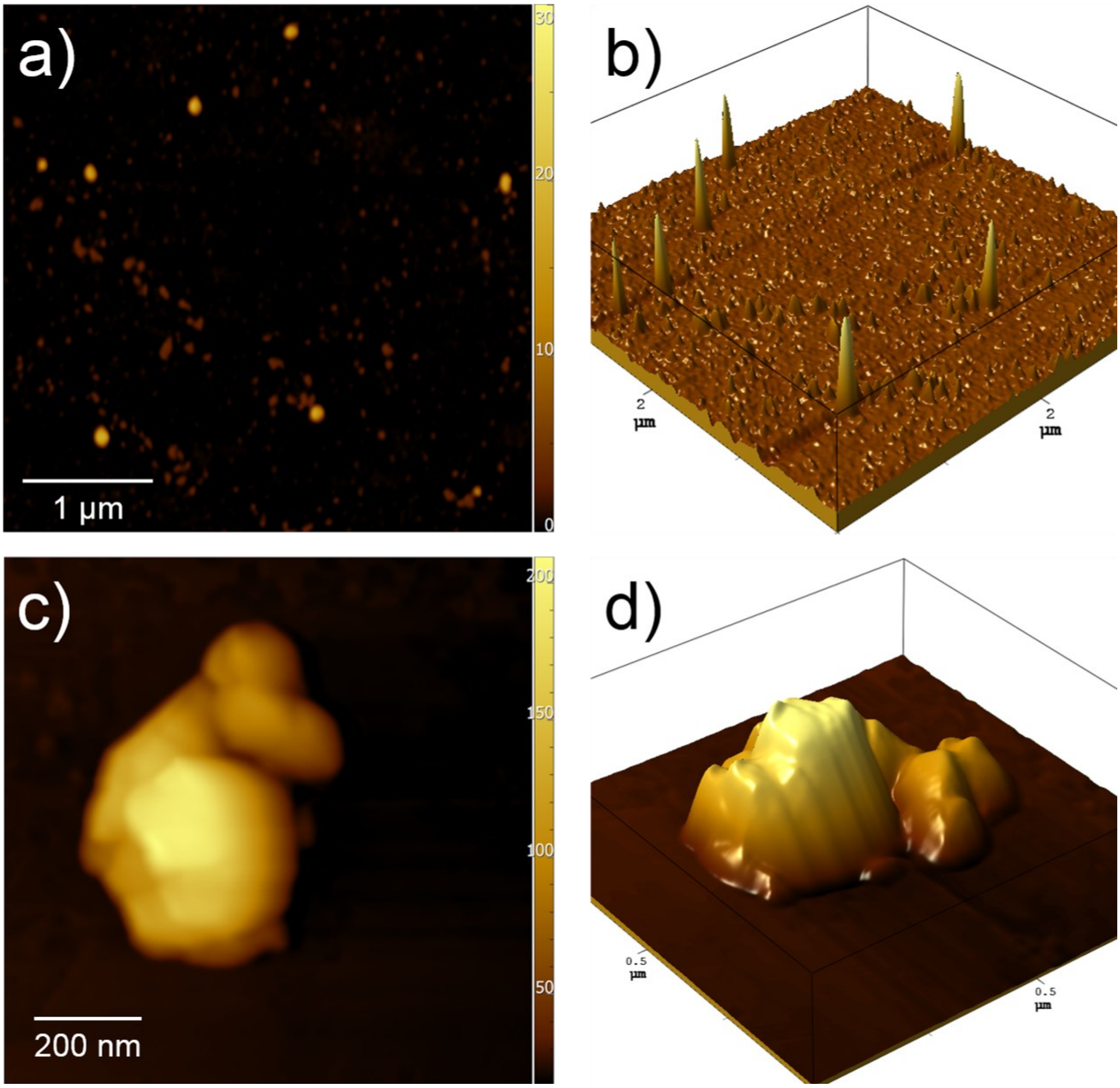

Figure 4.17. a) AFM topographic map of SFE-40/60. **b)** 3D representation of a). **c)** AFM topographic map of a SFE-40/60 agglomerate. **d)** 3D representation of c).

4.6.3 Measurement of Droplet Size and Velocity in the SFE Process

In order to obtain information about the acetone droplets size evolution and their axial and radial velocities as functions of the distance from the nozzle during the Spray Flash Evaporation (SFE) process, Phase Doppler particle analysis (PDPA) measurements were performed on a pure acetone spray using the same SFE conditions as presented in the experimental section of the main text (nozzle diameter: 80 µm; nozzle temperature: 160 °C; pressure: 40 bar). The used PDPA device consists of a FlowExplorer 2D (Dantec Dynamics, Danemark), a HiDense PDA receiver (Dantec Dynamics, Danemark) and a BSA P800 burst spectrum analyzer (Dantec Dynamics, Danemark). The FlowExplorer 2D act as light source and consists of two diode lasers with respective wavelengths of 532 nm and 561 nm and an output power of 300 mW. These laser beams form an intersection point at a set focal length of 200 mm behind the light source. The intersection volume of the two lasers defines the measurable volume which is formed by an ellipsoid with a length of 0.68 mm, a diameter of 0.1 mm and thus a resulting volume of $3.56 \cdot 10^{-3}$ mm^3. Light scattered at acetone droplets is collected by the FiberPDA receiver which is equipped with three photodiodes allowing a large measurable size range and a high resolution. The receiver optics provide a focal length of 310 mm from the laser intersection. The angle φ between light source and receiver optics is set to 120°. To enable spray investigations of different spray areas, the whole optical setup is installed on an adjustable 3D axis table. The axial droplet velocity U (z – direction, Figure 4.18.a) is measured by the 532 nm laser, the radial droplet velocity V (y – direction, Figure 4.18.a) is measured by the 561 nm laser. 20000 droplets were measured at each PDPA measurement. The axial velocity U and the radial velocity V was calculated from the Doppler frequency f_D with

$$U = \frac{\lambda}{2\sin(\theta/2)} f_D \qquad \text{Eq. 4.3}$$

Respectively

$$V = \frac{\lambda}{2\sin(\theta/2)} f_D \ , \qquad \text{Eq. 4.4}$$

where represents the angle between the two laser beams at the beam intersection. The droplet size s_d was calculated by the phase difference Φ between the signals of two detectors with

$$s_D = \frac{\Phi\lambda}{2\pi} \cdot \frac{\sqrt{2(1-\cos\theta\cos\psi\cos\varphi}}{\sin\theta\sin\psi}, \qquad \text{Eq. 4.5}$$

where ψ represents the angle between two scattered light beams receiving two different photo detectors at the laser beam intersection. Figure 4.18.a) and Figure 4.18.b) display the distribution of the axial respectively rotational velocity as a function of the scanned areas. Figure 4.18 c) depicts the droplet mean size distribution in the spray as a function of the scanned area. The origin of the coordinate system was set to the nozzle position. Figure 4.19 gives the evolution of the droplet mean size, the axial velocity and the radial velocity as functions of the distance from the nozzle. Thus, the droplet mean size was found as 2.6 µm ± 0.8 µm behind the nozzle. The shrinking of the droplet size follows approximately a linear decay. The partially negative velocity and the relatively large error bars of the radial velocity V (Figure 4.19, right) can be interpreted as turbulences inside the spray.

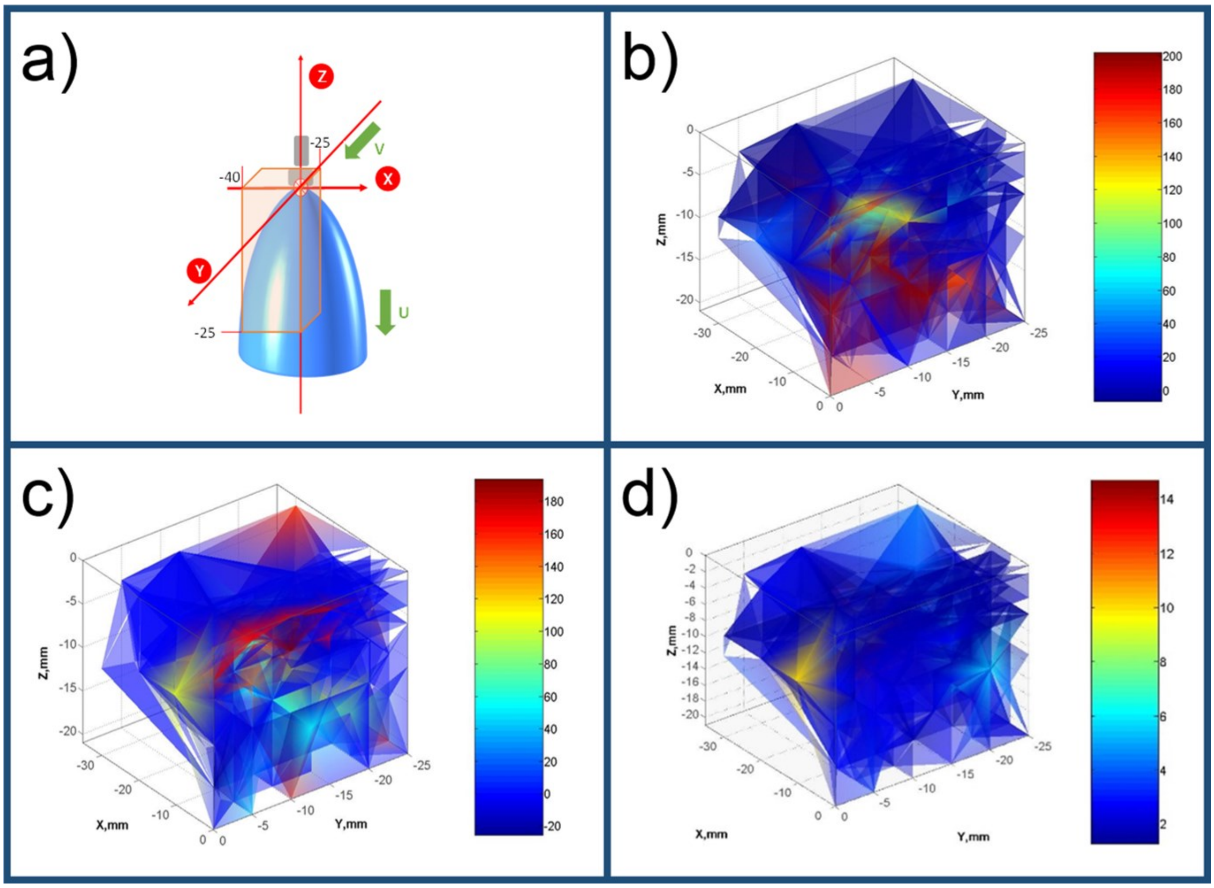

Figure 4.18. a) Schematic representation of the spray and the measurement zone. The measurement zone depends on x-, y- and z- positions set by the 3D axes table. The origin of the coordinate system is centered at the nozzle outlet position. Shown dimensions are (given in mm). **b)** Mean axial velocity *U* distribution in the first quarter of the spray (given in ms^{-1}). **c)** Mean radial velocity V distribution in the first quarter of the spray (given in ms^{-1}). **d)** Mean droplet size distribution in the first quarter of the spray (given in µm).

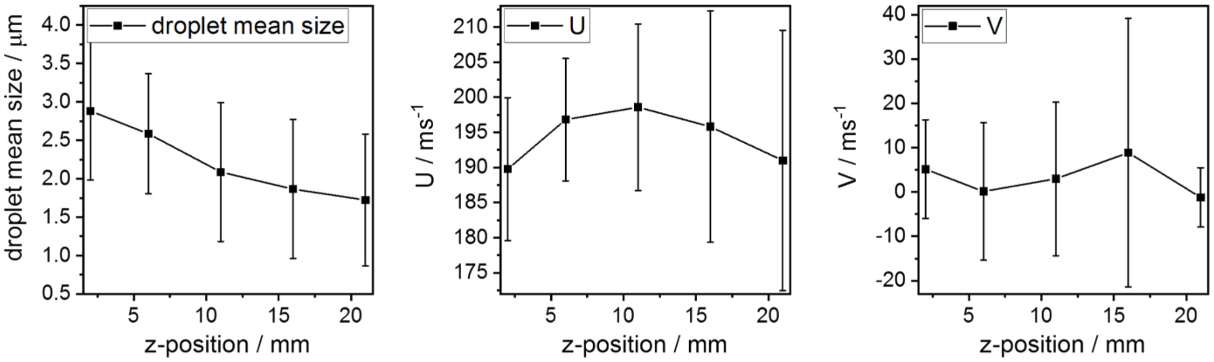

Figure 4.19. Left: Evolution of the droplet mean size as a function of the distance from the nozzle. **Middle:** Axial velocity U as a function as a function of the distance from the nozzle. **Right:** Axial velocity U as a function as a function of the distance from the nozzle.

4.6.4 Estimation of RDX Core Diameters and TNT Shell Thicknesses for Isotropic Hexolite Core/Shell Nanoparticles

The theoretical diameters of the RDX cores and the TNT shell thicknesses of the diverse isotropic hexolite core/shell nanoparticles were calculated from the RDX and TNT mass fractions (ω_{RDX}, ω_{TNT}), the measured particle means radius (r_{hex}) and the densities of RDX and TNT (ρ_{RDX}, ρ_{TNT}). A typical isotropic core/shell particle is presented in Figure 4.20.

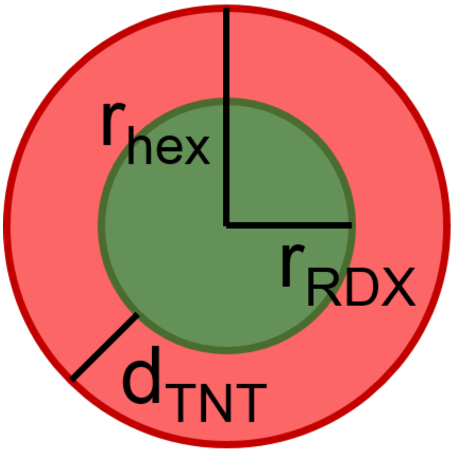

Figure 4.20. Schematic representation of an isotropic hexolite RDX/TNT core/shell nanoparticle; r_{hex} gives the particle radius, r_{RDX} represents the radius of the RDX core and d_{TNT} the TNT shell thickness.

For a given RDX/TNT mass fraction ratio, the RDX and TNT masses of a hexolite core/shell nanoparticle behave like:

$$\frac{m_{RDX}}{m_{TNT}} = \frac{\omega_{RDX}}{\omega_{TNT}} \,. \qquad \text{Eq. 4.6}$$

Furthermore, the densities of RDX and TNT behave like:

$$\frac{\rho_{RDX}}{\rho_{TNT}} = \frac{\frac{m_{RDX}}{V_{RDX}}}{\frac{m_{TNT}}{V_{TNT}}} = \frac{m_{RDX}}{V_{RDX}} \cdot \frac{V_{TNT}}{m_{TNT}} \,. \qquad \text{Eq. 4.7}$$

The Volume of a typical spherical hexolite core/shell nanoparticle can be given as the sum of RDX core volume and TNT shell volume:

$$V_{hex} = V_{RDX} + V_{TNT} \,. \qquad \text{Eq. 4.8}$$

In order to calculate the mean radius r_{RDX} of the RDX core, Eq. 4.6 is rearranged to m_{TNT} and Eq. 4.7 is rearranged to V_{TNT}:

$$m_{TNT} = \frac{\omega_{TNT} \cdot m_{RDX}}{\omega_{RDX}} \,. \qquad \text{Eq. 4.9}$$

$$V_{TNT} = \frac{m_{TNT} \cdot V_{RDX} \cdot \rho_{RDX}}{m_{RDX} \cdot \rho_{TNT}} \,. \qquad \text{Eq. 4.10}$$

Inserting Eq. 4.9 in Eq. 4.10 results in:

$$V_{TNT} = \frac{\omega_{TNT} \cdot V_{RDX} \cdot \rho_{RDX}}{\omega_{RDX} \cdot \rho_{TNT}} \,. \qquad \text{Eq. 4.11}$$

Inserting Eq. 4.11 in Eq. 4.8 and rearranging towards V_{RDX} result in:

$$V_{RDX} = \frac{V_{hex}}{1+\frac{\omega_{TNT}}{\omega_{RDX}} \cdot \frac{\rho_{RDX}}{\rho_{TNT}}} \ . \qquad \text{Eq. 4.12}$$

By using the sphere volume ($V = \frac{4}{3}r^3\pi$), r_{RDX} can be finally given as:

$$r_{RDX} = \frac{r_{hex}}{\sqrt[3]{1+\frac{\omega_{TNT}}{\omega_{RDX}} \cdot \frac{\rho_{RDX}}{\rho_{TNT}}}} \ . \qquad \text{Eq. 4.13}$$

Finally, the mean diameter of the TNT shell thickness is:

$$d_{TNT} = r_{hex} - r_{TNT} \ . \qquad \text{Eq. 4.14}$$

Calculated RDX core radii and diameters for the diverse assumed isotropic hexolite RDX/TNT core/shell nanoparticles are summed up in Table 4.6. The density of RDX amounts 1.82 g/cm^3, the density of TNT is given with 1.65 g/cm^3.

Table 4.6. Estimated RDX core radii and diameters and TNT shell thicknesses for isotropic hexolite core/shell nanoparticles

mass fraction ratio (RDX/TNT)	**particle mean size**	r_{hex}	r_{RDX}	**RDX core diameter**	**TNT shell thickness**
60/40	32.2 nm	16.1 nm	13.4 nm	26.7 nm	2.7 nm
40/60	29.4 nm	14.7 nm	10.6 nm	21.2 nm	4.1 nm
20/80	59.7 nm	29.9 nm	17.0 nm	34.0 nm	12.9 nm

4.7 References

1. Mochalin, V. N.; Shenderova, O.; Ho, D.; Gogotsi, Y., The properties and applications of nanodiamonds. *Nature Nanotechnology* **2012,** *7* (1), 11-23.
2. Danilenko, V. V., On the history of the discovery of nanodiamond synthesis. *Phys. Solid State* **2004,** *46*.
3. Chang, Y. R., Mass production and dynamic imaging of fluorescent nanodiamonds. *Nature Nanotech.* **2008,** *3*.
4. Mochalin, V. N.; Gogotsi, Y., Wet chemistry route to hydrophobic blue fluorescent nanodiamond. *J. Am. Chem. Soc.* **2009,** *131*.
5. Shimkunas, R. A., Nanodiamond–insulin complexes as pH-dependent protein delivery vehicles. *Biomaterials* **2009,** *30*.
6. Purtov, K. V.; Petunin, A. I.; Burov, A. E.; Puzyr, A. P.; Bondar, V. S., Nanodiamonds as carriers for address delivery of biologically active substances. *Nanoscale Res. Lett.* **2010,** *5*.
7. Alhaddad, A., Nanodiamond as a vector for siRNA delivery to Ewing sarcoma cells. *Small* **2011,** *7*.
8. Chow, E. K., Nanodiamond therapeutic delivery agents mediate enhanced chemoresistant tumor treatment. *Sci. Transl. Med.* **2011,** *3*.
9. Maze, J. R., Nanoscale magnetic sensing with an individual electronic spin in diamond. *Nature* **2008,** *455*.
10. Holt, K. B., Diamond at the nanoscale: Applications of diamond nanoparticles from cellular biomarkers to quantum computing. *Phil. Trans. Roy. Soc. A* **2007,** *365*.
11. Ivanov, M. G.; Pavlyshko, S. V.; Ivanov, D. M.; Petrov, I.; Shenderova, O., Synergistic compositions of colloidal nanodiamond as lubricant-additive. *J Vac. Sci. Technol. B* **2010,** *28*.
12. Dolmatov, V. Y., Detonation synthesis ultradispersed diamonds: Properties and applications. *Usp. Khim.* **2001,** *70*.
13. Guillevic, M.; Pichot, V.; Fioux, P.; Schnell, F.; Spitzer, D., Nanodiamond-based energetic core-shell composites: The route towards safer materials. *Diamond Relat. Mater.* **2019,** *93*, 150-158.
14. Danilenko, V. V., *Synthesis, Properties and Applications of Ultrananocrystalline Diamond*. 2005.
15. Shenderova, O. A.; Gruen, D. M., *Ultrananocrystalline Diamond: Synthesis, Properties, and Applications*. 2006.

16. Anischkin, V. F., Isotope Studies of Detonation Mechanisms of TNT, RDX and HMX. *Combustion, Explosion and Shock Waves* **2007,** *43*.

17. Kozyrev, N. V.; Golubeva, E. S., Investigation of the synthesis of ultradispersed diamonds in mixtures of TNT with RDX, HMX and PETN. *Combustion, Explosion and Shock Waves* **1992,** *28*.

18. Malkov, I. Y. u., Formation of diamond from the liquid phase carbon. *Combustion, Explosion and Shock Waves* **1993,** *29*.

19. Titov, V. M.; Tolochko, B. P.; Ten, K. A.; Lukyanchikov, L. A.; Zubkov, P. I., The formation kinetics of detonation nanodiamonds. In *Synthesis, Properties and Applications of Ultrananocrystalline Diamond*, Springer: 2005; pp 169–180.

20. Titov, V. M.; Anisichkin, V. F.; Mal'kov, I. Y. u., Synthesis of ultradispersed diamond in detonation waves. *Combustion, Explosion and Shock Waves* **1989,** *25*.

21. Titov, V. M.; Tolochko, B. P.; Ten, K. A.; Lukyanchikov, L. A.; Pruuel, E. R., Where and when are nanodiaomnds formed under explosion? *Diam. Relat. Mater.* **2007,** *16*.

22. Chernishev, A. P., Physical–chemical model of nanodiamond formation at explosion. *Nuclear Instruments and Methods in Physics Research A* **2004,** *575*.

23. Pichot, V.; Comet, M.; Risse, B.; Spitzer, D., Detonation of Nanosized Explosive: New Mechanistic Model for Nanodiamond Formation. *Diamond Relat. Mater.* **2015,** *54*, 59-63.

24. Pichot, V.; Risse, B.; Schnell, F.; Mory, J.; Spitzer, D., Understanding ultrafine nanodiamond formation using nanostructured explosives. *Sci. Rep.* **2013,** *3* (1), 2159.

25. Risse, B.; Hassler, D.; Spitzer, D. Preparation of Nanoparticles by Flash Evaporation. US20150000846A1, 2015.

26. Risse, B.; Spitzer, D.; Hassler, D.; Schnell, F.; Comet, M.; Pichot, V.; Muhr, H., Continuous Formation of Submicron Energetic Particles by the Flash-Evaporation Technique. *Chem. Eng. J.* **2012,** *203*, 158-165.

27. Risse, B.; Schnell, F.; Spitzer, D., Synthesis and Desensitization of Nano-β-HMX. *Propellants Explos. Pyrotech.* **2014,** *39* (3), 397-401.

28. Spitzer, D.; Pichot, V.; Risse, B. Method for manufacturing nanoparticles by detonation. US20150157997A1, 2013.

29. Spitzer, D.; Risse, B.; Schnell, F.; Pichot, V.; Klaumünzer, M.; Schaefer, M., Continuous Engineering of Nano-Cocrystals for Medical and Energetic Applications. *Sci. Rep.* **2014,** *4*.

30. Blas, L.; Klaumünzer, M.; Pessina, F.; Braun, S.; Spitzer, D., Nanostructuring of Pure and Composite-Based K6 Formulations with Low Sensitivities. *Propellants Explos. Pyrotech.* **2015,** *40* (6), 938-944.

31. Hübner, J.; Pichot, V.; Guillevic, M.; Spitzer, D., Structure Investigation of Energetic Nanocomposites Produced by Spray Flash Evaporation via AFM-TERS. In *ICORS*, South Korea, 2018.

32. Hübner, J.; Deckert-Gaudig, T.; Glorian, J.; Deckert, V. K.; Spitzer, D., Surface Characterization of Nanoscale Co-Crystals Enabled through Tip Enhanced Raman Spectroscopy. *Nanoscale* **2020**, *18*, 10306-10319.

33. Hübner, J.; Klaumünzer, M.; Comet, M.; Martin, C.; Vidal, L.; Schäfer, M.; Kryschi, C.; Spitzer, D., Insights into Combustion Mechanisms of Variable Aluminum-Based Iron Oxide/-Hydroxide Nanothermites. *Combust. Flame* **2017,** *184*, 186-194.

34. Trautmann, S.; Aizpurua, J.; Götz, I.; Undisz, A.; Dellith, J.; Schneidewind, H.; Rettenmayr, M.; Deckert, V., A Classical Description of Subnanometer Resolution by Atomic Features in Metallic Structures. *Nanoscale* **2017,** *9* (1), 391-401.

35. Deckert-Gaudig, T.; Taguchi, A.; Kawata, S.; Deckert, V., Tip-Enhanced Raman Spectroscopy–From Early Developments to Recent Advances. *Chem. Soc. Rev.* **2017**.

36. Roth, R. M.; Panoiu, N. C.; Adams, M. M.; Osgood, R. M.; Neacsu, C. C.; Raschke, M. B., Resonant-Plasmon Field Enhancement from Asymmetrically Illuminated Conical Metallic-Probe Tips. *Opt. Express* **2006,** *14* (7), 2921-2931.

37. Pettinger, B.; Domke, K. F.; Zhang, D.; Schuster, R.; Ertl, G., Direct Monitoring of Plasmon Resonances in a Tip-Surface Gap of Varying Width. *Phys. Rev. B: Condens. Matter* **2007,** *76* (11), 113409.

38. Watanabe, H.; Ishida, Y.; Hayazawa, N.; Inouye, Y.; Kawata, S., Tip-Enhanced Near-Field Raman Analysis of Tip-Pressurized Adenine Molecule. *Phys. Rev. B: Condens. Matter* **2004,** *69* (15), 155418-1-155418-11.

39. Ichimura, T.; Watanabe, H.; Morita, Y.; Verma, P.; Kawata, S.; Inouye, Y., Temporal Fluctuation of Tip-Enhanced Raman Spectra of Adenine Molecules. *J. Phys. Chem. C* **2007,** *111* (26), 9460-9464.

40. Deckert-Gaudig, T.; Rauls, E.; Deckert, V., Aromatic Amino Acid Monolayers Sandwiched Between Gold and Silver: A Combined Tip-Enhanced Raman and Theoretical Approach. *J. Phys. Chem. C* **2009,** *114* (16), 7412-7420.

41. Sonntag, M. D.; Klingsporn, J. M.; Garibay, L. K.; Roberts, J. M.; Dieringer, J. A.; Seideman, T.; Scheidt, K. A.; Jensen, L.; Schatz, G. C.; Van Duyne, R. P., Single-molecule tip-enhanced Raman spectroscopy. *J. Phys. Chem. C* **2011,** *116* (1), 478-483.

42. Klingsporn, J. M.; Jiang, N.; Pozzi, E. A.; Sonntag, M. D.; Chulhai, D.; Seideman, T.; Jensen, L.; Hersam, M. C.; Duyne, R. P. V., Intramolecular Insight Into Adsorbate–Substrate Interactions via Low-Temperature, Ultrahigh-Vacuum Tip-Enhanced Raman Spectroscopy. *J. Am. Chem. Soc.* **2014,** *136* (10), 3881-3887.

43. Bailo, E.; Deckert, V., Tip-Enhanced Raman Spectroscopy of Single RNA Strands: Towards a Novel Direct-Sequencing Method. *Angew. Chem. Int. Ed.* **2008,** *47* (9), 1658-1661.

44. Deckert-Gaudig, T.; Pichot, V.; Spitzer, D.; Deckert, V., High-Resolution Raman Spectroscopy for the Nanostructural Characterization of Explosive Nanodiamond Precursors. *ChemPhysChem* **2017,** *18* (2), 175-178.

45. Infante-Castillo, R.; Pacheco-Londoño, L.; Hernández-Rivera, S. P., Vibrational Spectra and Structure of RDX and its 13C-and 15N-Labeled Derivatives: A Theoretical and Experimental Study. *Spectrochim. Acta A* **2010,** *76* (2), 137-141.

46. Miao, M. S.; Dreger, Z. A.; Winey, J. M.; Gupta, Y. M., Density Functional Theory Calculations of Pressure Effects on the Vibrational Structure of α-RDX. *The Journal of Physical Chemistry A* **2008,** *112* (47), 12228-12234.

47. Dreger, Z. A.; Gupta, Y. M., High Pressure Raman Spectroscopy of Single Crystals of Hexahydro-1,3,5-trinitro-1,3,5-triazine (RDX). *The Journal of Physical Chemistry B* **2007,** *111* (15), 3893-3903.

48. Liu, Y.; Perkins, R.; Liu, Y.; Tzeng, N., Normal Mode and Experimental Analysis of TNT Raman Spectrum. *J. Mol. Struct.* **2017,** *1133*, 217-225.

49. Clarkson, J.; Smith, W. E.; Batchelder, D. N.; Smith, D. A.; Coats, A. M., A Theoretical Study of the Structure and Vibrations of 2, 4, 6-Trinitrotolune. *J. Mol. Struct.* **2003,** *648* (3), 203-214.

50. Bailo, E.; Deckert, V., Tip-enhanced Raman spectroscopy of single RNA strands: towards a novel direct-sequencing method. *Angew. Chem. Int. Ed.* **2008,** *47* (9), 1658-1661.

51. Goetz, F.; Brill, T., Laser Raman Spectra of Alpha.-, Beta.-, Gamma.-, and Delta-octahydro-1, 3, 5, 7-tetranitro-1, 3, 5, 7-tetrazocine and Their Temperature Dependence. *J. Phys. Chem.* **1979,** *83* (3), 340-346.

52. Goede, P.; Latypov, N. V.; Östmark, H., Fourier Transform Raman Spectroscopy of the Four Crystallographic Phases of α, β, γ and ε 2, 4, 6, 8, 10, 12-Hexanitro-2, 4, 6, 8, 10, 12-

hexaazatetracyclo-[5.5. 0.05, 9.03, 11]-dodecane (HNIW, CL-20). *Propellants Explos. Pyrotech.* **2004,** *29* (4), 205-208.

53. Infante-Castillo, R.; Pacheco-Londoño, L. C.; Hernández-Rivera, S. P., Monitoring the α→ β Solid–Solid Phase Transition of RDX with Raman Spectroscopy: A Theoretical and Experimental Study. *J. Mol. Struct.* **2010,** *970* (1-3), 51-58.

54. Watanabe, H.; Hayazawa, N.; Inouye, Y.; Kawata, S., DFT Vibrational Calculations of Rhodamine 6G Adsorbed on Silver: Analysis of Tip-Enhanced Raman Spectroscopy. *The Journal of Physical Chemistry B* **2005,** *109* (11), 5012-5020.

55. Stadler, J.; Schmid, T.; Zenobi, R., Nanoscale Chemical Imaging of Single-Layer Graphene. *ACS Nano* **2011,** *5* (10), 8442-8448.

56. Opilik, L.; Payamyar, P.; Szczerbiński, J.; Schütz, A. P.; Servalli, M.; Hungerland, T.; Schlüter, A. D.; Zenobi, R., Minimally Invasive Characterization of Covalent Monolayer Sheets Using Tip-Enhanced Raman Spectroscopy. *ACS Nano* **2015,** *9* (4), 4252-4259.

57. Karthika, S.; Radhakrishnan, T. K.; Kalaichelvi, P., A Review of Classical and Nonclassical Nucleation Theories. *Cryst. Growth Des.* **2016,** *16* (11), 6663-6681.

58. Oura, K.; Lifshits, V. G.; Saranin, A. A.; Zotov, A. V.; Katayama, M., Growth of Thin Films. In *Surface Science: An Introduction*, Springer: 2013; pp 357-387.

59. Chung, J. N., The Motion of Particles Inside a Droplet. *J. Heat Transfer* **1982,** *104* (3), 438-445.

60. Ali, A. M.; Deckert-Gaudig, T.; Egiza, M.; Deckert, V.; Yoshitake, T., Near- and far-field Raman spectroscopic studies of nanodiamond composite films deposited by coaxial arc plasma. *Appl. Phys. Lett.* **2020,** *116* (4), 041601.

5 Formation Mechanisms of Sub-Micron Pharmaceutical Composite Particles Derived from Far- and Near Field Raman Microscopy

The previously presented studies confirm that TERS respectively near-field Raman investigations of nanoscale organic composites provide new insights into their structure, arrangement and surface composition. These data allow to derive formation mechanisms and on the one hand and on the other hand they provide additional information which help to describe their specific chemical and physical behaviors. As described within chapter 2.4.1, bottom-illuminated TERS setups are limited to thin and opaque samples only. Moreover, TERS experiments are extremely time and material consuming in order to obtain statistically reliable results. So how to analyze in an appropriate time larger particles which exceed the maximal thickness accessible to TERS? Hence, a different way had to be found to enable near-field Raman structure investigations on thicker samples like sub-micron composite particles. Unfortunately, SERS experiments performed on typical SERS substrates cannot be applied for this purpose since incident light has to travel through the whole sample before it can couple to the LSPs. Accordingly, far-field signals containing information about the whole composite particle would dominate the Raman spectra and no conclusion about the surface composition could be drawn. Therefore, sub-micron composite particles consisting of Furosemide and PVP were directly coated with a thin layer of silver by sputtering. The thickness of the silver layer (40 nm) was chosen to correspond to silver nanoparticles providing a LSPR while interacting with laser light with a wavelength of 533 nm. In addition, a relatively high sputtering rate was adjusted to promote the formation of silver islands instead of a continuous silver layer. Strong Raman intensities attest that an enhanced field is formed at the surfaces of the silver island. SERS results hint on a formation of nanoscale Furosemide crystals encapsulated by PVP which agglomerate to sub-micron particles. This conclusion could be further confirmed by X-ray photoelectron spectroscopy. (This chapter is published at: Hübner, J.; Coty J.-B.; Busby, Y.; Spitzer, D., Formation Mechanisms of Sub-Micron Pharmaceutical Composite Particles Derived from Far- and Near Field Raman Microscopy, *chemRxiv.org*, **2020**, DOI: 10.26434/chemrxiv.12098478.v1)

5.1 Abstract

Surface-enhanced Raman spectroscopy (SERS) and confocal Raman microscopy are applied to investigate the structure and the molecular arrangement of a sub-micron pharmaceutical organic composite. As a model system, sub-micron Furosemide and polyvinylpyrrolidone (Furosemide/PVP) particles produced by spray flash evaporation (SFE) from a single solution are investigated. The morphology, size and crystallinity of Furosemide/PVP composites are first analyzed by scanning electron microscopy (SEM) and X-ray powder diffraction (XRPD). Afterwards, reference far-field Raman spectra and confocal far-field Raman maps of Furosemide/PVP particles are interpreted based on the far-field Raman spectra of pure Furosemide and pure PVP precursors. Confocal far-field Raman microscopy shows that Furosemide/PVP particles feature an intermixture of Furosemide and PVP molecules at the sub-micron scale. In order to have a better insight on the molecular arrangement of PVP and Furosemide in composite particles, SERS and surface-enhanced confocal Raman microscopy (SECoRM) are performed on Furosemide, PVP and Furosemide/PVP composites particles sputtered with silver (40 nm). Surface-sensitive SERS and SECoRM maps reveal that Furosemide/PVP particle surfaces mainly consist of PVP molecules coating Furosemide domains. Overall, the combination surface and bulk sensitive analyses allows drawing a clear picture of the particle morphology and the molecular arrangement in Furosemide/PVP sub-micron particles. Namely, SFE-produced Furosemide/PVP sub-micron particles are formed by the agglomeration of primary particles consisting of Furosemide nano-crystals embedded in a thin PVP matrix. Interestingly, both far-field (bulk-sensitive) and surface-enhanced (surface-sensitive) confocal Raman microscopies provide molecular information on a statistically-relevant amount of sub-micron particles in a single microscopic map; this combination is thus an effective and time-saving tool for investigating organic and inorganic sub-micron composites.

5.2 Introduction

Within the last decades, sub-micron and nanoparticles have found their use in a huge variety of medical and pharmaceutic applications. Among others composite particles are commonly used as drug delivery agents, as drug carriers, as contrast agents in diagnostic techniques like magnetic resonance imaging and in cancer therapies.[1-5] In pharmaceutic research and industry, the downsizing of active pharmaceutical ingredients (API) on the sub-micron or nanoscale is paramount topic attracting more and more interests. In particular, downsizing of pharmaceutic particles would allow increasing the aqueous solubility and the dissolution velocity of API molecules due to the increased surface-to-volume ratio.[6-8] Clinical tests confirm that downsizing of APIs on the sub-micron or nanoscale improves their solubility, their dissolution velocity and thus their bioavailability within the human body.[8-9] The formulation of nanoscale APIs is often undertaken by the use of biocompatible polymers working as host materials confining the drug within the polymeric network or as nanocapsules embedding nanocrystalline or amorphous APIs.[10-13] The development and the design of improved amorphous solid API/polymer composites, arranged in a high surface area matrix, requires the parallel development of advanced spectroscopies and microscopies capable of chemical and molecular imaging on such fragile organic sub-micron particles.[14-16] This information would allow determining the very crucial structure-to-function relations for solubility, dissolution velocity and bioavailability. Conventional analytical techniques struggle to face this challenge, because of the need of combining high sensitivity, high chemical and molecular selectivity versus possibly similar organic molecules, imaging capability with high lateral resolution (below 100 nm) and a sufficiently low energy input in order to preserve APIs and prevent their dissociation, oxidation or internal recombination.

Not surprisingly, it has been recently reported that the lack of methods allowing for the precise characterization of molecular nanocomposite at the sub-micron scale is hampering the development of such systems in the pharmaceutical area.[17-18] The first reason is that the poor knowledge about particles surface composition hinders the understanding of their *in vivo* behavior which depends on the interaction between biological elements encountered in the body and the particle surface.[17, 19] Secondly, for such increasingly complex molecular systems, the batch-to-batch consistency of needs to be validated with the highest accuracy, which is unfortunately not possible today with conventional methods. Therefore, the development of viable advanced characterization methods and protocols is very crucial for organic nanocomposites. In this work, surface-enhanced confocal Raman microscopy (SECoRM) and far-field confocal Raman microscopy are applied to investigate sub-micron pharmaceutic nanocomposite particles. The SECoRM technique ensures the high surface sensitivity of surface-enhanced Raman spectroscopy (SERS) and the high resolution of confocal Raman microscopy. Far-field Raman microscopy provides for additional information from a more volume-sensitive technique. Near-field (tip-enhanced) Raman spectroscopy was recently applied to investigate surface and structural properties of nanoscale organic composites.[20-22] However, up to now, SERS experiments were typically carried out by depositing the analyte onto special SERS substrates.[23-25] Typical SERS substrates consist of (precious) metal nanostructures (*e.g.* nanoparticles) providing a collective oscillation of their conductive band electrons in resonance with the incident light (localized surface plasmon resonances, LSPR) leading to a strong enhancement of the electric field close to the metal nanostructure surfaces.[23-26] A multitude of SERS substrates and manufacturing procedures have been reported in literature providing for nanostructures with different sizes, shapes, materials and arrangements.[23, 27-30] However, the deposition of sub-micron composite particles on SERS substrates may not lead to the desired accuracy in measuring the particle structure and arrangement since SECoRM maps are recorded in reflection-mode. Accordingly, the field-enhancing metal nanoparticles would be located below the sub-micron analyte particles from the view of the microscope objective. Thus, the incident light would have to travel through the whole analyte particle before interacting with the conductive band electrons of the metal nanoparticles in this configuration. Consequently, the far-field signals would dominate the Raman spectra. To overcome this limitation, in this study organic sub-micron particles are directly coated with silver nanoparticles deposited by sputtering. The so formed silver nano grains, better referred as silver *spasers* (surface plasmon amplification by stimulated emission of radiation), are directly formed on top of the analyte particle surface.[31] As a consequence of the strong local field enhancement the intensity of the incident laser light can be drastically reduced so that Raman spectra will be dominated by near-field signals. As a model system, results obtained on Furosemide/PVP sub-micron composite particles produced using the spray flash evaporation (SFE) process are presented. Furosemide is a poorly water-soluble loop diuretic and polyvinylpyrrolidone is a common biocompatible polymer. The technique has been previously described elsewhere and it has the advantage of allowing for the continuous production of sub-micron and nanoscale organic compounds and composites from the vacuum spraying of a pressurized and heated solution.[22, 32-38]

5.3 Experimental Section

5.3.1 Chemicals

Furosemide and Polyvinylpyrrolidone (PVP, K30) were purchased by Sigma-Aldrich (St. Louis, Missouri, USA) and were used without further purification. Ethanol absolute (>99.98%, AnalR NORMAPUR) was sourced by VWR (Radnor, Pennsylvania, USA) and Dichloromethane (DCM) (>99.5% for synthesis) was provided by Carl Roth GmbH (Karlsruhe, Germany). Both solvents were used without further purification.

5.3.2 Production of Furosemide/PVP Sub-Micron Composite Particles

Furosemide/PVP sub-micron composite particles were produced by SFE process (Figure 5.1). A solution of 3.0 g Furosemide and 1.0 g PVP in a solvent mixture of 240 mL ethanol and 160 mL dichloromethane was prepared first. This solution was given into the solution tank of a vertical SFE crystallizer pressurized at 40 bar (N_2). The Furosemide/PVP solution was sprayed through a 120 °C preheated hollow cone nozzle with a diameter of 100 µm into a vacuum reactor chamber with a base pressure below 0.1 mbar. The pressure inside the SFE atomization chamber varied between 5 and 10 mbar during the spraying process. After the fast solvent evaporation Furosemide/PVP submicron particles are collected with a steel filter as a white-yellowish ultra-fine powder.

5.3.3 Silver Coating of Furosemide, PVP and Furosemide/PVP Sub-Micron Particles

For surface-enhanced Raman spectroscopy, Furosemide, PVP and Furosemide/PVP submicron particles were deposited on glass substrates and uniformly distributed by a gentle robbing of two glasses. Afterwards, the cover glasses were sputtered with silver in an HHV Auto 306 (Bangalore, India) sputtering device at a distance of 15 cm from the silver target. All prepared samples were directly coated with 40 nm nominal thickness of silver at a deposition rate of

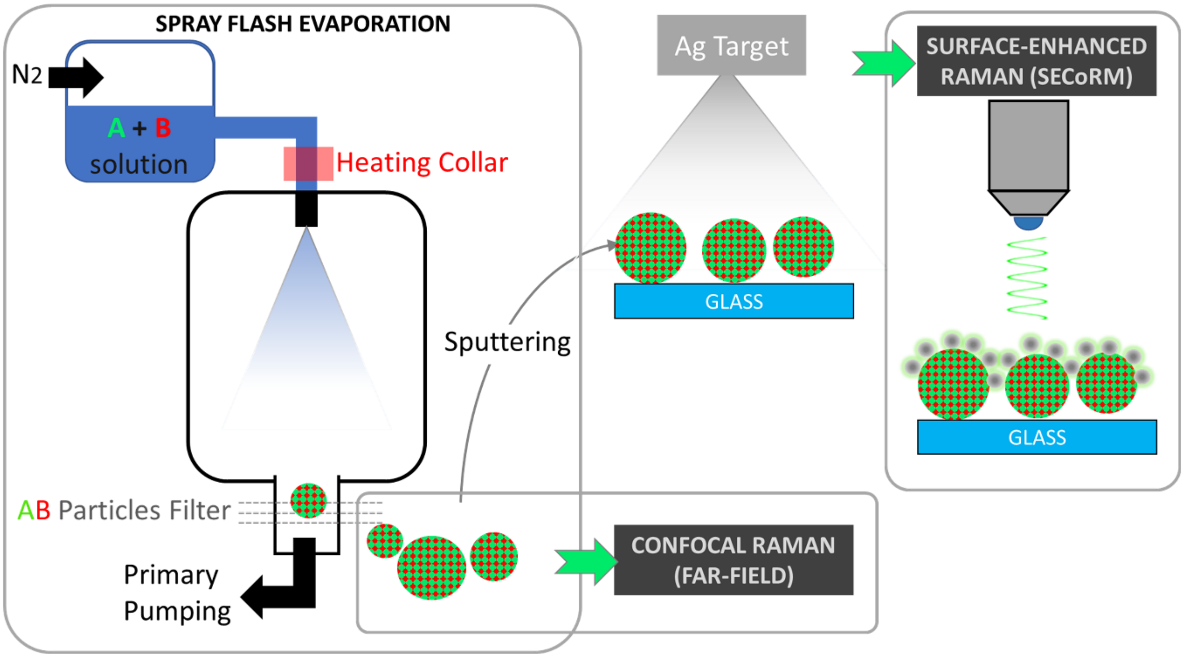

Figure 5.1. Schematic representation of the performed experiments. Furosemide/PVP sub-micron composites are produced by the Spray Flash Evaporation process. The structure of these particles is evaluated by comparing the results of bulk-sensitive confocal far-field Raman microscopy and surface-sensitive surface enhanced confocal Raman microscopy (SECoRM).

4.0 Å/s. A schematic representation of the silver coating and the formed silver spaser on a submicron composite particle formed by two compounds with random molecular arrangement is presented in Figure 5.1.

5.3.4 Analysis Methods

Scanning Electron Microscopy (SEM) images were recorded on a FEI Nova NanoSEM 450 (Hillsboro, Oregon, USA) at an acceleration voltage of 10 kV using an in-lens secondary electron detector. To prevent charge accumulation, Furosemide/PVP particles were coated with a 10 nm thick layer of gold by sputtering before the analysis. The size distribution and particle mean size of Furosemide/PVP sub-micron particles were determined by measuring 260 particles using ImageJ software. The particle size distribution was fitted with a Gaussian line shape using OriginPro 2019b (version 9.6.5.169).

X-ray powder diffraction (XRPD) was performed on a Bruker AXS Advance D8 (Karlsruhe; Germany) diffractometer using Cu-K$_{\alpha}$ radiation (λ= 1.54 Å) in Bragg–Brentano geometry. The acceleration voltage was 40 kV and the operating current 40 mA. The step size for all scans was set to 0.0148° (2 θ). The loose powder samples were measured on a rotating sample holder. The coherence length L_{hkl} was calculated from the full width at half maximum (FWHM) of single diffraction peaks by using the well-known Scherrer equation assuming Gaussian-shaped peaks.

Confocal Raman spectroscopy and microscopy were performed on a HORIBA (Kyoto, Japan) LabRam HR evolution confocal Raman microscope. Single point spectra of uncoated samples were obtained with a linear polarized 532 nm diode laser excitation with an adjusted output power of 1.8 mW at an acquisition time of 3 s/spectrum. Single-point SERS spectra of silver sputtered samples were taken with an acquisition time of 3 s and a laser output power of 54 µW. Confocal far-field Raman microscopy maps of pristine samples and surface-enhanced confocal Raman microscopy maps **(SECoRM)** of silver sputtered samples along the substrate plane were also recorded with the 532 nm diode laser and output power of 54 µW with an acquisition time of 0.5 s/spectrum, step size between 200 and 500 nm. The laser light was focused onto the sample through a 100×, 0.9 NA objective. Raman scattered photons were collected by the same objective through an edge filter, a confocal aperture with a diameter adjusted to 200 nm for far-field experiments and 50 nm for SERS experiments and a diffraction grating with 300 lines/mm before hitting a deep cooled CCD camera (- 60°C). Confocal Raman maps were analyzed and treated using LabSpec Spectroscopy Suite 6.4.4. (HORIBA; Kyoto, Japan).

X-Ray photoelectron spectroscopy (XPS) was carried on a Thermo Scientific Escalab 250 Xi (Waltham, Massachusetts, USA) by acquiring survey and high-resolution scans of C1s, N1s, Cl2p, O1s and S2p with a monochromatic Al k-α source. Two independent procedures are applied to determine the molecular fraction in the composite surface; the first is by peak fitting the C1s spectrum and comparing the peak area of the component associated to carboxylic groups (R-COOH) from Furosemide and the one from R-CNOH groups from PVP. Alternatively, from the N/Cl ratio in pure Furosemide formulated by SFE, we derive the Furosemide contribution to the total nitrogen content in the PVP/Furosemide surface which allows counting the ratio between Furosemide and PVP molecules at the composite surface. This ratio is compared with the Furosemide:PVP molar ratio in the precursor solution to evaluate the tendency of each compound to form a core/shell arrangement.

5.4 Results and Discussion

5.4.1 Structure and Morphology Analysis of Furosemide/PVP Particles

A first insight on the size, morphology and crystallinity of Furosemide/PVP particles is provided by SEM and XRPD analyses (Figure 5.2) showing the presence of spherical sub-micron particles with a rough cauliflower-like surface. Furosemide/PVP particles feature a mean diameter size of 0.38 µm (± 0.24 µm). The Furosemide/PVP sub-micron particles crystal structure was investigated by XRPD. XRPD pattern shows typical reflections from Furosemide crystals superimposed a broad amorphous reflection between 16° and 25° ascribed to PVP. The

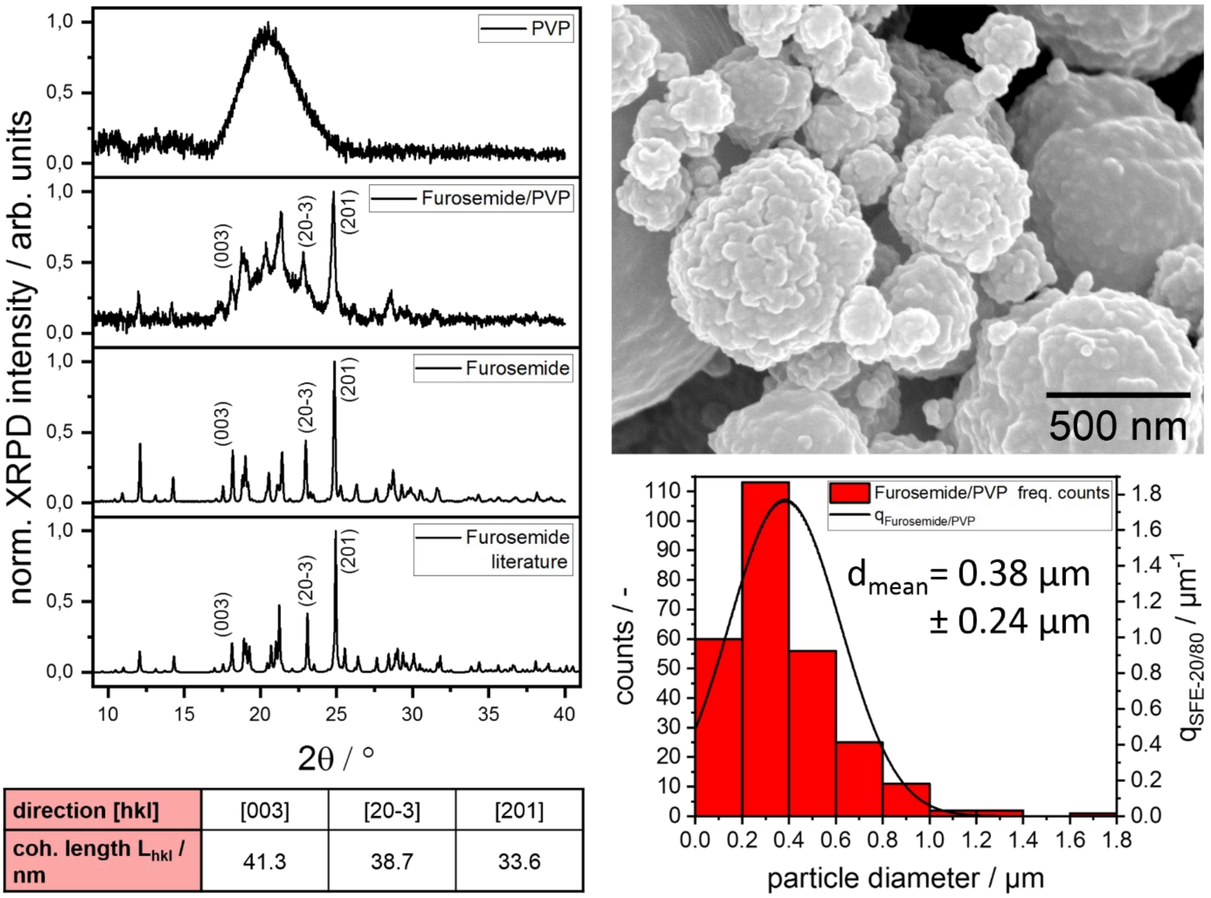

direction [hkl]	[003]	[20-3]	[201]
coh. length L_{hkl} / nm	41.3	38.7	33.6

Figure 5.2. Left: XRPD pattern of Furosemide and PVP precursors, Furosemide/PVP sub-micron particles and a reference XRD pattern of Furosemide. The coherence lengths derived from the XRPD pattern of Furosemide/PVP indicates the formation of nano-structured Furosemide crystals. **Right:** SEM image of Furosemide/PVP particles characterized by a rough cauliflower-like surface. Furosemide/PVP particles provide a mean size of 0.38 µm (± 0.24µm).

coherence lengths along the main crystallographic directions reveal that furosemide crystals dimensions are below 50 nm, i.e. about ten times smaller than the average particles size estimated from SEM analysis. From these results, we conclude that SEM particles correspond to large aggregates, however, no information is available on the arrangement of furosemide and PVP molecules within single sub-micron composite particles. To fill in this gap, far-field and SERS Raman spectroscopy is subsequently applied to investigate Furosemide/PVP sub-micron particles.

5.4.2 Far-Field Raman and SERS Investigations of Pure Furosemide and PVP

In order to facilitate the interpretation of Raman spectra from Furosemide/PVP composites, far-field Raman spectra and maps of pure, commercial Furosemide and PVP particles are characterized first. Afterwards, specific marker bands allowing to clearly distinguish between Furosemide and PVP signals in the composite particles spectra and images are identified from these datasets. Ideally, marker bands should be selected in wavenumber regions where no (or nearly no) signal superposition occurs. This procedure was already successfully applied in a TERS study aimed to identify RDX and TNT molecules in RDX/TNT composite nanoparticles and CL-20 and HMX layers in CL-20/HMX nanoscale co-crystals.[21-22] For Furosemide, the chosen marker band is the in-plane ring bending vibration at 686 cm^{-1}.[39] For PVP, the selected marker band is the most intense CH_2 asymmetric stretching vibrations of the saturated PVP chains at 2924 cm^{-1}.[40] The far-field Raman spectra and the marker bands of pure Furosemide (red) and PVP (green) compounds are shown in Figure 5.3.a. Specific molecular orientation is known to affect the relative peak intensities in surface-enhanced Raman spectra. Because of this, marker bands selected in far-field spectra may not be useful in the molecular identification in surface-enhanced spectra from silver-coated pure Furosemide and PVP particles. The eventual modification of relative peak intensities is useful to demonstrate that the silver spasers are effective in enhancing the local field at the particles surface. For this, pure compounds particles are sputtered with silver at the relatively high sputtering rate of 4.0 Å/s to favor the formation of silver islands spasers instead of a continuous metal layer. As expected, the obtained SECoRM maps of silver-coated Furosemide and PVP sensibly differ from the corresponding far-field Raman maps by slight peak position shifts and by the relative Raman

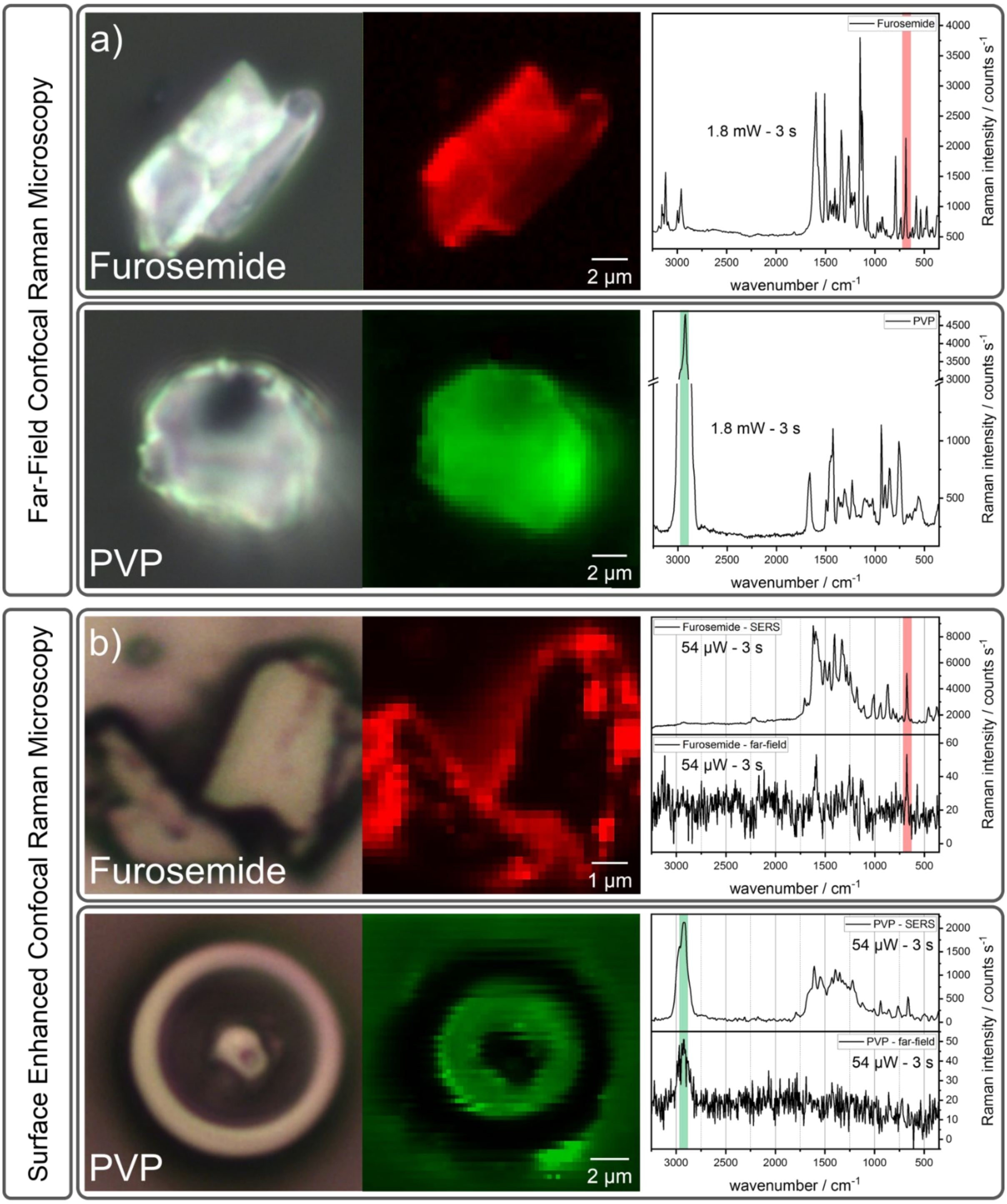

Figure 5.3.a) Optical microscopy images and the corresponding far-field Raman maps and spectra for pure Furosemide and PVP. The in-plane ring bending vibration localized at 686 cm^{-1} (red) is chosen as marker band for Furosemide and the CH$_2$ asymmetric stretching vibrations of PVP at 2924 cm^{-1} (green) is selected for PVP identification. **b)** SECoRM maps and SERS spectra of silver coated Furosemide and PVP showing the presence of the chosen marker bands.

intensities. Compared to far-field spectra, SERS spectra show sensibly higher intensities which allows reducing the intensity of the incoming laser beam by 1/33. The increase of the total Raman intensity points to a successful field enhancement by silver spasers. In far-field spectra, the brighter spots in the microscope image (generated from Raman intensity of the marker band) simply correspond to the region characterized by a higher number of molecules (bulk-sensitive). As evident from Figure 5.3.b, this is not the case in surface-enhanced spectra, for which the brightest spots are located at particles edges, while central regions display extremely weak signal enhancement. This phenomenon can be explained by the fact that the incident laser light (532 nm) is linearly polarized and focused (along the z - direction) on the sample by a 100× objective with a numeric aperture of 0.9 and that the local enhancement of the electromagnetic field is provided by the localized surface plasmon resonances (LSPR) at the silver nano grain surfaces. In our configuration the incident light electric field vector $\vec{E}_{in}$ oscillates in the plane parallel to the sample substrate (i.e. parallel to the xy-plane). Accordingly, the field created by the LSPR is also parallel to the xy-plane (Figure 5.4). In this geometry, silver particles lying on top of a flat crystal will not contribute to the measured Raman intensity enhancement because no (or nearly no) Raman scattering molecules are located in the enhanced field area (Figure 5.4, left). Reversely, silver spasers located at vertical surfaces (i.e. sharp edges) lead to a strong Raman intensity enhancement since a relatively high number of Raman scattering molecules are located within the provided enhanced electric field (Figure 5.4, left). Both Furosemide and PVP SERS spectra of silver-coated samples feature significantly higher Raman intensities of the selected marker bands especially for particles edges. Although an accurate calculation of the enhancement factor is not possible because the high variability of the number of molecules localized in the enhanced field areas, Raman intensities in SERS spectra exceed the intensities of far-field spectra by factor between 80 and 200. The real field enhancement factor is suposed to be much higher since in SERS spectroscopy the signal comes from only a few molecules in the proximity of silver spasers, while in far-field spectra all molecules contained in microscopic grains contribute to the scattering intensity.

Since the silver spasers are in direct contact with the sample surfaces also chemical enhancements may contribute to the total enhancement. This may be evident in the CH_2 asymmetric stretching vibration of PVP (marker band) occurring at the Stoke shift of 2924 cm^{-1}, equivalent to 630 nm, which seems to be additionally enhanced by a chemical interaction with the silver surfaces. Light of this wavelength does not (or only barely) induce a resonant oscillation of the localized surface plasmons of silver nanoparticles with a mean diameter of

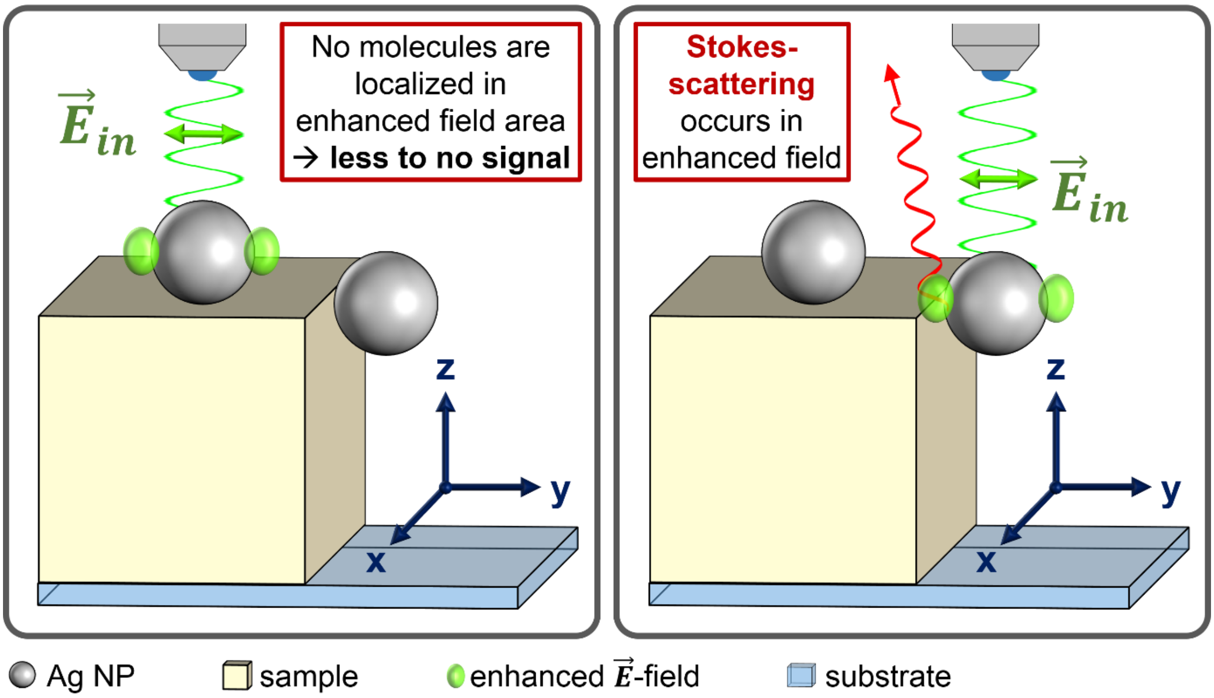

Figure 5.4. Schematic geometrical illustration of the coupling between the incident radiation field ($\vec{E}_{in}$) with localized surface plasmons generating a strong electric field parallel to $\vec{E}_{in}$ at the silver nanoparticle surface. **Left:** The illuminated Ag NP lies on a flat surface thus no (or nearly no) molecules are localized in the enhanced field area. Consequently, no (or nearly no) photons are Raman scattered and contribute the SERS spectrum. **Right:** The illuminated Ag NP is attached on a perpendicular surface (towards $\vec{E}_{in}$). Many molecules are localized within the enhanced field leading to frequent Raman scattering.

few tens of nm.[41] Therefore, Stoke shifted light emitted in this range is expected to be less enhanced as compared to resonant wavelengths (E^2 instead of E^4 enhancement).[26] Despite of this, the intensity ratio between the PVP marker band intensity and the next most intense band only decreases from about 5:1 (far-field spectra) to ~2:1 (in SERS spectra). Thus, it is supposed that a charge transfer between the silver surface and the absorbed PVP molecules may take place resulting in an amplification of the molecule polarizability. Interestingly, both Furosemide and PVP SERS spectra clearly display two very broad background signals (with point-to-point variable intensity) roughly centered at 1600 cm^{-1} and 1350 cm^{-1}. Mao *et al.* found similar signals in Raman spectra of PVP functionalized with one-dimensional silver nanowires and ascribed the signal at 1605 cm^{-1} to the shifted C=O stretching vibration (from 1665 to 1605 cm^{-1}) due to the chemical interaction of PVP carbonyl functional group from with the silver surfaces.[40] In our case the broad features at 1600 cm^{-1}, and 1350 cm^{-1} appearing in both

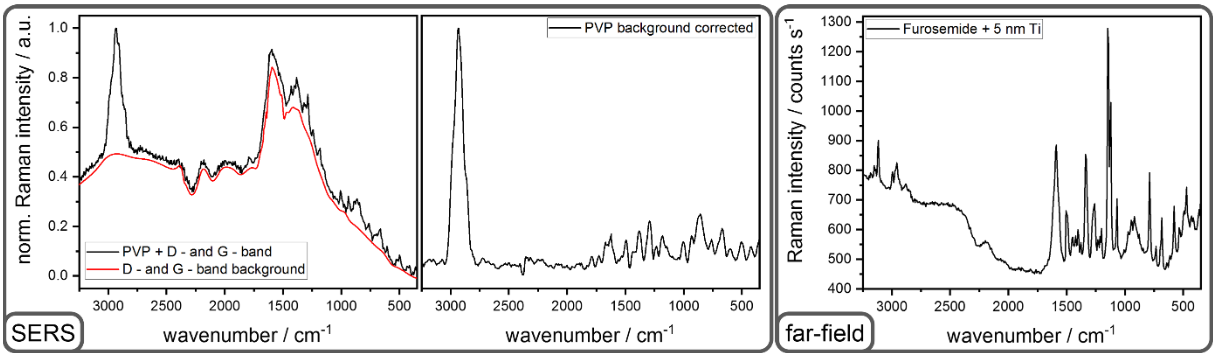

Figure 5.5. Left: SERS spectrum of PVP before and after background correction. Intense D and G bands from sp^2-hybridized amorphous carbon species are seen at between 1100 cm^{-1} and 1700 cm^{-1}. These signals are ascribed to carbon formed on silver nano grains during laser irradiation. A perfectly similar feature is observed for silver-coated Furosemide. **Right:** Far-field Raman spectrum of Furosemide coated with 5 nm Titanium. No signals from amorphous carbon species are found. The fluorescence band (between 3300 and 2000 cm^{-1}) is ascribed to nanoscale titanium particles.

silver-coated Furosemide and PVP SERS spectra, are rather ascribed to the D and G bands of the sp^2-hybridized carbon atoms from amorphous carbon species formed at the surface of the silver spasers during the exposure to the incident laser beam. More in details, the collective oscillation of the conductive band electrons induces the heating up of silver nanoparticles leading to the partial graphitization of organic molecules in the proximity of silver particles. In order to exclude that the organic material degradation occurs during the silver sputtering process, pure Furosemide and PVP were coated with a 5 nm thick titanium layer. Raman spectra of titanium-coated Furosemide and PVP show the absence of broad bands at 1600 cm^{-1} and 1350 cm^{-1} (Figure 5.5). Raman spectra from titanium-coated Furosemide and PVP samples differ from far-field spectra only by the presence of fluorescence signals arising from the titanium nano species formed at the organic particle surfaces (Figure 5.5). Anyway, since the origin of these broad peaks is related to amorphous carbon contamination, these bands can be removed by background subtraction for SERS spectra analysis.

Since a small amount of surface molecules contribute to most of the signal in SERS, band position shifts and the modification of relative intensities may occur due to electrostatic and chemical interactions with the metal nanoparticle surface inducing slight changes in molecular orientations and arrangement.[42-45] Despite of this, Furosemide and PVP marker bands identified in far-field spectra can still be applied in SERS to identify each compound in Furosemide/PVP composite particles.

5.4.3 Far-Field Raman and SERS Investigations of Sub-Micron Furosemide/PVP Particles

The previous results demonstrate that the formation of silver spasers through direct sputtering on the top of Furosemide and PVP microstructures allows for performing surface-enhanced Raman spectroscopy and microscopy. This section will apply this method to investigate Furosemide/PVP submicron composite particles. In a first step, far-field Raman microscopy maps of uncoated Furosemide/PVP particles are recorded. As expected, far-field spectra extracted from confocal Raman microscopy images show both marker bands from Furosemide and PVP (Figure 5.6.a). The ratio between the different compounds is visually illustrated in Figure 5.6.a showing a typical far-field color map of Furosemide/PVP sub-micron particles. The Raman intensities of both marker bands are depicted superimposed to generate a single map in which the Furosemide and the PVP marker bands appears in red and green respectively.

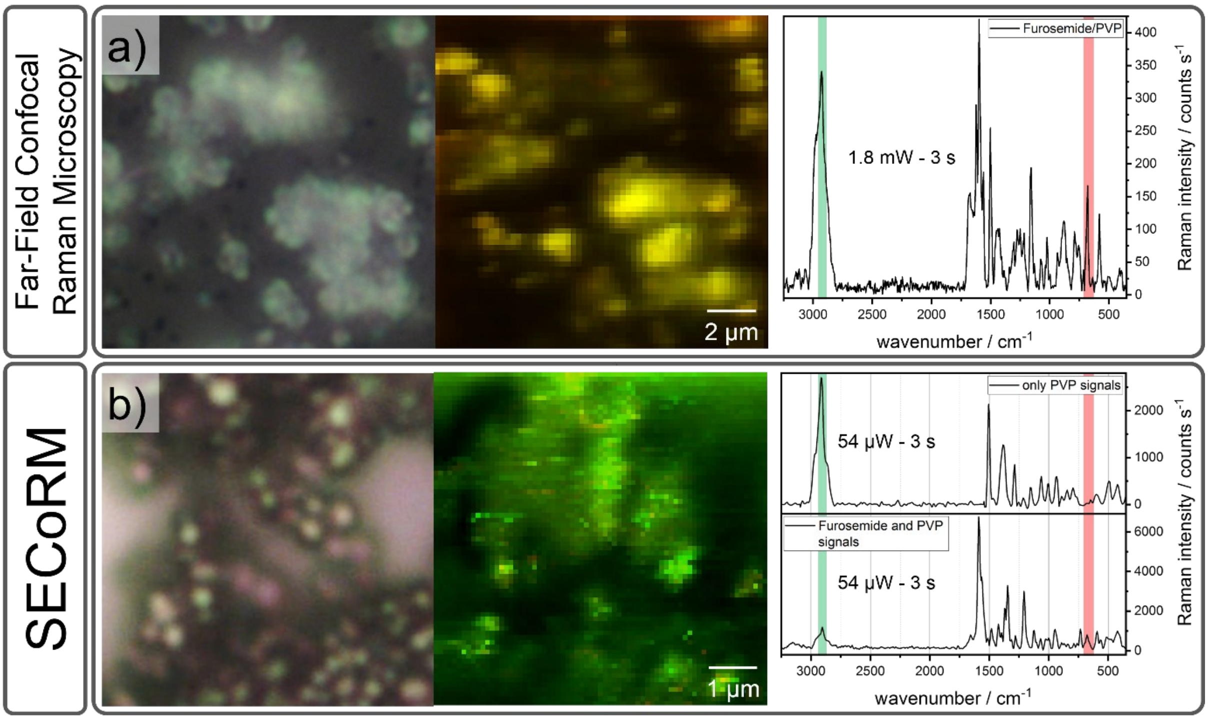

Figure 5.6.a) Far-field confocal Raman microscopy map of Furosemide/PVP sub-micro composite particles. The yellow pixels indicate the presence of both Furosemide and PVP marker bands in each single point Raman spectrum as shown in the background-corrected spectrum. **b)** SECoRM map of Furosemide/PVP sub-micro composite particles. The green colored pixels demonstrate that PVP is dominantly found at the Furosemide/PVP particle surface. Background-corrected SERS spectra showing only PVP markers (majority) and PVP-Furosemide markers are presented.

If in the Raman spectra both marker bands occur, the corresponding pixel color in the map is displayed in yellow. The dominant yellow color clearly indicates that Furosemide and PVP domains do not segregate in microscopic phases but rather form well-intermixed nanoscale domains. Even though far-field Raman maps can prove the formation of Furosemide/PVP sub-micron composite particles, they do not provide information about the arrangement of Furosemide and PVP molecules within single composite particles. Surprisingly, in SECoRM maps (Figure 5.6.b), contrary to far-field Raman maps, the majority of pixel clearly display a green color, indicating the dominant PVP marker band intensity in the SERS spectra (Figure 5.6). The absence of the Furosemide marker band within most of the SERS spectra can be only explained by the arrangement of Furosemide and PVP molecules within the Furosemide/PVP sub-micron particles. More in details, as SERS is highly surface sensitive and it is strongly modulated by molecular orientations and chemical interactions between silver and surface molecules, it can be safely concluded that PVP is most dominantly found at the surface of SFE-produced Furosemide/PVP composite particles.[23, 26, 46] Therefore, the combination of far-field Raman microscopy and SECoRM results points toward the formation of a kind of Furosemide/PVP core/shell arrangement.

5.4.4 Building Mechanism of Furosemide/PVP Sub-Micron Particles

Though most SERS spectra contain the PVP marker band only, some SERS spectra of SECoRM maps present both Furosemide and PVP marker bands. The occurrence of Furosemide signals within these SERS spectra cannot be explained by the formation of classical core/shell sub-micron particles with a completely closed PVP encapsulation of Furosemide spherical core. An estimation of the structure of a typical Furosemide/PVP particle with a diameter of 380 nm, based on the specific densities of Furosemide and PVP and their mass fractions within the precursor solution (0.75 respectively 0.25), would be consistent with a Furosemide core diameter of 336 nm and a PVP shell thickness of 22 nm. This core/shell structure is not compatible with SECoRM maps because the rapid decay of the electric field provided by the LSPR would not allow to record any signal from the core Furosemide molecules (Figure 5.7). Based on the rough Furosemide/PVP particle surface observed in SEM images and coherence lengths of Furosemide crystals derived from XRPD (<50 nm), it is concluded that Furosemide

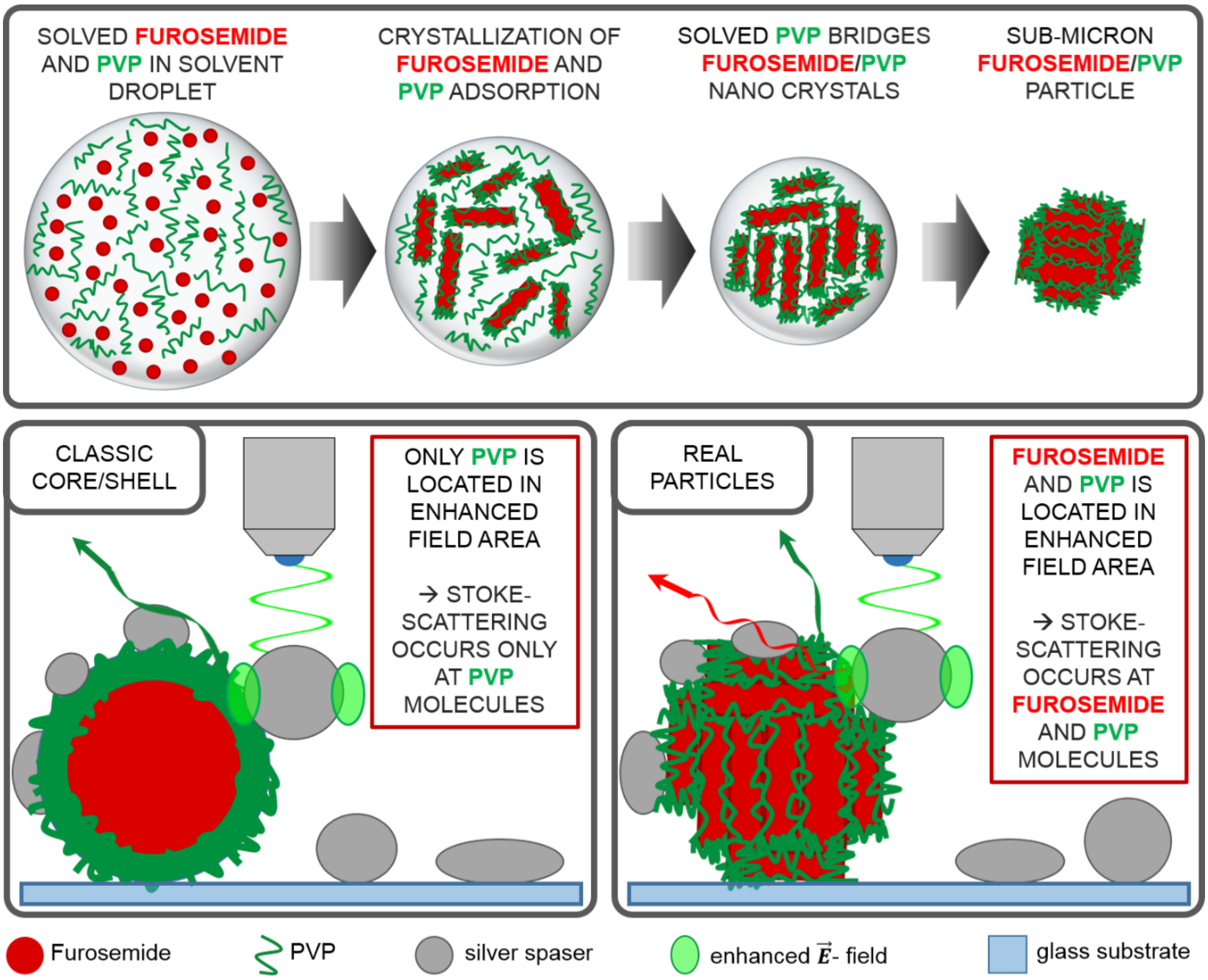

Figure 5.7. Top: Proposed building mechanism of Furosemide/PVP sub-micron composite particles. **Bottom left:** Schematic representation of a SERS experiment on an estimated classical Furosemide/PVP core/shell particle. In this arrangement no Furosemide molecules are located within the enhanced field area. Thus Stokes-scattering occur only on PVP molecules resulting in the absence of Furosemide vibrational modes within the SERS spectrum. **Bottom right:** Schematic representation of a SERS experiment on a real Furosemide/PVP sub-micron composite particle. Since the PVP shell appear much smaller in the real case, surface-near Furosemide molecules can be located in the enhanced field area. Consequently, Furosemide vibrational modes appear in some SERS spectra.

must be sensibly smaller than what predicted from an ideal core/shell structure. In the SFE process, the mixed solution is sprayed through a preheated hollow cone nozzle into the constantly-pumped vacuum reactor. The micron sized aerosol droplets undergo a fast solvent evaporation when travelling from the injection nozzle to the particles filter. When the saturation point is reached, the less soluble compound will be the first to crystallize. Since PVP has a 100× higher solubility in the used ethanol/DCM solvent mixture (about 1000 g/L) respect to Furosemide (10 g/L), Furosemide is very likely to crystallize before PVP transform into its amorphous solid phase (Figure 5.7, top). The primary Furosemide nano-crystals formed within the aerosol droplets are thought to have the dimensions calculated from the PXRD coherence lengths with a strongly anisotropic morphology. During further droplet evaporation, PVP molecules start to adsorb onto Furosemide crystal surfaces forming a PVP shell around these nano crystals and thus preventing their agglomeration or fusion (Figure 5.7, top). Because of the high PVP mass fraction (0.25), the PVP is much too abundant to stabilize the Furosemide suspensions in the droplets thus leading to a flocculation of PVP-coated Furosemide nanodomains. This flocculation is induced by solved PVP molecules forming bridges between single Furosemide/PVP core/shell nanoparticles leading to the aggregation of primary particles. Finally, further aggregation results in the formation of spherical Furosemide/PVP sub-micron particles which are seen in SEM images. Moreover, the rough surface morphology of these particles can be directly assigned to the formation of PVP coated anisotropic Furosemide nano-crystals. The proposed building mechanism can explain the presence of the Furosemide marker band as shown in SECoRM maps because the PVP shell (few nm) is considerably thinner than what would be expected from mass ration in a model spherical core/shell structure (22 nm). Consequently, Furosemide molecules are located within the field-enhanced volume and contribute to the SERS spectra (Figure 5.7, bottom right).

In order to double check the interpretation of far-field and near-field Raman results, XPS was additionally performed onto Furosemide/PVP sub-micron composite particles. From the surface composition (atomic percentage of C, N, O S and Cl species) and from the analysis of high-resolution C1s spectra of pure Furosemide and Furosemide/PVP particles (Figure 5.8), it is concluded that while in the precursor solution the Furosemide/PVP ratio is 53:47, the surface ratio derived by XPS analysis is found to be about 40:60. This confirms the PVP tendency to coat Furosemide by forming an ultrathin layer, reasonably less than 3 nm thick, on Furosemide in agreement with far- and near-field Raman results. More details on XPS analysis can be found in the Supporting Information.

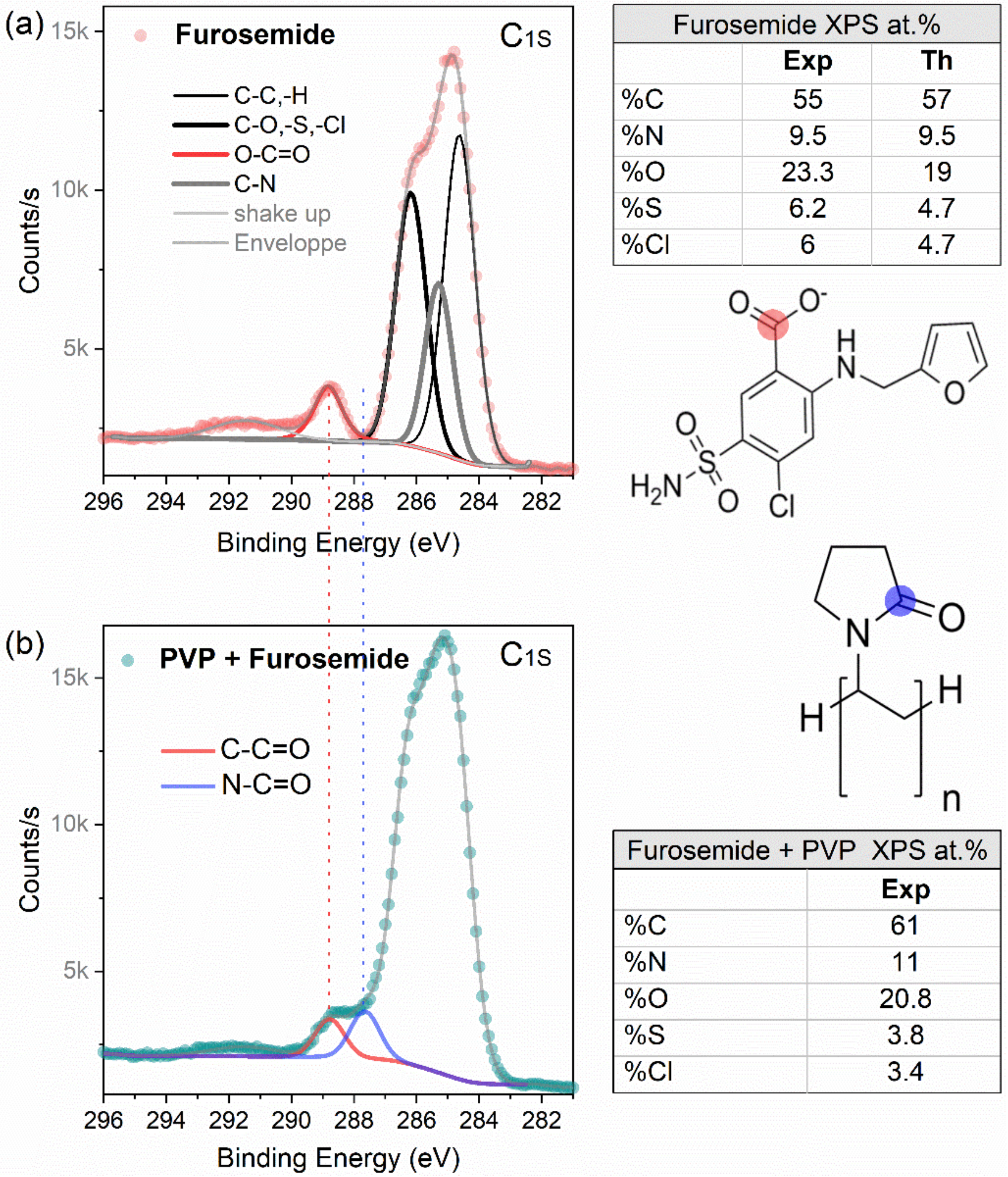

Furosemide XPS at.%		
	Exp	**Th**
%C	55	57
%N	9.5	9.5
%O	23.3	19
%S	6.2	4.7
%Cl	6	4.7

Furosemide + PVP XPS at.%	
	Exp
%C	61
%N	11
%O	20.8
%S	3.8
%Cl	3.4

Figure 5.8. Results from XPS analysis on Furosemide **(a)** and Furosemide-PVP composite **(b).** The peak fitting of the C1s spectra allows comparing the characteristic functional groups of Furosemide (R-COOH) and PVP (R-CNOH). The normalized fraction of PVP (0.55) and Furosemide (0.45) caAn be derived. Tables report the atomic percentage compositions derived from the quantification on high-resolution spectra (Exp) and the values calculated from the chemical formula of Furosemide (Th). The atomic percentage can be used to derive PVP (0.60) and Furosemide (0.40) molecular fractions at the surface.

5.5 Conclusion

The formation of sub-micron composite particles formed by Furosemide and PVP and produced by SFE was investigated. Particles were characterized by SEM, XRPD, XPS and far-field and near-field Raman spectroscopy and microscopy. First, SEM allowed demonstrating a sub-micron particle structure, XRPD investigations a nanoscale Furosemide domains. Finally, the comparison between far-field and near-field Raman spectroscopy and microscopies provided clear insights on the arrangement of Furosemide and PVP molecules within composite particles. Overall, spherical Furosemide/PVP composite sub-micron particles are demonstrated to be formed by nanoscale PVP-coated Furosemide crystals which aggregate to form the resulting superstructure. More interesting, we could show that silver coating of organic sub-micron composite particles leads to the formation of effective silver spasers capable of strongly enhancing Raman signals intensity from the particles surface. The formation of these spasers enables SERS investigations and thus the characterization of the surface chemical composition silver-coated particles. In particular, the combination of confocal Raman microscopy, in an effective method to obtain data from a statistically relevant number of particles in a single map in a short time span. The main challenges associated with this methodology on organic nanostructures come from assessing the eventual degradation of molecules in direct contact with laser-irradiated silver spasers possibly leading to the formation of amorphous carbon. The sp^2 hybridized carbon amount within these amorphous carbon species results in the appearance of strong broad of D and G bands within SERS spectra. Though the bands can be removed by background subtraction, they may mask weaker vibrational modes within the spectrum. This problem might be solved by protecting the sample surface with few nm of a poor thermal conductive insulation layer before silver coating. We believe that many composites could be tested by this combination of far- and near field Raman approach as a standard method for chemical surface characterizations and molecular arrangement investigations of sub-micron organic composite particles.

5.6 Supporting Information

The molecular fraction of PVP and Furosemide in the nanocomposite is investigated by X-Ray photoelectron spectroscopy (Escalab 250 Xi, Thermo Scientific, Waltham, Massachusetts, USA) by acquiring survey and high-resolution scans of C1s, N1s, Cl2p, O1s, S2p with a monochromatic Al k-a source.

Two independent procedures are applied to determine the molecular fraction in the composite; the first is by peak fitting the C1s spectrum and comparing the peak area of the Furosemide characteristic signal from R-COOH carboxylic groups (centered at a binding energy of 288.8 eV) and the well-separated characteristic component from R-CNOH groups from PVP (at 287.6 eV). This method allows directly estimating the PVP (55%) and Furosemide (45%) molecular fractions at the surface (Figure 8.b) with a sensitivity of few percent mainly limited by the peak fitting accuracy. Alternatively, from the XPS analysis of the surface composition of the pure Furosemide compound formed by SFE (Figure 8.a) we can determine the experimental N/Cl ratio R(exp)=1.6. This ratio is lower than the theoretical one based on the chemical compositions R(th)=2 probably because of the use of a chlorinated solvent (DCM). This ratio is then used to simply derive the Furosemide contribution within the total nitrogen content in the Furosemide/PVP composite ($\%N_{F+PVP}$) knowing that

$$\%N_{F+PVP} = \%N_F + \%N_{PVP} = (\%Cl \times 1.6) + \%N_{PVP} \,, \qquad \text{Eq. 5.1}$$

where $\%N_{PVP}$ and $\%N_F$ are nitrogen contributions from PVP and Furosemide surface molecules. This simple formula allows counting Furosemide and PVP molecules at the surface and gives a PVP surface content between 60% if we use R(th) and 65%, if we use R(exp). Both analyses point out that the PVP surface fraction is slightly higher than Furosemide while the average molecular composition in the SFE solution is 53% Furosemide and 47% PVP.

Overall, the XPS analysis confirms the tendency of PVP molecules organize on the top of nanoscale Furosemide domains; the average PVP layer thickness is extremely small (reasonably less than 3 nm) so that the Furosemide signal intensity is only slightly screened by PVP molecules.

5.7 References

1. Patra, J. K.; Das, G.; Fraceto, L. F.; Campos, E. V. R.; Rodriguez-Torres, M. d. P.; Acosta-Torres, L. S.; Diaz-Torres, L. A.; Grillo, R.; Swamy, M. K.; Sharma, S.; Habtemariam, S.; Shin, H.-S., Nano based drug delivery systems: recent developments and future prospects. *J. Nanobiotechnol.* **2018,** *16* (1), 71.
2. Lu, H.; Wang, J.; Wang, T.; Zhong, J.; Bao, Y.; Hao, H., Recent progress on nanostructures for drug delivery applications. *J. Nanomater.* **2016,** *2016*.
3. McNamara, K.; Tofail, S. A. M., Nanosystems: the use of nanoalloys, metallic, bimetallic, and magnetic nanoparticles in biomedical applications. *Phys. Chem. Chem. Phys.* **2015,** *17* (42), 27981-27995.
4. Oliveira, O. N.; Iost, R. M.; Siqueira, J. R.; Crespilho, F. N.; Caseli, L., Nanomaterials for Diagnosis: Challenges and Applications in Smart Devices Based on Molecular Recognition. *ACS Appl. Mater. Inter.* **2014,** *6* (17), 14745-14766.
5. Klein, S.; Hübner, J.; Menter, C.; Distel, L.; Neuhuber, W.; Kryschi, C., A Facile One-Pot Synthesis of Water-Soluble, Patchy Fe3O4-Au Nanoparticles for Application in Radiation Therapy. *Applied Sciences* **2019,** *9* (1), 15.
6. Onoue, S.; Yamada, S.; Chan, H.-K., Nanodrugs: pharmacokinetics and safety. *Int J Nanomedicine* **2014,** *9*, 1025-1037.
7. Kawabata, Y.; Wada, K.; Nakatani, M.; Yamada, S.; Onoue, S., Formulation design for poorly water-soluble drugs based on biopharmaceutics classification system: Basic approaches and practical applications. *Int. J. Pharm.* **2011,** *420* (1), 1-10.
8. Nagarwal, R.; Kumar, R.; Dhanawat, M.; Das, N.; K Pandit, J., Nanocrystal technology in the delivery of poorly soluble drugs: an overview. *Curr. Drug. Deliv.* **2011,** *8* (4), 398-406.
9. Kesisoglou, F.; Panmai, S.; Wu, Y., Nanosizing — Oral formulation development and biopharmaceutical evaluation. *Adv. Drug Deliv. Rev.* **2007,** *59* (7), 631-644.
10. Mirza, A. Z.; Siddiqui, F. A., Nanomedicine and drug delivery: a mini review. *Int. Nano Lett.* **2014,** *4* (1), 94.
11. Santhi, K.; Dhanaraj, S.; Joseph, V.; Ponnusankar, S.; Suresh, B., A study on the preparation and anti-tumor efficacy of bovine serum albumin nanospheres containing 5-fluorouracil. *Drug Dev. Ind. Pharm.* **2002,** *28* (9), 1171-1179.

12. Mu, L.; Feng, S., A novel controlled release formulation for the anticancer drug paclitaxel (Taxol®): PLGA nanoparticles containing vitamin E TPGS. *J. Controlled Release* **2003,** *86* (1), 33-48.

13. Chawla, J. S.; Amiji, M. M., Biodegradable poly (ε-caprolactone) nanoparticles for tumor-targeted delivery of tamoxifen. *Int. J. Pharm.* **2002,** *249* (1-2), 127-138.

14. Van den Mooter, G., The use of amorphous solid dispersions: A formulation strategy to overcome poor solubility and dissolution rate. *Drug Discov. Today Technol.* **2012,** *9* (2), e79-e85.

15. He, Y.; Ho, C., Amorphous Solid Dispersions: Utilization and Challenges in Drug Discovery and Development. *J. Pharm. Sci.* **2015,** *104* (10), 3237-3258.

16. Ma, X.; Williams, R. O., Characterization of amorphous solid dispersions: An update. *J. Drug. Deliv. Sci. Tec.* **2019,** *50*, 113-124.

17. Coty, J.-B.; Vauthier, C., Characterization of nanomedicines: A reflection on a field under construction needed for clinical translation success. *J. Controlled Release* **2018,** *275*, 254-268.

18. Johnston, L. J.; Gonzalez-Rojano, N.; Wilkinson, K. J.; Xing, B., Key challenges for evaluation of the safety of engineered nanomaterials. *NanoImpact* **2020,** *18*, 100219.

19. Rabanel, J.-M.; Adibnia, V.; Tehrani, S. F.; Sanche, S.; Hildgen, P.; Banquy, X.; Ramassamy, C., Nanoparticle heterogeneity: an emerging structural parameter influencing particle fate in biological media? *Nanoscale* **2019,** *11* (2), 383-406.

20. Hübner, J.; Pichot, V.; Guillevic, M.; Spitzer, D., Structure Investigation of Energetic Nanocomposites Produced by Spray Flash Evaporation via AFM-TERS. In *ICORS*, South Korea, 2018.

21. Deckert-Gaudig, T.; Pichot, V.; Spitzer, D.; Deckert, V., High-Resolution Raman Spectroscopy for the Nanostructural Characterization of Explosive Nanodiamond Precursors. *ChemPhysChem* **2017,** *18* (2), 175-178.

22. Hübner, J.; Deckert-Gaudig, T.; Glorian, J.; Deckert, V. K.; Spitzer, D., Surface Characterization of Nanoscale Co-Crystals Enabled through Tip Enhanced Raman Spectroscopy. *Nanoscale* **2020**, *18*, 10306-10319.

23. Langer, J.; Jimenez de Aberasturi, D.; Aizpurua, J.; Alvarez-Puebla, R. A.; Auguié, B.; Baumberg, J. J.; Bazan, G. C.; Bell, S. E. J.; Boisen, A.; Brolo, A. G.; Choo, J.; Cialla-May, D.; Deckert, V.; Fabris, L.; Faulds, K.; García de Abajo, F. J.; Goodacre, R.; Graham, D.; Haes, A. J.; Haynes, C. L.; Huck, C.; Itoh, T.; Käll, M.; Kneipp, J.; Kotov, N. A.; Kuang, H.; Le Ru, E.

C.; Lee, H. K.; Li, J.-F.; Ling, X. Y.; Maier, S. A.; Mayerhöfer, T.; Moskovits, M.; Murakoshi, K.; Nam, J.-M.; Nie, S.; Ozaki, Y.; Pastoriza-Santos, I.; Perez-Juste, J.; Popp, J.; Pucci, A.; Reich, S.; Ren, B.; Schatz, G. C.; Shegai, T.; Schlücker, S.; Tay, L.-L.; Thomas, K. G.; Tian, Z.-Q.; Van Duyne, R. P.; Vo-Dinh, T.; Wang, Y.; Willets, K. A.; Xu, C.; Xu, H.; Xu, Y.; Yamamoto, Y. S.; Zhao, B.; Liz-Marzán, L. M., Present and Future of Surface-Enhanced Raman Scattering. *ACS Nano* **2020,** *14* (1), 28-117.

24. McNay, G.; Eustace, D.; Smith, W. E.; Faulds, K.; Graham, D., Surface-Enhanced Raman Scattering (SERS) and Surface-Enhanced Resonance Raman Scattering (SERRS): A Review of Applications. *Appl. Spectrosc.* **2011,** *65* (8), 825-837.

25. Pilot, R.; Signorini, R.; Durante, C.; Orian, L.; Bhamidipati, M.; Fabris, L., A Review on Surface-Enhanced Raman Scattering. *Biosensors* **2019,** *9* (2).

26. Stiles, P. L.; Dieringer, J. A.; Shah, N. C.; Van Duyne, R. P., Surface-enhanced Raman spectroscopy. *Annu. Rev. Anal. Chem.* **2008,** *1*, 601-626.

27. Wheeler, D. A.; Green, T. D.; Wang, H.; Fernández-López, C.; Liz-Marzán, L.; Zou, S.; Knappenberger, K. L.; Zhang, J. Z., Optical Properties and Coherent Vibrational Oscillations of Gold Nanostars. *Chem. Phys. Lett.* **2012,** *543*, 127.

28. Sanchez-Gaytan, B. L.; Swanglap, P.; Lamkin, T. J.; Hickey, R. J.; Fakhraai, Z.; Link, S.; Park, S. J., Spiky Gold Nanoshells: Synthesis and Enhanced Scattering Properties. *J. Phys. Chem. C* **2012,** *116*, 10318.

29. Abalde-Cela, S.; Ho, S.; Rodríguez-González, B.; Correa-Duarte, M. A.; Álvarez-Puebla, R. A.; Liz-Marzán, L. M.; Kotov, N. A., Loading of Exponentially Grown LBL Films with Silver Nanoparticles and their Application to Generalized SERS Detection. *Angew. Chem. Int. Ed.* **2009,** *48*, 5326.

30. Itoh, T.; Yamamoto, Y. S.; Kitahama, Y.; Balachandran, J., One-Dimensional Plasmonic Hotspots Located Between Silver Nanowire Dimers Evaluated by Surface-Enhanced Resonance Raman Scattering. *Phys. Rev. B: Condens. Matter Mater. Phys.* **2017,** *95*, 115441.

31. Stockman, M. I., Spasers Explained. *Nat. Photonics* **2008,** *2*, 327.

32. Risse, B.; Hassler, D.; Spitzer, D. Preparation of Nanoparticles by Flash Evaporation. US20150000846A1, 2015.

33. Risse, B., Continuous formation of submicron energetic particles by the flash-evaporation technique. *Chem. Eng. J.* **2012,** *203*.

34. Spitzer, D.; Risse, B.; Schnell, F.; Pichot, V.; Klaumünzer, M.; Schaefer, M., Continuous Engineering of Nano-Cocrystals for Medical and Energetic Applications. *Sci. Rep.* **2014,** *4*.

35. Klaumünzer, M.; Hübner, J.; Spitzer, D., Production of Energetic Nanomaterials by Spray Flash Evaporation. *World Academy of Science, Engineering and Technology, International Journal of Chemical, Molecular, Nuclear, Materials and Metallurgical Engineering* **2016,** *10* (9), 1079-1083.

36. Sève, A.; Pichot, V.; Schnell, F.; Spitzer, D., Trinitrotoluene Nanostructuring by Spray Flash Evaporation Process. *Propellants Explos. Pyrotech.* **2017,** *42* (9), 1051-1056.

37. Pichot, V.; Comet, M.; Risse, B.; Spitzer, D., Detonation of Nanosized Explosive: New Mechanistic Model for Nanodiamond Formation. *Diamond Relat. Mater.* **2015,** *54*, 59-63.

38. Klaumünzer, M.; Pessina, F.; Spitzer, D., Indicating Inconsistency of Desensitizing High Explosives Against Impact through Recrystallization at the Nanoscale. *J. Energ. Mater.* **2016**, 1-10.

39. Bolukbasi, O.; Yilmaz, A., X-ray structure analysis and vibrational spectra of Furosemide. *Vib. Spectrosc.* **2012,** *62*, 42-49.

40. Mao, H.; Feng, J.; Ma, X.; Wu, C.; Zhao, X., One-dimensional silver nanowires synthesized by self-seeding polyol process. *J. Nanopart. Res.* **2012,** *14* (6), 887.

41. Smitha, S. L.; Nissamudeen, K. M.; Philip, D.; Gopchandran, K. G., Studies on surface plasmon resonance and photoluminescence of silver nanoparticles. *Spectrochim. Acta A* **2008,** *71* (1), 186-190.

42. Bailo, E.; Deckert, V., Tip-Enhanced Raman Spectroscopy of Single RNA Strands: Towards a Novel Direct-Sequencing Method. *Angew. Chem. Int. Ed.* **2008,** *47* (9), 1658-1661.

43. Watanabe, H.; Ishida, Y.; Hayazawa, N.; Inouye, Y.; Kawata, S., Tip-Enhanced Near-Field Raman Analysis of Tip-Pressurized Adenine Molecule. *Phys. Rev. B: Condens. Matter* **2004,** *69* (15), 155418-1-155418-11.

44. Bailo, E.; Deckert, V., Tip-Enhanced Raman Scattering. *Chem. Soc. Rev.* **2008,** *37* (5), 921-930.

45. Deckert-Gaudig, T.; Taguchi, A.; Kawata, S.; Deckert, V., Tip-Enhanced Raman Spectroscopy – From Early Developments to Recent Advances. *Chem. Soc. Rev.* **2017,** *46*, 4077.

46. Trautmann, S.; Aizpurua, J.; Götz, I.; Undisz, A.; Dellith, J.; Schneidewind, H.; Rettenmayr, M.; Deckert, V., A Classical Description of Subnanometer Resolution by Atomic Features in Metallic Structures. *Nanoscale* **2017,** *9* (1), 391-401.

6 General Conclusion and Outlook

Within this thesis, several nanostructured composites produced by Spray Flash Evaporation were investigated using Raman spectroscopy and microscopy, TERS and SERS. These are a nanostructured co-crystal consisting of CL-20 and HMX, different nanoscale RDX-TNT mixtures that differ in their mass ratio and Furosemide/PVP sub-micron particles.

Before TERS investigations were performed on CL-20/HMX nanoparticles, they were characterized previously via XRPD, far-field Raman and AFM to analyze co-crystallinity, size and morphology. XRPD and far-field Raman spectroscopy prove a successful formation of the co-crystalline system as only the characteristic reflexes and vibrational bands of the co-crystal were found in the XRPD pattern or Raman spectra respectively. Recorded AFM images depict the formation of CL-20/HMX nano-plates. The height of the nano-plates (~30 nm) could be assigned to the crystallographic [300] – direction. In this direction, bilayers of CL-20 alternate with layers of HMX molecules. Marker bands for HMX (CH_2 out of plane wagging vibration, 1416 cm^{-1}) and CL-20 (NO_2 asymmetric stretching vibrations, 1600 cm^{-1}) were chosen from far-field Raman spectra of the pristine compounds allowing to distinguish both substances in Raman spectra of the co-crystal. These marker bands appear with an intensity ratio of ~2.5 : 1 (CL-20 : HMX) in CL-20/HMX far-field Raman spectra. Afterwards, TERS spectra and maps were recorded to investigate the surface composition of single CL-20/HMX nano-plates. Interestingly, the intensity ratio of the marker band changes from the side of CL-20 to the side of HMX in TERS spectra (~1 : 1.5). The intensity ratio inversion indicates the formation of HMX layers at the nano co-crystal surfaces. A simplified theoretical approximation of the normal coordinates of the marker vibrations could demonstrate that this intensity ratio inversion arises not from a special arrangement of CL-20/HMX nano-plates towards the Raman scattering system. The formation of an HMX surface layer can be explained by the easier deformability of HMX compared to CL-20. Thus, HMX surface molecules can adopt an energetically preferred conformation decreasing surface energy. Furthermore, an HMX surface helps to understand the synergy between high explosive power and relatively high sensitivity thresholds of CL-20/HMX co-crystals. The concrete surface composition of CL-20/HMX nano-plates could only be figured out by TERS since it provides a spatial resolution enabling to distinguish between single molecular layers.

Besides CL-20/HMX nano-plates, four nanoscale hexolite mixtures of different RDX/TNT mass ratios, which are used as nanodiamond precursors, were characterized with far-field Raman and TERS. Far-field Raman spectra and maps of the diverse hexolite nano-composites could prove that an intermixture of RDX and TNT on the nanoscale took place during SFE process since all spectra of each hexolite contain as well the RDX (ring breathing vibration, 882 cm^{-1}) and the TNT (several NO_2 symmetric stretching vibrations, 1358-1371 cm^{-1}) marker band. TERS surface spectra of diverse hexolite mixtures contain TNT marker band only or TNT and RDX marker bands, no particle surface formed from RDX only could be identified. Since 13 of 15 TERS surface maps of SFE-80/20 hexolite nanoparticles contain RDX and TNT marker bands and only 2 of 15 the TNT marker band only, it was concluded that SFE-80/20 is formed from by nanoparticles built up by an RDX core partially covered with TNT patches. In case of the other SFE-produced hexolite mixtures, the surfaces are mainly formed by TNT only. The number of TERS maps containing only the TNT marker bands increases with the mass fraction of TNT hereby. By comparing far-field Raman data and TERS results, it could be concluded that SFE-60/40, SFE-40/60 and SFE-20/80 hexolites are formed from an RDX core covered by a TNT shell. However, due to the high lateral resolution of TERS, it was not expected that RDX signals appear in TERS spectra of SFE-80/20 since SFE-80/20 nanoparticles provide the thickest TNT shells and thus the RDX core would not be located in the enhanced electric field. Therefore, it is suggested that the growth of the RDX/TNT core/shell nanoparticles appears anisotropically. This anisotropic formation mechanism is explainable by the dynamics of the SFE process where acceleration forces influences the particle position within the micro droplets. Since RDX crystallizes first, RDX primary nanoparticle are forced to the droplet edges before TNT starts to crystallize on the RDX particle surfaces resulting in the described anisotropic RDX/TNT core/shell nanoparticles. Nanodiamonds characterized by various mean sizes and size distributions were obtained by detonation syntheses from the diverse nano hexolites. Based on the TERS characterization of the precursor materials, a direct correlation could be described between the nanodiamond mean size, the hexolite nanoparticle mean size, the RDX mass fraction, the TNT shell thickness, the hexolite nanoparticle size distribution and the level of anisotropy of the hexolite nanoparticles. Again, the combination of volume sensitive far-field Raman spectroscopy and surface sensitive TERS provided new information. On the one hand, new insights into the SFE process, especially into its dynamics, were obtained. On the other hand, a more detailed nanodiamond formation mechanism could be derived from Raman and TERS investigations. These new findings help to further improve the SFE process in order to produce tailored hexolite precursor for nanodiamonds with even smaller sizes and size distributions.

Since pharmaceutical SFE-produced sub-micron Furosemide/PVP composite particles exceed the size accessible to TERS in bottom-illumination setup, a combination between confocal Raman microscopy and SERS was chosen as characterization method. In contrast to common SERS experiments, where the sample is applied onto SERS substrates, silver nanostructures were formed on the sample surface by sputtering. In a first step, pure Furosemide and pure PVP were coated with a thin silver layer to determine whether direct sputtering leads to the formation of plasmonic nanostructures on the sample surfaces. Confocal Raman microscopy performed subsequently could prove the formation of SERS active silver spasers since the used laser power could be reduced on 1/33 compared to far-field Raman maps of non-silver-coated Furosemide and PVP without reducing Raman intensity. In addition, the successful formation of spasers could be further demonstrated at the position of the most intense Raman signals in the SECoRM maps. Due to the linear polarization of the incident laser, the strongest Raman intensities are recorded at particle edges instead of positions containing a high number of scattering molecules as in far-field Raman maps. However, also strong D and G bands appear in most of the Furosemide and PVP SERS spectra due to the formation of sp^2-hybridized carbon species at the silver spaser surfaces. If a LSPR is induced by the incident laser, the silver spacer surfaces heat up and induce a dissociation of surface molecules resulting in the formation of amorph carbon containing sp^2-hybridized species. Since the origin of the strong bands is known, they can be removed via background correction. Anyway, SERS investigation of Furosemide/PVP sub-micron particles reveal that their surfaces are mainly formed form PVP. However, some spectra contain also Furosemide signals indicating the formation of only a relatively thin PVP surface layer. Contrary, all Furosemide/PVP far-field Raman spectra demonstrate the presence of both Furosemide and PVP. By comparing far-field Raman microscopy and SECoRM results with XRPD patterns and SEM images, the concrete structure of Furosemide/PVP sub-micro particles and their formation mechanism could be derived. Thus, Furosemide/PVP particles are formed from anisotropic Furosemide nanoparticles (~ 40 nm) encapsulated by PVP which aggregate to the resulting superstructures. The combination of far-field Raman and SERS could provide, like the combination of far-field Raman and TERS, a new and deeper insight into the structure of organic composite particles.

In summary, structure investigations of organic nanoscale composites are not only possible, they also provide new information which are not accessible by standard measurement methods.

However, near-field Raman spectroscopy and microscopy methods do not only have advantages. TERS is an extremely time and material consuming measurement technique. As described within chapter 3 and 4, a lot of TERS spectra hast to be recorded and analyzed to obtain robust results. For example, all recorded hexolite TERS maps contain together 6600 individual TERS spectra. Furthermore, the tips can be easily damaged or contaminated while scanning making them TERS-inactive. Moreover, TERS tips must be produced before TERS measurements can be performed. Due to the manufacturing processes, not every tip produced is TERS active. Although, the manufacturing procedure presented provide a success rate of about 90 %, not each TERS tip show the same field enhancement. Thus, while it is possible to record single-point spectra and long exposed surface maps, TERS maps of larger areas require a large field enhancement factor, since the individual measuring points can be only exposed for a short time to ensure that the tip remains in the focus of the laser. Accordingly, further experiments have to be carried out to find a time-saving and reproducible manufacturing process that delivers strong field-enhancing TERS tips allowing TERS maps of several particles. For economic reasons, it is therefore advisable to use TERS for structure investigations of organic nano-composites only if other standard methods cannot provide the information sought. However, the results then found can provide insights into the molecular composition of organic nanocomposites, allowing new conclusions to be drawn about their specific reaction behaviors or their formation mechanisms.

On the other hand, SECoRM is a time-saving measurement method since it allows the investigation of a high number of particles in a single map. However, it does not provide the lateral resolution of TERS by far and is therefore only suitable for sub-micro or micro (composite) particles. Since the sample is directly coated with a thin metal layer, it is, moreover, a destructive measuring method. Despite these disadvantages, SECoRM can also provide information that is not accessible by other methods. However, the strong D and G bands still interfere with the spectrum evaluation. Possibly, the Raman intensity of these bands can be minimized by applying an insulating layer before the silver coating. Various rapidly oxidizing metals could be suitable for this purpose.

In conclusion, TERS and SERS are suitable methods for structure investigations of organic nanocomposites despite the described disadvantages. However, once these are eliminated, TERS and SERS themselves could become standard methods for structure investigations of organic nanoscale composites.

Investigation structurale de nanocomposites énergétiques et pharmaceutiques par AFM-TERS et SERS

Introduction

La cinétique des réactions chimiques et physiques dépend non seulement des produits chimiques utilisés, mais aussi de leur taille, de leur morphologie, de la composition de leur surface et de la disposition de leurs molécules. Cette relation peut être observée, par exemple, dans l'adsorption de gaz sur la surface des particules ou lorsque des produits chimiques sont dissous dans un solvant. L'influence de la taille, de la morphologie, de la composition et de la disposition des surfaces devient particulièrement évidente dans les réactions à l'état solide, par exemple les combustions des précurseurs de particules.[1-2] L'analyse de ces paramètres est une tâche difficile, en particulier pour les nanoparticules organiques et les nanoparticules submicroniques nanostructurées. Les molécules organiques métastables, en particulier les composés énergétiques et pharmaceutiques, ont tendance à se dissocier sous l'apport énergétique de diverses méthodes de mesure telles que la microscopie électronique. Il faut donc utiliser une technique d'analyse douce qui offre des résolutions latérale et spectroscopique suffisantes. Dans le cadre de cette thèse, divers composites organiques et énergétiques nano et submicroniques sont caractérisés par la spectroscopie Raman conventionnelle (Raman en champ lointain), la spectroscopie Raman exaltée au voisinage d'une pointe AFM (TERS) et la spectroscopie Raman exaltée en surface (SERS) (Raman en champ proche). Les détails expérimentaux, les résultats et les conclusions qui ont pu être tirés de ces recherches ainsi qu'une description détaillée du contexte théorique de la diffusion Raman, du SERS et du TERS sont présentés dans ce qui suit.

Contexte théorique

La diffusion Raman

Le TERS et le SERS sont basés sur l'effet Raman. L'effet Raman est un processus de diffusion inélastique de la lumière par la matière, par lequel l'énergie (respectivement la longueur d'onde ou la fréquence angulaire) de la lumière diffusée est soit diminuée soit augmentée (diffusion Raman). Si un photon ayant une énergie $h\nu_0$ qui ne coïncide pas avec la différence d'énergie entre deux états d'énergie moléculaire interagit avec une molécule (ou la matière en général), la molécule peut être excitée dans un état d'énergie virtuel V. L'énergie des photons est donc généralement inférieure à celle requise pour une transition électronique moléculaire (sauf pour la spectroscopie Raman par résonance). Les états virtuels sont des états de courte durée et non stationnaires d'une molécule car ils ne sont pas des fonctions propres d'un opérateur.[3] Si une molécule est excitée de son état électronique et vibratoire de base à un état virtuel en absorbant un photon ($S_0 v_0 \rightarrow V$), elle se relaxe immédiatement en émettant un photon. Dans la plupart

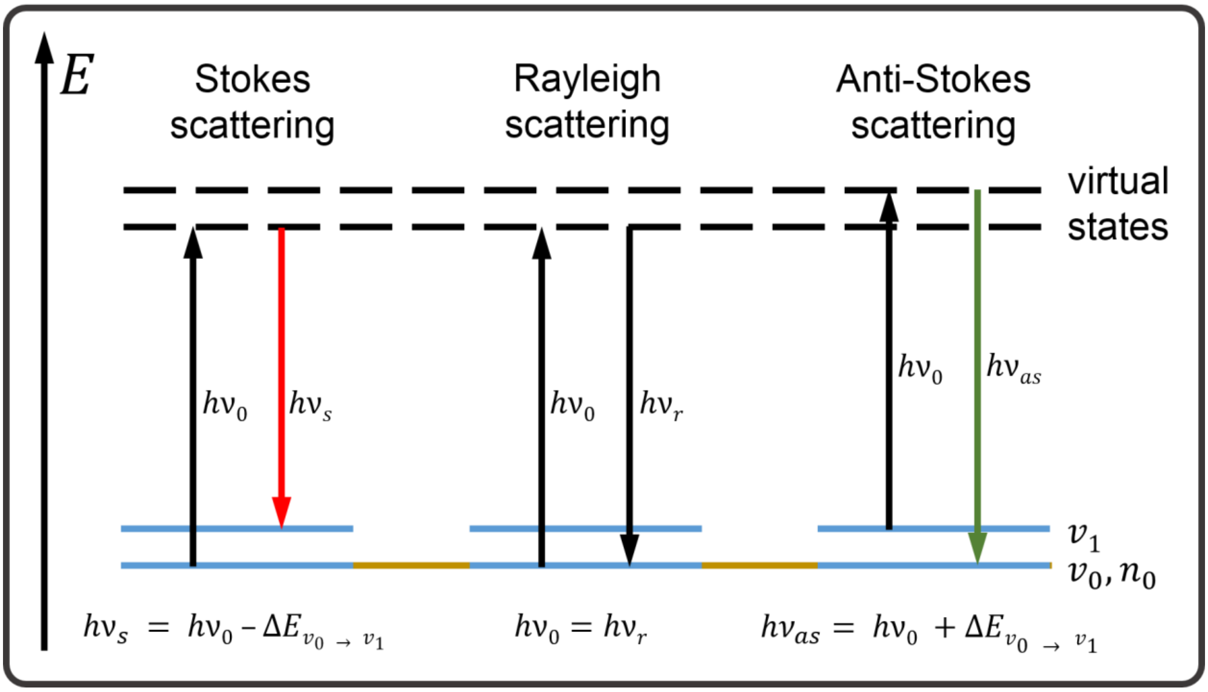

Figure 0.1. Représentation schématique de l'effet Raman. v_0 et v_1 représentent l'état vibratoire fondamental et le premier état vibratoire excité d'une molécule. Les flèches noires représentent l'énergie $h\nu_0$ et $h\nu_r$ d'un photon incident ainsi que l'énergie d'un photon diffusé de Rayleigh. La flèche rouge représente l'énergie $h\nu_s$ d'un photon diffusé de Stokes, la flèche verte symbolise l'énergie d'un photon diffusé Anti-Stokes $h\nu_{as}$.

des cas, la molécule se relaxe pour revenir à son état électronique et vibratoire de base ($V \rightarrow S_0v_0$). En conséquence, les énergies du photon absorbé et du photon émis sont égales (Figure 0.1). Ce processus de diffusion élastique est appelé *diffusion de Rayleigh*. La diffusion de Rayleigh se produit typiquement avec une probabilité de 10^{-4} – 10^{-3}. Toutefois, avec une probabilité de 10^{-8} – 10^{-5}, la molécule peut également se relaxer de l'état virtuel au premier état vibratoire excité de l'état électronique de base ($V \rightarrow S_0v_1$). Ce processus de diffusion inélastique est la *diffusion de Stokes*. La différence d'énergie entre le photon absorbé et le photon émis coïncide ainsi avec la différence d'énergie entre l'état vibratoire fondamental et le premier état vibratoire (Figure 0.1). Si la molécule est déclarée dans le premier état vibratoire excité de l'état électronique de base avant d'absorber un photon ($S_0v_1 \rightarrow V$), la molécule peut se relaxer à ses états vibratoires et électroniques de base ($S_0v_0 \rightarrow V$). Par conséquent, l'énergie du photon émis est augmentée par la différence d'énergie entre l'état vibratoire fondamental et le premier état vibratoire excité. Ce processus de diffusion inélastique est appelé *diffusion anti-Stokes*. Du fait que beaucoup moins de molécules se trouvent dans des états vibratoires excités à température ambiante, la diffusion Anti-Stokes se produit moins probablement que la diffusion Stokes, ce qui se traduit par des intensités de fréquence moindres dans les spectres Raman.

Spectroscopie Raman amplifiée de surface (SERS)

Comme nous l'avons déjà mentionné précédemment, la probabilité qu'un photon soit diffusé par effet Raman au niveau d'une molécule est de 10^{-8} - 10^{-5} ce qui est donc très faible. Par conséquent, un très grand nombre de molécules est nécessaire, ce qui rend impossible les recherches Raman sur des nanoparticules isolées. On peut cependant montrer que les intensités Raman se trouvent considérablement augmentées lorsque les molécules sont situées à proximité ou sur des surfaces de métaux (précieux) nanostructurés. Cet effet est devenu célèbre sous le nom de diffusion Raman exaltée de surface (SERS). Le mécanisme exact du SERS est toujours en cours de discussion, mais deux théories ont été avancées. D'une part, une amplification du champ électrique fournie par les nanostructures métalliques participe principalement à l'amélioration globale de l'intensité Raman (amplification électromagnétique). Si une surface métallique est placée dans le champ électrique de la lumière incidente, les électrons de valence commencent à osciller. En général, l'oscillation collective des électrons de valence par rapport aux noyaux des atomes peut être mathématiquement décrite comme une quasi-particule appelée plasmon. Dans le cas des nanoparticules métalliques, l'oscillation collective des électrons de valence est appelée plasmon de surface localisé (LSP). Si une nanoparticule métallique interagit avec la lumière, les électrons de valence sont forcés vers les bords de la particule dans la direction opposée au vecteur de champ électrique de la lumière incidente $\vec{E}_{in}$. En raison du déplacement des électrons de valence par rapport aux noyaux atomiques dans le réseau cristallin, il se produit une séparation de charge entre les noyaux atomiques chargés positivement et les électrons chargés négativement (Figure 0.2). Par conséquent, une force de restauration $\vec{F}_C$ résulte de l'attraction de Coulomb.[4] Cette force induit une oscillation des électrons de valence. En raison de l'oscillation collective des électrons de valence, un champ électrique est créé à la surface des nanoparticules parallèlement au vecteur de champ électrique $\vec{E}_{in}$ de la lumière incidente. L'intensité de ce champ électrique est fortement augmentée par

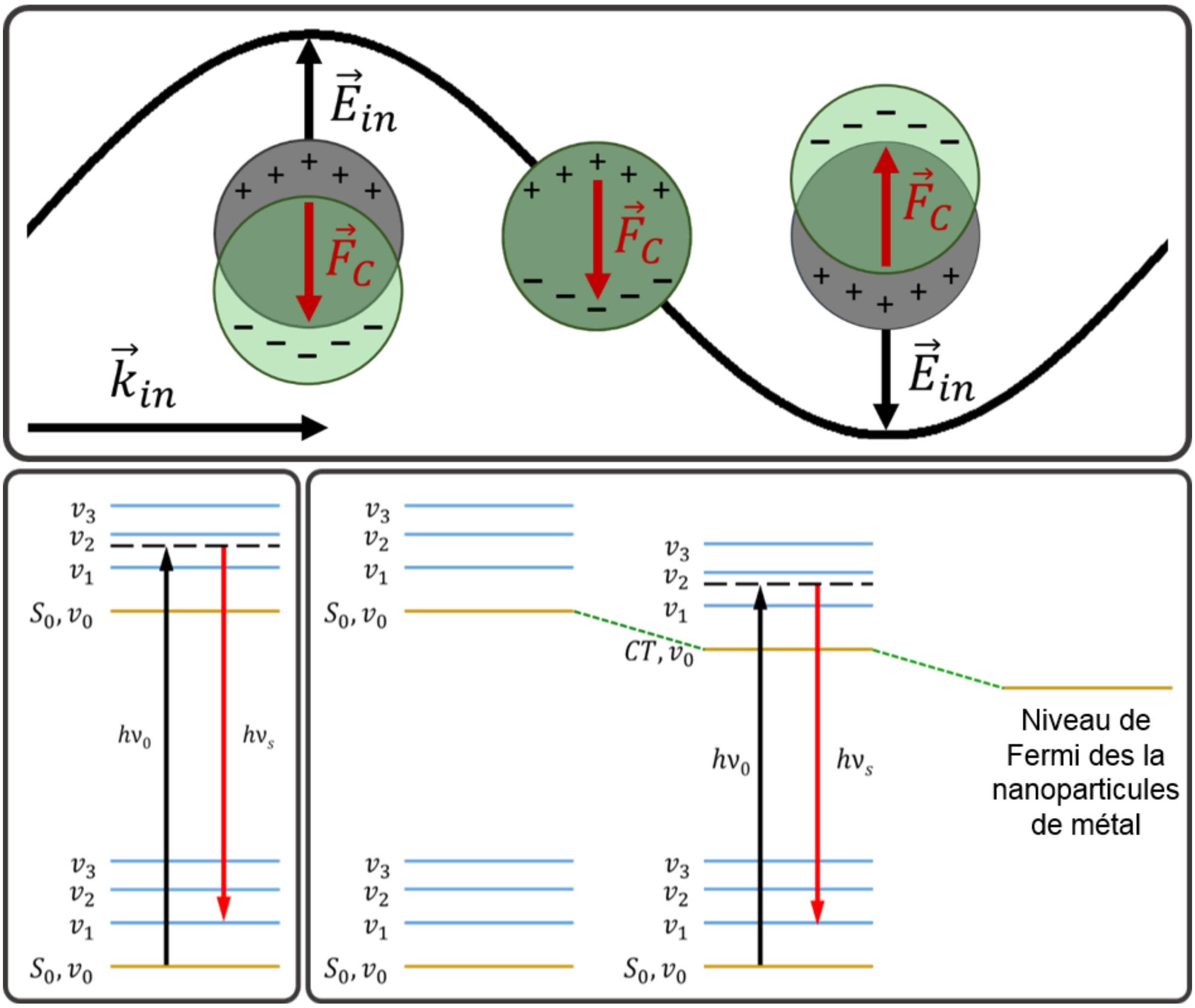

Figure 0.2. Haut : Représentation schématique de la résonance plasmonique de surface localisée (LSPR). **En bas à gauche :** Représentation schématique de l'effet Raman de résonance. **En bas à droite :** Représentation schématique de l'effet chimique de transfert de charge par résonance.

rapport à l'intensité de la lumière incidente. L'augmentation de champ la plus forte se produit si le LSP de la nanoparticule métallique oscille en résonance avec la lumière incidente (résonance plasmonique de surface localisée, LSPR). La fréquence de la LSPR dépend des propriétés du matériau comme la densité électronique, la masse électronique effective, la taille et la forme de la distribution de la charge.[4] Quoi qu'il en soit, l'augmentation du champ diminue rapidement par rapport à la surface des nanoparticules métalliques. Ainsi, après quelques nanomètres, l'augmentation du champ est à peine perceptible.[5-12] En fonction des nanoparticules utilisées, on peut atteindre des améliorations de l'intensité Raman de 10^4 - 10^{14}.[13-18]

Outre l'exaltation électromagnétique, les interactions chimiques entre les molécules et les nanoparticules métalliques peuvent également participer à l'exaltation globale de l'intensité Raman. L'exaltation chimique est fortement liée à l'effet Raman de résonance. Ici, la longueur d'onde de la lumière incidente coïncide avec la différence d'énergie entre niveau électronique fondamental et le premier état électronique excité (ou même supérieur) de la molécule (Figure 0.2, en bas à gauche). Comme il est plus probable qu'une transition électronique se produise de l'état électronique de base à un état électronique excité plutôt qu'à un état virtuel, les intensités Raman sont augmentées.[3] Dans le cas de la théorie de l'exaltation chimique, les molécules sont chimisorbées à la surface des nanoparticules. Si le niveau de Fermi de la nanoparticule est proche du niveau d'énergie des orbitales de la molécule, elles peuvent former un état de transfert électronique de charge (TC) métal-molécule (ou molécule-métal) (Figure 0.2, en bas à droite).[19] Si la longueur d'onde de la lumière incidente coïncide avec la différence d'énergie entre l'état moléculaire fondamental et l'état TC, les intensités Raman de certaines vibrations moléculaires peuvent être augmentées comme décrit ci-dessus. Le produit chimique participe avec des facteurs compris entre 10^2 et 10^4 à l'exaltation totale de l'intensité Raman.

Spectroscopie Raman à exaltation de pointe (TERS)

Fondamentalement, le TERS est la combinaison du SERS et de la microscopie à sonde à balayage (SPM) comme la microscopie à force atomique (AFM). La première expérience TERS a été réalisée par Stöckle *et al.* en 2000.[20] Afin de combiner le SERS avec l'AFM, la pointe de la sonde utilisée doit présenter une caractéristique plasmonique comme une simple nanoparticule d'argent ou d'or montée au sommet de la pointe. L'apex de la pointe doit être éclairé par un laser dont la longueur d'onde correspond au LSPR de la caractéristique plasmonique. En général, les pointes en argent sont utilisées pour des longueurs d'onde d'excitation comprises entre 488 nm et 568 nm, tandis que les pointes en or sont utilisées pour des longueurs d'onde comprises entre 633 nm et 785 nm.[5] La géométrie du dispositif TERS, c'est-à-dire l'alignement entre l'optique d'éclairage et la pointe, doit être choisie de manière à ce que l'échantillon soit placé dans la zone de champ électrique renforcé à la surface des nanoparticules d'argent ou d'or. En fonction de l'échantillon, la pointe du TERS peut être éclairée par le bas, par le côté ou par le haut (Figure 0.3). Comme le champ exalté provient d'une seule nanoparticule métallique dans le TERS et en raison de la rapide décroissance du champ, le TERS offre une haute résolution spatiale (< 1 nm).[12, 21-22] Les spectres de TERS et de SERS peuvent être différents des spectres Raman en champ lointain car le TERS est très sensible à la surface. Les molécules de surface s'adaptent à des conformations différentes de celles des molécules de masse, ce qui entraîne de légers changements de position de bande, des changements d'intensité et l'apparition et la disparition de modes vibratoires uniques.

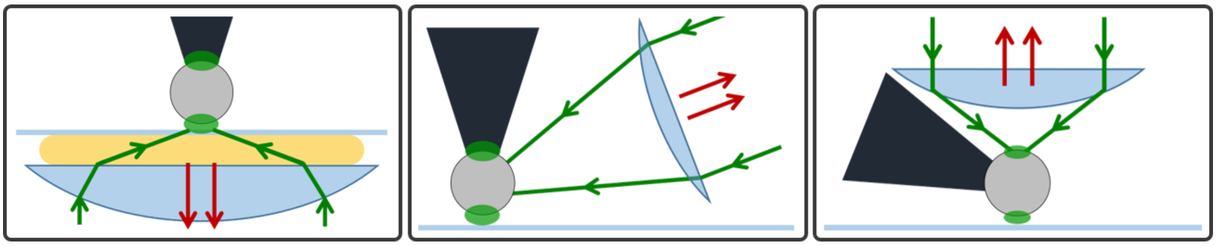

Figure 0.3. Représentation schématique des différentes géométries d'illumination du TERS. Les flèches vertes représentent la lumière laser incidente ; les flèches rouges représentent la lumière diffusée Raman ; les triangles et sphères gris représentent les pointes métalliques ; les ellipses vertes illustrent le champ amélioré fourni par les LSPR et l'effet paratonnerre ; les segments de cercle bleus représentent les lentilles optiques. **A gauche :** Configuration de l'éclairage du fond**. Au milieu** : Configuration de l'éclairage latéral. **A droite** : Configuration de l'éclairage par le haut.

Caractérisation de la surface des co-cristaux à l'échelle nanométrique grâce à la spectroscopie Raman exaltée par la pointe

Le premier composite à l'échelle nanométrique qui a été étudié était un co-cristal composé de CL-20 et de HMX dans un rapport molaire de 2:1. Les cocristaux sont des systèmes cristallins constitués de deux ou plusieurs composés chimiques.[23] En raison de différentes interactions intermoléculaires comme la liaison hydrogène, les forces de van der Waals ou l'empilement π-π, des composés chimiques de nature différente peuvent s'agencer d'une manière spécifique pendant le processus de cristallisation, sous la forme d'une structure moléculaire composite, qui est énergétiquement plus favorable que celle des cristaux des composés simples. Ces cocristaux diffèrent souvent de leurs composés uniques d'origine par leurs propriétés physiques, par exemple la solubilité, le point de fusion et leurs propriétés mécaniques.[24] L'un des composés très prometteur est un co-cristal entre CL-20 et HMX dans un rapport molaire de 2:1 (CL-20/HMX) qui a été synthétisé pour la première fois par Bolton et al. en 2012.[25] Le CL-20/HMX démontre parfaitement la synergie entre ses composants individuels. Ce co-cristal montre une vitesse de détonation plus élevée que celle du HMX pur, proche de la vitesse de détonation du CL-20 et des valeurs de sensibilité proches de celles du HMX.[25-27] Jusqu'à présent, on ne comprend pas complètement comment la structure du co-cristal influe sur les performances et la sensibilité. Cependant, on sait que la morphologie et l'état de surface des cristaux participent fortement à la sensibilité des matériaux énergétiques, surtout s'ils sont nanostructurés.[1, 28-29] Par conséquent, une étude TERS détaillée de ces paramètres pourrait donner une idée plus précise de la sensibilité à l'impact des nanocristaux de CL-20/HMX.

(Ce chapitre est publié à l'adresse suivante : Hübner, J.; Deckert-Gaudig, T.; Glorian, J.; Deckert, V. K.; Spitzer, D., Surface Characterization of Nanoscale Co-Crystals Enabled through Tip Enhanced Raman Spectroscopy. *Nanoscale* **2020**, *18*, 10306-10319, DOI: 10.1039/D0NR00397B).

Section expérimentale

Le co-cristal CL-20/HMX a été produit par le procédé d'évaporation flash de spray.[30-31] La Figure 0.4 montre une photographie de la version laboratoire d'un réacteur SFE ainsi qu'un schéma de l'installation. Une solution à 2 % en masse de 2,4 g (5,4 mM) ϵ-CL-20 et de 0,80 g (2,7 mM) β-HMX dans 200 ml d'acétone est préparée. Cette solution est introduite dans le réservoir de stockage de solution du dispositif SFE. Pour le processus de pulvérisation, une buse à cône creux de 80 µm a été utilisée. Elle a été chauffée à 160 °C. La pression en amont de la buse a été réglée à 40 bar. La pression après la buse à l'intérieur de la chambre d’atomisation s'élève à 8 - 15 mbar pendant le processus. Après la pulvérisation de la solution complète d'acétone CL-20/HMX, le produit final est recueilli sur les parois du système de filtration sous forme de poudre blanc-jaunâtre (n-CL-20/HMX).

Les pointes TERS ont été préparées par une procédure de pulvérisation. Les pointes AFM AppNano ACCESS-NC (Mountain View, USA) ont été fixées sur un gabarit à prisme de 30° pour générer un arrangement perpendiculaire entre la pointe et la cible de pulvérisation. Ce gabarit a été installé dans la chambre à vide d'un système de pulvérisation à plasma d'argon HHV Auto 306 (Bangalore, Inde) à une distance de 10 cm de la cible de pulvérisation. Dans une première étape, 3 nm de titane ont été déposés sur la pointe à une vitesse de dépôt de 0,5 Å/s. Le titane est utilisé comme promoteur d'adhésion entre la couche d'oxyde native de la pointe en Si et l'argent. Ensuite, les pointes Si/Ti ont été recouvertes d'une couche d'argent de 25 nm (vitesse de pulvérisation de 0,5 Å/s). Enfin, les pointes Si/Ti/Ag ont été recuites sur une plaque chauffante pendant 1 minute à 300 °C.

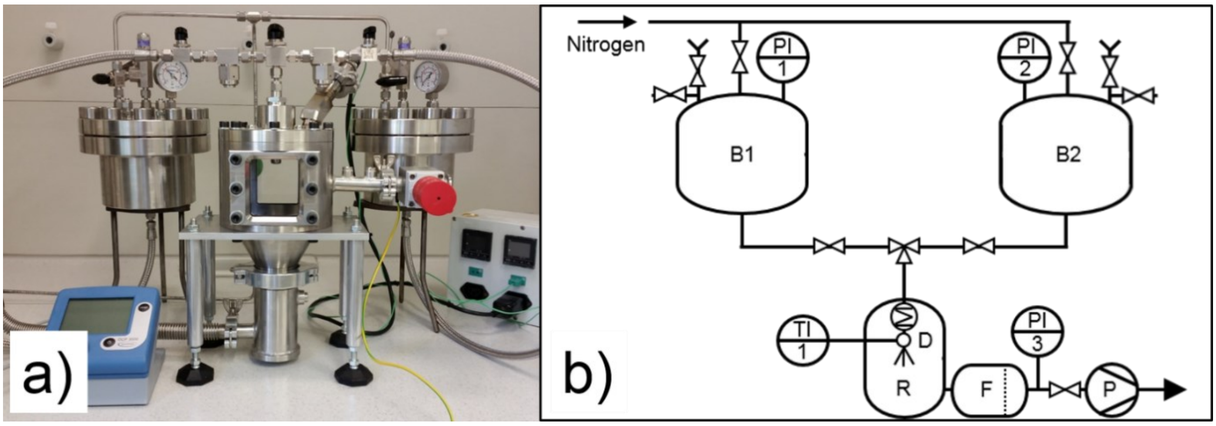

Figure 0.4. a) Photographie d'une version de laboratoire SFE - réacteur. **b)** Schéma du SFE. B1, B2 : réservoir de solvant et de solution ; R : chambre de réaction ; D : buse à cône creux, F : filtre, P : pompe à vide ; PI : capteur de pression ; TI : capteur de température.

Résultats et discussion

Des profils XRPD ont été enregistrés pour étudier la structure cristalline de n-CL-20/HMX. Le diagramme XRPD obtenu montre les mêmes positions des raies de Bragg que le diffractogramme XRPD simulé à partir des résultats de diffraction des rayons X des cristaux de monocliniques CL-20/HMX (rapport molaire CL-20 : HMX 2 : 1) de Bolton et al. La Figure 0.5 compare les diagrammes XRPD des n-CL-20/HMX synthétisés et les données de la

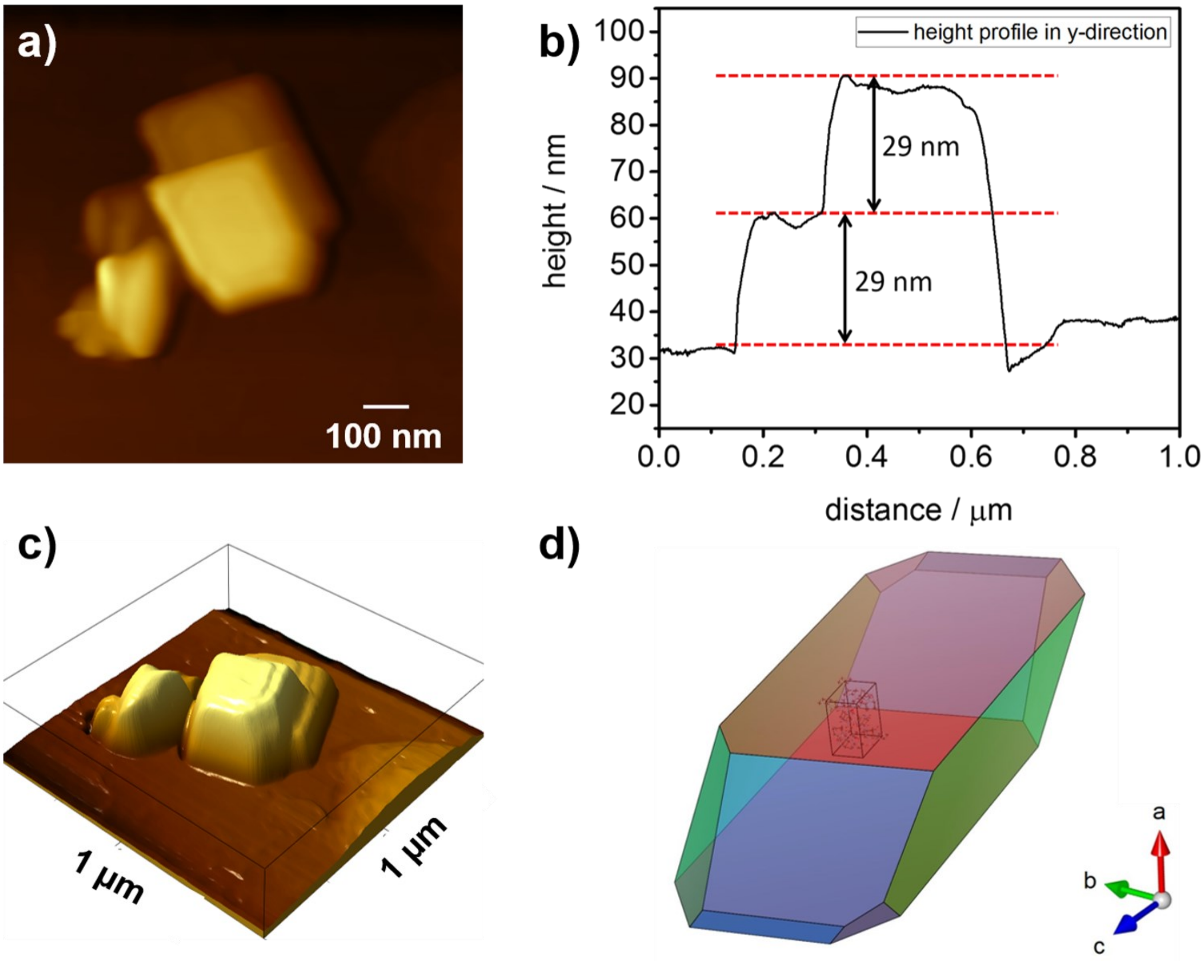

Figure 0.5.a) Topographie AFM des co-cristaux n-CL-20/HMX. **b)** Profil de hauteur des particules indiquées en a) selon la direction y. **c)** Image 3D de a). **d)** Morphologie du cristal simulée en utilisant les faces du cristal et les longueurs de cohérence correspondantes à partir des données XPRD. Les formes calculées et mesurées se ressemblent fortement. De plus, les hauteurs des particules correspondent à la longueur de cohérence dans la direction [300]. Les tailles des particules dans le plan cristallographique bc sont plus grandes que la longueur de cohérence correspondante. Cela peut être dû à des défauts de structure cristalline dus à la fixation orientée des nanoparticules primaires sur les plaques n-CL-20/HMX.

littérature dans la plage de données pertinente entre 10° et 40° (2θ).[25] Dans ce système cristallin, des couches de HMX alternent avec des bicouches de CL-20 dans la direction [300]. En outre, la morphologie cristalline des nanocristaux simples a été simulée par des longueurs de cohérence calculées (tableau de la Figure 0.5). Les recherches AFM visaient à mieux comprendre la taille et la structure des nanoparticules de CL-20/HMX. CL-20/HMX forme des plaques angulaires d'une hauteur de ~29 nm. Leurs longueurs et largeurs varient entre 100 nm et 400 nm. Les hauteurs détectées de 29 nm correspondent à la longueur de cohérence calculée dans la direction [300]. De plus, la morphologie des particules mesurées ressemble fortement aux formes simulées (Figure 0.5).

Les spectres Raman en champ lointain de β-CL-20, γ-CL-20, β-HMX et n CL-20/HMX ont été enregistrés pour avoir un aperçu de la façon dont les modes vibratoires des composés purs, contribuent au spectre Raman. Afin d'analyser les contributions des composés simples dans le spectre du n-CL-20/HMX, des bandes de référence ont été sélectionnées pour CL-20 et β-HMX à partir des ensembles de données Raman acquises. Pour le CL-20, on a choisi une vibration asymétrique d'étirement du NO_2 (1602 cm^{-1}) et pour le HMX, une vibration hors plan CH_2 (1417 cm^{-1}) (Figure 0.6). [26, 32-35] Les bandes de référence apparaissent dans le spectre de CL-20/HMX avec un rapport d'intensité d'environ 2,5:1 (CL-20/HMX). Des cartographies de Raman confocal en champ lointain ont été enregistrées pour déterminer si les bandes de référence de CL-20 et de HMX sont également réparties sur l'ensemble de l'échantillon (Figure 0.6). Les intensités des bandes de référence de CL-20 sont significativement plus importantes que celles des bandes de référence HMX. Cette tendance est reconnaissable dans la Figure 0.6 qui présente une superposition des intensités des deux modes vibratoires. Les spectres en champ lointain enregistrés, tout comme les cartographies, montrent que la différence d'intensité entre les bandes de référence CL-20 et HMX se produit indépendamment de l'orientation du cristal en fonction de la polarisation de la lumière incidente et de la géométrie de mesure.

Comme les résultats de la XRPD montrent que la surface principale du n-CL-20/HMX est constituée de couches uniques de CL-20 ou de HMX, une analyse TERS a été effectuée pour déterminer si la composition de la surface dans la direction [300] alterne entre CL-20 et HMX en tenant compte de leur rapport molaire ou si une couche moléculaire spécifique est privilégiée. Tous les modes vibratoires CL-20 et β-HMX pertinents, en particulier les bandes de référence, apparaissent uniformément répartis dans les spectres TERS sur toutes les particules, bien qu'ils apparaissent légèrement décalés et diffèrent dans leurs intensités

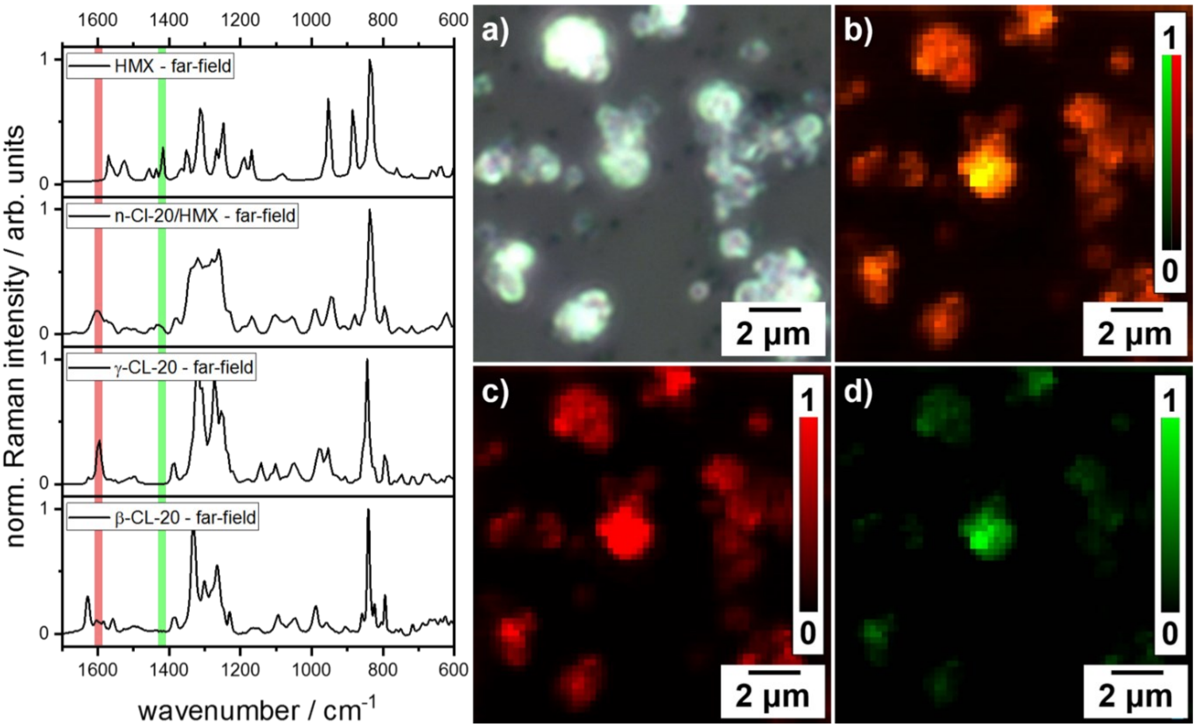

Figure 0.6. À gauche : Spectres Raman en champ lointain de β-CL-20, γ-CL-20, n-CL-20/HMX et β-HMX entre 1700 cm 1 et 600 cm-1. Bandes de référence du CL-20 (β-CL-20 : 1595 cm^{-1}, γ-CL-20 : 1598 cm^{-1}, O-N-O vibration d'étirement asymétrique, rouge) et HMX (1417 cm^{-1}, CH_2 vibration d'étirement, vert) ont été choisies pour indiquer la contribution des composés vierges dans n cartes TERS CL-20/HMX. Les intensités Raman sont normalisées pour améliorer la comparaison. **A droite : a)** Images microscopiques optiques des agglomérats de n-CL-20/HMX. **b) - d)** Cartes Raman confocale des agglomérats de n-CL-20/HMX présentés en a). La surface balayée est de 15 µm x 15 µm avec un pas de mesure de 250 nm. Les intensités Raman sont normalisées dans toutes les cartes indiquées. **b)** Les bandes de référence de CL-20 (vibration d'étirement asymétrique O-N-O ; 1602 cm^{-1}; rouge) et HMX (vibration d'agitation CH_2; 1416 cm^{-1}; vert), sont représentées en superposition. En général, si les deux signaux présentent la même intensité, les superpositions sont illustrées en jaune. Comme l'intensité de la bande de référence CL-20 double l'intensité de la bande de marqueurs HMX dans le spectre Raman CL-20/HMX, le CL-20 domine, ce qui donne un aspect plus rougeâtre. **c)** Cartes Raman confocal de la bande de référence CL-20 (1602 cm^{-1}) colorées en rouge. **d)** Cartes Raman confocal de la bande de référence HMX (1416 cm^{-1}) colorées en vert.

(Figure 0.7). La détectabilité de tous les modes vibratoires montre clairement que le TERS peut démontrer la co-cristallinité sur des nanoparticules individuelles. De plus, une inversion du rapport d'intensité des bandes de référence de 2,5 : 1 à 1 : 1,5 (CL-20 : HMX) en moyenne est reconnaissable dans les cartes TERS (Figure 0.7). L'inversion du rapport d'intensité indique une couche de finition de surface faite des molécules de HMX.

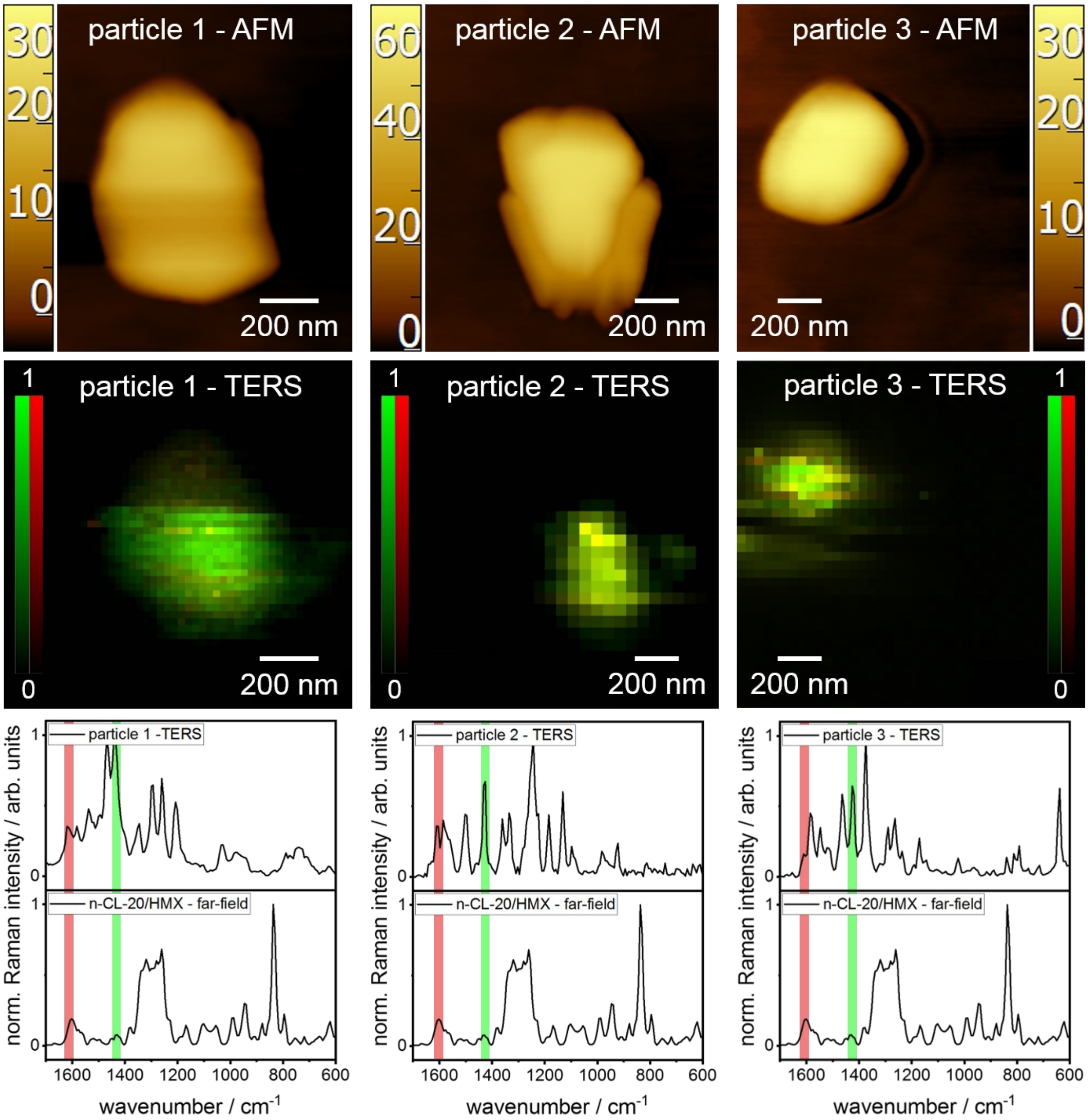

Figure 0.7. Images topographiques de l'AFM, cartes TERS et spectres correspondants de n plaques nano CL-20/HMX. Les spectres TERS représentent la moyenne de tous les spectres TERS sur les surfaces des particules. Sur toutes les surfaces mesurées, il y a une inversion d'intensité entre les bandes de marqueurs CL-20 et HMX. Les cartes TERS et les spectres TERS sont normalisés pour une meilleure comparaison. Les images topographiques AFM ont été enregistrées après la cartographie TERS. **Taille des pas :** particle_1 20 nm, particle_2 et particle_3 50 nm.

Pour vérifier cette présomption, une étude qualitative approximative de l'arrangement entre les nanoplaques n-CL-20/HMX et le système de diffusion TERS actuel est nécessaire. Il a été tenu compte du fait que le plan bc des nanoplaques CL-20/HMX est aligné parallèlement dans le plan xy du système de diffusion Raman. Ainsi, des approximations 3D des coordonnées normales des modes normaux des marqueurs de β-CL-20, γ-CL-20 et β-HMX ont été générées ($q_{0;z;CL-20}$, $q_{0;z;HMX}$, Figure 0.8). Le rapport des produits scalaires de ces vecteurs et du vecteur de champ électrique $E_{z;nf}$ de la lumière incidente donne alors le rapport d'intensité théorique entre les bandes de référence CL-20 et HMX :

$$\frac{I_{CL-20}}{I_{HMX}} = \frac{|E_{z;nf} \cdot q_{0;z;CL-20}|}{|E_{z;nf} \cdot q_{0;z;HMX}|} = \frac{|q_{0;z;CL-20}|}{|q_{0;z;HMX}|} = \frac{1.60}{0.53} \approx \frac{3}{1} \quad . \qquad \text{Équation 1}$$

Le rapport d'intensité théorique de 3:1 (CL-20 : HMX) est proche de la valeur déterminée expérimentalement dans les expériences Raman en champ lointain de ~ 2,5:1 et il est donc très peu probable que l'inversion du rapport d'intensité dans le TERS se produise en raison de l'orientation entre les nanoplaques CL-20/HMX avec le système de diffusion Raman.

Outre la disposition moléculaire par rapport au système de diffusion TERS, la distance entre la nanoparticule d'Ag à l'apex de la pointe et la surface de l'échantillon influence fortement les intensités Raman. Cette dépendance est due à la diminution rapide du champ amélioré localisé au sommet de la pointe en fonction de la distance. Dans le mode AFM dynamique sans contact, le champ principal renforcé est localisé à une distance inférieure à 2 nm de la surface des nanoparticules d'Ag (sphères vertes sur la Figure 0.8).[12] Par conséquent, la couche de surface est toujours située dans une zone de champ plus étendue que les couches moléculaires suivantes. Ainsi, les inversions d'intensité Raman entre les bandes de référence CL-20 et HMX de ~2,5:1 à ~1,5:1 (CL-20 : HMX) dans les spectres TERS peuvent être expliquées par HMX comme couche de finition de surface. Comme l'inversion d'intensité se produit à chaque surface de n nanoplaques CL-20/HMX mesurées, on suppose qu'une finition de surface HMX est énergétiquement favorisée. Cette hypothèse est explicable par la structure moléculaire de HMX. Contrairement à la structure de la cage de CL-20, HMX est une nitramine cyclique et donc plus facile à déformer. A cet égard, HMX devrait pouvoir adopter une conformation énergétiquement plus favorable que CL-20. Par conséquent, l'énergie de surface des nanoplaques CL-20/HMX est minimisée grâce à un traitement de surface par HMX.

On suppose que la couche de finition HMX contribue à la sensibilité à l'impact du CL-20/HMX, qui est beaucoup plus proche de celle de HMX que de celle de CL-20. Ainsi, le mécanisme suivant est proposé. Dans une première étape, l'énergie d'impact d'entrée qui peut être absorbée par la compression du co-cristal CL-20/HMX est suffisante pour enflammer le β-HMX pur et

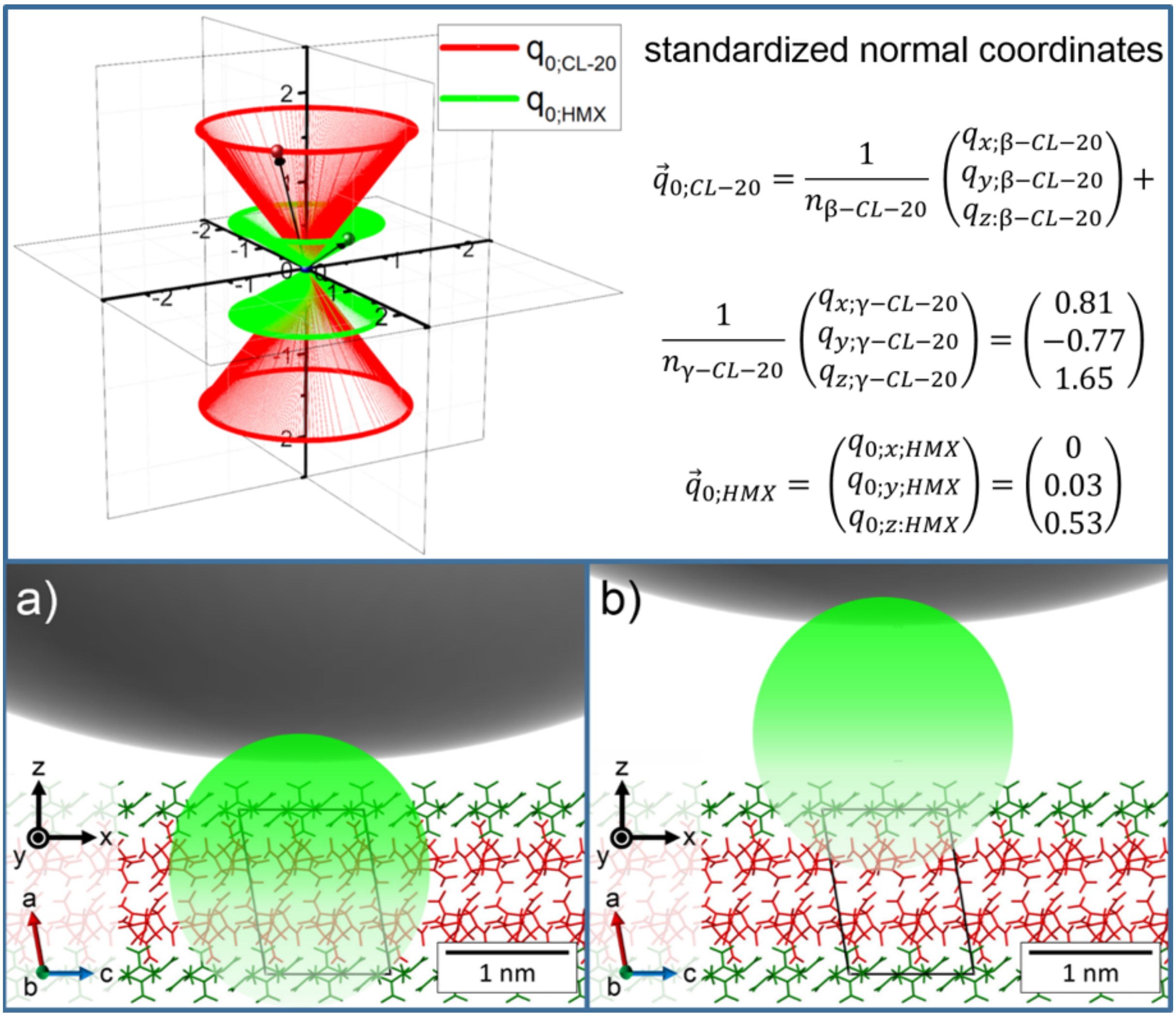

Figure 0.8. En haut : Coordonnées normales approximatives ; $\vec{q}_{0;CL-20}$ est représenté en rouge, $\vec{q}_{0;HMX}$ est représenté en vert. Comme le plan cristallographique bc - est aligné parallèlement au plan xy -, toutes les orientations possibles entre les coordonnées normales et le vecteur de champ électrique $\vec{E}_{nf}$ peuvent être illustrées sous forme de cônes autour de l'axe z -. Par conséquent, la semi-orientation actuelle n'affecte pas le rapport d'intensité Raman dans le TERS, puisque les angles inclus par les coordonnées normales et l'axe z ($\vec{E}_{nf}$) restent inchangés dans tous les alignements possibles. **En bas :** Représentation schématique d'une mesure TERS dynamique sans contact de n CL-20/HMX. La sphère grise représente la nanoparticule d'Ag active du TERS. Le cercle vert symbolise le champ renforcé localisé au sommet de la pointe. **a)** Distance la plus proche entre la pointe de la nanoparticule TERS active Ag et la surface de la particule. **b)** La pointe de la nanoparticule TERS active Ag se déplace vers le haut. **a) et b)** Pendant toute la durée des mesures TERS, la couche de surface HMX est toujours située dans une région de champ électrique présentant un renforcement Raman plus important. Ainsi, la bande de référence HMX apparaît plus intense dans les spectres TERS.

donc le β-CL-20 et le γ-CL-20 comprimé dans CL-20/HMX. Pendant la relaxation du cristal comprimé, l'énergie d'impact est convertie en énergie thermique se dissipant sur le réseau cristallin. Si la quantité d'énergie thermique dissipée en atteignant la surface des particules terminées par HMX (ou le défaut de structure) est encore suffisamment élevée pour surmonter l'énergie de dissociation de HMX, les molécules HMX se dissocieront. La chaleur de réaction libérée induit la dissociation des molécules HMX et CL-20 voisines, ce qui conduit une réaction en chaîne et finalement à la combustion du co-cristal CL-20/HMX.

Conclusion

En conclusion, cette étude démontre à nouveau les possibilités extraordinaires qui se cachent derrière le TERS. Il a été possible de déterminer la co-cristallinité sur des co-cristaux uniques à l'échelle nanométrique. Cela présente un intérêt analytique, par exemple, si les nano co-cristaux synthétisés ne sont pas présents en quantité suffisante pour permettre l'application de méthodes analytiques plus courantes comme la XRPD. En outre, il pourrait être démontré que le TERS permet d'étudier la surface des nanoparticules co-cristallines, ce qui pourrait aider à mieux comprendre la formation des co-cristaux et la conception des co-cristaux pour des applications spécifiques.

Mécanisme de formation des nanoparticules anisotropes de RDX/TNT à noyau/enveloppe et leur influence sur les synthèses par détonation des nanodiamants

Les mélanges de RDX et de TNT ou les mélanges d'hexolite sont des précurseurs bien connus pour les synthèses par détonation de nanodiamants. Dans cette étude, divers mélanges d'hexolites à l'échelle nanométrique, dont les rapports de masse du RDX et du TNT varient, sont synthétisés par évaporation flash de spray. Les mélanges d'hexolites sont caractérisés par la spectroscopie Raman confocale et par la spectroscopie Raman exaltée au voisinage d'une pointe (TERS) pour obtenir des informations sur la composition de leur structure moléculaire. Les bandes de référence de RDX et de TNT purs permettent d'identifier et de distinguer les deux composés dans les spectres Raman. La spectroscopie Raman confocale indique un mélange de molécules de RDX et de TNT à l'échelle nanométrique puisque les deux bandes de référence sont détectées dans tous les spectres. Les études TERS de particules d'hexolite simples révèlent que les surfaces des particules sont principalement composées de TNT. La comparaison des résultats de Raman confocal et de TERS suggère que (selon le rapport de masse) les particules d'hexolite sont soit des nanoparticules de RDX/TNT disparates et inhomogènes, soit des nanoparticules de RDX/TNT anisotropes de type cœur/coquille. Les données spectroscopiques et la dynamique du processus SFE permettent d'élaborer un mécanisme pour expliquer la formation/croissance de ces nanoparticules. Enfin, une corrélation entre l'épaisseur de la coquille de TNT, la symétrie des nanoparticules précurseurs de l'hexolite anisotrope et la taille des nanodiamants qui en résultent, est examinée en détail.

(Ce chapitre est publié à l'adresse suivante : Hübner, J.; Pichot, V.; Lobry, E.; Deckert-Gaudig, T.; Deckert, V.; Spitzer, D., Formation Mechanism of Anisotropic RDX-TNT Core-Shell Nanoparticles and their Influence onto Nanodiamond Detonation Syntheses, *chemrxiv.org,* **2020**, DOI: 10.26434/chemrxiv.12005625.v1)

Section expérimentale

Divers mélanges d'hexolite ont été produits par évaporation flash de spray (SFE) comme décrit dans la section précédente. Pour la production de mélanges d'hexolite, des solutions à 2 % en masse de diverses fractions massiques de RDX et de TNT dans 500 ml d'acétone ont été préparées et pulvérisées dans la chambre d'atomisation SFE. La masse de RDX plus TNT s'élevait à 8,2 g dans chaque solution. Les quantités de RDX et de TNT pour chaque solution de mélange d'hexolite sont résumées dans le Tableau 1. L'échantillon porte le nom du processus de production et du rapport de masse entre le RDX et le TNT, c'est-à-dire SFE-80/20, SFE-60/40, SFE-40/60 et SFE-20/80.

À partir de chaque mélange d'hexolite, des nanodiamants ont été synthétisés par détonation. À cette fin, le mélange d'hexolite produit par SFE a été pressé en cylindres de 15,8 mm de long à température ambiante pendant 10 minutes. Ces cylindres ont ensuite été cimentés avec de la colle pyrotechnique. Les charges explosives cylindriques ont été transférées dans une poche remplie d'eau avant d'être tirées dans une cuve de détonation. Les nanodiamants obtenus étaient séchés par évaporation par rotation. Les nanodiamants obtenus ont été nommés d'après le rapport RDX/TNT du précurseur de l'hexolite, c'est-à-dire ND-80/20, ND-60/40, ND-40/60 et ND-20/80.

Les pointes TERS ont été préparées comme décrit dans la section précédente.

Tableau 1. Masse et quantité de substance du RDX et du TNT pour chaque mélange d'hexolite

fraction massique de l'hexolite (RDX/TNT)	**RDX**		**TNT**	
	masse / g	**quantité de substance / mmol**	**masse / g**	**quantité de substance / mmol**
80/20	6,5	29,3	1,7	7,3
60/40	4,9	22,1	3,3	14,3
40/60	3,3	14,7	4,9	21,6
20/80	1,7	7,5	6,5	28,6

Résultats et discussion

Dans un premier temps, des spectres Raman en champ lointain de RDX et de TNT purs ont été pris et des bandes de référence ont été choisies pour chaque composé. La bande de référence de RDX à 882 cm^{-1} peut être attribuée à la vibration du cycle.[36-39] La bande de référence TNT comprise entre 1358 et 1371 cm^{-1} peut être attribuée à trois vibrations d'étirements symétriques NO_2.[37, 40-41] Ensuite, des cartes de Raman confocal en champ lointain ont été enregistrées pour chaque mélange d'hexolite afin d'obtenir un premier aperçu de l'interpénétration des molécules de RDX et de TNT dans les divers mélanges d'hexolites. Le TERS a été réalisé pour étudier la morphologie, la taille et la composition structurale des mélanges d'hexolites à l'échelle nanométrique. Des cartes de surface TERS contenant chacune 100 spectres TERS (10 x 10 spectres) avec des pas de 2 nm -5 nm (selon la taille des nanoparticules) ont été enregistrées. 15 nanoparticules de chaque mélange d'hexolite ont été étudiées. Ainsi, les différences entre les spectres Raman en champ lointain et les spectres TERS des nanoparticules d'hexolite ont permis de conclure sur la disposition distincte des molécules de RDX et de TNT dans les particules. Les cartes Raman confocal en champ lointain révèlent un mélange de molécules RDX et TNT à l'échelle nanométrique dans tous les mélanges d'hexolite, puisque tous les spectres enregistrés contiennent à la fois les bandes de référence RDX et TNT, comme le montre la Figure 0.9 sur l'exemple du SFE-40/60. Contrairement au Raman en champ lointain, les cartes TERS sensibles à la surface contiennent soit la bande de référence TNT uniquement, soit les bandes de référence RDX et TNT. Pas une seule surface de nanoparticule d'hexolite n'est formée uniquement de RDX. Le nombre de surfaces terminées uniquement par le TNT augmente avec la diminution de la fraction massique de RDX dans les mélanges d'hexolites (voir l'histogramme de la ligne inférieure de la Figure 0.9). En outre, de légers décalages de position des groupes fonctionnels $N\text{-}NO_2$ et NO_2 du RDX et du TNT sont présents dans les spectres TERS, ce qui indique une interaction électrostatique entre les molécules de surface du RDX et du TNT. La différence entre la spectroscopie Raman en champ lointain sensible au volume et le TERS sensible à la surface peut être comprise en prenant l’hypothèse que les mélanges d'hexolite sont constitués de nanoparticules composites structurées hiérarchiquement comme les particules de type patch ou les particules de type cœur/coquille (Figure 0.9). Un mécanisme de formation des diverses nanoparticules d'hexolite est dérivé des données spectroscopiques, de la dynamique du processus SFE et des différentes solubilités du RDX (6,8 g dans 100 g d'acétone) et du TNT (42,4 g pour 100 g) dans l'acétone.[37] Dans le procédé SFE, une solution de précurseur sous

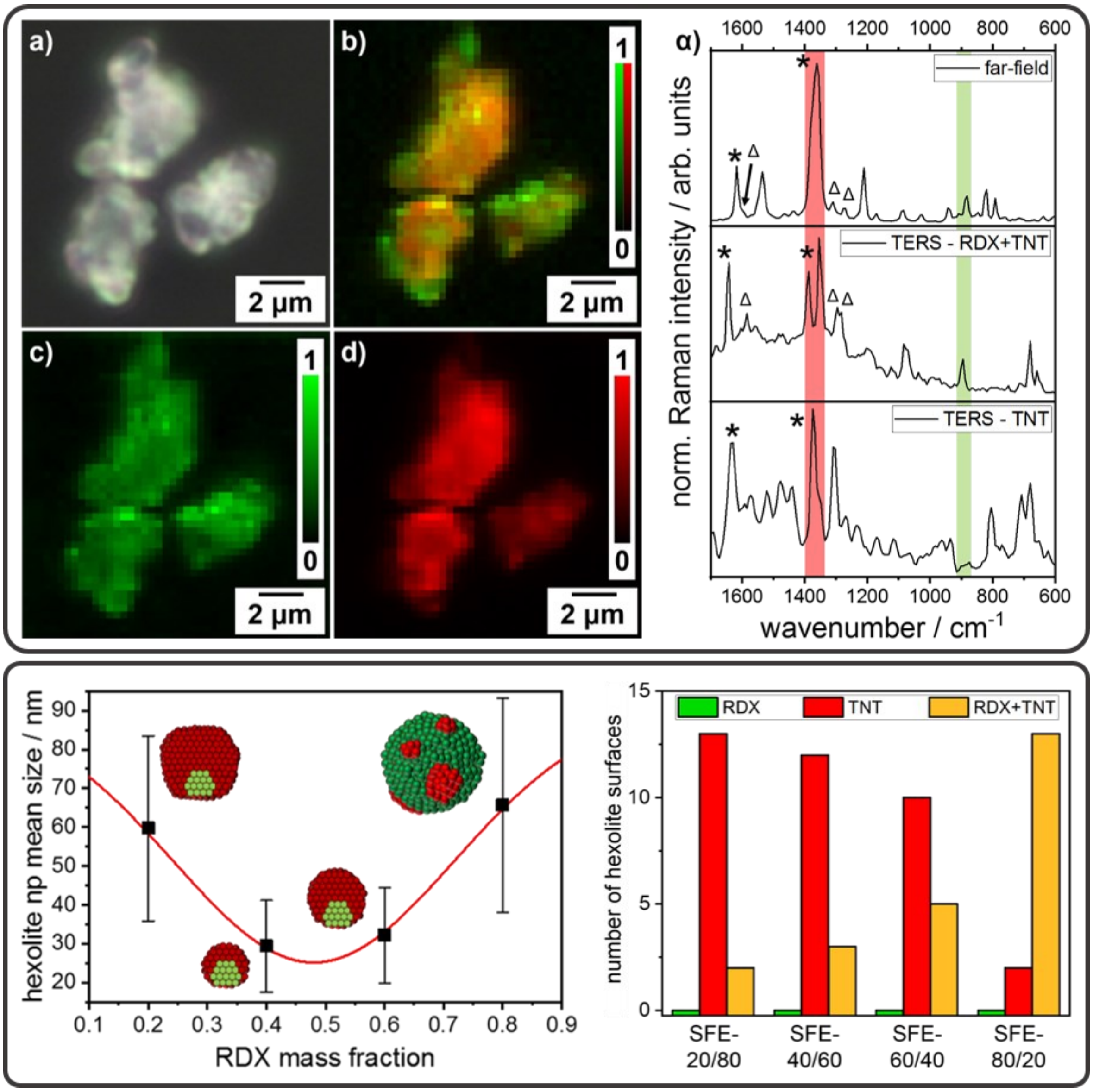

Figure 0.9. Top: Cartes de microscopie confocale Raman du SFE 40/60. Les intensités Raman sont normalisées pour une meilleure comparaison. **a)** Image microscopique de la nano hexolite SFE-40/60. **b)** Carte Raman confocal correspondante des intensités Raman superposées des bandes de référence RDX et TNT. **c)** Carte Raman confocal des intensités Raman des bandes de référence RDX. **d)** Carte Raman confocal des intensités Raman des bandes de référence TNT. **α)** Spectres Raman et TERS en champ lointain de la poudre d'hexolite 40/60 produite par SFE. Les spectres TERS typiques montrent soit les deux bandes de référence RDX (882 cm^{-1}; vibration de cycle) et TNT (1358 cm^{-1} - 1371 cm^{-1}; trois vibrations d'étirement symétriques de NO_2), soit seulement la bande de marqueurs TNT. Δ indique la vibration d'étirement N-NO_2 et la vibration d'étirement asymétrique de NO_2 du RDX ; * indique les vibrations d'étirement NO_2 du TNT étudiées.

En bas à gauche : Tailles moyennes des nanoparticules anisotropes à cœur/coquille d'hexolite (SFE 80/20, SFE 60/40, SFE 40/60) et des particules d'hexolite de taille inférieure au micron (SFE 20/80) en fonction de la fraction massique du RDX dans les solutions précurseurs. Les sphères vertes représentent les molécules de RDX ; les sphères rouges symbolisent les molécules de TNT. **En bas à droite :** Nombre de nanoparticules d'hexolite anisotropes et de nanoparticules de type patch donnant des surfaces de RDX uniquement, de TNT uniquement et de RDX/TNT mélangés.

pression est injectée par une buse à cône creux préchauffée dans une chambre d'atomisation sous vide. En passant par la buse à cône creux, la solution de précurseur est pulvérisée finement sous la forme de gouttelettes d'une taille moyenne de 2,6 µm ± 0,8 µm. Les gouttelettes sont accélérées en translation et angulairement et se rétractent continuellement jusqu'à évaporation complète. La diminution permanente de la taille des gouttelettes entraîne une augmentation des concentrations de RDX et de TNT dans les gouttelettes individuelles jusqu'à ce qu'une sursaturation soit atteinte. En raison de la solubilité six fois moindre du RDX dans l'acétone par rapport à celle du TNT, le RDX cristallised'abord en formant des nanoparticules primaires de RDX. Ces nanoparticules se déplacent vers les bords des gouttelettes sous l'effet de forces résultant de l'accélération angulaire et de la translation des gouttelettes d'acétone. Au cours du rétrécissement supplémentaire des gouttelettes, les gouttelettes d'acétone deviennent sursaturées par les molécules de TNT, ce qui entraîne une croissance de TNT sur les surfaces des nanoparticules primaires de RDX. Comme les nanoparticules primaires de RDX sont situées sur ou près des bords des gouttelettes, la formation des nanoparticules de RDX/TNT de type cœur/coquille se fait de manière anisotrope, c'est-à-dire que le noyau de RDX n'est pas centré dans la nanoparticule d'hexolite sphérique. (Figure 0.10). La formation de cette anisotropie provoque des zones de coquilles TNT partiellement plus épaisses et plus fines, ce qui explique la présence de signaux RDX dans certains spectres TERS. Dans le cas d'une

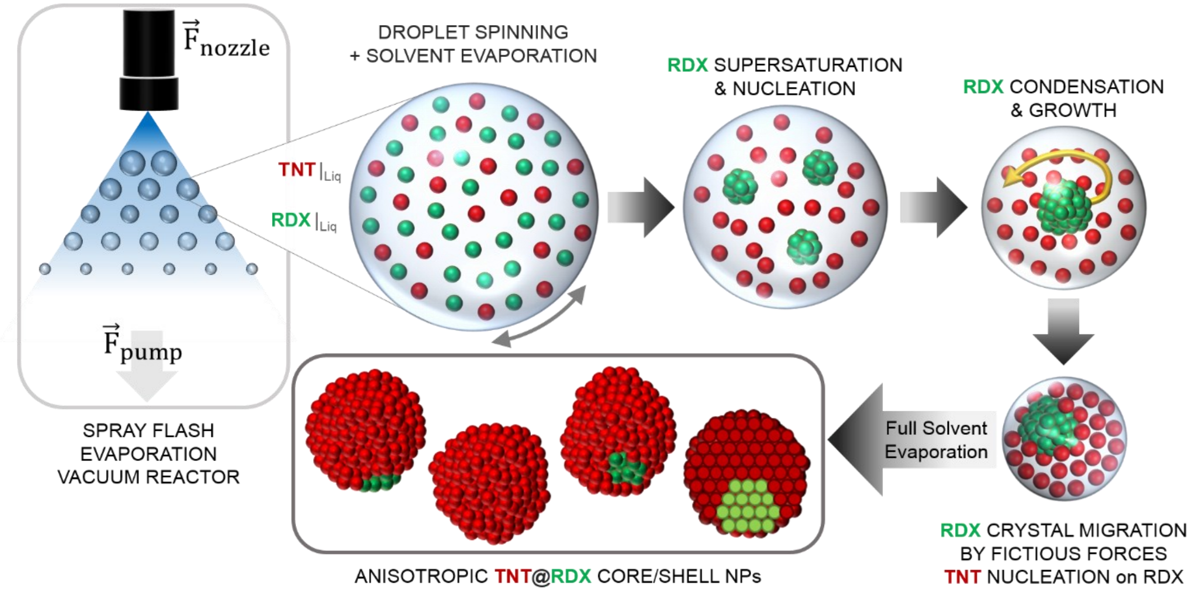

Figure 0.10. Schéma du mécanisme supposé de formation des nanoparticules anisotropes RDX/TNT de type cœur/coquille. La particule de droite dans l'encadré est représentée en coupe transversale pour illustrer l'anisotropie des nanoparticules d'hexolite cœur/coquille.

formation isotrope de nanoparticules de type cœur/coquille, c'est-à-dire si le noyau de RDX était situé exactement au centre de la nanoparticule d'hexolite et entouré d'une coquille de TNT de quelques nm d'épaisseur, les signaux de RDX ne contribueraient pas aux spectres TERS en raison de la rapide décroissance du champ au sommet de l'extrémité de la sonde TERS. En raison de la fraction massique plus faible du TNT dans le SFE-80/20, la quantité de TNT n'est pas suffisante pour couvrir complètement les noyaux de RDX avec une coquille fermée de TNT, ce qui donne des nanoparticules de RDX/TNT par endroits.

Les synthèses par détonation de nanodiamants montrent que la taille des nanodiamants obtenus ne correspond généralement pas à la taille des particules de la structure précurseur de l'hexolite (Figure 0.10). Afin de déterminer la relation entre la structure du précurseur et la taille des nanodiamants, un cas idéal, défini par des nanoparticules monodisperses et isotropes de RDX/TNT de type cœur/coquille formant un matériau précurseur hexagonal compact est d'abord examiné (Figure 4.13). Après l'allumage et la détonation, les produits de réaction du RDX sont accélérés en s'éloignant des centres des particules, tandis que les produits de réaction du TNT sont accélérés à la fois vers et à l’opposé des centres des particules. La migration des produits de réaction du RDX et du TNT est déterminée par leurs pressions de détonation spécifiques. En fonction du rapport massique RDX/TNT, les effets de migration concurrents peuvent être dominés soit par la pression de détonation du RDX, soit par celle du TNT. En général, le RDX fournit une pression de détonation plus élevée que le TNT. Dans le cas où la pression de détonation du RDX domine, les produits de réaction du TNT sont poussés au centre du tétraèdre composé de particules d'hexolite adjacentes très serrées, tandis que les produits de réaction du RDX forment une barrière de diffusion sphérique autour de celui-ci. Si la pression de détonation du TNT domine les effets de migration, les produits de réaction du RDX forment des barrières de diffusion sphériques autour du centre d'un tétraèdre. Selon que la pression de détonation du RDX ou du TNT domine, différentes conditions thermodynamiques de pression et de température prévalent dans les zones de diffusion. Comme dans le cas de la pression de détonation du RDX, les produits de la réaction du TNT sont poussés vers les centres du tétraèdre, la pression et la température sont plus élevées dans ces zones de diffusion résultantes que dans les zones de diffusion formées dans un système dominé par le TNT. Des pressions et des températures plus élevées favorisent une conversion plus complète des atomes de carbone en nanodiamants, ce qui conduit à des particules de nanodiamants plus grosses. Par conséquent, une pression et une température plus basses entraînent une diminution du nombre d'atomes de carbone formant des nanodiamants et donc des nanoparticules plus petites. En raison de la

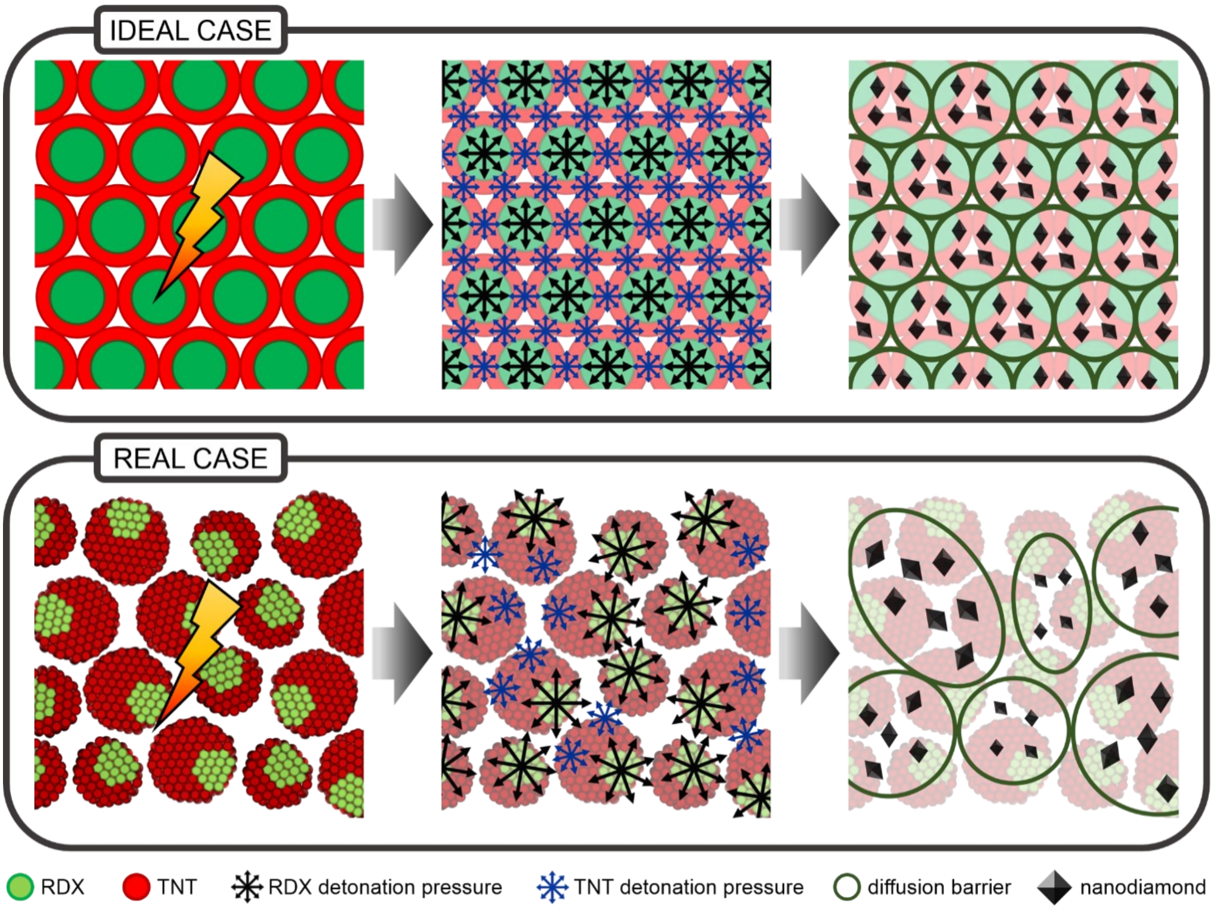

Figure 0.11. En haut : Mécanisme supposé de formation des nanodiamants dans des conditions idéales présenté sous forme de sections transversales en 2D. Le précurseur de l'hexolite est constitué de nanoparticules isotropes hexagonales à cœur/coquille RDX/TNT très serrées. En raison de la pression de détonation plus élevée du RDX par rapport à celle du TNT et de la grande symétrie du précurseur, les produits de réaction du RDX forment des barrières de diffusion sphériques après la détonation. À l'intérieur de la zone de diffusion, des nanodiamants sont formés à partir des atomes de carbone du TNT. Dans le cas idéal, toutes les zones de diffusion ont la même taille et contiennent la même quantité d'atomes de carbone et de sites de nucléation. Ainsi, la même quantité de nanodiamants monodisperses en taille se forme dans les zones de diffusion. Par conséquent, la taille des nanodiamants ne dépend que de l'épaisseur de l'enveloppe du TNT et de la fraction massique du RDX dans le cas idéal. **En bas :** Mécanisme supposé de construction de nanodiamants dans des conditions réelles, présenté sous forme de sections transversales en 2D. Les nanoparticules anisotropes à cœur/coquille produites par SFE sont très denses. En raison de la distribution de taille des particules précurseurs d'hexolite, une compression hexagonale parfait n'est pas possible. La disposition aléatoire des particules anisotropes cœur/coquille conduit à la formation de zones de diffusion plus ellipsoïdes de tailles légèrement différentes. Par conséquent, les zones de diffusion contiennent des quantités différentes d'atomes de carbone et de sites de nucléation. Ainsi, les nanodiamants synthétisés présentent des tailles légèrement différentes, ce qui conduit à une distribution de la taille des nanodiamants. Par conséquent, la taille moyenne et la distribution de taille des nanodiamants dépendent de l'épaisseur de la coquille du TNT, de la fraction massique du RDX, de la taille moyenne des particules du précurseur d'hexolite, de la distribution de taille du précurseur d'hexolite et du niveau d'anisotropie au sein de la structure du précurseur.

grande symétrie des particules isotropes à cœur/coquille d'hexolite idéalement tassées et parfaitement monodisperses, la taille et les conditions thermodynamiques dans toutes les zones de diffusion sont constantes pour un rapport de masse RDX/TNT donné. Par conséquent, le nombre de sites de nucléation dans les zones de diffusion semble constant et, enfin, le nombre et la taille des nanodiamants obtenus dans une zone de diffusion (Figure 4.13, haut). Ainsi, dans ce système modèle, la taille des nanodiamants ne dépend que de la fraction massique du RDX et de l'épaisseur de la coquille de TNT. Dans des conditions réelles, le matériau précurseur d'hexolite est constitué de particules cœur/coquille anisotropes présentant une distribution de taille. En raison de cette distribution, il est impossible d'obtenir une compression hexagonale parfaitement symétrique. De plus, l'anisotropie des particules précurseurs entraîne une diminution supplémentaire de la symétrie au sein de la structure du précurseur. Cette diminution de symétrie conduit à la formation de zones de diffusion ou de barrières de diffusion de nature plus ellipsoïdale et de dimensions différentes (Figure 4.13, bas). Par conséquent, les conditions thermodynamiques et cinétiques ainsi que la quantité d'atomes de carbone provenant du TNT dans les différentes zones de diffusion diffèrent, ce qui entraîne un nombre variable de sites de nucléation. Il en résulte des tailles et des distributions de tailles de nanodiamants légèrement différentes. Par conséquent, la taille moyenne des nanodiamants d_{ND} dépend non seulement de la fraction massique du RDX ω_{RDX} et de l'épaisseur de la coquille du TNT d_{TNT}, mais aussi des paramètres définissant la symétrie du matériau précurseur. Il s'agit de la taille moyenne des particules du précurseur d'hexolite d_{hex}, de l'écart-type de la taille du précurseur d'hexolite s_{hex} et du niveau d'anisotropie a_{hex} au sein de la structure du précurseur. Ainsi, d_{ND} peut être estimé par la corrélation suivante :

$$d_{ND} \sim \omega_{RDX} d_{TNT} + d_{TNT}\left(a_{hex} + \frac{|s_{hex}|}{d_{hex}}\right) \qquad \text{Équation 2}$$

Le niveau d'anisotropie est défini comme la distance entre le centre de la particule d'hexolite et le centre du noyau de RDX correspondant $d_{hex \to RDX}$ divisée par le rayon moyen de la particule d'hexolite r_{hex} :

$$a_{hex} = \frac{d_{hex \to RDX}}{r_{hex}} \qquad \text{Équation 3}$$

Cette corrélation permet enfin d'interpréter les tailles moyennes et les distributions de taille des nanodiamants et indique que les paramètres de symétrie influencent les tailles de nanodiamants obtenus au moins aussi fortement que la taille des particules précurseurs.

Conclusion

La combinaison du Raman en champ lointain et du TERS permet d'élucider la structure des hexolites à structure hiérarchisée de type cœur/coquille et des nanoparticules fragmentées. Le mécanisme de formation de ces particules a été déduit des résultats de la spectroscopie TERS et Raman en champ lointain en tenant compte de la cinétique du processus SFE. L'élucidation de la structure des nanoparticules d'hexolite permet de mieux décrire la corrélation entre la structure du précurseur d'hexolite et la taille des nanodiamants synthétisés par détonation.

Mécanismes de formation des particules composites pharmaceutiques submicroniques dérivées de la microscopie Raman en champ lointain et proche

La spectroscopie Raman exaltée de surface (SERS) et la microscopie Raman confocale sont appliquées pour étudier la structure et l'arrangement moléculaire d'un composite organique pharmaceutique submicronique. Comme système modèle, on étudie les particules submicroniques de furosémide et de polyvinylpyrrolidone (furosémide/PVP) produites par évaporation flash de spray (SFE) à partir d'une seule solution. La morphologie, la taille et la cristallinité des composites furosémide/PVP sont d'abord analysées par microscopie électronique à balayage (MEB) et par diffraction des rayons X sur poudre (XRPD). Ensuite, les spectres Raman en champ lointain de référence et les cartographies en Raman confocal en champ lointain des particules de furosémide/PVP sont interprétés sur la base des spectres Raman en champ lointain du furosémide pur et de la PVP pure. La microscopie Raman confocal en champ lointain montre que les particules de furosémide/PVP présentent un mélange de molécules de furosémide et de PVP à l'échelle submicronique. Afin d'avoir une meilleure idée de la disposition moléculaire de la PVP et du furosémide dans les particules composites, la SERS et la microscopie Raman confocale exaltée de surface (SECoRM) sont réalisées sur des particules composites de furosémide, de PVP et de furosémide/PVP pulvérisées avec de l'argent (40 nm). Les cartes SERS et SECoRM sensibles à la surface révèlent que les surfaces des particules de furosémide/PVP sont principalement constituées de molécules de PVP recouvrant les domaines du furosémide. Dans l'ensemble, la combinaison des analyses sensibles à la surface et à la masse permet de dresser un tableau clair de la morphologie des particules et de la disposition des molécules dans les particules de furosémide/PVP submicroniques. Les particules submicroniques de furosémide/PVP produites par le SFE sont formées par l'agglomération de particules primaires constituées de nanocristaux de furosémide, incorporés dans une fine matrice de PVP. Il est intéressant de noter que les microscopies Raman confocal à champ lointain (sensibles au volume) et exaltée de surface (sensibles à la surface) fournissent des informations moléculaires sur une quantité statistiquement pertinente de particules submicroniques sur une seule cartographie microscopique ; cette combinaison est donc un outil efficace et rapide pour étudier les composites organiques et inorganiques submicroniques.

(Ce chapitre est publié à l'adresse suivante : Hübner, J.; Coty J.-B.; Busby, Y.; Spitzer, D., Formation Mechanisms of Sub-Micron Pharmaceutical Composite Particles Derived from Far- and Near Field Raman Microscopy, *chemRxiv.org*, **2020**, DOI: 10.26434/chemrxiv.12098478.v1).

Section expérimentale

Les particules composites submicroniques de furosémide/PVP ont été produites par le procédé SFE. Une solution de 3,0 g de furosémide et de 1,0 g de PVP dans un mélange de solvants composé de 240 ml d'éthanol et de 160 ml de chlorure de méthylène a d'abord été préparée. Cette solution a été introduite dans le réservoir d'un cristallisateur SFE vertical pressurisé à 40 bar (N_2). La solution de furosémide/PVP a été pulvérisée à travers une buse à cône creux préchauffée à 120 °C, d'un diamètre de 100 µm, dans une chambre d’atomisation sous vide dont la pression de base est inférieure à 0,1 mbar. La pression à l'intérieur de la chambre d'atomisation SFE varie entre 5 et 10 mbar pendant le processus de pulvérisation. Après l'évaporation rapide du solvant, les particules submicroniques de furosémide/PVP sont recueillies sous forme de poudre ultrafine blanc-jaunâtre à l'aide d'un filtre en acier.

Pour la spectroscopie Raman exaltée de surface, les particules submicroniques de furosémide, de PVP et de furosémide/PVP ont été déposées sur des substrats en verre. Tous les échantillons préparés ont été directement recouverts d'une épaisseur nominale de 40 nm d'argent avec une vitesse de dépôt de 4,0 Å/s.

Résultats et discussion

Un premier aperçu de la taille, de la morphologie et de la cristallinité des particules de furosémide/PVP est fourni par les analyses MEB et XRPD montrant la présence de particules sphériques submicroniques avec une surface rugueuse en forme de choufleur (Figure 0.12). Les particules de furosémide/PVP ont un diamètre moyen de 0,38 µm (± 0,24 µm). La structure cristalline des particules submicroniques de furosémide/PVP a été étudiée par XRPD. Cette technique montre des réflexions typiques des cristaux de furosémide superposés et une large

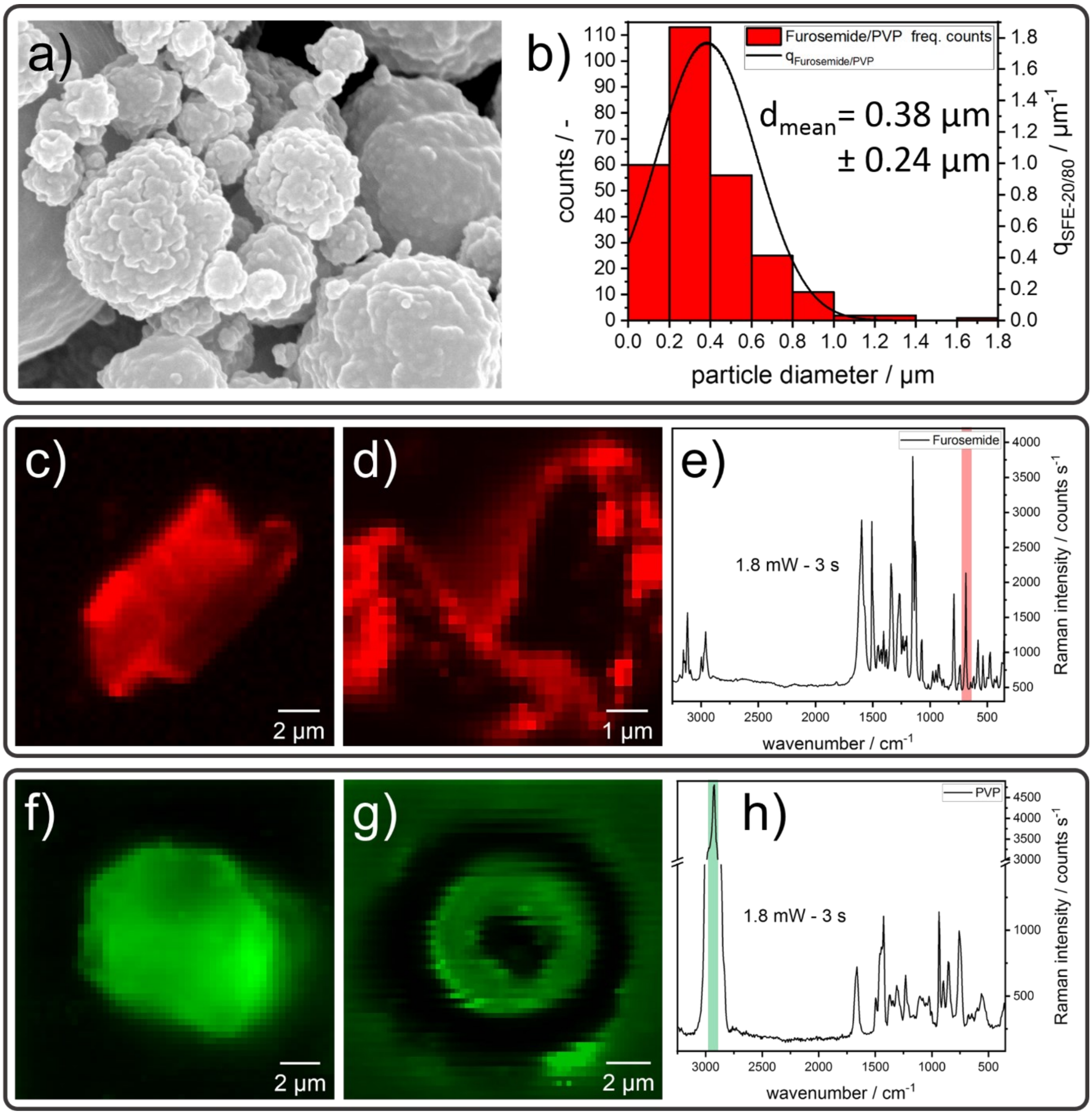

Figure 0.12. a) Image MEB de particules de furosémide/PVP caractérisée par une surface rugueuse semblable à un chou fleur. **b)** Les particules de furosémide/PVP ont une taille moyenne de 0,38 µm (± 0,24 µm). **c)** Cartographie Raman d'une particule de furosémide pur. **d)** Carte SECoRM de particules de furosémide enrobées d'argent. **e)** Spectre Raman de furosémide pur. La vibration de flexion de l'anneau dans le plan localisée à 686 cm^{-1} (rouge) est choisie comme référence pour le furosémide. **f)** Cartographie Raman d'une particule de PVP pur. **g)** Cartographie SECoRM d'une particule de PVP enrobée d'argent. h) Spectre Raman de PVP pure. La vibration d'étirement asymétrique CH_2 à 2924 cm^{-1} (vert) est choisie pour l'identification due la PVP.

réflexion amorphe entre 16° et 25° attribuée de la PVP. Les longueurs de cohérence le long des principales directions cristallographiques révèlent que les dimensions des cristaux de furosémide sont inférieures à 50 nm, c'est-à-dire environ dix fois plus petites que la taille moyenne des particules estimée par analyse MEB. Sur cette base, les spectres Raman du furosémide pur et de la PVP ont été enregistrés et des bandes de marquage ont été choisies. Pour le furosémide, la bande choisie est la vibration de flexion annulaire dans le plan à 686 cm^{-1}.[42] Pour la PVP, la bande de référence sélectionnée est la vibration d'étirement asymétrique CH_2 la plus intense des chaînes saturées de la PVP, qui culmine à 2924 cm^{-1} (Figure 0.12).[43] Ensuite, les échantillons recouverts d'argent ont été analysés par spectroscopie Raman pour vérifier si les nanoparticules d'argent pulvérisées entraînent une amélioration du champ et si les bandes de référence choisies peuvent être détectées dans les spectres SERS. Par rapport aux spectres en champ lointain, les spectres SERS enregistrés présentent des intensités sensiblement plus élevées, ce qui permet de réduire l'intensité du faisceau laser entrant de 1/33. L'augmentation de l'intensité Raman totale indique une exaltation du champ par les nanoparticules d'argent. En outre, l'emplacement des points les plus brillants diffère entre la microscopie Raman en champ lointain et le SECoRM. Les points les plus brillants des images Raman en champ lointain correspondent simplement à la région caractérisée par un nombre plus élevé de molécules (sensibilité au volume). Au contraire, sur les cartographies SECoRM, les points les plus brillants sont situés sur les bords des particules, tandis que les régions centrales présentent une amélioration du signal extrêmement faible (Figure 0.12). Ce phénomène peut s'expliquer par le fait que la lumière laser incidente (532 nm) est polarisée linéairement et focalisée sur l'échantillon par un objectif 100X avec une ouverture numérique de 0,9 et que l'exaltation locale du champ électromagnétique est assurée par les résonances plasmoniques de surface (LSPR) localisées à la surface des nano-grains d'argent. Dans notre configuration, le vecteur de champ électrique de la lumière incidente $\vec{E}_{in}$ oscille dans le plan parallèle au substrat. En conséquence, le champ créé par le LSPR est également parallèle au plan du substrat. Dans cette géométrie, les particules d'argent se trouvant sur un cristal plat ne contribueront pas à l'exaltation de l'intensité Raman mesurée car aucune (ou presque) molécule active en Raman n'est située dans la zone du champ exalté. À l'inverse, les nanoparticules d'argent situées sur des surfaces verticales (c'est-à-dire sur des bords tranchants) entraînent une forte augmentation de l'intensité Raman puisqu'un nombre relativement élevé de molécules actives en Raman sont situées dans le champ électrique exalté délivré. Ainsi, la position différente des points lumineux laisse également entrevoir une formation réussie de nanoparticules d'argent actives en SERS. De plus, les bandes de référence du furosémide et de la PVP se trouvent dans les spectres SERS correspondants.

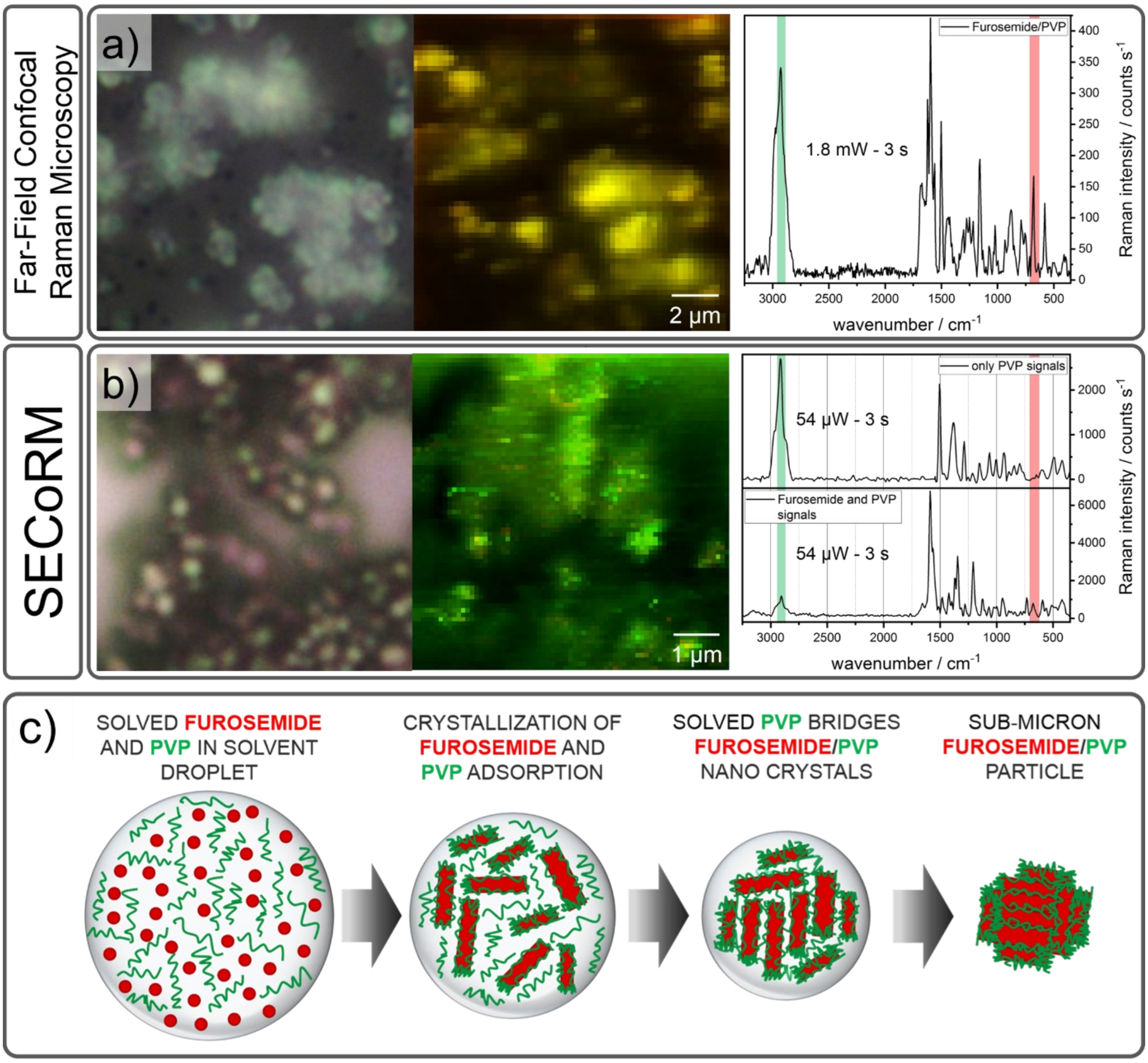

Figure 0.13. a) Cartographie de microscopie Raman confocale en champ lointain des particules submicrométriques composites de furosémide/PVP. Les pixels jaunes indiquent la présence de bandes de référence de furosémide et de PVP dans chaque point du spectre Raman, comme le montre le spectre corrigé du fond. **b)** Cartographie SECoRM des particules submicrométriques composites de furosémide/PVP. Les pixels de couleur verte montrent que la PVP est principalement présente à la surface des particules de furosémide/PVP. Des spectres SERS corrigés du fond montrant uniquement les signux de références de la PVP (majorité) et les signaux de référence de PVP-Furosémide sont présents. **c)** Mécanisme de construction proposé pour les particules composites submicroniques de furosémide/PVP.

Comme ces résultats démontrent que la formation de nanoparticules d'argent par pulvérisation directe permet l'obtention du SERS et du SECoRM sur des particules organiques, cette méthode est utilisée pour caractériser l'arrangement discret des molécules de furosémide et de PVP dans les particules submicroniques de furosémide/PVP. Les spectres en champ lointain extraits des images de microscopie Raman confocale montrent les deux bandes de référence du furosémide et de la PVP (Figure 0.13.a). Au contraire, sur les cartes SECoRM sensibles à la surface, on trouve principalement la bande de référence de la PVP (Figure 0.13.b). La combinaison de la microscopie Raman en champ lointain et des résultats du SECoRM indique la formation d'une sorte d'arrangement noyau/coque Furosémide/PVP. En considérant les résultats de la XRPD et du MEB, un mécanisme de formation peut être déduit. Au cours du processus SFE, le furosémide cristallise d'abord en raison de sa moindre solubilité dans le mélange de solvants utilisés par rapport à la PVP. Ensuite, les molécules de PVP s'adsorbent sur les surfaces des nano cristaux primaires de furosémide. L'excès de molécules de PVP forme des ponts entre les nanocristaux primaires de furosémide/PVP, ce qui donne les particules composites furosémide/PVP obtenues (Figure 0.13.c).

Conclusion

La combinaison de la microscopie Raman en champ lointain et de la microscopie Raman confocale exaltée en surface donne de nouvelles idées sur la structure et l'arrangement moléculaire des composites organiques submicroniques. On suppose donc que de nombreux composites pourraient être testés par cette combinaison comme une méthode standard pour la caractérisation chimique des surfaces et l'étude de l'arrangement moléculaire des particules organiques composites submicroniques.

Conclusion générale

Dans le cadre de cette thèse, plusieurs composites nanostructurés produits par évaporation flash de spray ont été étudiés en utilisant la spectroscopie et la microscopie Raman, TERS et SERS. Il s'agit d'un co-cristal nanostructuré composé de CL-20 et HMX, de différents mélanges RDX-TNT à l'échelle nanométrique qui diffèrent par leur rapport massique et de particules submicroniques de Furosémide/PVP. Il a pu être démontré que le TERS et le SERS sont des outils puissants pour l'étude des particules composites submicrométriques structurées à l'échelle nanométrique et nanostructurées. Cela a donc permis d'obtenir de nouvelles informations sur les arrangements moléculaires au sein de ces particules qui ne sont pas accessibles à d'autres méthodes de mesure. En conclusion, TERS et SERS sont des méthodes appropriées pour l'étude de la structure des nanocomposites organiques et pourraient devenir elles-mêmes des méthodes standard pour l'étude de la structure des composites organiques à l'échelle nanométrique.

References

1. Hübner, J.; Klaumünzer, M.; Comet, M.; Martin, C.; Vidal, L.; Schäfer, M.; Kryschi, C.; Spitzer, D., Insights into Combustion Mechanisms of Variable Aluminum-Based Iron Oxide/-Hydroxide Nanothermites. *Combust. Flame* **2017,** *184*, 186-194.

2. Pichot, V.; Risse, B.; Schnell, F.; Mory, J.; Spitzer, D., Understanding ultrafine nanodiamond formation using nanostructured explosives. *Sci. Rep.* **2013,** *3* (1), 2159.

3. Long, D. A., *The Raman Effect: A Unified Treatment of the Theory of Raman Scattering by Molecules*. Wiley: 2002.

4. Kelly, K. L.; Coronado, E.; Zhao, L. L.; Schatz, G. C., The optical properties of metal nanoparticles: The influence of size, shape, and dielectric environment. *J. Phys. Chem. B* **2003,** *107* (3), 668-677.

5. Deckert-Gaudig, T.; Taguchi, A.; Kawata, S.; Deckert, V., Tip-Enhanced Raman Spectroscopy – From Early Developments to Recent Advances. *Chem. Soc. Rev.* **2017,** *46*, 4077.

6. Yano, T.-a.; Ichimura, T.; Taguchi, A.; Hayazawa, N.; Verma, P.; Inouye, Y.; Kawata, S., Confinement of enhanced field investigated by tip-sample gap regulation in tapping-mode tip-enhanced Raman microscopy. *Appl. Phys. Lett.* **2007,** *91* (12), 121101.

7. Hartschuh, A.; Sánchez, E. J.; Xie, X. S.; Novotny, L., High-Resolution Near-Field Raman Microscopy of Single-Walled Carbon Nanotubes. *Physical Review Letters* **2003,** *90* (9), 095503.

8. Roth, R. M.; Panoiu, N. C.; Adams, M. M.; Osgood, R. M.; Neacsu, C. C.; Raschke, M. B., Resonant-Plasmon Field Enhancement from Asymmetrically Illuminated Conical Metallic-Probe Tips. *Opt. Express* **2006,** *14* (7), 2921-2931.

9. Jiang, N.; Foley, E.; Klingsporn, J.; Sonntag, M.; Valley, N.; Dieringer, J.; Seideman, T.; Schatz, G.; Hersam, M.; Van Duyne, R., Observation of multiple vibrational modes in ultrahigh vacuum tip-enhanced Raman spectroscopy combined with molecular-resolution scanning tunneling microscopy. *Nano letters* **2012,** *12* (10), 5061-5067.

10. Pettinger, B.; Domke, K. F.; Zhang, D.; Schuster, R.; Ertl, G., Direct Monitoring of Plasmon Resonances in a Tip-Surface Gap of Varying Width. *Phys. Rev. B: Condens. Matter* **2007,** *76* (11).

11. Pashaee, F.; Hou, R.; Gobbo, P.; Workentin, M. S.; Lagugné-Labarthet, F., Tip-Enhanced Raman Spectroscopy of Self-Assembled Thiolated Monolayers on Flat Gold

Nanoplates Using Gaussian-Transverse and Radially Polarized Excitations. *J. Phys. Chem. C* **2013,** *117* (30), 15639-15646.

12. Trautmann, S.; Aizpurua, J.; Götz, I.; Undisz, A.; Dellith, J.; Schneidewind, H.; Rettenmayr, M.; Deckert, V., A Classical Description of Subnanometer Resolution by Atomic Features in Metallic Structures. *Nanoscale* **2017,** *9* (1), 391-401.

13. Stiles, P. L.; Dieringer, J. A.; Shah, N. C.; Van Duyne, R. P., Surface-enhanced Raman spectroscopy. *Annu. Rev. Anal. Chem.* **2008,** *1*, 601-626.

14. Langer, J.; Jimenez de Aberasturi, D.; Aizpurua, J.; Alvarez-Puebla, R. A.; Auguié, B.; Baumberg, J. J.; Bazan, G. C.; Bell, S. E. J.; Boisen, A.; Brolo, A. G.; Choo, J.; Cialla-May, D.; Deckert, V.; Fabris, L.; Faulds, K.; García de Abajo, F. J.; Goodacre, R.; Graham, D.; Haes, A. J.; Haynes, C. L.; Huck, C.; Itoh, T.; Käll, M.; Kneipp, J.; Kotov, N. A.; Kuang, H.; Le Ru, E. C.; Lee, H. K.; Li, J.-F.; Ling, X. Y.; Maier, S. A.; Mayerhöfer, T.; Moskovits, M.; Murakoshi, K.; Nam, J.-M.; Nie, S.; Ozaki, Y.; Pastoriza-Santos, I.; Perez-Juste, J.; Popp, J.; Pucci, A.; Reich, S.; Ren, B.; Schatz, G. C.; Shegai, T.; Schlücker, S.; Tay, L.-L.; Thomas, K. G.; Tian, Z.-Q.; Van Duyne, R. P.; Vo-Dinh, T.; Wang, Y.; Willets, K. A.; Xu, C.; Xu, H.; Xu, Y.; Yamamoto, Y. S.; Zhao, B.; Liz-Marzán, L. M., Present and Future of Surface-Enhanced Raman Scattering. *ACS Nano* **2020,** *14* (1), 28-117.

15. Kneipp, K.; Wang, Y.; Kneipp, H.; Perelman, L. T.; Itzkan, I.; Dasari, R. R.; Feld, M. S., Single Molecule Detection Using Surface-Enhanced Raman Scattering (SERS). *Phys. Rev. Lett.* **1997,** *78*, 1667.

16. Nie, S.; Emory, S. R., Probing Single Molecules and Single Nanoparticles by Surface-Enhanced Raman Scattering. *Science* **1997,** *275*, 1102.

17. Xu, H.; Aizpurua, J.; Käll, M.; Apell, P., Electromagnetic Contributions to Single-Molecule Sensitivity in Surface-Enhanced Raman Scattering. *Phys. Rev. E: Stat. Phys., Plasmas, Fluids, Relat. Interdiscip. Top.* **2000,** *62*, 4318.

18. Yamamoto, Y. S.; Ozaki, Y.; Itoh, T., Recent Progress and Frontiers in the Electromagnetic Mechanism of Surface-Enhanced Raman Scattering. *J. Photochem. Photobiol., C* **2014,** *21*, 81.

19. Pilot, R.; Signorini, R.; Durante, C.; Orian, L.; Bhamidipati, M.; Fabris, L., A Review on Surface-Enhanced Raman Scattering. *Biosensors* **2019,** *9* (2), 57.

20. Stockle, R.; Suh, Y.; Deckert, V.; Zenobi, R., Nanoscale Chemical Analysis by Tip-Enhanced Raman Spectroscopy. *Chem. Phys. Lett.* **2000,** *318*, 131.

21. Deckert-Gaudig, T.; Kämmer, E.; Deckert, V., Tracking of Nanoscale Structural Variations on a Single Amyloid Fibril with Tip-Enhanced Raman Scattering. *J. Biophotoics.* **2012,** *5*, 215.

22. Deckert-Gaudig, T.; Kurouski, D.; Hedegaard, M. A. B.; Singh, P.; Lednev, I. K.; Deckert, V., Spatially resolved spectroscopic differentiation of hydrophilic and hydrophobic domains on individual insulin amyloid fibrils. *Sci. Rep.* **2016,** *6* (1), 33575.

23. Aitipamula, S.; Banerjee, R.; Bansal, A. K.; Biradha, K.; Cheney, M. L.; Choudhury, A. R.; Desiraju, G. R.; Dikundwar, A. G.; Dubey, R.; Duggirala, N., Polymorphs, Salts and Cocrystals: What's in a Name? *Cryst. Growth Des.* **2012,** *12* (5), 2147-2152.

24. Braga, D.; Grepioni, F.; Maini, L.; Polito, M., Crystal Polymorphism and Multiple Crystal Forms. In *Molecular networks*, Springer: 2009; pp 87-95.

25. Bolton, O.; Simke, L. R.; Pagoria, P. F.; Matzger, A. J., High Power Explosive with Good Sensitivity: A 2:1 Cocrystal of CL-20:HMX. *Cryst. Growth Des.* **2012,** *12* (9), 4311-4314.

26. Ghosh, M.; Sikder, A. K.; Banerjee, S.; Gonnade, R. G., Studies on CL-20/HMX (2: 1) Co-crystal: A New Preparation Method, Structural and Thermo Kinetic Analysis. *Cryst. Growth Des.* **2018,** *18* (7), 3781-3793.

27. Klaumünzer, M.; Hübner, J.; Spitzer, D., Production of Energetic Nanomaterials by Spray Flash Evaporation. *World Academy of Science, Engineering and Technology, International Journal of Chemical, Molecular, Nuclear, Materials and Metallurgical Engineering* **2016,** *10* (9), 1079-1083.

28. Klaumünzer, M.; Pessina, F.; Spitzer, D., Indicating Inconsistency of Desensitizing High Explosives Against Impact through Recrystallization at the Nanoscale. *J. Energ. Mater.* **2016**, 1-10.

29. Klaumünzer, M.; Hübner, J.; Spitzer, D.; Kryschi, C., Surface Functionalization and Electrical Discharge Sensitivity of Passivated Al Nanoparticles. *ACS Omega* **2017,** *2* (1), 52-61.

30. Risse, B.; Hassler, D.; Spitzer, D. Preparation of Nanoparticles by Flash Evaporation. US20150000846A1, 2015.

31. Risse, B.; Spitzer, D.; Hassler, D.; Schnell, F.; Comet, M.; Pichot, V.; Muhr, H., Continuous Formation of Submicron Energetic Particles by the Flash-Evaporation Technique. *Chem. Eng. J.* **2012,** *203*, 158-165.

32. Ghosh, M.; Venkatesan, V.; Sikder, N.; Sikder, A. K., Quantitative Analysis of α-CL-20 Polymorphic Impurity in ε-CL-20 Using Dispersive Raman Spectroscopy. *Cent. Eur. J. Eenerg. Mat.* **2013,** *10.*

33. Brand, H. V.; Rabie, R. L.; Funk, D. J.; Diaz-Acosta, I.; Pulay, P.; Lippert, T. K., Theoretical and Experimental Study of the Vibrational Spectra of the α, β, and δ Phases of Octahydro-1, 3, 5, 7-tetranitro-1, 3, 5, 7-tetrazocine (HMX). *The Journal of Physical Chemistry B* **2002,** *106* (41), 10594-10604.

34. Goetz, F.; Brill, T., Laser Raman Spectra of Alpha.-, Beta.-, Gamma.-, and Delta-octahydro-1, 3, 5, 7-tetranitro-1, 3, 5, 7-tetrazocine and Their Temperature Dependence. *J. Phys. Chem.* **1979,** *83* (3), 340-346.

35. Iqbal, Z.; Bulusu, S.; Autera, J. R., Vibrational Spectra of β-Cyclotetramethylene Tetranitramine and some of Its Isotopic Isomers. *J. Chem. Phys.* **1974,** *60* (1), 221-230.

36. Infante-Castillo, R.; Pacheco-Londoño, L.; Hernández-Rivera, S. P., Vibrational Spectra and Structure of RDX and its 13C-and 15N-Labeled Derivatives: A Theoretical and Experimental Study. *Spectrochim. Acta A* **2010,** *76* (2), 137-141.

37. Deckert-Gaudig, T.; Pichot, V.; Spitzer, D.; Deckert, V., High-Resolution Raman Spectroscopy for the Nanostructural Characterization of Explosive Nanodiamond Precursors. *ChemPhysChem* **2017,** *18* (2), 175-178.

38. Miao, M. S.; Dreger, Z. A.; Winey, J. M.; Gupta, Y. M., Density Functional Theory Calculations of Pressure Effects on the Vibrational Structure of α-RDX. *The Journal of Physical Chemistry A* **2008,** *112* (47), 12228-12234.

39. Dreger, Z. A.; Gupta, Y. M., High Pressure Raman Spectroscopy of Single Crystals of Hexahydro-1,3,5-trinitro-1,3,5-triazine (RDX). *The Journal of Physical Chemistry B* **2007,** *111* (15), 3893-3903.

40. Liu, Y.; Perkins, R.; Liu, Y.; Tzeng, N., Normal Mode and Experimental Analysis of TNT Raman Spectrum. *J. Mol. Struct.* **2017,** *1133*, 217-225.

41. Clarkson, J.; Smith, W. E.; Batchelder, D. N.; Smith, D. A.; Coats, A. M., A Theoretical Study of the Structure and Vibrations of 2, 4, 6-Trinitrotolune. *J. Mol. Struct.* **2003,** *648* (3), 203-214.

42. Bolukbasi, O.; Yilmaz, A., X-ray structure analysis and vibrational spectra of Furosemide. *Vib. Spectrosc.* **2012,** *62*, 42-49.

43. Mao, H.; Feng, J.; Ma, X.; Wu, C.; Zhao, X., One-dimensional silver nanowires synthesized by self-seeding polyol process. *J. Nanopart. Res.* **2012,** *14* (6), 887.

Abbreviations

a	nanoparticle radius
AFM	atomic force microscopy
AFM-TERS	atomic force microscopy – tip enhanced Raman spectroscopy
CL-20	2,4,6,8,10,12-hexanitro-2,4,6,8,10,12-hexaazaisowurtzitane
CL-20/HMX	CL-20/HMX co-crystal
CT	charge transfer
DFT	density functional theory
DFT-D	dispersion-corrected density functional theory
$\vec{E}$	electric field vector
E_{el}	electronic energy
$\vec{E}_{in}$	electric field vector of incident light
$E(\lambda)$	extinction spectrum
E_{nuc}	nuclear energy
E_{rot}	rotational energy
E_{tot}	total energy
E_{trans}	translational energy
E_{vib}	vibrational energy
EDX	energy dispersive X-ray spectroscopy
EF	enhancement factor
Eout, Eout'	enhanced field
F	fluorescence
f_{rot}	rotational degree of freedom
f_{tot}	total degree of freedom
f_{trans}	translational degree of freedom
f_{vib}	vibrational degree of freedom
$\vec{F}_C$	restoring force from Coulomb attraction
$\hat{H}$	Hamiltonian

h	Planck's constant
$\hbar$	reduced Planck's constant
H_v	Hermite polynomials
HMX	1,3,5,7-tetranitro-1,3,5,7-tetrazocane
I(R)	Raman intensity
IC	internal conversion
IR A	infrared absorption
ISC	intersystem crossing
k	force constant
LSP	localized surface plasmon
LSPR	localized surface plasmon resonance
m	mass
N	number of nanoparticles
NA	numerical aperture
ND-x/y	nanodiamonds synthesized from SFE-x/y
NIR	near-infrared light
NUV	near-ultraviolet light
$\hat{o}$	transition operator
$\hat{p}$	momentum operator
P	phosphorescence
p-60/40	physically mixed hexolite with a mass ratio of 60/40 (RDX/TNT)
q	normal coordinate
r	radial distance
RDX	1,3,5-Trinitro-1,3,5-triazine
S	electronic singlet
SECoRM	surface enhanced confocal Raman microscopy
SEM	scanning electron microscopy
SERS	surface enhanced Raman spectroscopy
SFE	Spray Flash Evaporation
SFE-x/y	SFE produce hexolite nanoparticles with a mass ratio RDX/TNT

SPM	scanning probe microscopy (or microscope)
STM	scanning tunnel microscopy (or microscope)
$\hat{T}$	kinetic energy operator
T	electronic triplet state
TEM	transmission electron microscopy
TERS	tip enhanced Raman spectroscopy
TNT	2-Methyl-1,3,5-trinitrobenzene
UV-VIS A	UV-Vis absorption
v	vibrational energy state
V	virtual state
ν	frequency
$\hat{V}$	potential energy operator
VIS	visible light
x, y, z	cartesian coordinates
$\vec{x}, \vec{y}, \vec{z}$	vectors of a cartesian coordinate system
XPS	X-ray photoelectron spectroscopy
XRPD	X-ray powder diffraction
$\hat{\alpha}$	polarizability operator
$\alpha_{v_0 \to v_1}^{trans}$	polarizability transition moment integral
$\tilde{\alpha}$	polarizability tensor
$\Gamma_{\phi_0 \hat{\alpha} \phi_1}$	product of the irreducible representations Γ_{ϕ_0}, $\Gamma_{\hat{\alpha}}$ and Γ_{ϕ_1}
$\Gamma_{\hat{\alpha}}$	irreducible representation of $\hat{\alpha}$
Γ_{ϕ_0}	irreducible representation of ϕ_0
Γ_{ϕ_1}	irreducible representation of ϕ_1
$\varepsilon_i(\lambda)$	imaginary components of metal dielectric function
ε_{in}	metal dielectric constant
$\varepsilon_{in}(\lambda)$	metal dielectric function
ε_{out}	dielectric constant of the environment
$\varepsilon_r(\lambda)$	real components of metal dielectric function
μ	induced dipole moment

λ	wavelength
ϕ	vibrational wavefunction
ϕ^*	complex conjugated vibrational wavefunction
χ	shape factor
ψ	wavefunction
ψ^*	complex conjugated wavefunction
ω	angular frequency

Jakob HÜBNER

Structure Investigation of Energetic and Pharmaceutical Nanocomposites via AFM-TERS and SERS

Résumé

La spectroscopie Raman exaltée par effet de pointe basée sur la microscopie à force atomique (AFM-TERS) est utilisée pour étudier la structure de divers composites énergétiques et pharmaceutiques à l'échelle nanométrique.

Les études AFM-TERS sur des co-cristaux de CL-20/HMX à l'échelle nanométrique démontrent que les surfaces de CL-20/HMX sont constituées d'une couche moléculaire de HMX. Les résultats expérimentaux sont étayés par une approximation des coordonnées vibratoires normales permettant d'exclure l'apparition d'intensités Raman relativement fortes liées au HMX en raison d'un arrangement spécifique entre les nanocristaux de CL-20/HMX et les systèmes de diffusion Raman.

Différents mélanges RDX et TNT à l'échelle nanométrique, dont le rapport en pourcentage massique est différent, sont analysés par AFM-TERS. La combinaison de la spectroscopie Raman en champ lointain et du TERS sensible à la surface a permis l'identification de nanoparticules anisotropes RDX/TNT cœur/coquille.

Les particules de furosémide-PVP submicroniques sont étudiées par microscopie Raman confocale à champ lointain et la microscopie Raman exaltée de surface. Pour ce faire, les particules de furosémide-PVP sont directement pulvérisées avec de fines couches d'argent. La comparaison des spectres Raman en champ lointain et en champ proche révèle que les coquilles de PVP encapsulent des noyaux de furosémide.

Mots-clés: AFM-TERS, SERS, microscopie Raman confocale, nano-composites, cœur-coquille

Résumé en anglais

Tip Enhanced Raman Spectroscopy based on Atomic Force Microscopy (AFM-TERS) is applied to study the structure of diverse nanoscale energetic and pharmaceutical composites.

AFM-TERS investigations of nanoscale CL-20/HMX co crystals demonstrate that CL-20/HMX surfaces consist of a molecular layer of HMX. Experimental results are supported by an approximation of vibrational normal coordinates allowing to exclude the appearance of relatively strong HMX Raman intensities because of a specific arrangement between CL-20/HMX nano co crystals and the Raman scattering systems.

Diverse nanoscale RDX and TNT mixtures differing in their weight percentage ratio are analyzed with AFM-TERS. The combination of far-field Raman spectroscopy and surface sensitive TERS enabled the identification of anisotropic RDX/TNT core/shell nanoparticles.

Submicron Furosemide-PVP particles are investigated by confocal far-field Raman microscopy and Surface Enhanced Raman microscopy. For this purpose, Furosemide-PVP particles are directly sputtered with thin layers of silver. The comparison of far- and near-field Raman spectra reveals that shells of PVP encapsulate Furosemide cores.

Key words: AFM-TERS, SERS, confocal Raman microscopy, nano-composites, core/shell